PHILIPPS-UNIVERSITÄT MARBURG

KUMULATIVE DISSERTATION

Processing of Polarization Patterns and Visual Self-Motion in the Locust Central Complex for Spatial Orientation

Zur Erlangung des Grades
Doktor der Naturwissenschaften
(Doctor rerum naturalium)

des Fachbereichs Biologie der Philipps-Universität Marburg

Vorgelegt von
Frederick Zittrell
aus Nördlingen

Marburg (Lahn), 2021

Die vorliegende Dissertation wurde von Februar 2016 bis Dezember 2021 am Fachbereich Biologie, Fachgebiet Tierphysiologie, Abteilung Neuroethologie unter Leitung von Prof. Dr. Uwe Homberg angefertigt.

Vom Fachbereich Biologie der Philipps-Universität Marburg (Hochschulkennziffer 1180) als Dissertation angenommen am: 07.12.2021

Erstgutachter: Prof. Dr. Uwe Homberg

Zweitgutachterin: Prof. Dr. Monika Hassel

Drittgutachter: Prof. Dr. Frank Bremmer

Tag der Disputation: 25.02.2022

Declaration of Authorship

I, Frederick Zittrell, declare that this thesis entitled, "Processing of Polarization Patterns and Visual Self-Motion in the Locust Central Complex for Spatial Orientation" was authored by myself alone without external help. I confirm that:

- I have not composed a dissertation in pursuit of this academic degree before, not at this university or any other institution.
- It is clearly stated where any part of this thesis has previously been submitted for a degree or any other qualification at this University or any other institution.
- It is clearly attributed where I have consulted the published work of others.
- Where the thesis is based on work done by myself jointly with others, I have made clear exactly what was done by others and what I have contributed myself.
- I have acknowledged all main sources of help.

Signed:

Date:

Declaration of Own Contributions

Chapter 1: Two Compasses in the Central Complex of the Locust Brain

This chapter is published as: Pegel U, Pfeiffer K, Zittrell F, Scholtyssek C, and Homberg U (2019). "Two compasses in the central complex of the locust brain". *J. Neurosci.* 39, pp. 3070–3080. DOI: 10.1523/JNEUROSCI.0940-18.2019.

It is part of a previous dissertation (Pegel, 2018). My contributions are:

- Contribution of analysis code necessary for the core conclusion of the article (Fig. 3) and for a secondary finding (Fig. 5).
- Text descriptions regarding these analyses.
- Copy editing of the manuscript.

Chapter 2: Matched-Filter Coding of Sky Polarization Results in an Internal Sun Compass in the Brain of the Desert Locust

This chapter is published as: Zittrell F, Pfeiffer K, and Homberg U (2020). "Matched-filter coding of sky polarization results in an internal sun compass in the brain of the desert locust". *Proc. Natl. Acad. Sci. U.S.A.* 117.41, pp. 25810–25817. DOI: 10.1073/pnas.2005192117.

My contributions are:

- Acquisition (animal dissection, experiment performance, histological processing, and histological image acquisition) of 22 out of 23 data sets.
- Experimental design: Equipment setup and stimulation protocol based on a previous publication (Bech et al., 2014).
- Design of all analysis code based on a core conception from Prof. Dr. Keram Pfeiffer.
- Analysis of all data sets and composition of all figures.
- Drafting of the manuscript with editorial support from Prof. Dr. Keram Pfeiffer and Prof. Dr. Uwe Homberg.

Chapter 3: Receptive Field Structures for Two Celestial Compass Cues at the Input Stage of the Central Complex in the Locust Brain

This chapter has been submitted for publication in the *Journal of Experimental Biology* on 01.12.2021 as: Takahashi N, Zittrell F, Hensgen R, and Homberg U. **takahashiReceptiveFieldStructures**.

My contributions are:

- Contribution of analysis code necessary for core conclusions of the article.
- Copy editing of the manuscript.

Chapter 4: Performance of Polarization-Sensitive Neurons of the Locust Central Complex at Different Degrees of Polarization

This chapter has been submitted for publication in the *Journal of Comparative Physiology A* on 08.09.2021 as: Hensgen R, Zittrell F, Pfeiffer K, and Homberg U. **hensgenPerformancePolarizations**

My contributions are:

- Design of all analysis code including figure generating code (Figs. 4–7).
- Text descriptions for the implemented analysis algorithms and figures.
- Copy editing of the manuscript.

Chapter 5: Flexible Integration of Visual Self-Motion Cues in Locust Central Complex Neurons

This chapter has been submitted for publication in the *Journal of Neuroscience* on 18.11.2021 as: Zittrell F, Carlomagno E, Pabst K, Rosner R, Endres D, and Homberg U. "Flexible integration of visual self-motion cues in locust central complex neurons".

My contributions are:

- Acquisition (animal dissection, experiment performance, histological processing, and histological image acquisition) of 43 out of 62 data sets. Two data sets were already presented in a previous dissertation (Pegel, 2018).
- Experimental design: Equipment setup and stimulation protocol.
- Design of all analysis code for experiments (excluding computational modelling).
- Analysis of all data sets and composition of Figs. 1–8. Fig. 9 (the computational model) and associated texts were contributed by co-authors.
- Drafting of the manuscript with editorial support from Prof. Dr. Uwe Homberg and Dr. Ronny Rosner.

Chapter 6: A Unified Platform To Manage, Share, and Archive Morphological and Functional Data in Insect Neuroscience

This chapter is published as: Heinze S, el Jundi B, Berg BG, Homberg U, Menzel R, Pfeiffer K, Hensgen R, Zittrell F, Dacke M, Warrant E, Pfuhl G, Rybak J, and Tedore K (2021). "A unified platform to manage, share, and archive morphological and functional data in insect neuroscience". *eLife* 10, e65376. DOI: 10.7554/eLife.65376.

My contributions are:

- Contribution of experimental data for data base testing and validation.
- Implementation of a MATLAB interface for programmatic access to the online data base (github.com/zifredder/IBdb-matlab).
- Copy editing of the manuscript.

References

Bech M, Homberg U, and Pfeiffer K (2014). "Receptive fields of locust brain neurons are matched to polarization patterns of the sky". *Curr. Biol.* 24.18, pp. 2124–2129. DOI: 10.1016/j.cub.2014.07.045.

Pegel U (2018). "Processing of sky compass cues and wide-field motion in the central complex of the desert locust (*Schistocerca gregaria*)". PhD thesis. Philipps-Universität Marburg.

Zusammenfassung

Trotz ihrer relativ kleinen Gehirne und vergleichsweise geringen Anzahl an Nervenzellen zeigen Insekten komplexes Navigationsverhalten. Navigation erfordert einen Sinn für die aktuelle Bewegungsrichtung im Raum. Diese Richtung ist relativ, sie muss deshalb an markante externe Punkte gebunden sein und kontinuierlich durch interne, aus der Eigenbewegung entstehende Signale korrigiert werden.

Der Sonnenstand kann als globaler externer Ankerpunkt für Navigation dienen. Sonnenlicht wird durch Streuung in der Atmosphäre polarisiert, wodurch ein systematisches Muster an Polarisationswinkeln im Himmel entsteht, das wie die Sonne selbst als externe Referenz dienen kann. Intern erzeugt Fortbewegung optischen Fluss – die Bewegung des Umgebungsbildes auf der Retina. Daraus können Drehbewegungen, Geschwindigkeit und die zurückgelegte Strecke abgeleitet werden. Viele Insekten nutzen diese externen und internen Signale zur Orientierung; im Gehirn bildet vermutlich der Zentralkomplex (ZK) das Navigationszentrum. In diesem Gehirnareal führt die Verarbeitung sensorischer Informationen zur Entstehung eines internen Kompass-Signals, das fortlaufend die Körperausrichtung widerspiegelt.

Diese Dissertation beschäftigt sich mit der Verarbeitung von Himmelskompass-Signalen, im Speziellen dem Polarisationsmuster, und optischem Fluss im ZK der Wüstenheuschrecke, einem über weite Strecken migrierenden Insekt. Alle Kapitel mit Ausnahme von Kapitel 6 sind elektrophysiologische Arbeiten, bei denen einzelne Nervenzellen intrazellulär abgeleitet und gleichzeitig das Tier visuell stimuliert wurde. Durch Farbstoff-Injektion konnte die Zellanatomie nachvollzogen werden und auf die Rolle im Nervensystem geschlossen werden.

Kapitel 1 und 2 zeigen, dass im ZK ein neuronaler Kompass implementiert ist, der sowohl durch Verarbeitung direkten Sonnenlichts als auch des Polarisationsmusters die Sonnenposition anzeigt. Das zeigt, dass das Heuschreckengehirn verschiedene Himmelskompass-Signale so verarbeitet, dass ein einheitliches Kompass-Signal entsteht, das Navigation unter unterschiedlichen Umweltbedingungen ermöglicht.

Darauf aufbauend wird in Kapitel 3 beleuchtet, wie in der Eingangs-Station des ZK Himmelskompass-Signale verarbeitet werden. Einzelne Zellen integrieren schon auf dieser Ebene visuelle Eindrücke über große Bereiche des Himmels und verfügen über rezeptive Felder, mit denen das Himmelskompass-Signal gebildet werden kann.

In Kapitel 4 wird die Wahrnehmungs-Schwelle für den Polarisationswinkel untersucht und gezeigt, dass ZK-Zellen in dieser Hinsicht hochsensitiv sind und deshalb nahezu das gesamte Polarisationsmuster des Himmels analysieren können.

Kapitel 5 behandelt die Verarbeitung optischen Flusses. Auf fast allen Netzwerk-Ebenen des ZK reagieren Einzelzellen auf optische Flussreize, und zwar weitgehend unabhängig von der Empfindlichkeit für Himmelskompass-Signale. Das impliziert, dass die Verarbeitung sensorischer Eindrücke im ZK vom Verhaltenskontext abhängt. Ferner wird gezeigt, wie Drehbewegungen verarbeitet werden könnten, um das interne Kompass-Signal zu justieren, gestützt durch eine rechnerische Modellierung, die auf anatomischen und physiologischen Daten basiert. Zusammengenommen tragen diese Arbeiten zum Verständnis dessen bei, wie im Insektengehirn die Verarbeitung externer und interner Sinneseindrücke dazu führt, den Orientierungssinn zu formen.

Schließlich trug ich mit Datensätzen und Programmcode zur Entwicklung der *InsectBrainDatabase* (`insectbrainDB.org`) bei, einer frei zugänglichen Onlineplattform für die Verwaltung, Verteilung und Publikation von Forschungsdaten (Kapitel 6).

Abstract

Despite their relatively small brains with comparatively low neuron counts, insects show complex navigation behavior such as seasonal long-range migration, path integration, and precise straight-line movement. Spatial navigation requires a sense of current heading, which must be tethered to prominent external cues and updated by internal cues that result from movement.

Global external cues such as the position of the sun may provide a reference frame for orientation. Sunlight is polarized by scattering in the atmosphere, which results in a sky-spanning polarization pattern that directly depends on the current solar position and makes polarization information, like the sun itself, useful as an external reference cue. Internally, moving through the environment generates optic flow—the motion of the viewed scenery on the retina—, which may inform about turning maneuvers, movement speed, and covered distance. Many insects use these external and internal cues for orientation, and the neuronal center for spatial navigation likely is the central complex, a higher-order brain structure where sensory information is integrated to form an internal compass representation of the current heading.

This thesis addresses the question how celestial compass cues, specifically the polarization pattern, and optic flow are processed in the central complex of the desert locust, a long-range migratory insect. All chapters except the last one are electrophysiological studies in which single central-complex neurons were intracellularly recorded while presenting visual stimuli. The neurons' anatomy was histologically determined by dye injection in order to infer their role in the neural network.

The studies in Chapters 1 and 2 show that the central complex contains a neuronal compass that robustly signals the sun direction based on direct sunlight and the integration of the whole solar polarization pattern. This shows that the locust brain uses all available skylight cues in order to form a unified compass signal, enabling robust navigation under different environmental conditions.

The study in Chapter 3 further examines how neurons at the input stage of the central complex process skylight cues. Already at this stage, single neurons integrate visual information from large areas of the sky and have receptive fields suitable to build the skylight compass.

Chapter 4 sheds light on the detection sensitivity for the angle of polarization, finding that central-complex neurons are highly sensitive in this regard, adapted to analyze the skylight polarization pattern almost in its entirety and under unfavorable environmental conditions.

In Chapter 5 the locust central complex was scanned for neurons that receive optic flow information. Neurons at virtually all network stages are sensitive to optic flow, mainly uncoupled from skylight-cue sensitivity. This highlights that sensory information is flexibly processed in the central complex, presumably depending on the animal's current behavioral demands. Further, the study hypothesizes how horizontal turning motion is processed in order to update the internal heading representation, backed up by a computational model that adheres to brain anatomy and physiological data. Altogether, these studies advance the understanding of how external and internal cues are processed in the central-complex network in order to establish a sense of orientation in the insect brain.

Finally, I contributed with data sets and programming code to the development of the *InsectBrainDatabase* (`insectbrainDB.org`), a free online database tool designed to manage, share and publish anatomical and functional research data (Chapter 6).

Acknowledgements

Above all I am grateful to Prof. Dr. Uwe Homberg for the opportunity to work on this topic, who always had an open office door and provided benevolent guidance at all times. I thank Prof. Dr. Keram Pfeiffer for our invaluable interchange, both professional and personal. Thanks to all members of the department with whom I worked and laughed. Gratitude is due to Martina Kern for keeping the laboratory running and the locusts breeding.

Finally, thanks to my close friends and family from whom I have never received anything but support.

Contents

Introduction

Having a sense of direction is crucial, as virtually any active behavior requires knowledge about the current spatial location, be it relative—like being in front of a conspecific, close to a food source, or out of a predator's range—or be it absolute, such as 300 m south of one's home. Therefore, physicists, philosophers, psychologists, and, most important for this thesis, neuroethologists have asked what "sense of direction" actually means and how it comes about in a living being (reviewed by O'Keefe and Nadel (1978)). The hippocampal formation was discovered as the neuronal center of this sense in mammals decades ago (reviewed by Moser et al. (2017)) and is still under active investigation (Finkelstein et al., 2016).

In insect brains, the neuronal orientation headquarter was identified rather recently: The so-called central complex is an unpaired group of neuropils sitting in the brain's center, wired downstream of sensory organs and upstream of the locomotor system (Fig. 1A–D). It is crucial for navigation (reviewed by Pfeiffer and Homberg (2014), Heinze (2017), and Honkanen et al. (2019)) and the object of study in this thesis. More precisely, I engaged with the desert locust, a long-range migrator, and asked how specific visual signals are processed in its central complex so the locust can find its way. "Asking" in this case means using experimental electrophysiology—in layman's terms: Sticking an electroconductive glass needle in the brain of an immobilized, alive locust in order to measure the activity of a single nerve cell while the animal is being shown something interesting; the cell is then injected with a dye so its morphology can be microscopically identified afterwards. I approached this research question in the context of different projects. The following introductory sections are aimed to give an informal overview of each of these projects.

Why insects and why the locust? Insect brains are simpler than vertebrate brains in terms of neuron numbers and the cells are generally much larger, especially in the desert locust, which makes it easier to study single neurons in a working brain. Further, in contrast to vertebrates, the identity of nerve cells is highly conserved in insects, so the same cell at the very same place in the brain can be found again in a different individual. Consequently, an identified neuron likely does the same job in each individual animal, so the brain can be explored cell by cell, experiment after experiment. Neuron morphology is so conserved in insects that the same neuron can often be found even in a different species, thus findings from one species, for instance the fruit fly—probably the most-researched insect—, are highly relevant for research in other species, making insect neuroscience a large and diverse field.

Two Compasses in the Central Complex of the Locust Brain .... Chapter 1

In order to fly a long distance in a specific direction, locusts need some kind of spatial reference—similar to when a human decides to go west for two hours, they need to have an idea of where west is. A human could simply use a magnetic compass device; a locust must get this information from somewhere else.

The sun is a reliable source of global compass information: If visible—or rather, *not occluded*—, it is a glaring stationary spot in the sky that can easily be used as a reference direction in order to keep a steady course (Fig. 2A). If occluded by clouds or trees, the one half of the sky where the sun is currently positioned is visibly brighter,

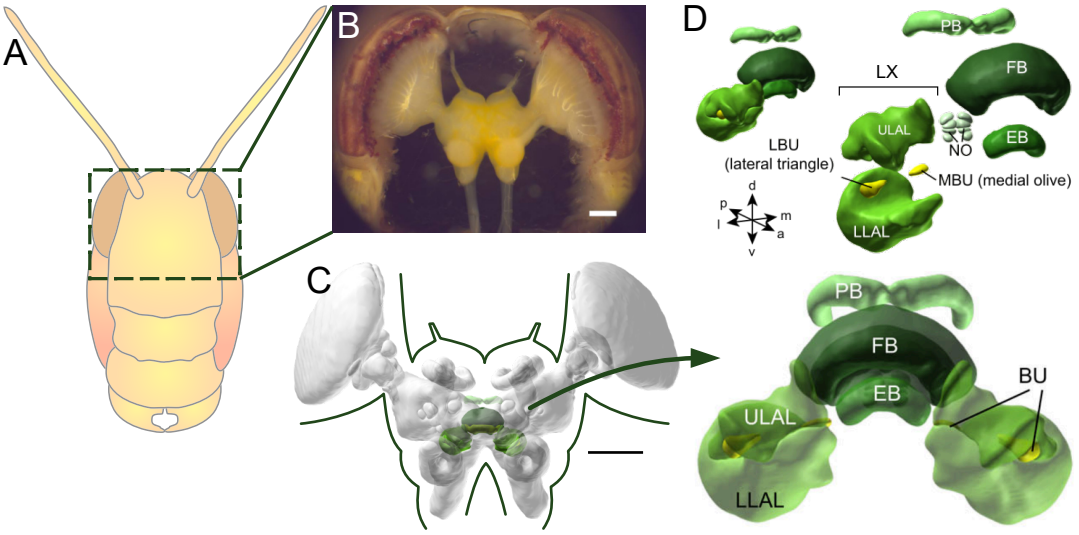

FIGURE 1: The locust central complex (CX). (**A–C**) Frontal view of a schematized locust head, brain preparation and three-dimensional model of brain areas (neuropils) with the CX and LX, a closely associated neuropil formation, colored. (**D**) Detailed three-dimensional models of the CX neuropils and LX. Scale bars in *B* and *C* 500 µm. Locust head in *A* from Turner-Evans and Jayaraman (2016), photo in *B* from Dominik Aumann, CX model in *C* generated with `insectbrainDB.org` based on data from Kurylas et al. (2008), *D* from Honkanen et al. (2019), modified. Abbreviations: BU, bulb; EB, ellipsoid body; FB, fan-shaped body; LBU, lateral bulb; LLAL, lower shell of the LAL (lateral accessory lobe); LX, lateral complex; MBU, medial bulb; NO, nodulus; PB, protocerebral bridge; ULAL, upper shell of the LAL.

still providing a direction cue, although somewhat coarser (Fig. 2B). Further, insects are capable of distinguishing between the solar and anti-solar side because they can see UV light: Comparing the intensity of green and UV light in the sky can likewise inform about the solar side (el Jundi et al., 2014) (Fig. 2C). Lastly, insects possess specialized photoreceptors in their eyes to analyze the angle of polarization, allowing them to perceive the skylight polarization pattern (Labhart and Meyer, 1999), a sensory impression inaccessible to humans. This pattern results from atmospheric light scattering and spans the whole sky; it systematically depends on the solar position and can thus be used as a robust celestial orientation cue (Fig. 2D).

Single neurons in the locust central complex are tuned to these celestial cues, which means that a neuron's activity is higher when a cue has a particular orientation (the *preferred* orientation) relative to the locust, implying a function in celestial navigation (el Jundi et al., 2014; Pegel et al., 2018). The study (Pegel et al., 2019) in this chapter investigated whether neurons in specific cell populations are systematically tuned based their anatomic position in the brain, building up on a previously found compass-like organization (Heinze and Homberg, 2007). "Compass-like" means topographic tuning: Neurons tuned to similar cue-orientations are also physically close to one another; along the central complex, the individual cell tuning changes gradually—like a rotating compass needle (Fig. 3A,A'). Such a topographic tuning is common in specialized brain areas and heavily implies involvement in a specific task (Cang and Feldheim, 2013), spatial navigation in this case.

Indeed, the study found two compass representations (Fig. 3A–B'): A *sun compass*, meaning a compass for the solar azimuth (the horizontal component of the sun position) and a *polarization compass*, meaning a compass for the polarization angle of light in the animal's zenith (the celestial hemisphere's center, directly above the animal). This shows strong involvement of the central complex in celestial-cue processing; however, the compasses do not match: Figuratively, the two compass needles have different spin directions (Fig. 3A',B'), which suggests that different

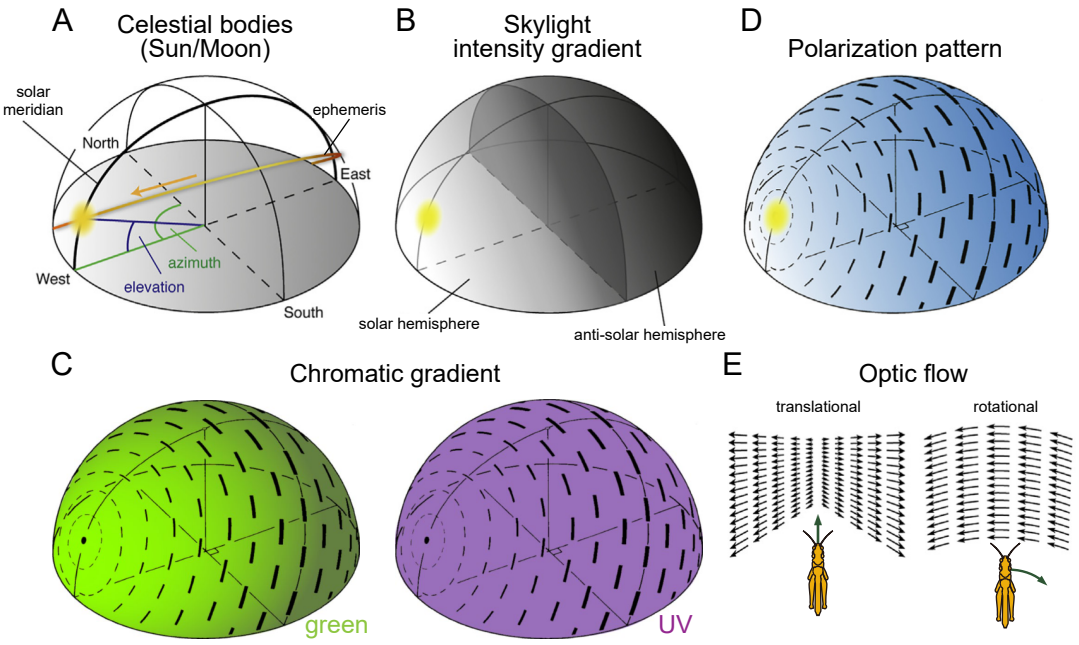

FIGURE 2: Examples of external and internal orientation cues. (**A**) Celestial bodies as orientation reference. The solar position can be described by the azimuth angle, the horizontal component, and the elevation angle, the vertical component. (**B–D**) The light-intensity gradient, chromatic gradient and polarization pattern provide information about the solar position. (**E**) Internally, self-motion generates optic flow on the retina, informing about the direction and speed of motion. *A, B, D,* and *E* from Heinze (2017), modified, and *C* from el Jundi et al. (2014), modified.

streams of information—direct sunlight versus scattered sunlight—are processed separately. This is intriguing because it seems much more reasonable to combine the information streams in order to form a unified compass.

Matched-Filter Coding of Sky Polarization Results in an Internal Sun Compass in the Brain of the Desert Locust ..... Chapter 2

In this project, I investigated the aforementioned polarization compass with higher spatial resolution. In most studies, polarization sensitivity is probed using a single stimulation point, namely the animal's zenith. This makes sense because, generally, the polarization detectors of insects are aimed at this point (Heinze, 2014). However, the sensitivity field of all detectors combined covers a large area of the sky (Schmeling et al., 2015), which makes sense evolutionarily because the celestial polarization pattern covers the whole sky (Fig. 3C).

A previous study showed that single locust central-complex neurons indeed respond to polarization angles from virtually the whole sky (Bech et al., 2014). Notably, the tuning pattern of a single neuron may match the polarization pattern as it is generated in the sky when the sun is at a particular position. Casually speaking, such a neuron *knows* what the polarization pattern looks like when the sun is in a particular direction and constantly compares reality with this expectation; if expectation and reality match, the neuron signals "I know where the sun is!". Such a tuning is termed *matched filter tuning* (Wehner, 1987), and a single neuron would code for a specific sun direction because it is tuned to the polarization pattern that arises from this specific sun position. Not all central-complex neurons are tuned like this, but it is widespread.

I expanded this knowledge by connecting matched-filter coding with the sun compass: It turned out that central-complex neurons topographically code for sun azimuth based on their matched-filter tuning (Fig. 3C′). Notably, this *matched-filter*

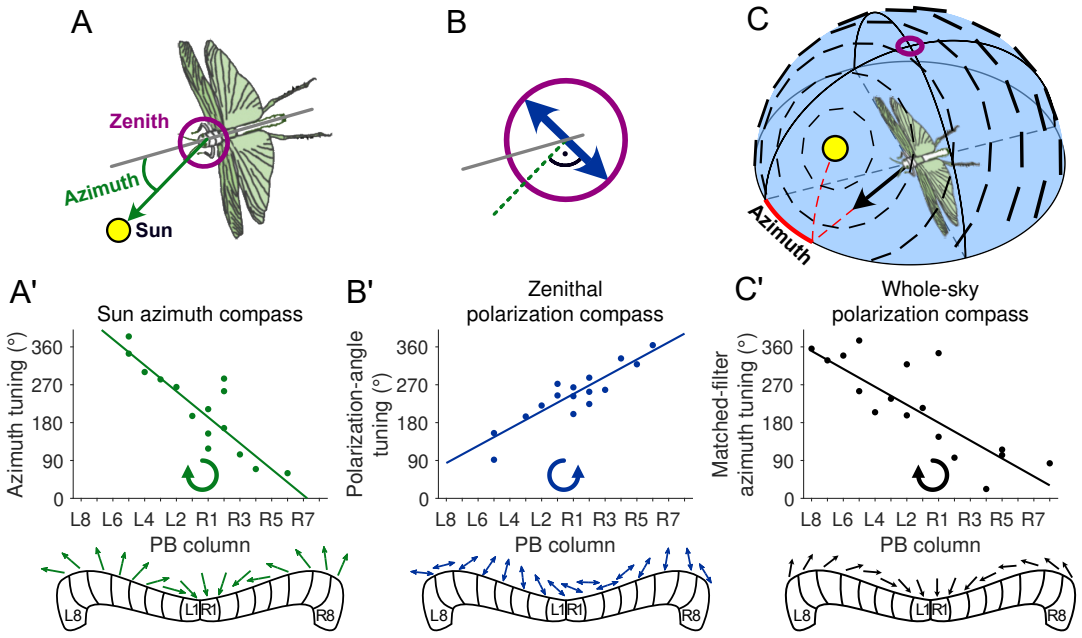

FIGURE 3: Compass-like cue tuning in the locust brain. (**A**) Schematic of a locust flying in a direction relative to the sun, viewed from above. The azimuth is the angle between the current heading and the horizontal sun direction (arrow), 30° in this case. (**B**) Polarization angle (double arrow) in the locust's zenith (directly above it), same point of view as in *A*. At any point in the sky, the angle of polarization has a 90° relationship to the great circle through this point and the sun. (**C**) Schematized polarization pattern as produced by the sun at 40° elevation and 30° azimuth. Bar orientation and thickness indicate angle of polarization and degree of polarization, respectively. (**A'–C'**) Topographic tuning of central-complex neurons to different cues. The tuning angle, meaning the preferred cue-angle of a single neuron, is significantly correlated with the column in the PB where the neuron arborizes. Each data point corresponds to one neuron. The circle-shaped arrow symbolizes the compass *spin direction*, indicating whether the tuning angle changes in clockwise (decreasing angle) or counterclockwise manner from L8 to R8. The bottom arrows symbolize this tuning change along the PB: Each arrow is directed in the preferred direction of a neuron in the respective PB column, according to the data regression line. (**A'**) Compass tuning of CPU1 neurons for the azimuth of a green LED that was rotated around the animal, simulating the sun. (**B'**) Compass tuning of the same set of CPU1 neurons for the angle of polarization in the animal's zenith, simulating skylight polarization. (**C'**) Compass tuning of different central-complex neurons for the matched-filter azimuth. This azimuth angle results from the collective tuning to polarization angles at different positions in the sky. The pattern of preferred angles matches the polarization pattern as it is produced by the sun at a particular azimuth and elevation. *A* and *B* adapted from Bockhorst and Homberg (2017), *C* and *A'*–*C'* reproduced from Zittrell et al. (2020) (see also Chapter 2 Fig. 1D,E on P. 27 and Chapter 2 Fig. 5B,C on P. 30). Abbreviations: PB, protocerebral bridge.

compass matches the *sun compass* described above: The internal compass needle keeps track of the locust's current orientation relative to the sun, irrespective of whether the sun itself is visible or only the polarization pattern that is generated from it. This resolves the previously found puzzling mismatch between polarization compass and sun compass (Fig. 3A',B'), likely because the previously reported polarization compass was based only on a single point of the polarization pattern. If the full pattern is taken into account, polarization compass and sun compass coincide (Fig. 3A',C'), making the orientation system flexible and robust.

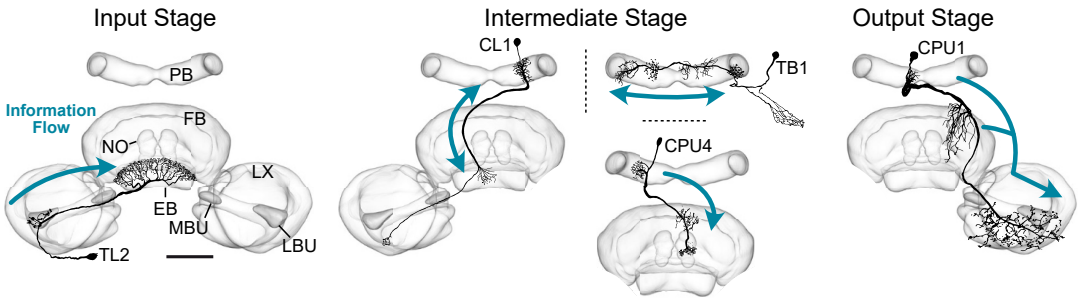

FIGURE 4: Processing stages in the central complex with selected neurons. TL2 neurons provide sensory input to neurons in the EB. CL1 neurons have mixed arborizations (in- and output) in both EB and PB, forming a feedback loop between the two neuropils. TB1 neurons have input and output sites distributed across the PB, interconnecting neurons in this neuropil. CPU4 neurons connect the PB with the FB and NO. CPU1 neurons provide output to the LX, where dendrites of descending neurons are located. Scale bar 100 µm. Image data from Pegel et al. (2018), modified. Abbreviations: EB, ellipsoid body; FB, fan-shaped body; LBU, lateral bulb; LX, lateral complex; MBU, medial bulb; NO, nodulus; PB, protocerebral bridge; ULAL, upper shell of the LAL.

Receptive Field Structures for Two Celestial Compass Cues at the Input Stage of the Central Complex in the Locust Brain ..... Chapter 3

The central complex is an intricate network consisting of different populations of neurons, each population characterized by neural anatomy: Neurons in the same population share similar morphological features such as branching pattern and the distribution of input and output synapses. In the context of the central complex, these populations can be categorized into different processing stages (Fig. 4). Much simplified, particular neuronal stages provide input to the central complex from other brain areas, for instance giving visual information. Intermediate stages within the central complex then perform the computations—the interpretation of input information in the animal's current behavioral context, such as feeding, resting, or flying. Finally, output stages relay the computation results again to other brain areas where the animal's actual behavior is controlled, for instance leading to a flight direction change (Honkanen et al., 2019).

In the previous project, I looked at neurons in intermediate stages and found the described whole-sky polarization compass (Fig. 3C′). This project—not a main project of myself but of a postdoc colleague—focused on an input stage, addressing the question how celestial cues are processed at this stage of the central-complex network. The data showed that already at the input stage to the central complex, single neurons have large receptive fields with sensitivity for direct sunlight and the polarization angle of light, meaning that they process visual input from large parts of the sky. Further, these receptive fields are specially organized, having different sectors where the neuron is excited or inhibited by direct sunlight. These neurons are not matched-filter tuned to the solar polarization pattern, so their downstream partners in the intermediate stage probably gain this feature by summing up the signals from the input stage, thereby forming the compass signal.

Performance of Polarization-Sensitive Neurons of the Locust Central Complex at Different Degrees of Polarization ..... Chapter 4

As we have seen, locust central-complex neurons are tuned to the skylight polarization pattern as a whole, which may lead to the naive assumption that locusts are able to *detect* the whole pattern of polarization angles. However, the degree of polarization (the percentage of light that is polarized) is not constant across the pattern (Fig. 2D,

the bar thickness indicates polarization degree). Instead under ideal conditions (clear sky) it systematically varies between zero (direct sunlight) and 75 % (90° away from the sun), and it may be disturbed by haze, clouds, or dust. Similar to when a light is too dim for us to see, insects cannot perceive the angle of polarization if the degree of polarization is too low. Only, how much is too low—where is the locust's sensitivity threshold? The threshold of the photoreceptors (Schmeling et al., 2015) and some non-central-complex neurons (Pfeiffer et al., 2011) is known, but this threshold is not necessarily passed on along the signal processing chain to the central complex.

This study—again a colleague's project—aimed to close this knowledge gap by analyzing locust central-complex neurons from different processing stages for their sensitivity threshold. The data show that these neurons are capable of detecting the angle of polarization at degrees as low as 5 %, a level that occurs under completely overcast skies (Labhart, 1996). This again illustrates how effective the polarization-vision system in locusts was built by evolution.

Flexible Integration of Visual Self-Motion Cues in Locust Central Complex Neurons . . . . . Chapter 5

Skylight cues provide a universally available large-scale reference frame for directions. However, the current direction must also be kept up to date on a smaller scale and when skylight cues are unavailable. To this end, animals use optic-flow information, which means that they keep track of the current image of their surroundings and interpret the speed and direction of image shifts as self motion (Fig. 2E). Exemplified, the street scenery left and right passes by slower or faster, depending on how fast you are driving, which gives an impression of driving speed, and it unmistakably tells you whether you are going forward or backward.

Insects use optic-flow information for orientation behavior (Srinivasan, 2015) and it is known from research on fruit flies that the internal compass in the central complex combines many kinds of information in order to keep track of the current heading direction (reviewed by Honkanen et al. (2019) and Hulse and Jayaraman (2020)). "Internal compass" here means that along a brain region, a neuron population keeps track of a specific, but arbitrary, spatial direction—maybe where a large tree is. When turning left or right, this internal compass needle must be rotated so it still points in the direction of the tree, telling other brain areas that a turning maneuver just happened (Fig. 5). Optic flow is a good indicator of turning movement and likely rotates the internal compass needle in the insect central complex. However, it is unknown at which network stage optic-flow information is fed in.

I investigated this question by visually simulating self-motion in different directions to locusts and searching for central-complex neurons that react to this simulation (Fig. 6). Surprisingly, neurons almost anywhere in the central complex are sensitive to visual self-motion, however, not always: The same neuron in different individuals may or may not be motion sensitive, likely depending on the current inner state of the individual animal—whether or not paying attention to optic flow is currently important. This state may be influenced by the animal's individual history, whether it is currently hungry, the time of day, inner motivation, and many more unknowns—a state that can hardly be measured or controlled experimentally. Most of these neurons also process skylight cues, also optionally, and mainly independent of motion sensitivity. This shows that diverse central-complex neurons can flexibly integrate different cues and that there is no specific network node designated for processing optic flow; the current context decides. However, data from specific neurons that were mirror symmetrically tuned to left and right turning motion allowed to hypothesize how the locust's internal heading signal might be kept up to date during horizontal turns. This computational process is well understood in the fruit fly (Fig. 5), but probably

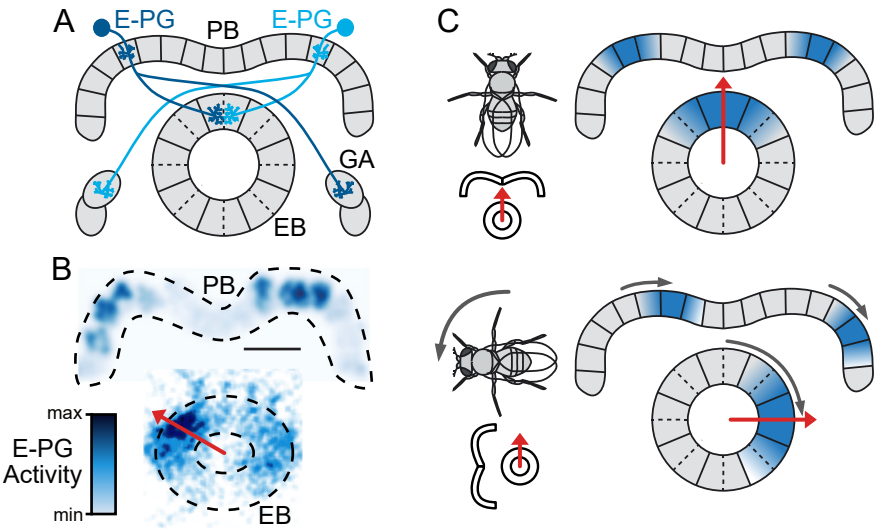

FIGURE 5: The internal compass in the fruit fly brain. (**A**) Schematic of the fruit fly's central complex with one pair of E-PG neurons, which carry the internal compass signal. These neurons are analogous to CL1 neurons in the locust. Note that here the EB forms a closed ring as opposed to the locust EB. (**B**) Snapshot of the E-PG neuron population activity, visualized by a fluorescent calcium indicator. The activity peak in the EB tracks the fly's heading based on the peak's position, or phase angle, along the EB (arrow). Due to E-PG morphology (see *A*), this peak results in two peaks with constant distance along the PB. (**C**) The E-PG activity peak is shifted due to horizontal turning. The peak's phase angle is tethered to an arbitrary horizontal direction (top), in this case pointing forward. When the fly turns (bottom), the peak is shifted along the EB so that the phase angle matches the initial direction, thereby tracking the fly's heading during turning like a compass. Scale bar for PB in *A* 20 µm. Central-complex scheme, fly drawing, and PB activity image from Green et al. (2017), modified, EB activity image from Turner-Evans et al. (2017), modified, and *C* adapted from Lu et al. (2020). Abbreviations: EB, ellipsoid body; GA, gall; PB, protocerebral bridge.

works differently in other insects, and this study gives insight into how it may be implemented in the locust.

A Unified Platform To Manage, Share, and Archive Morphological and Functional Data in Insect Neuroscience ..... Chapter 6

This last chapter presents a free online research tool for insect neuroscience, the *InsectBrainDatabase* (`insectbrainDB.org`), a joint project of several research groups. The database is intended to store research data of various types: Three-dimensional reconstructions of selected insect brains—such as the desert locust (Fig. 1C,D)—, single-cell stainings of identified neurons (Fig. 4) and physiological measurements, such as intracellular recordings (Fig. 6). Via a browser interface data can be uploaded, administered, and shared. The database can be conveniently searched for specific cell types or brain regions and the results are visualized in high quality (Fig. 7A). The platform is specifically designed to contain data from different species (Fig. 7B), making it easy to find similarities and differences between insects, paving the way for comparative meta studies.

I contributed substantial data sets of electrophysiological and morphological findings in the locust and validated the platform's functions and usability, supporting its expansion and development. Further, I developed a programming interface for MATLAB, a widespread script-based application for data analysis, that can be used to programmatically access the platform (`github.com/zifredder/IBdb-matlab`). This allows for direct integration of the *InsectBrainDatabase* into a researcher's existing

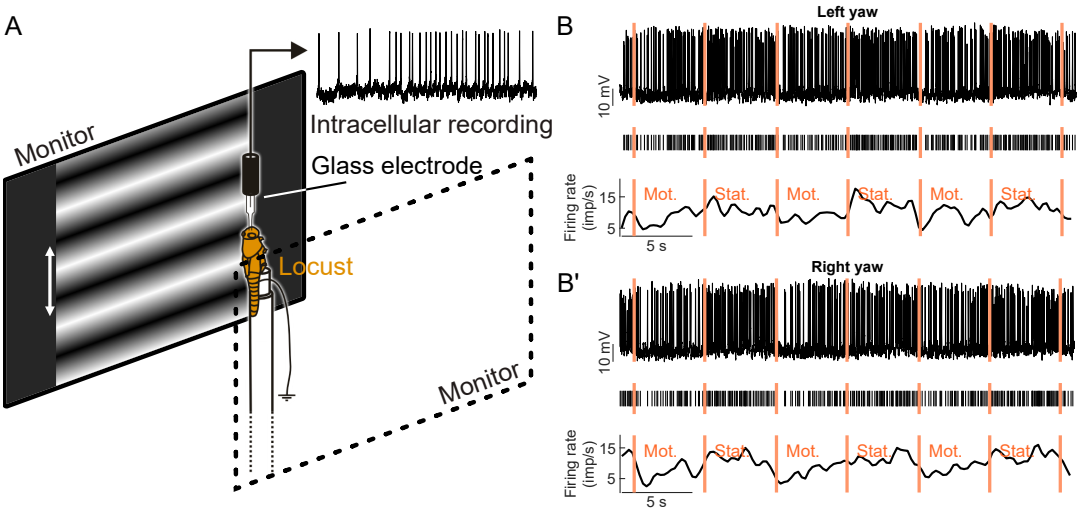

FIGURE 6: Testing neurons for sensitivity to visual self-motion. (**A**) Schematic of the experimental setup (not to scale). Locusts were mounted vertically and stimulated with motion of sinusoidal grating patterns on two laterally placed monitors. (**B**) Response of a CL1 neuron to left yaw motion, meaning that the pattern motion simulated leftward turning to the locust: During motion phases (Mot.) the pattern on the left monitor was moved upward and the one on the right monitor downward. Both patterns stood still during standstill phases (Stat.). Raw data (top), detected spikes (middle) and smoothed firing rate estimate (bottom). (**B'**) Response of the same neuron to right yaw motion. This neuron can be considered sensitive to both motion directions because pattern motion led to a significant firing rate reduction compared to standstill. See Chapter 5 Fig. 1 on P. 134 for further statistic analysis of this data set.

data management workflow by providing algorithms for automated upload and administration of data without needing to manually use the browser interface.

References

Bech M, Homberg U, and Pfeiffer K (2014). "Receptive fields of locust brain neurons are matched to polarization patterns of the sky". *Curr. Biol.* 24.18, pp. 2124–2129. DOI: 10.1016/j.cub.2014.07.045.

Bockhorst T and Homberg U (2017). "Interaction of compass sensing and object-motion detection in the locust central complex". *J. Neurophysiol.* 118.1, pp. 496–506. DOI: 10.1152/jn.00927.2016.

Cang J and Feldheim DA (2013). "Developmental mechanisms of topographic map formation and alignment". *Annu. Rev. Neurosci.* 36.1, pp. 51–77. DOI: 10.1146/annurev-neuro-062012-170341.

de Vries L, Pfeiffer K, Trebels B, Adden AK, Green K, Warrant E, and Heinze S (2017). "Comparison of navigation-related brain regions in migratory versus non-migratory noctuid moths". *Front. Behav. Neurosci.* 11, p. 158. DOI: 10.3389/fnbeh.2017.00158.

el Jundi B, Heinze S, Lenschow C, Kurylas A, Rohlfing T, and Homberg U (2010). "The locust standard brain: A 3D standard of the central complex as a platform for neural network analysis". *Front. Syst. Neurosci.* 3, p. 21. DOI: 10.3389/neuro.06.021.2009.

el Jundi B, Pfeiffer K, Heinze S, and Homberg U (2014). "Integration of polarization and chromatic cues in the insect sky compass". *J. Comp. Physiol. A* 200, pp. 575–589. DOI: 10.1007/s00359-014-0890-6.

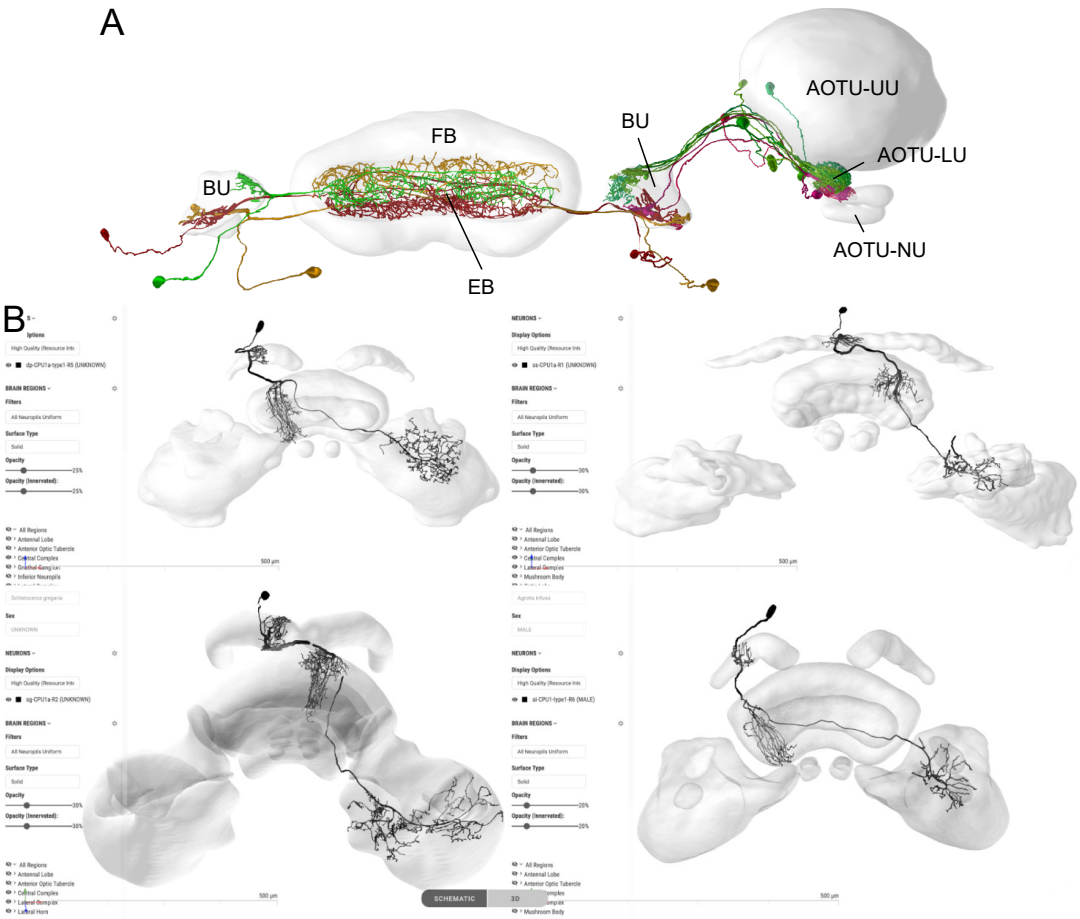

FIGURE 7: Three-dimensional visualization of neuroanatomical research data with the *InsectBrainDatabase*. (**A**) Visualization of neuronal input pathways to the butterfly central-complex; underlying data from Heinze et al. (2013). Each neuron was independently stained and three-dimensionally reconstructed, then linked to the same model of the butterfly brain. Collected in the *InsectBrainDatabase*, the neurons can be interactively combined. (**B**) Side-by-side neuron viewer, showing three-dimensional central-complex models of four insect species with the same type of neuron (CPU1) displayed. Data sources, from top left to bottom right: Monarch butterfly (Heinze et al., 2013), dung beetle (el Jundi et al., 2015), desert locust (el Jundi et al., 2010), and bogong moth (de Vries et al., 2017). Figure based on Heinze et al. (2021) (see also Chapter 6 Fig. 3 on P. 152). Abbreviations: AOTU, anterior optic tubercle; BU, bulb; EB, ellipsoid body; FB, fan-shaped body; LU, lower unit; NU, nodular unit; UU, upper unit.

el Jundi B, Warrant EJ, Byrne MJ, Khaldy L, Baird E, Smolka J, and Dacke M (2015). "Neural coding underlying the cue preference for celestial orientation". *Proc. Natl. Acad. Sci. U.S.A.* 112.36, pp. 11395–11400. DOI: 10.1073/pnas.1501272112.

Finkelstein A, Las L, and Ulanovsky N (2016). "3-D maps and compasses in the brain". *Annu. Rev. Neurosci.* 39.1, pp. 171–196. DOI: 10.1146/annurev-neuro-070815-013831.

Green J, Adachi A, Shah KK, Hirokawa JD, Magani PS, and Maimon G (2017). "A neural circuit architecture for angular integration in *Drosophila*". *Nature* 546.7656, pp. 101–106. DOI: 10.1038/nature22343.

Heinze S (2014). "Polarized-light processing in insect brains: Recent insights from the desert locust, the monarch butterfly, the cricket and the fruit fly". *Polarized Light and Polarization Vision in Animal Sciences*. Ed. by G Horváth. Berlin, Heidelberg: Springer Berlin Heidelberg, pp. 61–111. DOI: 10.1007/978-3-642-54718-8_4.

Heinze S (2017). "Unraveling the neural basis of insect navigation". *Curr. Opin. Insect Sci.* 24, pp. 58–67. DOI: 10.1016/j.cois.2017.09.001.

Heinze S, el Jundi B, Berg BG, Homberg U, Menzel R, Pfeiffer K, Hensgen R, Zittrell F, Dacke M, Warrant E, Pfuhl G, Rybak J, and Tedore K (2021). "A unified platform to manage, share, and archive morphological and functional data in insect neuroscience". *eLife* 10, e65376. DOI: 10.7554/eLife.65376.

Heinze S, Florman J, Asokaraj S, el Jundi B, and Reppert SM (2013). "Anatomical basis of sun compass navigation II: The neuronal composition of the central complex of the monarch butterfly". *J. Comp. Neurol.* 521, pp. 267–298. DOI: 10.1002/cne.23214.

Heinze S and Homberg U (2007). "Maplike representation of celestial *E*-vector orientations in the brain of an insect". *Science* 315.5814, pp. 995–997. DOI: 10.1126/science.1135531.

Honkanen A, Adden A, da Silva Freitas J, and Heinze S (2019). "The insect central complex and the neural basis of navigational strategies". *J. Exp. Biol.* 222.Suppl_1, jeb188854. DOI: 10.1242/jeb.188854.

Hulse BK and Jayaraman V (2020). "Mechanisms underlying the neural computation of head direction". *Annu. Rev. Neurosci.* 43, pp. 31–54. DOI: 10.1146/annurev-neuro-072116-031516.

Kurylas AE, Rohlfing T, Krofczik S, Jenett A, and Homberg U (2008). "Standardized atlas of the brain of the desert locust, *Schistocerca gregaria*". *Cell Tissue Res.* 333.1, pp. 125–145. DOI: 10.1007/s00441-008-0620-x.

Labhart T (1996). "How polarization-sensitive interneurones of crickets perform at low degrees of polarization". *J. Exp. Biol.* 199.7, pp. 1467–1475. DOI: 10.1242/jeb.199.7.1467.

Labhart T and Meyer EP (1999). "Detectors for polarized skylight in insects: A survey of ommatidial specializations in the dorsal rim area of the compound eye". *Microsc. Res. Tech.* 47.6, pp. 368–379. DOI: 10.1002/(SICI)1097-0029(19991215)47:6<368::AID-JEMT2>3.0.CO;2-Q.

Lu J, Westeinde EA, Hamburg L, Dawson PM, Lyu C, Maimon G, Druckmann S, and Wilson RI (2020). "Transforming representations of movement from body- to world-centric space". *bioRxiv*, p. 2020.12.22.424001. DOI: 10.1101/2020.12.22.424001.

Moser EI, Moser MB, and McNaughton BL (2017). "Spatial representation in the hippocampal formation: a history". *Nat. Neurosci.* 20.11, pp. 1448–1464. DOI: 10.1038/nn.4653.

O'Keefe J and Nadel L (1978). *The hippocampus as a cognitive map*. Oxford University Press.

Pegel U, Pfeiffer K, and Homberg U (2018). "Integration of celestial compass cues in the central complex of the locust brain". *J. Exp. Biol.* 221.2, jeb171207. DOI: 10.1242/jeb.171207.

Pegel U, Pfeiffer K, Zittrell F, Scholtyssek C, and Homberg U (2019). "Two compasses in the central complex of the locust brain". *J. Neurosci.* 39, pp. 3070–3080. DOI: 10.1523/JNEUROSCI.0940-18.2019.

Pfeiffer K and Homberg U (2014). "Organization and functional roles of the central complex in the insect brain". *Annu. Rev. Entomol.* 59.1, pp. 165–184. DOI: 10.1146/annurev-ento-011613-162031.

Pfeiffer K, Negrello M, and Homberg U (2011). "Conditional perception under stimulus ambiguity: polarization- and azimuth-sensitive neurons in the locust brain are inhibited by low degrees of polarization". *J. Neurophysiol.* 105.1, pp. 28–35. DOI: 10.1152/jn.00480.2010.

Schmeling F, Tegtmeier J, Kinoshita M, and Homberg U (2015). "Photoreceptor projections and receptive fields in the dorsal rim area and main retina of the locust eye". *J. Comp. Physiol. A* 201.5, pp. 427–440. DOI: 10.1007/s00359-015-0990-y.

Srinivasan MV (2015). "Where paths meet and cross: navigation by path integration in the desert ant and the honeybee". *J. Comp. Physiol. A* 201.6, pp. 533–546. DOI: 10.1007/s00359-015-1000-0.

Turner-Evans D and Jayaraman V (2016). "The insect central complex". *Curr. Biol.* 26.11, R453–R457. DOI: 10.1016/j.cub.2016.04.006.

Turner-Evans D, Wegener S, Rouault H, Franconville R, Wolff T, Seelig JD, Druckmann S, and Jayaraman V (2017). "Angular velocity integration in a fly heading circuit". *eLife* 6, p. 23496. DOI: 10.7554/eLife.23496.

Wehner R (1987). "'Matched filters' — neural models of the external world". *J. Comp. Physiol. A* 161.4, pp. 511–531. DOI: 10.1007/BF00603659.

Zittrell F, Pfeiffer K, and Homberg U (2020). "Matched-filter coding of sky polarization results in an internal sun compass in the brain of the desert locust". *Proc. Natl. Acad. Sci. U.S.A.* 117.41, pp. 25810–25817. DOI: 10.1073/pnas.2005192117.

Chapter 1

Two Compasses in the Central Complex of the Locust Brain

3070 • The Journal of Neuroscience, April 17, 2019 • 39(16):3070–3080

Systems/Circuits

Two Compasses in the Central Complex of the Locust Brain

Uta Pegel,[1] Keram Pfeiffer,[2] Frederick Zittrell,[1] Christine Scholtyssek,[3] and Uwe Homberg[1]

[1]Animal Physiology, Department of Biology and Center for Mind, Brain and Behavior, Philipps-Universität Marburg, 35032 Marburg, Germany, [2]Behavioral Physiology and Sociobiology (Zoology II), Biozentrum, University of Würzburg, Am Hubland, 97074 Würzburg, Germany, and [3]School of Experimental Psychology, University of Bristol, Bristol BS8 1TU, United Kingdom

Many migratory insects rely on a celestial compass for spatial orientation. Several features of the daytime sky, all generated by the sun, can be exploited for navigation. Two of these are the position of the sun and the pattern of polarized skylight. Neurons of the central complex (CX), a group of neuropils in the central brain of insects, have been shown to encode sky compass cues. In desert locusts, the CX holds a topographic, compass-like representation of the plane of polarized light (*E*-vector) presented from dorsal direction. In addition, these neurons also encode the azimuth of an unpolarized light spot, likely representing the sun. Here, we investigate whether, in addition to *E*-vector orientation, the solar azimuth is represented topographically in the CX. We recorded intracellularly from eight types of CX neuron while stimulating animals of either sex with polarized blue light from zenithal direction and an unpolarized green light spot rotating around the animal's head at different elevations. CX neurons did not code for elevation of the unpolarized light spot. However, two types of columnar neuron showed a linear correlation between innervated slice in the CX and azimuth tuning to the unpolarized green light spot, consistent with an internal compass representation of solar azimuth. Columnar outputs of the CX also showed a topographic representation of zenithal *E*-vector orientation, but the two compasses were not linked to each other. Combined stimulation with unpolarized green and polarized blue light suggested that the two compasses interact in a nonlinear way.

Key words: **central complex; head direction; insect brain; navigation; polarization vision; sky compass**

Significance Statement

In the brain of the desert locust, neurons sensitive to the plane of celestial polarization are arranged like a compass in the slices of the central complex (CX). These neurons, in addition, code for the horizontal direction of an unpolarized light cue possibly representing the sun. We show here that horizontal directions are, in addition to *E*-vector orientations from the dorsal direction, represented in a compass-like manner across the slices of the CX. However, the two compasses are not linked to each other, but rather seem to interact in a cell-specific, nonlinear way. Our study confirms the role of the CX in signaling heading directions and shows that different cues are used for this task.

Introduction

Many animals rely on visual cues for navigation. Some of them, including certain insects, exploit global compass cues of the sky to extract heading information and maintain directions during walking and flight (Wehner, 1984; Merlin et al., 2012; Homberg, 2015). Sky compass cues are highly reliable due to their persistent presence during locomotion (Gould, 1998; Frost and Mouritsen, 2006). In addition to direct sunlight, the polarization pattern and the chromatic gradient across the sky, both generated by scattering of sunlight in the atmosphere, provide reference to the position of the sun. In addition to sky compass cues, insects also rely on landmarks and perhaps even map-like mechanisms of orientation, especially in familiar terrain (Collett, 1992; Menzel et al., 2005; Zars, 2009; Wystrach and Graham, 2012). Large landscape features such as coastlines or mountain ranges may also serve as guiding cues for long-distance migrators (Reppert et al., 2016).

Several insect species show orientation behavior dependent on sky compass cues or, under laboratory settings, signals that mimic zenithal sky polarization or solar position. These include honey bees (von Frisch, 1949; Brines and Gould, 1979), desert ants (Wehner and Müller, 2006), dung beetles (Dacke et al., 2003; el Jundi et al., 2014b), fruit flies (Weir and Dickinson, 2012), field crickets (Brunner and Labhart, 1987), and locusts (Mappes and Homberg, 2004). All of these species possess specialized photoreceptors working as *E*-vector analyzers located in the dorsal rim

Received April 13, 2018; revised Jan. 10, 2019; accepted Jan. 29, 2019.

Author contributions: U.P., K.P., and U.H. designed research; U.P. performed research; U.P., F.Z., and C.S. contributed unpublished reagents/analytic tools; U.P. analyzed data; U.P. wrote the first draft of the paper; U.P., K.P., F.Z., C.S., and U.H. edited the paper; U.P. and U.H. wrote the paper.

This work was supported by the Deutsche Forschungsgemeinschaft (Grants HO 950/23-1 and HO 950/24-1). We thank Erich Buchner and Christian Wegener (University of Würzburg) for supplying anti-synapsin antibodies and Martina Kern for maintaining locust cultures.

The authors declare no competing financial interests.

Correspondence should be addressed to Uwe Homberg at homberg@biologie.uni-marburg.de.

https://doi.org/10.1523/JNEUROSCI.0940-18.2019

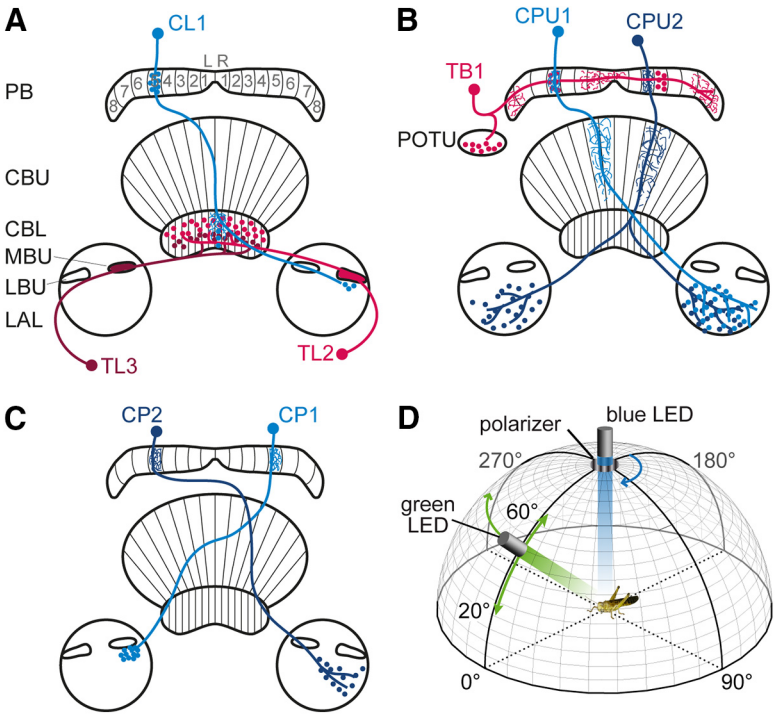

Figure 1. Neuronal cell types and visual stimulation. ***A–C***, Schematic illustration of tangential (red) and columnar (blue) neurons of the sky compass network in the locust CX. Vertical lines mark the edges of slices occupied by arborizations of columnar neurons. Slices are termed R1–R8 (right hemisphere) and L1–L8 (left hemisphere). Fine processes illustrate likely dendritic input regions of the neuron; dots represent varicose arborizations und thus likely presynaptic output regions. The filled lateral and medial bulb (LBU, MBU) in ***A*** indicate input synapses arranged in microglomerular complexes. LAL, Lateral accessory lobe; POTU, posterior optic tubercle. ***D***, Schematic illustration of visual stimulation. The light of a blue LED positioned in the zenith was passed through a rotating polarizer. A green LED appeared to the animal as an unpolarized light spot. It rotated around the animal's head (green horizontal arrow) at elevations ranging from 20° to 60° (green vertical arrow).

areas of their compound eyes (Labhart and Meyer, 1999; Schmeling et al., 2014).

Visual pathways from the dorsal rim areas of both compound eyes converge on the central complex (CX), a group of midline-spanning neuropils in the brain (Homberg et al., 2011; Heinze, 2014). The CX consists of the upper and lower division of the central body (CBU and CBL, respectively), the paired noduli (NO), and the protocerebral bridge (PB; Fig. 1*A*). In the desert locust, the CBU, CBL, and PB are structured in rows of 16 vertical slices. Many CX neurons arborize in adjacent bilateral structures, the lateral accessory lobes, and the medial and lateral bulbs. Several types of CX neuron are involved in the processing of polarized light. These include tangential neurons of the CBL (TL2) serving as input neurons to the CX and contacting columnar neurons of the CBL (CL1; Fig. 1*A*). CL1 neurons arborize in distinct slices of the PB, where they might contact tangential neurons (TB1; Fig. 1*B*). Columnar neurons, termed CPU1, CPU2, CP1, and CP2, likely serve as output neurons of the network (Fig. 1*B*,*C*).

Functional studies provide strong evidence for a role of the CX in navigational tasks (Ofstad et al., 2011; Varga et al., 2017). In locusts and fruit flies, the CX holds an internal representation of head orientation relative to a visual reference. Whereas in fruit flies head orientation relative to bright landmarks is represented in the ellipsoid body (corresponding to the CBL in other species; Seelig and Jayaraman, 2013) and the PB (Green et al., 2017), a topographic representation of zenithal *E*-vectors is present in the PB of the locust (Heinze and Homberg, 2007). In dung beetles, monarch butterflies, and locusts, CX neurons code for the orientation of zenithal polarized light as well as for the azimuth of an unpolarized green light spot, likely representing the sun (Heinze and Reppert, 2011; el Jundi et al., 2014a, 2015; Pegel et al., 2018). This raises the question of whether the azimuth of the sun, like the *E*-vector angle, is represented topographically in the slices of the CX. If so, an internal azimuth compass phase shifted by 90° to the *E*-vector compass would be expected because this is the angular distance between the zenithal *E*-vector and the solar azimuth in the sky. We show here that several types of columnar neuron in the locust CX represent, not only zenithal *E*-vectors, but also azimuth angles of unpolarized light cues in a compass-like manner. However, the two compasses are not simply connected by a 90° relationship.

Materials and Methods

Animals and preparation. Desert locusts (*Schistocerca gregaria*) were reared under crowded conditions in a 12/12 h light/dark cycle. Only sexually mature male and female animals at least 1 week after final molt were used for experiments. Animals were mounted onto a metal holder using dental wax with their anterior–posterior body axis oriented vertically (Pfeiffer et al., 2005). Wings and legs were cut off. The head capsule was opened from anterior and fat tissue, tracheal air sacs, and gut were removed to reduce body movements. Mouthparts, leg stumps, and abdomen were immobilized by wax. Muscles close to the brain were cut for further stabilization. A small twisted metal wire was used to support the brain from posterior. The neural sheath covering the central brain was removed to allow access for the electrode. During preparation and intracellular recording the brain was immersed in locust saline (Clements and May, 1974) containing 0.09 mol l^{-1} saccharose.

Electrophysiology and visual stimulation. Sharp glass microelectrodes were drawn from borosilicate capillaries (Hilgenberg) using a Flaming/Brown horizontal puller (P-97; Sutter Instruments). Electrode tips were filled with 4% Neurobiotin (Vector Laboratories) diluted in 1 mol l^{-1} KCl. Electrode shanks were filled with 1 mol l^{-1} KCl. Neuronal signals were amplified 10× by a custom-built amplifier (University of Regensburg), visualized by an oscilloscope (DS 1052Eh; Rigol Technologies), digitized by an analog-to-digital converter (CED1401 plus; Cambridge Electronic Design) at a rate of 20 kHz, and stored on a PC using Spike2 version 6.02 software (Cambridge Electronic Design). Neuronal responses to polarized and unpolarized light stimuli were studied (Fig. 1*D*). Polarized light was generated by passing light of a blue LED (Oslon SSL 80, LDCQ7P, 452 nm; Osram Opto Semiconductors, or LXML-PR01-0500, 447.5 nm, Philips Lumileds) through a polarizer (HNP'B; Polaroid). Both were positioned in the animal's zenith (with respect to its natural head orientation) to stimulate the dorsal part of the eye. The polarized light stimulus covered a visual angle of 32.5° or 18.6° and had an intensity of 1.7×10^{13} photons cm^{-2} s^{-1}. The polarizer was rotated at angular velocities of 40°/s or 36°/s. The unpolarized light spot was generated by light from a green LED (LED535-series, 535 nm, Roithner Lasertechnik, or Oslon SSL 80, LT CP7P, 528 nm; Osram Opto Semiconductors) passing through a diffusor. The unpolarized light stimulus appeared at a visual angle of 16.3° and had an intensity of 10^{14} photons cm^{-2} s^{-1}. It was moved around the animal's head at an elevation of 45° and an angular velocity of 40°/s or 36°/s. In experiments testing for elevation-dependent coding the elevation of the light spot could be

3072 • J. Neurosci., April 17, 2019 • 39(16):3070–3080

changed to 20°, 30°, 40°, 50°, and 60° (Fig. 1*D*). At the end of the recording, Neurobiotin was injected into the neuron by applying a positive constant current of ~1 nA for 1–4 min.

Histology and image processing. Brains were dissected in locust saline, immersed overnight at 4°C in fixative containing 4% PFA, 0.25% glutaraldehyde, and 0.2% saturated picric acid diluted in 0.1 mol l^{-1} PBS. Brains were stored for up to 2 weeks at 4°C in sodium phosphate buffer. Subsequently, they were incubated in PBS with 0.3% Triton X-100 and Cy3-conjugated streptavidin (1:1000) for 3 d, dehydrated in an ascending ethanol series (30%, 50%, 70%, 90%, 95%, 100%) with 15 min steps, and cleared in a 1:1 mixture of 100% ethanol and methyl salicylate for 20 min, followed by 1 h in 100% methyl salicylate. Finally, brains were embedded in Permount (Fisher Scientific) between two coverslips. For synapsin immunostaining, brains were rehydrated in a decreasing ethanol series (100%, 95%, 90%, 70%, 50%, 30%) in 15 min steps, embedded in albumin/gelatin, fixed overnight in 8% formaldehyde at 4°C, and sectioned in 130 μm slices using a vibrating-blade microtome (VT 1000S; Leica). Sections were preincubated overnight in PBS with 5% Triton X-100 and 5% normal goat serum (NGS) and then incubated for 5 d at 4°C in PBS with 5% Triton X-100, 1% NGS, and anti-synapsin antibody (1:50). The monoclonal anti-synapsin antibody was generated in mouse against fusion proteins consisting of glutathione-S-transferase and the *Drosophila* Syn1 protein (Klagges et al., 1996) kindly provided by Drs. Erich Buchner and Christian Wegener (University of Würzburg). The antibody labels synapse-rich neuropils in various insect species (Brandt et al., 2005; Kurylas et al., 2008; Held et al., 2016). Following incubation in anti-synapsin, sections were incubated in PBS with 5% Triton X-100, 1% NGS, and the secondary antibody (goat anti-mouse) conjugated with Cy5 (1:300) for 3 d at 4°C. The sections were finally dehydrated in an increasing ethanol series (as described above), cleared in methyl salicylate (as described above), and mounted in Permount between two coverslips (for a more detailed description of the protocol, see Heinze and Homberg, 2008). Preparations were scanned with a confocal laser scanning microscope (Leica) using a DPSS laser (561 nm) for detection of Cy3 and a He-Ne laser (633 nm) for detection of Cy5. Scans were visualized in AMIRA (version 5.4.5; FEI Visualization Sciences Group). Images were processed in Adobe Illustrator CC version 2017.1.0.

Preprocessing of physiological data. Recording traces were visualized using Spike2. Action potentials were detected as events with a threshold-based mechanism. The data were exported to a mat file. All subsequent analysis was performed using custom functions written in MATLAB version 2017a (The MathWorks).

Experimental design and statistical analysis. For each stimulus presentation, a stimulus–response curve was obtained by calculating the mean spiking activity in 10° bins. To assess the response of a neuron to a stimulus condition, the stimulus–response curves of all presentations were averaged. At least one clockwise and one counterclockwise rotation of the polarizer/unpolarized light spot were averaged. Responses to clockwise and counterclockwise tests were always pooled in equal numbers to avoid a shift in the preferred calculated angle due to rotation direction. A directed modulation of spike rate by the orientation of the *E*-vector or the azimuth of the unpolarized light spot was determined by an angular–linear correlation analysis (Zar, 1999). The responsiveness of the neuron to a stimulus was indicated by the significance ($\alpha = 0.05$) of the correlation coefficient (r_{al}). The coefficient of determination (r_{al}^2) describes the strength of correlation between *E*-vector orientation or light spot azimuth and the spike rate (for a detailed description, see Pegel et al., 2018). To calculate the preferred *E*-vector or azimuth (Φ_{max}), spike times were transformed into angles by multiplying them with the stimulus rotation velocity. From these angles, the mean vector Φ was calculated (Batschelet, 1981) and defined as the preferred angle (Φ_{max}). The anti-preferred angle (Φ_{min}) was defined as the angle 180° to Φ_{max} (azimuth tuning) or 90° to Φ_{max} (*E*-vector tuning). For all analyses of axial data (*E*-vector stimulation), the angles were doubled (Batschelet, 1981). Background activity was determined by selecting parts of the recording without any stimulation and dividing them into 1 s bins. In each bin, the spikes were counted. Spike counts were used to calculate the median background activity. The correlation between the location of arborization in the PB and Φ_{max} was assessed by a circular–linear correlation analysis as described by Kempter et al. (2012). The slice of PB arborization was used as the linear variable (values ranging from 0 to 15) and Φ_{max} as the circular variable. A linear regression model was fitted to the circular–linear data by minimizing the circular error between measured and predicted angles (Kempter et al., 2012). The slope of the regression line was used to transform the linear variable into a circular one. Finally, a circular correlation coefficient (ρ) was calculated. No prior assumptions on the data were necessary except for an estimate of the range of reasonable slopes. It was determined as the slope α of the regression line with minimum mean circular distance from the data points within a reasonable range of ± 80° per PB column (Equation 1 in Kempter et al., 2012). The circular–linear correlation coefficient is an analog to the Pearson's product–moment correlation coefficient for linear–linear data, but with higher validity when analyzing circular–linear associations (Kempter et al., 2012).

For Figures 5 and 6, stimulus–response curves were smoothed. The stimulus–response curve was normalized to the median background activity of the neuron. A smoothing spline was fitted onto the curve using the MATLAB curve-fitting toolbox (smoothing parameter set to 10^{-4}, 360 array elements). For experiments with different light spot elevations, additional characteristics of the stimulus–response curve were calculated using the smoothed stimulus–response curve: the tuning amplitude, and the tuning width. The amplitude was determined by calculating the difference in normalized spike rate between the peak and the trough of the fit curve. The tuning width was defined as the angular difference between two points on the fit curve at half amplitude.

For experiments with combined stimulation (see Fig. 5), we calculated the relative impact of the green and polarized light stimulation alone on the response to simultaneous stimulation. We followed the assumption that the tuning is constituted as follows:

$$f(\Phi) = p(\Phi + 90) \cdot w_p + g(\Phi) \cdot w_g,$$

Where Φ is the stimulus angle in degrees, f is the hypothetic tuning curve to simultaneous stimulation, p is the measured tuning curve to polarized light stimulation, g is the measured tuning curve to green-light-spot stimulation, and $w_{p|g}$ are the respective weighting factors. Tuning curves were smoothed before calculations. We used an optimization approach to find the weighting factors where the summed absolute difference between the measured response to simultaneous stimulation and f is minimal. To this end, we used the MATLAB built-in function fminbnd to minimize the function $h(w) = \sum_\Phi |c(\Phi) - (p(\Phi + 90) \cdot w + g(\Phi) \cdot w_g)|$, where c is the measured tuning curve to simultaneous stimulation and w is the minimization parameter that was constrained to the interval $(-10, 10)$. In each optimization iteration, w_g was calculated by solving f for w_g and inserting the measured tuning curve for the hypothetic one: $w_g = \frac{c - p \cdot w}{g}$, where w is the optimization parameter of the current iteration. At $\min(h(w))$, the lowest absolute difference between measured and hypothetic tuning curve w was taken as w_p and w_g was calculated as above.

Results

Most of the data analyzed here are from recordings presented previously (Pegel et al., 2018). In that study, we analyzed basic response features of the neurons, including their tuning to the plane of polarized light, unpolarized green and UV light spots, response amplitudes, tuning widths, and tuning differences when comparing clockwise and counterclockwise rotations of the stimuli. Here, we investigated whether morphological characteristics of the neurons such as the innervated layer in the CBL and columnar domains in the PB, CBU, and CBL correspond to tuning angles of the neurons in a topographic manner.

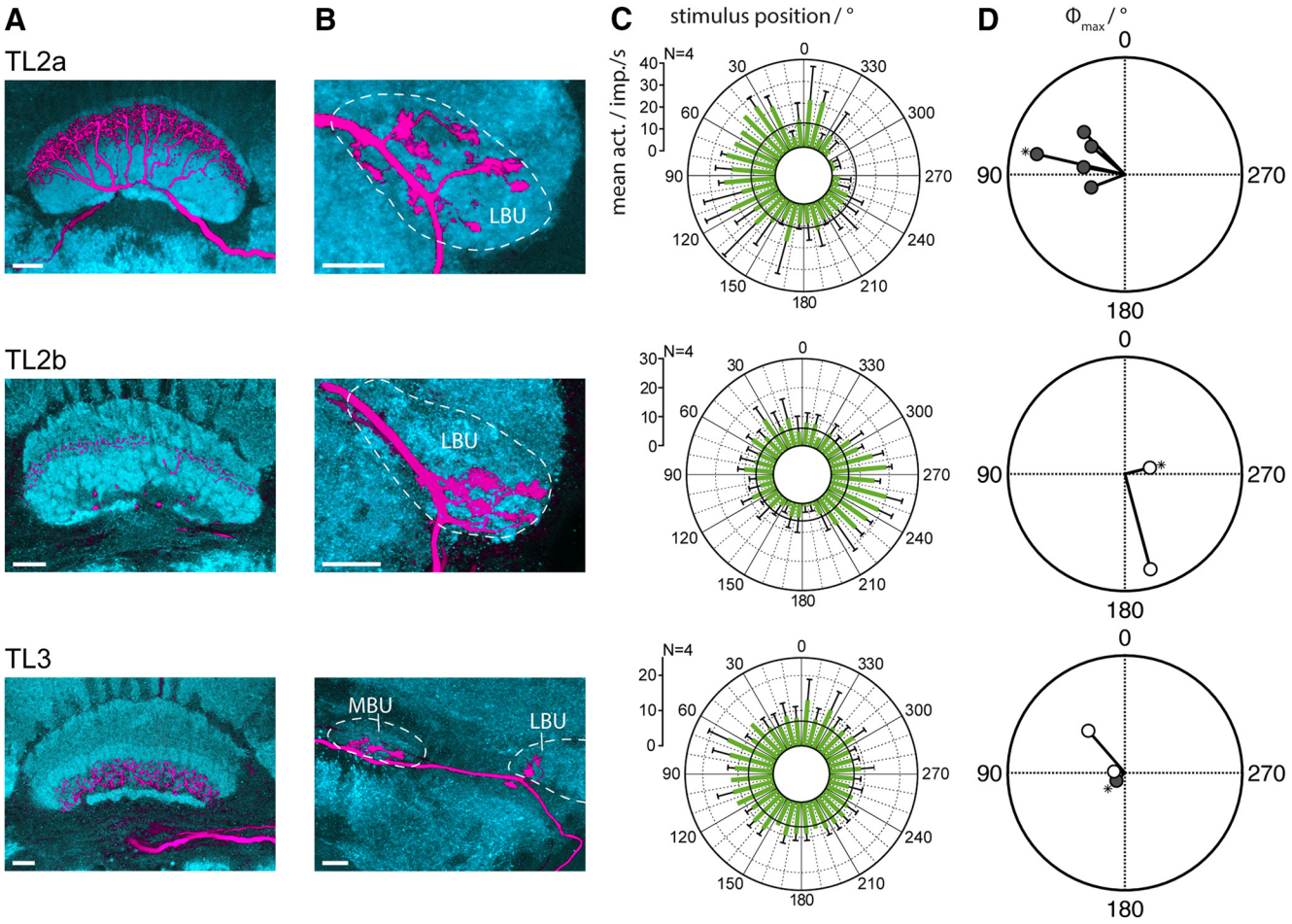

Figure 2. Morphology and physiology of TL neurons. ***A***, ***B***, Cy3 stainings of TL neurons (magenta). Neuropils were visualized by synapsin immunostaining (cyan). Scale bars, 20 μm. ***A***, Arborizations of a TL2a neuron (top), a TL2b neuron (middle), and a TL3 neuron (bottom) in the CBL; single optical sections. ***B***, Arborizations of the neurons in the lateral (LBU) or medial bulb (MBU); projections of stacks of several optical sections. ***C***, Circular histograms showing the average response of the TL2a ($\Phi_{max} = 76°$), TL2b ($\Phi_{max} = 284°$), and TL3 ($\Phi_{max} = 133°$) neuron presented in ***A*** and ***B*** to a rotating green light spot (elevation = 45°). Green bars indicate mean spiking activity. Error bars indicate SD. Black circles indicate median background activity. *n*, Number of stimulus presentations. ***D***, Population vector averages for the green spot from the recorded TL2a, TL2b, and TL3 neurons (means from two or four green light spot rotations) indicated by their preferred azimuth angle and vector length. Vector length ranges from 0 to unity (outer circle). Open dots indicate a preferred azimuth on the ipsilateral side; filled gray dots indicate a preferred angle on the contralateral side. Asterisks indicate data from the histograms in ***C***.

Tuning angles of TL neurons innervating different layers of the CBL

To investigate whether azimuthal preference is topographically represented in the layering of the CBL, we compared azimuthal tuning and innervated layer in 10 recorded TL neurons. Six types of tangential neuron termed TL1–TL6 have been distinguished in the CBL of the locust (Müller et al., 1997; Bockhorst and Homberg, 2015). We recorded from seven TL2 and three TL3 neurons, invading different layers of the CBL. Five TL2 neurons invaded layer 2 of the CBL and are termed here TL2a (Fig. 2*A*). Two TL2 neurons invaded layer 3 and are termed here TL2b (Fig. 2*A*). The three TL3 neurons arborized in layers 4 and 5 (Müller et al., 1997). In the lateral bulb, TL2 and TL3 neurons receive signals via microglomerular complexes (Träger et al., 2008). Whereas TL2a neurons innervated microglomeruli in dorsal parts of the lateral bulb, TL2b neurons innervated microglomeruli of more ventral parts (Fig. 2*B*). In TL3 neurons, arborizations were located in the medial bulb, but one neuron additionally invaded a few microglomeruli at the most mediodorsal tip of the lateral bulb (Fig. 2*B*). All TL2 neurons responded with excitation at Φ_{max} and inhibition at Φ_{min}. TL3 neurons were generally tuned only weakly to the azimuth of the green spot and either showed exclusively excitation at Φ_{max} (Fig. 2*C*), inhibition at Φ_{min}, or both. In all TL2a neurons, the preferred azimuth of the green light spot was on the contralateral side (Fig. 2*C*,*D*). In contrast, in the two TL2b neurons, the preferred azimuth was on the ipsilateral side (Fig. 2*C*,*D*). The three TL3 neurons showed mixed responses, with Φ_{max} on the ipsilateral side in two neurons and on the contralateral side in the third neuron (Fig. 2*C*,*D*).

Topographic representation of *E*-vector and azimuth angles in the PB

In the PB, zenithal *E*-vectors are topographically represented, indicating that the PB acts as an internal sky polarization compass (Heinze and Homberg, 2007). This representation was found for TB1, CPU1, CP1, and CP2 neurons (Heinze and Homberg, 2007), but not for CL1 neurons (Heinze and Homberg, 2009). Here, we investigated whether a topographic representation of azimuth of unpolarized light representing the sun is likewise present across the PB. We recorded from CL1, TB1, CPU1, CP1, and CP2 neurons and from an additional cell type, CPU2 neurons (Fig. 1*A*–*C*). Neurons were tested for *E*-vector coding by presenting polarized light from the zenith and for azimuth coding by presenting an unpolarized green light spot rotating at an

3074 • J. Neurosci., April 17, 2019 • 39(16):3070–3080

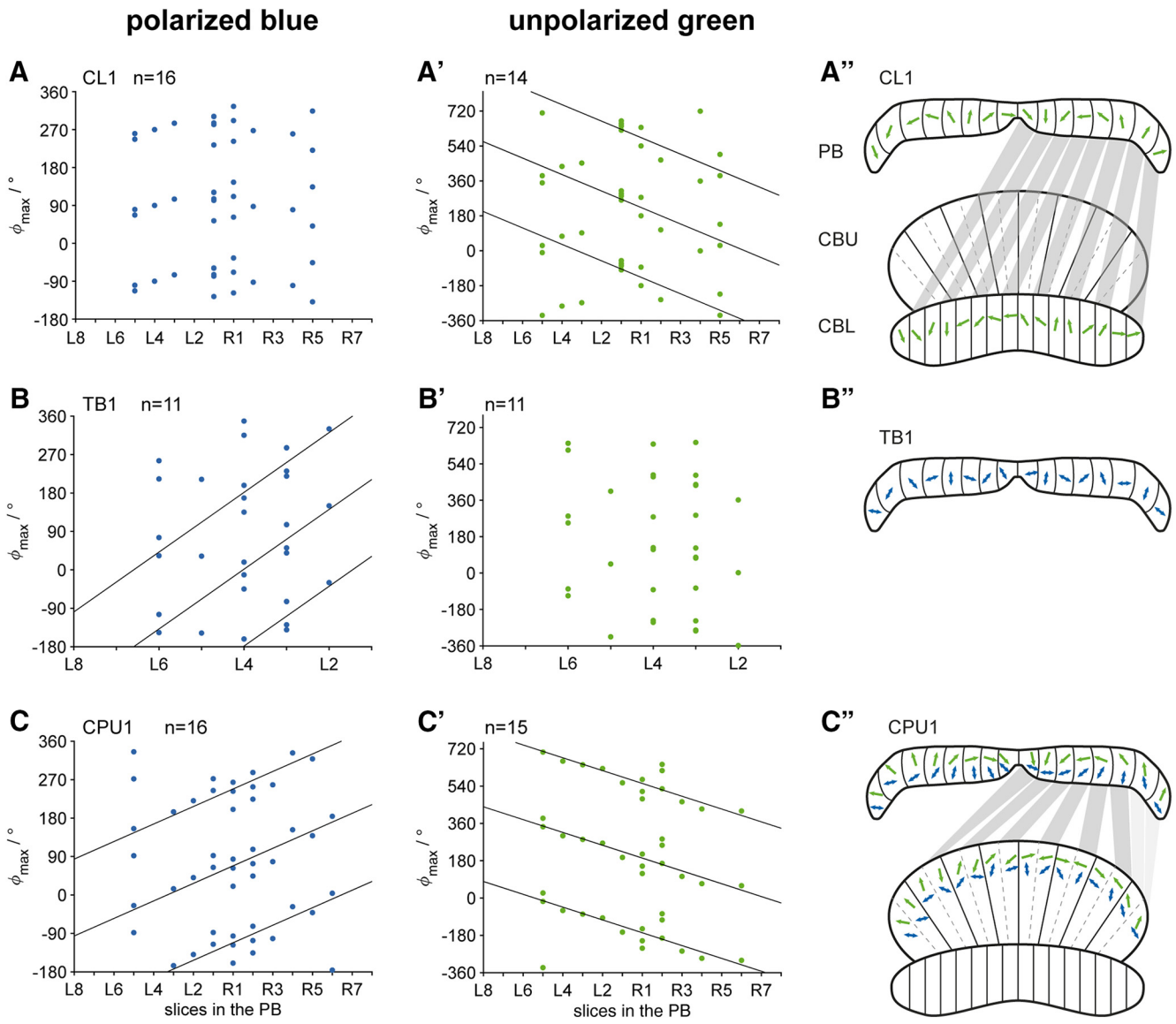

Figure 3. Internal representation of zenithal *E*-vector and azimuth in the CX. Preferred *E*-vector angles (***A***–***C***, blue markers) and preferred azimuth angles of the unpolarized light spot (***A′***,***B′***,***C′***, green markers) are plotted against the slice of arborization of the respective neuron in the PB. Datasets are plotted three times: ± 180° for preferred *E*-vectors and ± 360° for preferred azimuths. Data points are means from two or four stimulus presentations. *n*, Number of recordings. Solid lines show the best fit line only in cases in which $|\rho| > 0.25$. Light spot elevation was at 45°. ***A″***, ***B″***, ***C″***, Mean *E*-vectors (blue double arrows) and mean azimuth angles (green arrows) taken from the circular–linear fits. For neurons arborizing additionally in the CB, the mean preferred angles were transferred from the PB to the CB according to the wiring schemes as shown by Heinze and Homberg (2008). Wiring is indicated by shades of gray for the right brain hemisphere. Light gray indicates unknown and thus hypothetical connections. ***A***, ***A′***, Preferred angles of CL1 neurons. Circular–linear regression shows low correlation between innervated slice and preferred angles for polarized blue light ($\rho = 0.11$), but high correlation between innervated slice and unpolarized green light ($y = -42.5x + 202.9$, $\rho = -0.72$). ***B***, ***B′***, Preferred angles of TB1 neurons. Correlation exists for polarized blue light ($y = 70.0x + 81.5$, $\rho = 0.60$) but not for unpolarized green light ($\rho = -0.04$). Due to similar location of varicose arborizations of TB1 neurons in the left and right PB hemisphere, only data of the left hemisphere are shown. ***C***, ***C′***, Preferred angles of CPU1 neurons. Correlation exists for polarized blue light ($y = 20.5x + 84.0$, $\rho = 0.33$) and unpolarized green light ($y = -30.9x + 80.0$, $\rho = -0.54$).

elevation of 45° around the animals' head. The preferred angles were plotted against the slice of arborization in the PB. Linear–circular regression analysis was performed for CL1, TB1, and CPU1 neurons because only for those cell types sample size was above the critical limit of $n = 10$ recordings (Kempter et al., 2012). Because TB1 neurons have varicose arborizations in one PB slice of each brain hemisphere (separated by seven slices), their preferred angles were plotted only for the left brain hemisphere. In CL1 neurons, the preferred *E*-vector was not correlated with the slice of arborization in the PB (Fig. 3*A*). These observations are consistent with previous results (Heinze and Homberg, 2009). TB1 neurons showed a correlation between preferred *E*-vector and slice of arborization (Fig. 3*B*). The data confirm the results of Heinze and Homberg (2007), who showed a topographic representation of *E*-vectors for TB1 neurons. As in Heinze and Homberg (2007), the fit line had a positive slope. However, it covered an angular range of 490° across one PB hemisphere, substantially larger than the range of 169.4° found by Heinze and Homberg (2007). In CPU1 neurons, the preferred *E*-vector angle was highly correlated with the slice of arborization in the PB (Fig. 3*C*), indicating an internal compass for zenithal *E*-vectors in the PB (Fig. 3*C″*). The circular–linear fits covered an angular range of 307° in CPU1 neurons from L8 to R8. The steepness of the fit line was again different from that of Heinze and

Homberg (2007), who reported a representation of 410° in CPU1 neurons.

A correlation between the slice of arborization in the PB and the preferred azimuth of the unpolarized light spot was found in CL1 and CPU1 neurons (Fig. 3*A′*,*C′*). This indicates that, in addition to the *E*-vector of polarized light, the azimuth of the green spot is topographically represented in the PB (Fig. 3*A″*,*C″*). However, in contrast to the positive correlation between *E*-vector and PB slice, the correlation between azimuth and PB arborization was negative in both cell types. The fits for the preferred azimuth of the unpolarized green spot covered 637.5° in CL1 neurons and 463.5° in CPU1 neurons across the PB. Because CPU1 and CL1 neurons arborize, not only in slices of the PB, but also in distinct slices of the central body, we transferred the mean preferred angle (i.e., the *y*-value of the fit line in the center of each slice) from the PB to the CB following the wiring scheme of the respective neuron type (Heinze and Homberg, 2008). In CL1 neurons, mean preferred azimuth angles resulted in a representation of 277.1° across the CBL (Fig. 3*A″*). CPU1 neurons innervating PB slices L6–R6 arborize in two neighboring slices of the CBU. For the PB slices L8, L7, R8, and R7, however, the wiring scheme is not known because CPU1 neurons arborizing in these slices have never been stained. By extrapolating the logic of connections from the central slices, Heinze and Homberg (2008) suggested that they invade corresponding outermost slices of the CBU. Following that scheme, mean *E*-vector angles across the eight double slices covered a range of 127° in the CBU (Fig. 3*C″*). Interestingly, the mean azimuth angles of CPU1 neurons in double slices of the CBU were almost spatially opponent to each other except for the outermost double slices, which were approximately parallel (Fig. 3*C″*).

Interaction between polarized and unpolarized light stimulus

Because the regression lines for preferred *E*-vectors and preferred azimuth angles have different signs, we examined their relationship in more detail. First we investigated whether the angular distance between the tuning to both stimuli (*E*-vector and green azimuth) and the slice of arborization in the PB were correlated in any way. Across all cell types, distances were independent of the slice of PB arborization (Fig. 4) and varied greatly for a given slice. In CL1 neurons, distances were widely dispersed from 0° to 180° (Fig. 4*A*). In contrast, in most TB1 neurons, distances were smaller than 90° (Fig. 4*B*). In CPU1 neurons, the distances clustered between 45° and 90° (Fig. 4*C*).

Second, to test for a possible cue preference or linear relationship between the two cues, we presented the unpolarized light spot in combination with the zenithal *E*-vector (Fig. 5). The relative angle between both stimuli was set to 90°, corresponding to the relationship between solar azimuth and zenithal *E*-vector in the sky. We analyzed the responses of two TL2, three CL1, four TB1, six CPU1, two CPU2, and one CP1 neuron. A hypothetical response curve to combined stimulation was calculated to estimate the relative contribution of the single stimuli (*E*-vector or light spot) to the measured response to combined stimulation. The absolute values and the ratio of weighting factors varied from neuron to neuron and could not be related to cell type, slice of PB innervation, or distance between tuning to the *E*-vector and green light spot. Weighting factors for azimuth tuning ranged from 0 to 1.7 and, for *E*-vector tuning, from −2 to 1.2. Their ratio ranged from −1.1 to 11.5. Some neurons showed a strong preference in the combined response for the *E*-vector or the unpolarized light spot, as shown for a CPU1 neuron preferring the *E*-vector (Fig. 5*A*). Other cells showed a less pronounced preference for the *E*-vector, as shown for a CL1 and a TB1 neuron (Fig. 5*B*,*C*), or for the azimuth of the green spot, as shown for a CPU1 and a CPU2 neuron (Fig. 5*D*,*E*). Some neurons showed responses to combined stimulation, in which the contributions of *E*-vector tuning and light spot tuning were similar (CL1; Fig. 5*F*). Nonetheless, in neurons not showing a strong preference, the response to combined stimulation always revealed one higher peak or one deeper trough in spike rate modulation across 360°.

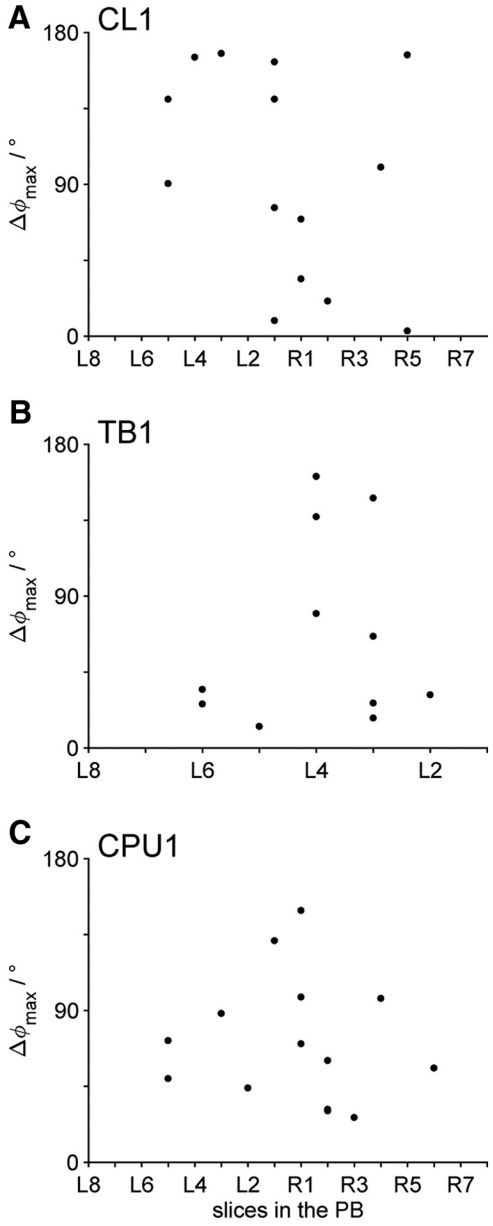

Figure 4. Distances between preferred *E*-vectors and azimuth angles. ***A–C***, Distances between preferred *E*-vector angles and preferred azimuth angles (black markers) plotted against the slice of arborization in the PB. Distances were calculated by subtracting the preferred *E*-vector angle from the preferred azimuth of the green spot. Data points are means from two or four stimulus presentations. ***A***, Distances of CL1 neurons ($n = 14$). ***B***, Distances of TB1 neurons ($n = 11$). ***C***, Distances of CPU1 neurons ($n = 14$).

Influence of elevation on azimuth tuning

In addition to its horizontal component (azimuth), the position of the sun has a vertical component (elevation). Although only

3076 • J. Neurosci., April 17, 2019 • 39(16):3070–3080

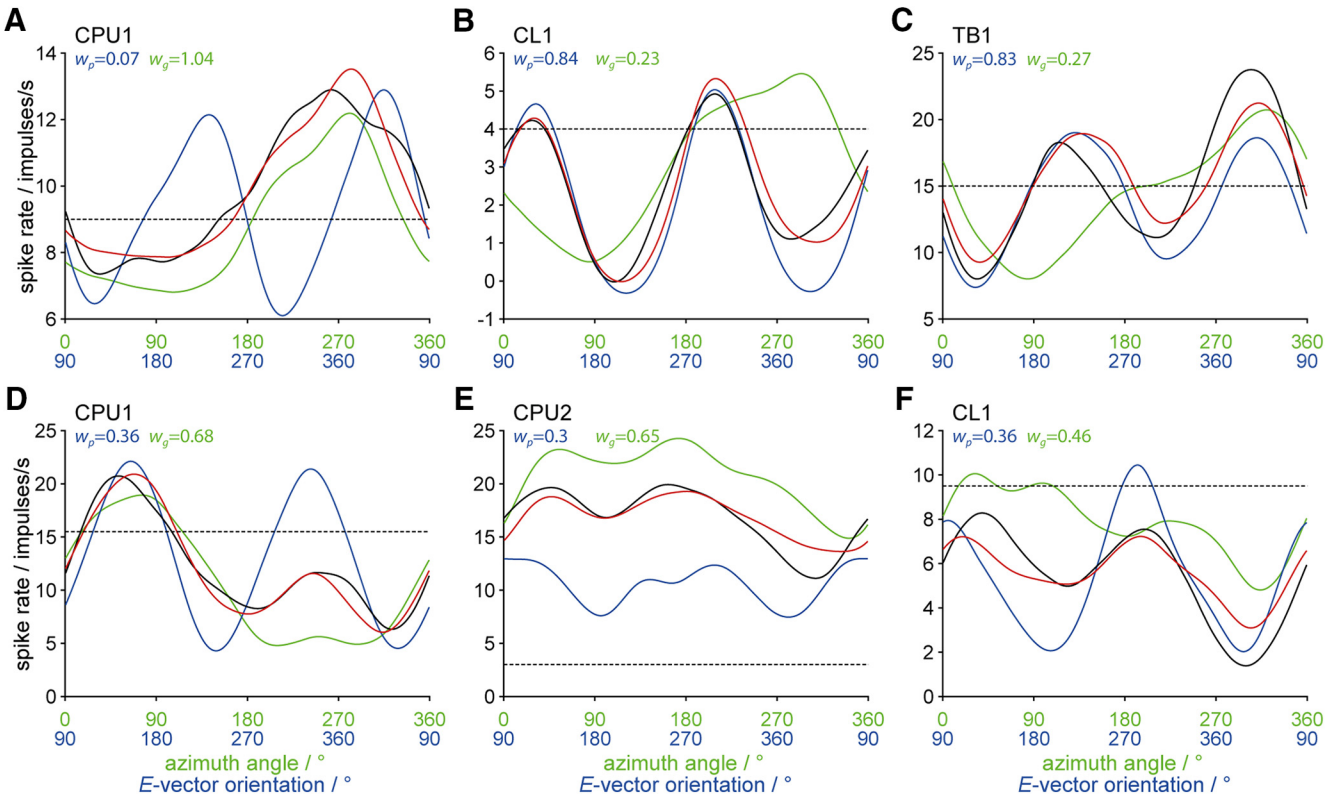

Figure 5. Responses to combined stimulation with polarized light and an unpolarized light spot. ***A–F***, Tunings of individual CX neurons to the *E*-vector (blue), to the azimuth of the unpolarized light spot (green), and to both stimuli presented simultaneously (black). Tunings are presented as smoothed stimulus–response curves based on means from four stimulus presentations except for the *E*-vector data in ***C*** and ***F***, which are means from two stimulus presentations. During combined stimulation, the *E*-vector was adjusted at 90° angular distance from the green light spot. Therefore, the *x*-axis shows the orientation of the *E*-vector (blue) separated from the azimuth angle (green). Responses to the *E*-vector alone are shifted by 90°. Solid red lines show the best fit curves resulting from summation of *E*-vector tuning and light spot tuning multiplied by a weighting factor w_p for the *E*-vector tuning and w_g for the azimuth tuning. Dotted lines indicate background activity. ***A***, Responses of a CPU1 neuron showing strong preference for the green light spot. *E*-vector tuning: $\Phi_{max} = 40°; p = 6 \cdot 10^{-5}$. Azimuth tuning: $\Phi_{max} = 264°; p = 2{\cdot}10^{-5}$. Combined response bidirectional tuning: $p = 0.83$. Combined response unidirectional tuning: $\Phi_{max} = 249°; p = 1{\cdot}10^{-3}$. ***B–F***, Responses of CL1 neurons (***B***, ***F***), a TB1 neuron (***C***), a CPU1 neuron (***D***), and a CPU2 neuron (***E***) to combined stimulation with less pronounced preference for the *E*-vector or the azimuth of the green spot. ***B***, Responses of a CL1 neuron showing a preference for polarized light. *E*-vector tuning: $\Phi_{max} = 120°; p = 3{\cdot}10^{-6}$. Azimuth tuning: $\Phi_{max} = 261°; p = 2{\cdot}10^{-6}$. Combined response bidirectional tuning: $\Phi_{max} = 117°; p = 2{\cdot}10^{-5}$. Combined response unidirectional tuning: $p = 0.64$. ***C***, Responses of a TB1 neuron. *E*-vector tuning: $\Phi_{max} = 39°; p = 2{\cdot}10^{-5}$. Azimuth tuning: $\Phi_{max} = 285°; p = 4{\cdot}10^{-5}$. Combined response bidirectional tuning: $\Phi_{max} = 36°; p = 2{\cdot}10^{-4}$. Combined response unidirectional tuning: $p = 0.2$. ***D***, Responses of a CPU1 neuron. *E*-vector tuning: $\Phi_{max} = 152°; p = 2{\cdot}10^{-7}$. Azimuth tuning: $\Phi_{max} = 69°; p = 8{\cdot}10^{-7}$. Combined response bidirectional tuning: $\Phi_{max} = 154°; p = 3{\cdot}10^{-3}$. Combined response unidirectional tuning: $\Phi_{max} = 73°; p = 2{\cdot}10^{-3}$. ***E***, Responses of a CPU2 neuron. *E*-vector tuning: $\Phi_{max} = 99°; p = 4{\cdot}10^{-3}$. Azimuth tuning: $\Phi_{max} = 145°; p = 2{\cdot}10^{-4}$. Combined response bidirectional tuning: $\Phi_{max} = 116°; p = 1{\cdot}10^{-2}$. Combined response unidirectional tuning: $\Phi_{max} = 121°; p = 1{\cdot}10^{-3}$. ***F***, Responses of a CL1 neuron. *E*-vector tuning: $\Phi_{max} = 104°; p = 2{\cdot}10^{-5}$. Azimuth tuning: $\Phi_{max} = 92°; p = 5{\cdot}10^{-3}$. Combined response bidirectional tuning: $\Phi_{max} = 119°; p = 1{\cdot}10^{-3}$. Combined response unidirectional tuning: $\Phi_{max} = 117°; p = 3{\cdot}10^{-3}$.

the azimuth provides compass information, coding for solar elevation might provide daytime-dependent information and thus could aid in time-compensated sun compass navigation. We therefore tested different elevations of the unpolarized green light spot in recordings of four CL1, four TB1, and six CPU1 neurons. Only a few recordings showed an impact of elevation on the azimuth tuning. One CL1 neuron showed a second peak in azimuth tuning when stimulated at low elevations (Fig. 6*A*). At higher elevations of 50° or 60°, the second peak disappeared so that the tuning was more directed toward Φ_{max}. Another phenomenon occurred in a CPU1 neuron: the tuning curve was flat at high elevations and of higher amplitude at low elevations (Fig. 6*B*). Of all recordings, these two neurons showed the strongest influence of elevation on azimuth tuning. The general effects on the correlation strength of the tunings were small (Fig. 6*C*). Different elevations changed the significance of the correlation coefficient only in one CL1 (red), one TB1 (blue), and one CPU1 neuron (purple). All other neurons were either responsive to all tested elevations ($n = 10$) or to none of them ($n = 1$). Elevations different from 45° were often tested later in the recording so that tuning parameters might have been altered by a change of neuronal background state. Across all cell types, the correlation strength was most dispersed between elevations, whereas tuning amplitude and width were only slightly affected. Nonetheless, no common systematic change of tuning parameters occurred in any neuron type.

Discussion

Side-specific azimuth representation in tangential inputs to the CBL

In this study, we analyzed the relevance of solar azimuth and elevation and of the zenithal *E*-vector for the internal representation of heading direction in locust CX neuropils. TL2 and TL3 neurons are the likely input elements of polarization and azimuth information to the CX (Pegel et al., 2018). We identified two TL2 subtypes arborizing in different parts of the lateral bulb and different layers of the CBL (Müller et al., 1997) preferring a bright light spot on either the ipsilateral (TL2a) or contralateral side (TL2b) of the animal. Our findings are similar to characteristics of ring neurons (R neurons; equivalent to locust TL neurons) of

Pegel et al. • Two Compasses in the Central Complex J. Neurosci., April 17, 2019 • 39(16):3070–3080 • 3077

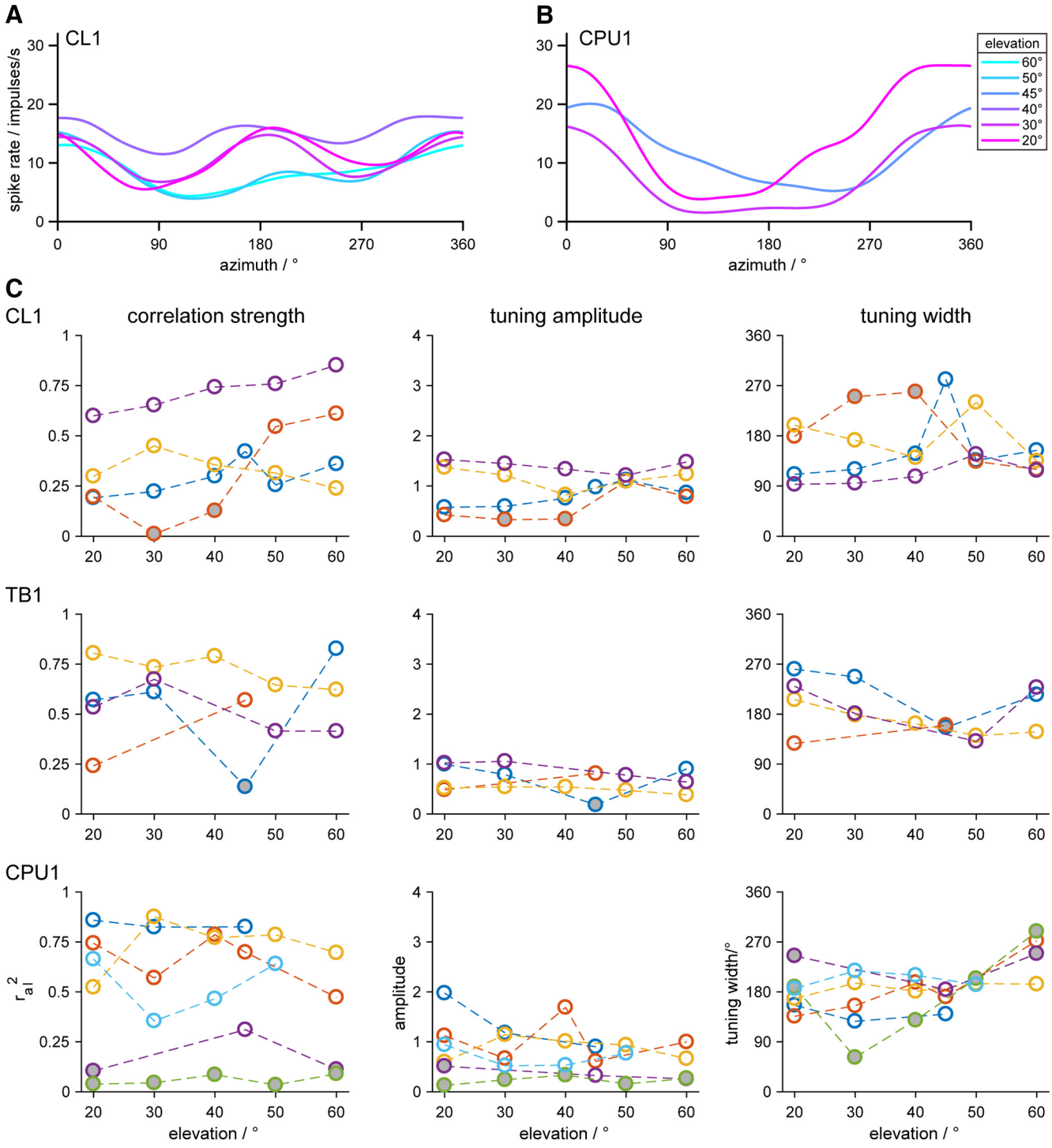

Figure 6. Influence of stimulus elevation on tuning parameters of CL1, TB1, and CPU1 neurons. ***A***, ***B***, Smoothed stimulus–response curves of a CL1 neuron (***A***) and a CPU1 neuron (***B***) to rotation of the green light spot presented at different elevations. Number of trials: $n = 4$ for all elevations in the CL1 neuron and the 45° elevation in the CPU1 neuron and $n = 6$ for all other elevations in the CPU1 neuron. ***C***, Tuning parameters of all recorded CL1, TB1, and CPU1 neurons. Tuning amplitude, tuning width, and correlation strength (r_{al}^2) of the average stimulus–response curve of each neuron plotted against the tested elevation. Colors code for individual neurons of the respective cell type. Open circles indicate data from significant responses; circles filled in gray indicate data from nonsignificant responses. Data from the CL1 neuron coded in red are from the same neuron as data in ***A*** and data from the CPU1 neuron coded in dark blue are from the same neuron as data in ***B***. Number of trials ranged from $n = 2$ to $n = 6$ in all cell types.

Drosophila. R neurons arborizing in ventral parts of the bulb have contralateral receptive fields for visual cues and innervate outer layers of the ellipsoid body, whereas R neurons connecting microglomeruli in dorsal parts of the bulb to inner layers of the ellipsoid body respond to ipsilateral targets (Shiozaki and Kazama, 2017). The latter also encode the recent visual experience of targets. These data suggest that different layers of the CBL/ellipsoid body not only receive input from different parts of the visual field, but also different types of information related to memory and decision making.

3078 • J. Neurosci., April 17, 2019 • 39(16):3070–3080

Compass representations in CX slices

A compass-like representation of zenithal *E*-vectors in the PB has been shown for TB1, CPU1, and CP1/CP2 neurons (Heinze and Homberg, 2007). These findings are confirmed here for TB1 and CPU1 neurons. As in Heinze and Homberg (2007), all regression lines had a positive slope and, in CPU1 neurons, covered ~360° of compass directions from L8–R8. For TB1 neurons, the slope of the regression line representing *E*-vectors differed from that shown by Heinze and Homberg (2007), but this may be because of the low sample size for TB1 neurons studied here. We found no correlation between preferred *E*-vector and PB slice in CL1 neurons, confirming the findings of Heinze and Homberg (2009).

Although Heinze and Homberg (2007) calculated coefficients using a linear–linear correlation analysis, we used a circular–linear approach, which affects the results in a negative way as follows: (1) with small sample size ($n < 10$), the correlation has only low reliability (Kempter et al., 2012) and our sample size of TB1 neurons was just above this number and (2) for the analysis of axial data such as the preferred *E*-vectors, the angles need to be doubled to convert them into a circular variable. This artificially increases the dispersion of data, thus decreasing the likelihood of correlation or, in the case of correlation, its strength. Nonetheless, the circular–linear analysis is highly superior to a linear–linear model. For the analysis of circularity, data points are already present multiple times on the *y*-axis. This eliminates the need to select the data points within the circular space to be used for the linear–linear correlation analysis, which strongly influences its result.

In addition to *E*-vector topography, we found a topographical representation of azimuth (green light spot) in CL1 and CPU1 neurons. In both cell types, the regression line had a negative slope from L8 to R8, opposite to that for *E*-vector coding. It covered a range of 638° in CL1 neurons. This range is close to the twofold representation of 360° space of E-PG neurons (equivalents to locust CL1 neurons) in the fly (Green et al., 2017), which was also a necessary assumption for a computational model of path integration in bees (Stone et al., 2017). In contrast, the CPU1 columnar output neurons represented only 464° of azimuthal directions. Because CPU1 neurons have so far not been found in the two outermost columns (R7/8, L7/8) and also appear to be absent in these columns in bees (Stanley Heinze, personal communication), this range might be further reduced to 340° from R6–L6. Being the output elements of the CX, CPU1 neurons, in contrast to CL1 neurons, may not show a purely sensory signal anymore, but rather a steering motor command signal. It is therefore reasonable that columnar outputs of the PB represent a range of just 180° in one PB hemisphere because neurons from one hemisphere have their presynaptic arborizations in the same lateral accessory lobe so that they might elicit turning behavior either to the left or to the right.

Elevation independence

In *Drosophila*, R neurons have approximately circular receptive fields for a bright bar defined by a preferred azimuth and preferred elevation (Seelig and Jayaraman, 2013). In contrast, in the locust, elevation of the green light spot was not encoded by PB neurons because most neurons were either responsive to all elevations or to none. Whether this difference is species specific or results from the fact that we did not collect data from TL neurons, only from downstream columnar neurons that have not been studied in *Drosophila*, remains to be established. The elevation independence in the tuning to the green light suggests that only the azimuth information is relevant for the coding properties of the neurons studied here. Theoretically, information on solar elevation could be useful for daytime estimation, but is apparently ignored in birds (Keeton, 1974; Wiltschko, 1980), honey bees (von Frisch, 1965), and desert ants (Duelli and Wehner, 1973) in favor of a circadian clock input for time-compensated sun compass orientation.

Biological significance

Honeybees, desert ants, and dung beetles are able to use both the sun and the polarization pattern of the sky as navigational cues (Brines and Gould, 1979; Wehner and Müller, 2006; el Jundi et al., 2015). Both signals are processed in the CX. In addition to encoding the plane of zenithal polarized light, CX neurons of dung beetles (el Jundi et al., 2015) and monarch butterflies (Heinze and Reppert, 2011) show azimuth-dependent responses to a bright light spot assumed to represent the sun. In *Drosophila*, azimuthal tunings to bright light spots are topographically represented in the ellipsoid body and PB (Seelig and Jayaraman, 2015; Turner-Evans et al., 2017). We show here that both the representation of zenithal *E*-vectors and the azimuth of an unpolarized light spot are mapped to the PB slices in a compass-like manner.

The two internal compasses for *E*-vector orientation and azimuth angle, however, do not support each other; they differ, not only in their orientation, but also in the total angular range they represent across the PB. Moreover, there is no 90° distance between preferred *E*-vector and preferred azimuth in any of the PB slices, so that the natural distance between zenithal *E*-vector and sun is not encoded. This raises the question of how the two compasses may interact in a natural setting. All data presented here were obtained from animals harnessed tightly for intracellular recordings. It is conceivable that the measured offset of the two compasses may be altered by active locomotion and turning movements of the locust. As shown in cockroaches (Varga and Ritzmann, 2016) and flies (Turner-Evans et al., 2017), certain CX neurons are tuned, not only to heading direction, but also to turning velocity of the animal and even to turning history. Addressing these effects in locusts would likewise require recordings during turning movements, ideally in freely moving animals.

Confinement of polarized light stimulation to a small area in the zenith has probably also affected the *E*-vector representation in the CX. Bees and ants need to see a sufficiently large part of the sky polarization pattern to calculate solar position and make systematic errors when they observe only a small part of the blue sky (Rossel and Wehner, 1984; Rossel, 1993; Wehner and Müller, 2006). Bech et al. (2014) showed that locust CX neurons encode sky-like patterns of differently oriented *E*-vectors. If the receptive fields of CX neurons are not zenith centered, then the internal *E*-vector compass based on the zenithal *E*-vector may substantially differ from a polarization compass based on a complete Rayleigh sky. Support for this hypothesis comes from a computational model of an insect-inspired polarization compass (Gkanias et al., 2018). Signals from a fan-shaped arrangement of *E*-vector analyzers as present in the dorsal rim area of the eye were fed into an array of compass neurons covering a 360° azimuth range. When stimulating the *E*-vector analyzers with a rotating polarizer instead of a Rayleigh pattern of *E*-vectors, the array of compass neurons showed an ~180°-representation of directions instead of 360° and, moreover, a paradox mirror-symmetric topography compared with Rayleigh sky stimulation. Unfortunately, stimulation with a pattern of polarizers mimicking the Rayleigh sky is hardly possible in a laboratory setting. Therefore, the polarization compass in the CX based on matched-filter

mechanisms for the Rayleigh sky may indeed be organized differently than revealed by the "single-polarizer" stimulation used here.

In conclusion, our results support the assumption that CX neurons are involved in navigation, not only by using a sky polarization compass, but also an azimuth compass possibly representing the sun. Both internal compasses emerge in neurons of the PB and are present in columnar output neurons. Experiments under the open sky are likely to reveal how both compasses interact with each other in a natural setting to produce a robust head direction signal.

References

Batschelet E (1981) Circular statistics in biology. London: Academic.

Bech M, Homberg U, Pfeiffer K (2014) Receptive fields of locust brain neurons are matched to polarization patterns of the sky. Curr Biol 24:2124–2129.

Bockhorst T, Homberg U (2015) Amplitude and dynamics of polarization-plane signaling in the central complex of the locust brain. J Neurophysiol 113:3291–3311.

Brandt R, Rohlfing T, Rybak J, Krofczik S, Maye A, Westerhoff M, Hege HC, Menzel R (2005) Three-dimensional average-shape atlas of the honeybee brain and its applications. J Comp Neurol 492:1–19.

Brines ML, Gould JL (1979) Bees have rules. Science 206:571–573.

Brunner D, Labhart T (1987) Behavioural evidence for polarization vision in crickets. Physiological Entomology 12:1–10.

Clements AN, May TE (1974) Studies on locust neuromuscular physiology in relation to glutamic acid. J Exp Biol 60:673–705.

Collett TS (1992) Landmark learning and guidance in insects. Philos Trans R Soc Lond B 337:295–303.

Dacke M, Nordström P, Scholtz CH (2003) Twilight orientation to polarized light in the crepuscular dung beetle *Scarabaeus zambesianus.* J Exp Biol 206:1535–1543.

Duelli P, Wehner R (1973) The spectral sensitivity of polarized light orientation in *Cataglyphis bicolor* (Formicidae, Hymenoptera). J Comp Physiol 86:37–53.

el Jundi B, Pfeiffer K, Heinze S, Homberg U (2014a) Integration of polarization and chromatic cues in the insect sky compass. J Comp Physiol A Neuroethol Sens Neural Behav Physiol 200:575–589.

el Jundi B, Smolka J, Baird E, Byrne MJ, Dacke M (2014b) Diurnal dung beetles use the intensity gradient and the polarization pattern of the sky for orientation. J Exp Biol 217:2422–2429.

el Jundi B, Warrant EJ, Byrne MJ, Khaldy L, Baird E, Smolka J, Dacke M (2015) Neural coding underlying the cue preference for celestial orientation. Proc Natl Acad Sci U S A 112:11395–11400.

Frost BJ, Mouritsen H (2006) The neural mechanisms of long distance animal navigation. Curr Opin Neurobiol 16:481–488.

Gkanias E, Risse B, Mangan M, Webb B (2018) From skylight input to behavioural output: a computational model of the insect polarised light compass. Available at https://www.biorxiv.org/content/10.1101/504597v1.

Gould JL (1998) Sensory bases of navigation. Curr Biol 8:R731–R738.

Green J, Adachi A, Shah KK, Hirokawa JD, Magani PS, Maimon G (2017) A neural circuit architecture for angular integration in *Drosophila.* Nature 546:101–106.

Heinze S (2014) Polarized-light processing in insect brains: recent insights from the desert locust, the monarch butterfly, the cricket, and the fruit fly. In: Polarized light and polarization vision in animal sciences (Horváth G, ed), pp 61–111. Berlin, Heidelberg: Springer.

Heinze S, Homberg U (2007) Maplike representation of celestial *E*-vector orientations in the brain of an insect. Science 315:995–997.

Heinze S, Homberg U (2008) Neuroarchitecture of the central complex of the desert locust: intrinsic and columnar neurons. J Comp Neurol 511:454–478.

Heinze S, Homberg U (2009) Linking the input to the output: new sets of neurons complement the polarization network in the locust central complex. J Neurosci 29:4911–4921.

Heinze S, Reppert SM (2011) Sun compass integration of skylight cues in migratory monarch butterflies. Neuron 69:345–358.

Held M, Berz A, Hensgen R, Muenz TS, Scholl C, Rössler W, Homberg U, Pfeiffer K (2016) Microglomerular synaptic complexes in the sky-compass network of the honeybee connect parallel pathways from the anterior optic tubercle to the central complex. Front Behav Neurosci 10:186.

Homberg U (2015) Sky compass orientation in desert locusts - evidence from field and laboratory studies. Front Behav Neurosci 9:346.

Homberg U, Heinze S, Pfeiffer K, Kinoshita M, el Jundi B (2011) Central neural coding of sky polarization in insects. Philos Trans R Soc Lond B Biol Sci 366:680–687.

Keeton WT (1974) The orientational and navigational basis of homing in birds. In: Recent advances in the study of behavior (Lehrman DS, Hinde RA, Shaw E, eds), pp 47–132. New York: Academic.

Kempter R, Leibold C, Buzsáki G, Diba K, Schmidt R (2012) Quantifying circular–linear associations: hippocampal phase precession. J Neurosci Methods 207:113–124.

Klagges BR, Heimbeck G, Godenschwege TA, Hofbauer A, Pflugfelder GO, Reifegerste R, Reisch D, Schaupp M, Buchner S, Buchner E (1996) Invertebrate synapsins: a single gene codes for several isoforms in *Drosophila.* J Neurosci 16:3154–3165.

Kurylas AE, Rohlfing T, Krofczik S, Jenett A, Homberg U (2008) Standardized atlas of the brain of the desert locust, *Schistocerca gregaria.* Cell Tissue Res 333:125–145.

Labhart T, Meyer EP (1999) Detectors for polarized skylight in insects: a survey of ommatidial specializations in the dorsal rim area of the compound eye. Microsc Res Tech 47:368–379.

Mappes M, Homberg U (2004) Behavioral analysis of polarization vision in tethered flying locusts. J Comp Physiol A Neuroethol Sens Neural Behav Physiol 190:61–68.

Menzel R, Greggers U, Smith A, Berger S, Brandt R, Brunke S, Bundrock G, Hülse S, Plümpe T, Schaupp F, Schüttler E, Stach S, Stindt J, Stollhoff N, Watzl S (2005) Honey bees navigate according to a map-like spatial memory. Proc Natl Acad Sci U S A 102:3040–3045.

Merlin C, Heinze S, Reppert SM (2012) Unraveling navigational strategies in migratory insects. Curr Opin Neurobiol 22:353–361.

Müller M, Homberg U, Kühn A (1997) Neuroarchitecture of the lower division of the central body in the brain of the locust (*Schistocerca gregaria*). Cell Tissue Res 288:159–176.

Ofstad TA, Zuker CS, Reiser MB (2011) Visual place learning in *Drosophila melanogaster.* Nature 474:204–207.

Pegel U, Pfeiffer K, Homberg U (2018) Integration of celestial compass cues in the central complex of the locust brain. J Exp Biol 221:jeb171207.

Pfeiffer K, Kinoshita M, Homberg U (2005) Polarization-sensitive and light-sensitive neurons in two parallel pathways passing through the anterior optic tubercle in the locust brain. J Neurophysiol 94:3903–3915.

Reppert SM, Guerra PA, Merlin C (2016) Neurobiology of monarch butterfly migration. Annu Rev Entomol 61:25–42.

Rossel S (1993) Navigation by bees using polarized skylight. Comp Biochem Physiol A 104:695–708.

Rossel S, Wehner R (1984) How bees analyse the polarization patterns in the sky: experiments and model. J Comp Physiol A Neuroethol Sens Neural Behav Physiol 155:605–613.

Schmeling F, Wakakuwa M, Tegtmeier J, Kinoshita M, Bockhorst T, Arikawa K, Homberg U (2014) Opsin expression, physiological characterization and identification of photoreceptor cells in the dorsal rim area and main retina of the desert locust, *Schistocerca gregaria.* J Exp Biol 217:3557–3568.

Seelig JD, Jayaraman V (2013) Feature detection and orientation tuning in the *Drosophila* central complex. Nature 503:262–266.

Seelig JD, Jayaraman V (2015) Neural dynamics for landmark orientation and angular path integration. Nature 521:186–191.

Shiozaki HM, Kazama H (2017) Parallel encoding of recent visual experience and self-motion during navigation in *Drosophila.* Nat Neurosci 20:1395–1403.

Stone T, Webb B, Adden A, Weddig NB, Honkanen A, Templin R, Wcislo W, Scimeca L, Warrant E, Heinze S (2017) An anatomically constrained model for path integration in the bee brain. Curr Biol 27:3069–3085.e11.

Träger U, Wagner R, Bausenwein B, Homberg U (2008) A novel type of microglomerular synaptic complex in the polarization vision pathway of the locust brain. J Comp Neurol 506:288–300.

Turner-Evans D, Wegener S, Rouault H, Franconville R, Wolff T, Seelig JD, Druckmann S, Jayaraman V (2017) Angular velocity integration in a fly heading circuit. Elife 6:e23496.

Varga AG, Ritzmann RE (2016) Cellular basis of head direction and contextual cues in the insect brain. Curr Biol 26:1816–1828.

Varga AG, Kathman ND, Martin JP, Guo P, Ritzmann RE (2017) Spatial navigation and the central complex: sensory acquisition, orientation, and motor control. Front Behav Neurosci 11:4.

von Frisch K (1949) Die Polarisation des Himmelslichtes als orientierender Faktor bei den Tänzen der Bienen. Experientia 5:142–148.

von Frisch K (1965) Tanzsprache und Orientierung der Bienen. Berlin/Heidelberg/New York: Springer.

Wehner R (1984) Astronavigation in insects. Annu Rev Entomol 29: 277–298.

Wehner R, Müller M (2006) The significance of direct sunlight and polarized skylight in the ant's celestial system of navigation. Proc Natl Acad Sci U S A 103:12575–12579.

Weir PT, Dickinson MH (2012) Flying *Drosophila* orient to sky polarization. Curr Biol 22:21–27.

Wiltschko R (1980) Die Sonnenorientierung der Vögel. I. Die Rolle der Sonne im Orientierungssystem und die Funktionsweise des Sonnenkompasses. J Ornithol 121:121–143.

Wystrach A, Graham P (2012) View-based matching can be more than image matching: the importance of considering an animal's perspective. Iperception 3:547–549.

Zar JH (1999) Biostatistical analysis, Ed 4. Upper Saddle River, NJ: Prentice Hall.

Zars T (2009) Spatial orientation in *Drosophila*. J Neurogenet 23:104–110.

Chapter 2

Matched-Filter Coding of Sky Polarization Results in an Internal Sun Compass in the Brain of the Desert Locust

Matched-filter coding of sky polarization results in an internal sun compass in the brain of the desert locust

Frederick Zittrell[a,b], Keram Pfeiffer[c,1], and Uwe Homberg[a,b,1,2]

[a]Department of Animal Physiology, Philipps-University Marburg, 35032 Marburg, Germany; [b]Center for Mind, Brain and Behavior (CMBB), Philipps-University Marburg and Justus Liebig University Giessen, 35032 Marburg, Germany; and [c]Biocenter, Behavioral Physiology and Sociobiology, University of Würzburg, 97074 Würzburg, Germany

Edited by John G. Hildebrand, University of Arizona, Tucson, AZ, and approved August 3, 2020 (received for review March 19, 2020)

Many animals use celestial cues for spatial orientation. These include the sun and, in insects, the polarization pattern of the sky, which depends on the position of the sun. The central complex in the insect brain plays a key role in spatial orientation. In desert locusts, the angle of polarized light in the zenith above the animal and the direction of a simulated sun are represented in a compass-like fashion in the central complex, but how both compasses fit together for a unified representation of external space remained unclear. To address this question, we analyzed the sensitivity of intracellularly recorded central-complex neurons to the angle of polarized light presented from up to 33 positions in the animal's dorsal visual field and injected Neurobiotin tracer for cell identification. Neurons were polarization sensitive in large parts of the virtual sky that in some cells extended to the horizon in all directions. Neurons, moreover, were tuned to spatial patterns of polarization angles that matched the sky polarization pattern of particular sun positions. The horizontal components of these calculated solar positions were topographically encoded in the protocerebral bridge of the central complex covering 360° of space. This whole-sky polarization compass does not support the earlier reported polarization compass based on stimulation from a small spot above the animal but coincides well with the previously demonstrated direct sun compass based on unpolarized light stimulation. Therefore, direct sunlight and whole-sky polarization complement each other for robust head direction coding in the locust central complex.

sky compass | polarized light | spatial orientation | central complex | desert locust

Animals need to navigate effectively through their environment, be it for foraging, mating, or migration. One aspect of spatial navigation is a sense of direction. In mammals, certain neurons of the hippocampal formation and associated areas fire maximally when the animal's head faces a particular direction (1–3). These neurons are termed "head direction cells." They encode head orientation based on visual background information, memory, and self-motion cues (3). A simple version of a head direction network has also been found in insects. Here neurons of the central complex (CX) encode heading direction to control turns in flight or walking (4–8). In the fruit fly *Drosophila*, Ca^{2+} imaging revealed a bump of activity that shifts through the columns of the ellipsoid body, fan-shaped body, and protocerebral bridge (PB), three substructures of the CX, as the fly turns, mapping the 360° space around the fly in a compass-like manner (4, 7, 8). Manipulating the position of the bump experimentally leads to shifts in flight orientation relative to the bump, indicating that the activity bump not only monitors head directions but actually controls them (9, 10). Whereas in the fly visual landscape information seems to play a major role in generating and updating the internal representation of heading in the CX (4, 5, 10), work in the desert locust, monarch butterfly, dung beetle, and bee showed that neurons are highly sensitive to celestial cues, including the sun and the sky polarization pattern (11–14). Nevertheless, flies, too, perform menotactic orientation with respect to sky polarization or a simulated sun (15, 16). Sun compass orientation is lost after silencing a particular CX cell type, suggesting that the CX in *Drosophila*, like in other insects, is also involved in celestial navigation. The polarization pattern of the sky is generated by the sun: sunlight is scattered at air molecules in the atmosphere and becomes partly linearly polarized in a systematic manner, which produces a polarization pattern in the sky (Fig. 1*A*). This pattern directly depends on the position of the sun, thereby signaling the solar azimuth, making it suitable for celestial navigation.

Field observations showed that several insect species including desert ants (17), honey bees (18), monarch butterflies (19), and dung beetles (20) use the polarization pattern of the sky for spatial orientation while in others [field crickets (21), desert locusts (22), and fruit flies (23, 24)], laboratory studies demonstrated orientation depending on the angle of polarization (AoP) of dorsally presented light. The AoP of light is detected by photoreceptors in specialized dorsal rim areas of the compound eyes (25). From the dorsal rim areas of both eyes, polarization vision pathways converge via the optic lobes, anterior optic tubercles, and lateral accessory lobes on the lower division of the central body (CBL), equivalent to the ellipsoid body in flies. Signals are processed further in the PB and upper division of the CBL (equivalent to fan-shaped body in flies) and are believed to affect descending pathways for motor control in the paired lateral accessory lobes adjacent to the CX (26) (Fig. 1 *B* and *C*). The CX is organized in layers and columns, which are mainly interconnected by neurons of two categories: tangential neurons

Significance

Many animals rely on the sun as a reference during spatial orientation. Insects can also use the pattern of polarization of the sky, generated by scattering of sunlight, as a guiding cue. We show here that certain neurons in the protocerebral bridge of the brain of the desert locust encode particular sun positions by responding best to a pattern of polarization generated by those sun positions. Across the protocerebral bridge, these neurons are arranged in a topographic, 360° compass with respect to angular orientation to the sun. This polarization-based compass is in line with a previously reported compass based on direct sunlight. Therefore, direct sunlight and whole-sky polarization complement each other in head direction coding in the locust.

Author contributions: F.Z., K.P., and U.H. designed research; F.Z. performed research; K.P. contributed analytic tools; F.Z. analyzed data; and F.Z., K.P., and U.H. wrote the paper.

The authors declare no competing interest.

This article is a PNAS Direct Submission.

[1]K.P. and U.H. contributed equally to this work.

[2]To whom correspondence may be addressed. Email: homberg@staff.uni-marburg.de.

This article contains supporting information online at https://www.pnas.org/lookup/suppl/doi:10.1073/pnas.2005192117/-/DCSupplemental.

First published September 28, 2020.

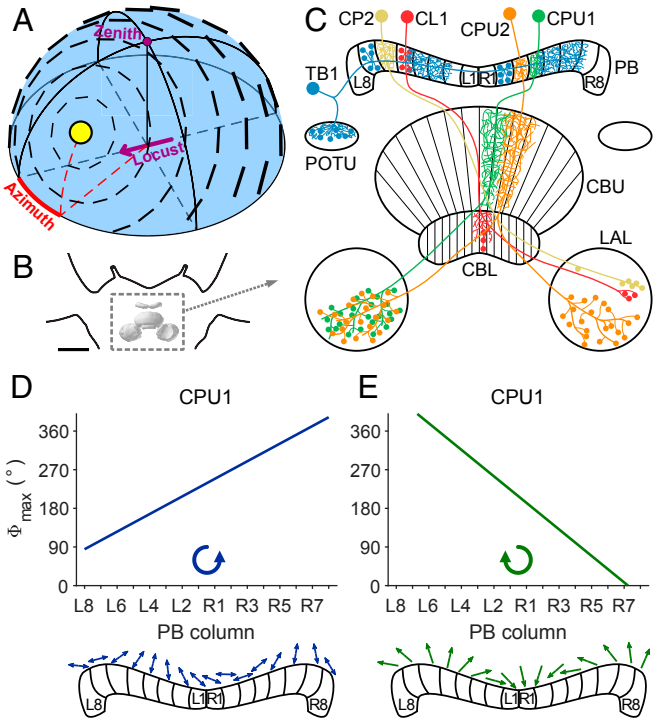

Fig. 1. Celestial compass cues and compass coding in the CX. (*A*) Schematized polarization pattern of the sky as produced by the sun at 40° elevation and 30° azimuth relative to an observer indicated by the purple arrow. Bar orientation and thickness indicate AoP and degree of polarization, respectively. (*B*) Frontal diagram of the locust brain indicating the location of the CX (boxed in dashed lines). Reprinted by permission from ref. 63, Springer Nature: Cell and Tissue Research, copyright (2008). (*C*) Schematic drawing of the locust CX with cell types investigated in this study. Fine branches indicate smooth (dendritic) arborizations, small dots symbolize varicose (presynaptic) arborizations, and large dots represent somata. Columnar neurons (CL1, CP2, CPU1, and CPU2) exist as isomorphic sets of 16 neurons, covering all 16 columns of the PB. Tangential neurons (TB1) exist as four subtypes per brain hemisphere, each having varicose ramifications in two columns that are eight columns apart. (*D* and *E*) Topographic representation of AoP to zenithal stimulation with blue polarized light (*D*) and azimuth of a green LED (*E*) in the same set of CPU1 neurons innervating different columns of the PB. The tuning to AoP changes from L8 to R8 in counterclockwise manner (*D, Bottom*), and the azimuth tuning changes in clockwise fashion (*E, Bottom*). CBL, lower division of the central body; CBU, upper division of the central body; L1 and L8, innermost, respectively outermost column in the left hemisphere of the PB; LAL, lateral accessory lobe; POTU, posterior optic tubercle; R1 and R8, innermost, respectively outermost column in the right hemisphere of the PB. CX model in *B* is after ref. 63, visualized with insectbraindb.org. *C*, *D*, and *E* reprinted from ref. 29, which is licensed under CC BY 4.0.

typically provide input to the CX and distribute activity along a single neuropil or a specific layer, and columnar neurons connect specific columns between different neuropils (27) and finally provide output from the CX.

In the desert locust *Schistocerca gregaria*, intracellular recordings showed that many neurons of the CX are tuned to the polarization angle in the animal's zenith as well as to the azimuth of a simulated sun stimulus (11, 28, 29). In neurons with arborization domains in single columns of the PB, tunings to these cues vary along the 16 columns of the bridge in a topographic manner (28, 29), indicating a compass-like representation of celestial cues, which could be used as a heading estimate suitable to aid spatial navigation. In a similar way, the azimuth of a simulated sun or the orientation of a visual panorama is represented in the PB and CBL of *Drosophila*. However, while recordings across different individuals suggest that the compass representation in the CX of locusts is consistent across animals, in *Drosophila* the representation of azimuthal space shows an individual offset between animals (4, 8, 16).

Owing to the physics of Rayleigh scattering, the position of the sun in the sky is linked to a unique pattern of polarization (Fig. 1*A*). Thus, one might expect that central maps within the CX converge, such that cells within particular columns are excited by the combination of solar azimuth and AoP that would be coupled in a natural sky. Prior research suggests this is not the case, however (29). Whereas the preferred AoP changed across the PB from left to right in a counterclockwise fashion, the preferred azimuth in the same set of neurons changed in a clockwise manner (ref. 29 and Fig. 1 *D* and *E*). It has, therefore, remained unclear how these compass systems may interact to generate a consistent heading estimate.

Studies on homing behavior showed that ants and bees make systematic navigation errors when they were allowed to see just a small part of polarized skylight (30, 31). This is not surprising, given that the full celestial pattern of polarization cannot be unambiguously reconstructed from a narrow aperture and suggests that faithful directional information requires visual input from large parts of the sky. In line with these observations, Bech et al. (32) found that unidentified neurons at the input stage of the locust CX sample polarization information from nearly the entire hemisphere above the animal. The AoP tuning in these neurons varied across the receptive field in a pattern that matched the sky polarization pattern produced by a distinct solar position (32). We show here that several types of neuron in the PB have similar coding properties. Their tunings, moreover, vary topographically depending on the location of their arborizations in the PB and, as a population, cover the full range of azimuthal directions, consistent with a polarization-pattern based sun compass. This compass resembles the azimuth compass that was found in CX neurons when stimulated with an unpolarized light spot simulating the sun (29). The data significantly advance our understanding of the integration of polarization vision in the CX network and support the idea that the locust CX acts as a hub for skylight navigation combining all available cues in the sky to form a robust compass signal.

Results

We recorded intracellularly from AoP-sensitive neurons in the locust CX in order to investigate their tuning properties across the full sky. We stimulated the animals with blue light passed through a rotating polarizer from different positions in the dorsal visual field (Fig. 2*A*). Neurons showed sinusoidal modulation of activity during a 360° rotation of the polarizer (Fig. 2*B*), but the preferred AoP of a single neuron typically varied depending on stimulation position (Fig. 2 *C*–*F*). Tracer injection after measurements allowed for identification of neuron types and reconstruction of their morphology. Recordings from 23 neurons with ramifications in particular columns of the PB of the CX were analyzed. These include four types of columnar neurons with ramifications in single columns of the PB (CL1, 6×; CP2, 1×; CPU1, 4×; and CPU2, 5×) and TB1 tangential neurons (7×) with dendritic and axonal ramifications in particular sets of columns (Fig. 1*C*). The number of stimulation positions ranged from 9 to 33 (median 19; 22 to 33 in CL1, 9 in CP2, 9 to 21 in CPU1, 13 to 18 in CPU2, and 9 to 33 in TB1).

Receptive Fields of CX Neurons Span Large Parts of the Sky. Most previous studies have assessed the AoP sensitivity of CX neurons by stimulation with a rotating polarizer in the animal's zenith. In the present study, we stimulated from positions in the entire dorsal hemisphere of the animal, which allowed us to analyze the AoP sensitivity across the dorsal visual field (Fig. 2). Briefly, we used the R^2 value of the AoP responses as a measure of AoP

NEUROSCIENCE

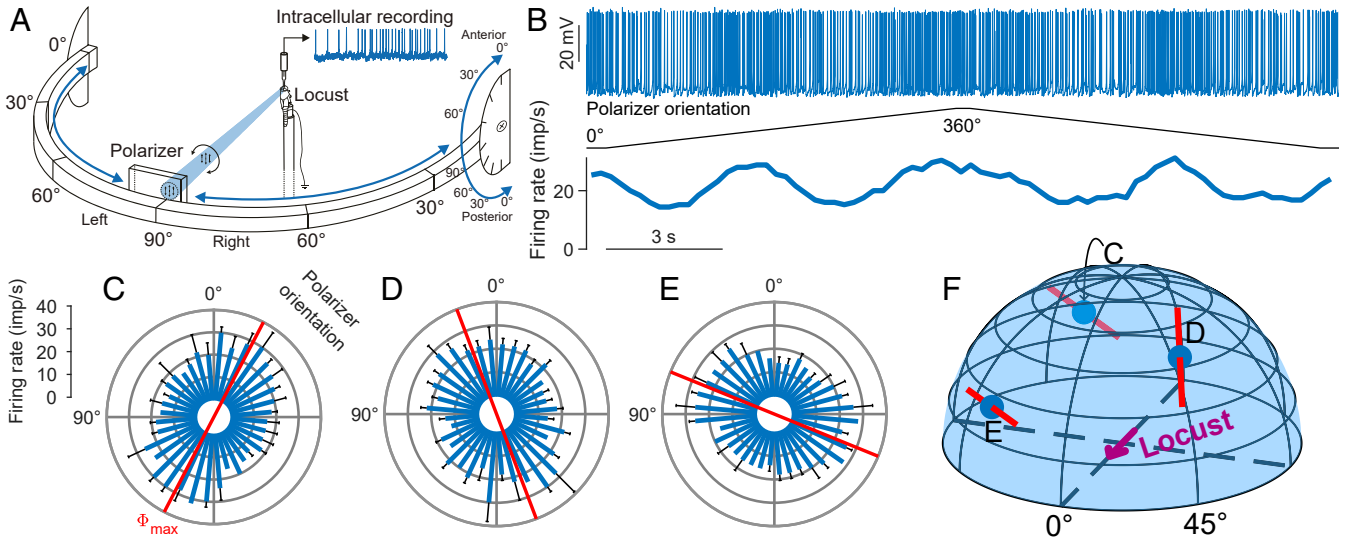

Fig. 2. Polarization sensitivity of a TB1 neuron to stimulation from different points in the virtual sky. (*A*) Experimental setup. Locusts were stimulated with blue light (465 nm) that was passed through a rotating polarizer to assess AoP sensitivity of single cells. The light source was movably mounted on a perimeter that could be tilted, allowing for stimulation from directions in the entire dorsal visual field. Reprinted from ref. 32. Copyright (2014), with permission from Elsevier. (*B*) Spike train (*Top*) of the neuron during rotation of the polarizer at stimulus position C indicated in *F*. Two successive full rotations with opposing turning direction of the polarizer (*Middle*) elicit two activity peaks per rotation (*Bottom*). (*C*) Circular response plot showing the data from *B* after pooling. Responses are pooled by assigning each spike the polarizer orientation at its time of occurrence and treating the resulting angle array as a single set; the preferred AoP (Φ_{max} = 152.4°; red axis) equals the axially corrected average angle of all spikes. The blue bars show the mean binned spike count from both rotations, converted to firing rate; error bars indicate SD. The firing rate is significantly correlated with polarizer orientation (linear-circular correlation, $P < 0.001$, $R^2 = 0.82$). The (azimuth|elevation) stimulus coordinates were (213.7°|25.7°), resulting from the LED positioned at 60° right on the perimeter, the perimeter tilted 30° to posterior. Response plots from the same neuron analogous to *C* at stimulus positions (*D*) (49.1°|48.6°) (LED at 60° left on perimeter, perimeter tilt 60° anterior) and (*E*) (326.3°|25.7°) (LED at 60° right on perimeter, perimeter tilt 30° anterior). Φ_{max} = 20.8° and 67.9°, $P < 0.001$ for all responses, R^2 = 0.49 and 0.79, respectively. (*F*) Illustration of the stimulus positions corresponding to the response data shown in *C*–*E*. Red bars indicate Φ_{max}, and blue dots indicate the spherical stimulus coordinates.

sensitivity, resulting in a sensitivity map for each neuron. We normalized the R^2 values to the value range of each neuron and defined receptive fields as the regions that remained after applying a 75% threshold to these maps (Fig. 3 and *SI Appendix*, Figs. S2 and S3). The fields generally varied in shape and size, in several instances extending from the zenith down to the horizon

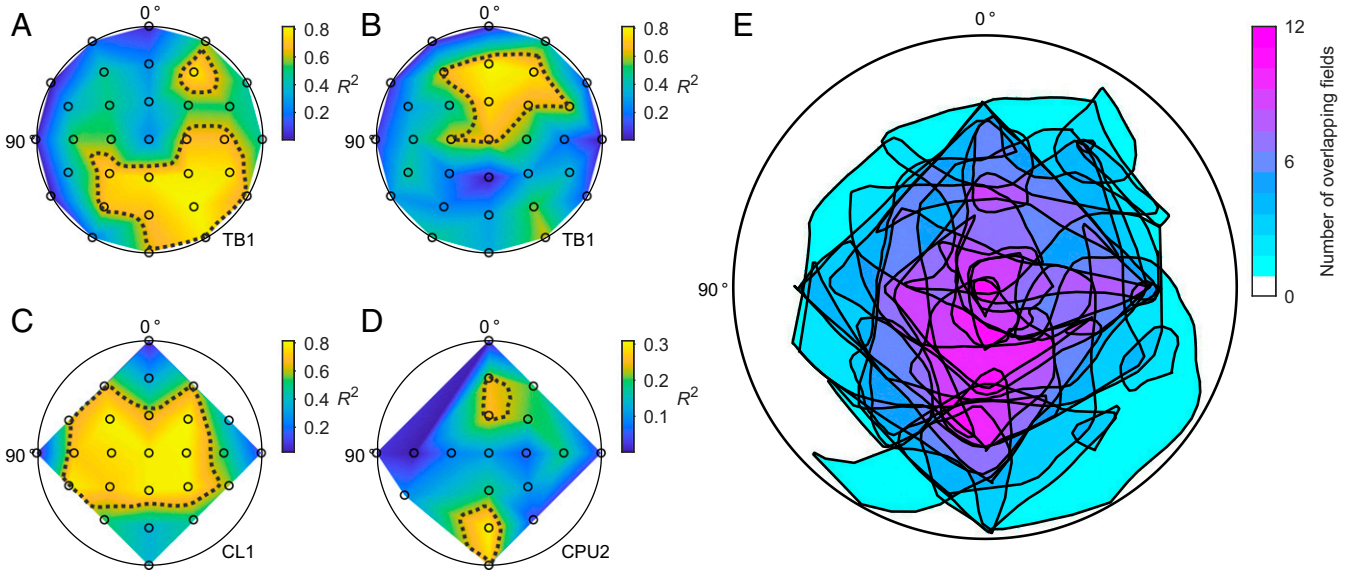

Fig. 3. Receptive fields for AoP sensitivity of CX neurons. (*A*–*D*) Example datasets: polarization sensitivity as a function of stimulus position in the dorsal visual field (view on flattened hemispheres; see *SI Appendix*, Fig. S1, for clarification of the coordinate system) of two TB1 neurons (*A* and *B*), a CL1 neuron (*C*), and a CPU2 neuron (*D*). The sensitivity to polarization angle indicated by the R^2 value of AoP responses is color-coded at each tested position (black circles) and linearly interpolated in between. Dotted lines are smoothed 75% isolines of the normalized R^2 values. (*E*) Superimposed smoothed borders of all 75% fields of all recorded neurons (23 neurons with 31 fields) with color-coded degree of overlap. See *SI Appendix*, Fig. S2, for a graphical description of the analysis; *SI Appendix*, Fig. S3, for the significance of the chosen R^2 threshold; and *SI Appendix*, Fig. S4, for all individual sensitivity maps.

(Fig. 3*A*); some neurons had more than one field (Fig. 3*D*). Based on visual inspection (cf. *SI Appendix*, Fig. S4), we found no trend in field size, shape, or position regarding cell type. Many fields were centered at a medium elevation (Fig. 3 *A*, *B*, and *D*); however, the overlap of all fields was maximum posterior from the zenith at about 60° elevation (Fig. 3*E*).

Neurons in the CX Show Matched-Filter Properties. Extracellular recordings showed previously that neurons of the CBL, most likely TL neurons, possess matched-filter properties (32) for polarization patterns of the blue sky that theoretically allow for unambiguous solar azimuth coding solely based on polarization sensitivity. Using intracellular recordings, we found that other types of CX neuron also show this feature (Fig. 4).

To test whether the measured patterns of preferred AoPs match a particular sky polarization pattern, we fitted them to generated patterns of AoPs that correspond to sky polarization patterns calculated from various solar coordinates (cf. Fig. 1*A*). This procedure yielded a matched-filter tuning in the form of solar coordinates that corresponded to the best matching, or least deviating, sky polarization pattern. Typically, we found a rather conspicuous match between the response pattern and the best matching pattern, with a clear minimum deviation (Fig. 4 *A* and *B*). To statistically assess the fitting quality of the best match, we tested the associated pattern deviation against a bootstrapped population of pattern deviations. This population was calculated from randomized response patterns, generated from the same dataset (Fig. 4*C*); all 6 CL1 neurons, 6 of 7 TB1 neurons, 2 of 4 CPU1 neurons, and 3 of 5 CPU2 neurons (in total 17 of 23 neurons) passed this bootstrap test and were used for further analysis.

Azimuthal Tuning of the Matched Filter Is Represented Topographically along the Protocerebral Bridge. Because preferred zenithal AoPs are topographically represented in the PB (28), we searched for a connection between neuroanatomy and the azimuthal component of the matched-filter tuning. We determined the arborization column in the PB of each neuron based on the tracer injections after recording. Recent work in *Drosophila* strongly suggests that different types of columnar neuron innervating the same column in the PB share a common heading preference (7). Neurobiotin injections showed that our recordings in the locust were from four different types of columnar neuron of the PB and one type of tangential neuron. All neurons arborized in a distinct column (Fig. 1*C*), except for TB1 neurons, for which we considered the ipsilateral column of the PB that is innervated by varicose arborizations. Tuning direction was uniformly distributed in our dataset (Fig. 5*A*) and, when pooling all cell types, was highly correlated with the arborization column in the PB (Fig. 5*B*). The resulting regression indicates that the full range of possible directions around the animal is covered by the solar azimuths of the preferred polarization patterns (Fig. 5*C*).

Discussion

We show here that several types of CX neuron in the locust brain integrate polarization information in the dorsal visual field consistent with a matched filter that is tuned to specific solar polarization patterns. The azimuthal component of this tuning depends on the arborization position in the PB, varying along this neuropil in a topographic manner with full coverage of azimuthal space. This polarization-based sun compass closely resembles the previously reported sun compass derived from unpolarized light stimulation (29), suggesting that these neurons reliably and congruently signal the solar azimuth irrespective of cue modality. Our finding sheds light on polarization vision processing in insects and elucidates its role for the constitution of a sun compass in the insect CX.

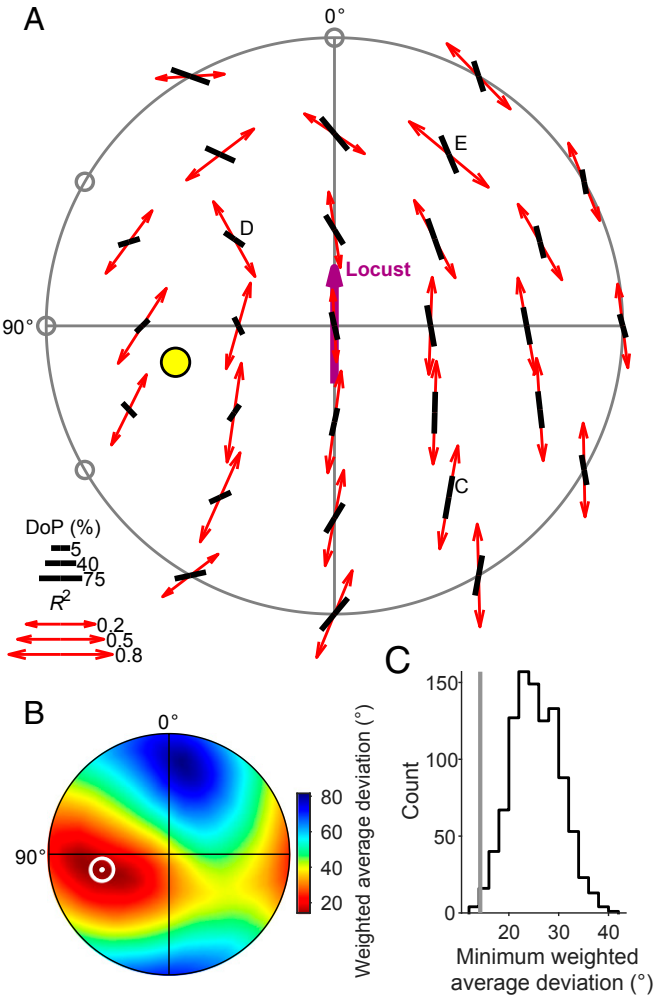

Fig. 4. Receptive fields of CX neurons are matched to sky polarization patterns. (*A*) Top view on the pattern of preferred AoPs (Φ_{max}; red double arrows) of a TB1 neuron and the AoPs that belong to the best-matching sky polarization pattern (black bars). This pattern corresponds to a sun position at 39.1° elevation and 102.9° azimuth (yellow dot). Arrow and bar length scale with response R^2 value and degree of polarization (DoP), respectively; gray circles indicate statistically nonsignificant AoP responses (linear-circular correlation, $P \geq 0.05$). Note that the originally spherical stimulus coordinates and AoP axes were transformed into polar coordinate space for visualization on a flattened hemisphere surface (cf. *SI Appendix*, Fig. S1). The labeled positions refer to the responses of the TB1 neuron shown in Fig. 2; Fig. 3*A* shows the AoP sensitivity map of this dataset. (*B*) Flattened hemispherical heat map of the deviation between the measured Φ_{max} pattern and calculated sky polarization patterns as a function of solar position used for calculation. The pattern deviation for a given solar coordinate is the average of the angular deviations between the Φ_{max} and the sky polarization pattern at each stimulus position, weighted by degree of polarization and R^2 value at each stimulus position. The white dot and circle have the same coordinates as the solar marker in *A* and mark the minimum (14.26°) of the deviations of all tested solar positions (n = 32,760 equally distributed positions). Color scale is shown to the right. (*C*) Distribution of 1,000 bootstrapped pattern deviations of randomized response patterns based on the data in *A* from the resulting best matching polarization pattern. The gray line indicates the observed deviation (14.26°; white marker in *B*), which significantly differs from the bootstrap distribution (P = 0.004, equals the fraction of bootstrapped deviations that are lower than or equal to the observed deviation). See *SI Appendix*, Fig. S7, for all individual response patterns with best-matching sky polarization pattern.

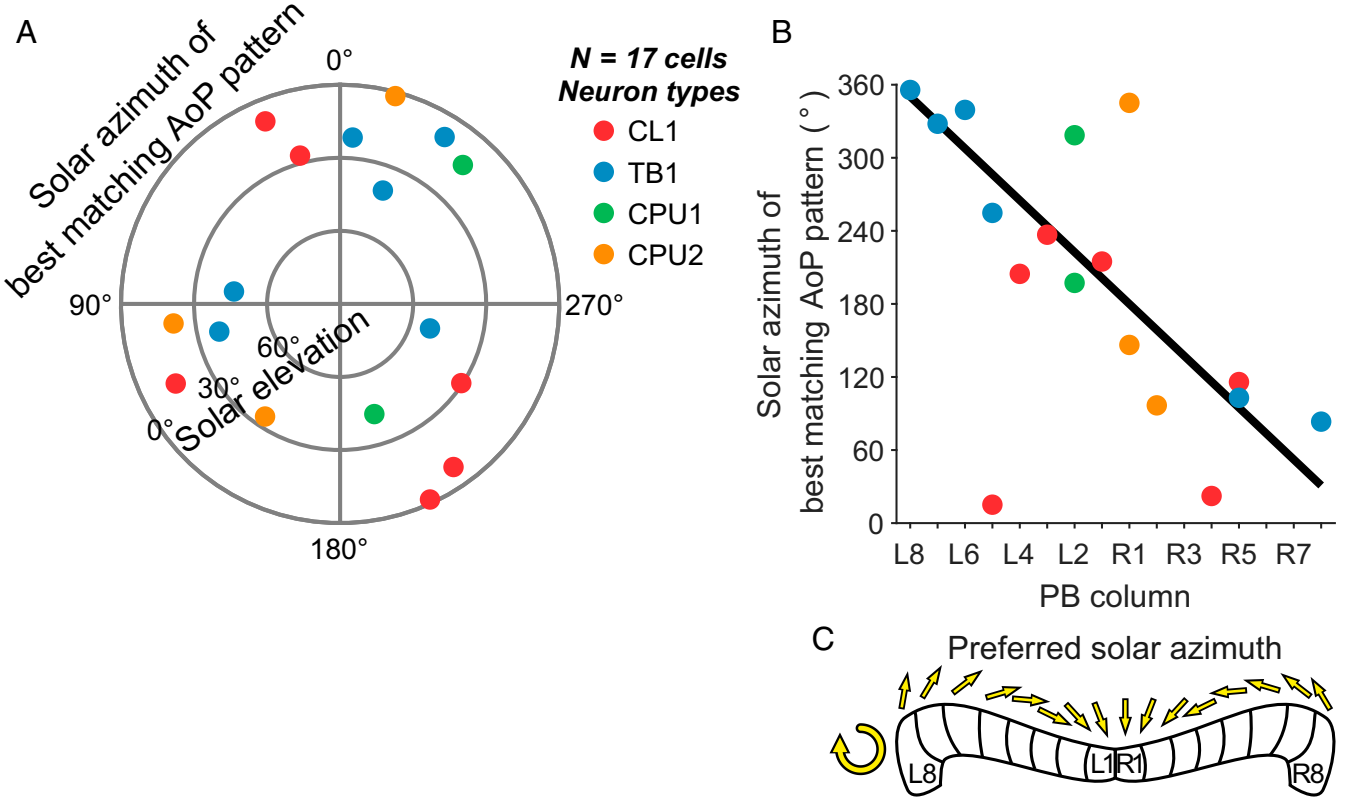

Fig. 5. The azimuthal tuning of matched filters is represented topographically along the PB. (*A*) Polar plot showing the solar positions that correspond to the best matching polarization patterns of single cells. Azimuth data are uniformly distributed (Rayleigh test, $P = 0.89$, $n = 17$). (*B*) Regression diagram of the column of arborization in the PB vs. the azimuthal component of the solar coordinates in *A*. The azimuth depends on PB column (circular–linear correlation, $\rho = -0.51$, $P = 0.028$). The estimated regression covers nearly 360° along the PB ($y = -21.3x + 350.3$; column L8 corresponds to $x = 0$). (*C*) Schematic compass topography according to the resulting regression. The preferred azimuth covers a range of nearly 360° along the PB.

CX Neurons Are AoP Sensitive across the Entire Dorsal Visual Field. Many CX neurons are sensitive to the AoP of light in a large proportion of the locust's dorsal visual field (Fig. 3), which is in line with the receptive field properties of dorsal rim area photoreceptors (33). While the dorsal rim areas are directed toward areas in the sky centered slightly contralaterally from the zenith, they show considerable overlap in the zenith, and the summed receptive fields of their receptors extend far down to the contralateral side, covering most parts of the sky (33). The striking differences in receptive field size and organization of the recorded neurons (Fig. 3 and *SI Appendix*, Fig. S4) were unexpected and suggest major cell-specific differences in input from the right and left dorsal rim ommatidia. Although some receptive fields were substantially offset from the zenith (e.g., Fig. 3*A*), superposition of all fields revealed a mean arrangement symmetric to the midline indicating an overall balanced input from both eyes. The fan-like arrangement of microvilli orientations across the dorsal rim ommatidia in the locust and other insects (34–36) might be a preadaptation to the sky polarization pattern, as suggested by ref. 37, and likely facilitates the matched-filter properties for AoP coding of CX neurons. Inspection of the fitting data shows that at certain points in the sky, the fit between celestial AoP and AoP tuning of the neuron is nearly perfect, while at others, they deviate significantly from each other (Fig. 4*A* and *SI Appendix*, Fig. S5*D*). Mismatches often occurred near the calculated sun position, where the degree of polarization is low (Fig. 4*A* and *SI Appendix*, Fig. S5*D*). These points in the sky would, therefore, contribute only little to the tuning of the neurons. In an area upstream of the CX, the anterior optic tubercle, neurons are even blind to polarization within a circle of 50° around the sun (38). All recordings presented here were obtained from laboratory-raised animals that had not been exposed to a natural sky. This shows that AoP tuning is largely determined genetically but does not exclude that fine tuning of the neurons to sky polarization patterns might require learning-related adaptations when the animals experience a natural sky.

Representation of Heading Directions in the CX. Data from various insect species, specifically fly, dung beetle, butterfly, cockroach, locust and bee, point to a role of the CX in integrating external and self-generated sensory information for the control of goal-directed navigation (27, 39–43). In *Drosophila*, Ca^{2+}-imaging revealed a single bump of activity in the columns of the ellipsoid body (4), the fan-shaped body (7), and the PB (6, 8) of the CX corresponding to a head direction signal based on visual landmark information and self-motion cues (4, 44). Differences in the angular offset between bump position and actual heading in different individual flies together with physiological manipulation of bump position and connectivity data strongly suggest that heading representation is based on a ring attractor network in the ellipsoid body and the PB (9, 45–47). Ring attractor networks have been previously proposed to underlie head direction coding in mammals and are characterized in flies by a single bump of activity within the circular CX network relating directly to an angular direction (3, 9, 48). While in *Drosophila*, emphasis has been on the role of landmark and self-motion cues in driving the position of this bump, sky compass signals, as demonstrated to drive neural activity in CX neurons in the locust, dung beetle, sweat bee, and monarch butterfly (12, 29, 49, 50), apparently play a role in *Drosophila*, too (16). In flies and locusts, directional

heading signals are represented in the CX in a compass-like, topographic fashion (4, 8, 16, 28, 29). In the locust, compass-like representations of zenithal AoP and azimuth of a simulated sun, found in the columns of the PB, are based on recordings from single neurons innervating different columns within the PB (28, 29). Because topographies in the locust were extracted from data obtained from different individual animals, representation of celestial cues appears to be fixed across individuals unlike the highly flexible topography in *Drosophila* (4, 16, 28, 29). Despite these apparent differences in sensory inputs and internal topographies between locust and fly, a ring attractor network as suggested to underlie heading representation in the fly CX may operate in locusts as well (13).

Matched-Filter Tuning Is Topographically Represented in the PB. A puzzling result of the study by Pegel et al. (29) was that the compass representations based on the preference angle of polarized zenithal light (28, 29) and azimuth representation of an unpolarized light spot (29), obtained from the same set of neurons, generated contradicting spatial information (Fig. 1 *D* and *E*) although these cues are tightly coupled under natural conditions and, therefore, should provide the same directional information. Whereas the zenithal AoP preference changed in a counterclockwise manner from PB column L8 to column R8, the preferred azimuth changed in a clockwise fashion. Assessing the matched-filter properties of the neurons for whole-sky polarization tuning allowed us to calculate hypothetical sun positions corresponding to those matched filters. The azimuthal component of these calculated sun positions is again represented topographically along the PB, consistent with a sun compass solely based on the polarization pattern of the sky (Fig. 5 *B* and *C*). This compass covers the full range of directions around the animal, making it suitable to unambiguously signal solar azimuth. The azimuth compass for unpolarized light spots (29), directly indicating the solar position (Fig. 1*E*), is highly similar to the matched-filter polarization compass (Fig. 5 *B* and *C*), both in terms of 360° coverage and sign of the regression slope, i.e., both compasses provide the same output, however, based on different environmental cues.

The compass mismatch reported by Pegel et al. (29) may be based on inadequate compass information provided by the zenithal AoP alone. It has been suggested previously that insects need to perceive large parts of the sky polarization pattern in order to orient correctly: behavioral experiments showed that honey bees make systematic orientation errors when their view on the sky is restricted to a small patch (30, 31). These errors might explain the conflicting outputs of the previously reported azimuth and polarization compasses (29). Because of its 180° periodicity, a single AoP as presented in previous studies does not provide an unambiguous orientation signal, especially if the receptive field center of the recorded neuron is not in the zenith (51), which is the case for several of the neurons studied here. The matched-filter compass, instead, matches well with the azimuth compass because it results from integrating the AoP over large parts of the visual field, which solves the ambiguity that arises from perceiving a single AoP at a small patch in the sky. A recent computational study (52) presenting a model of the insect polarization compass also suggests that the compass output generated under visual stimulation from a single spot conflicts with the output generated under whole-sky stimulation in a similar way as shown by Pegel et al. (29).

The matched-filter polarization compass presented here is based on pooling data from different cell types in the PB and, therefore, assumes that different neurons innervating the same PB column share a common heading preference. This is supported by previous data in locust (28, 29) revealing highly similar tuning preference to zenithal AoP in different types of columnar neuron of the same PB column and by a recent study in *Drosophila*, showing matching bump activity in neurons innervating corresponding columns of the ellipsoid and fan-shaped body (7). In addition, we investigated the impact of each cell type on the regression results and found that the compass topography is robust even when individual cell types are excluded (*SI Appendix*, Fig. S9). Nevertheless, differences between individual animals as well as phase shifts between different cell types might contribute to the relatively high variability of our tuning data (Fig. 5*B*). Because large interindividual differences in the angular offset of activity bump position and environmental cues are a key feature of head direction coding in *Drosophila* (4), a combination of data from different individual flies would most likely not result in a common compass representation across flies.

The CX has been shown to be a navigation hub, and in the desert locust's natural habitat, where local cues are scarce and celestial cues are reliable, it is conceivable that the polarization-based compass proposed in this study pervades the entire network, contributing to robust, multimodal celestial navigation.

Methods

Animals and Preparation. Adult desert locusts (*S. gregaria*), reared under crowded conditions at 28 °C in a 12 h/12 h light/dark cycle, were used for experiments. After removing legs and wings, they were mounted on a metal holder using dental wax. The head capsule was opened frontally, and ocelli and antennae were removed in the process; tracheal, fat, and muscle tissue were partially removed to expose the brain and mechanically isolate it for means of stabilization. The esophagus was cut near the mandibles and removed together with the gut through the abdomen. A twisted metal wire covered in wax, forming a small platform, was placed posterior to the brain and was fixed to the ventral head capsule to increase recording stability. Finally, the neural sheath was partly removed with forceps to allow brain penetration by the recording electrode. Specimens were kept moist during preparation, recording, and dissection with locust saline (53).

Intracellular Recording and Histology. We measured neural activity with sharp microelectrodes drawn from borosilicate capillaries (Hilgenberg) with a Flaming/Brown filament puller (P-97; Sutter Instrument), their tips filled with a solution of Neurobiotin tracer (Vector Laboratories; 4% in 1 M KCl) and shanks filled with 1 M KCl. Signals were amplified ×10 and filtered (Bessel filter, 20-kHz cutoff frequency) with an SEC 05L amplifier (npi electronic GmbH), monitored via a custom-built audio monitor (University of Marburg, Germany) and an oscilloscope (HAMEG Instruments GmbH), digitized with a Power1401-mkII (Cambridge Electronic Design) at 12.5 kHz, recorded with Spike2 (Cambridge Electronic Design), and analyzed offline with custom scripts for MATLAB (MathWorks). After stimulation, Neurobiotin was injected by applying positive current of 0.2 to 2 nA for at least 2 min. For histology, brains were dissected and then fixed overnight in a solution of 4% paraformaldehyde, 0.25% glutaraldehyde, and 0.2% saturated picric acid diluted in 0.1 M PBS and optionally kept at 4 °C in sodium phosphate buffer until further processing. They were rinsed in PBS (4 × 15 min) and incubated with Cy3-conjugated Streptavidin (Dianova; 1:1,000 in PBS with 0.3% Triton X-100 [PBT]) for 3 d at 4 °C. After rinsing in PBT (2 × 30 min) and PBS (3 × 30 min), they were dehydrated in an ascending ethanol series (30%, 50%, 70%, 90%, 95%, and 2 × 100%, 15 min each) and cleared in a 1:1 solution of ethanol (100%) and methyl salicylate for 20 min and in pure methyl salicylate for 35 min, to finally mount them in Permount (Fisher Scientific) between two coverslips. To identify cell morphologies, specimens were scanned with a confocal laser-scanning microscope (Leica TCS SP5; Leica Microsystems). Cy3 fluorescence was elicited with a diode-pumped solid-state laser at 561 nm wavelength. Image stacks were then processed into maximum intensity projections using Fiji (54, 55), and projections were edited in Adobe Photoshop and Illustrator (Adobe Systems Inc.). Ramification domains of neurons were deduced from their relative position within neuropils, identifiable through tissue autofluorescence, and morphological characteristics as described previously (56, 57).

Stimulation. Animals were stimulated with polarized blue light (465 nm) from various directions as previously described (32), except that we added a diffuser between LED (ELJ-465-627; Roithner LaserTechnik) and polarizer (HN38S; Polaroid), which resulted in a photon flux of 7.76×10^{13} photons $\cdot$ cm^{-2} $\cdot$ s^{-1}. Briefly, we measured the preferred AoP of single cells depending on stimulus position in the animal's dorsal visual field, ranging

down to 0° elevation. We successively stimulated from 33 positions, each stimulation composed of three consecutive full rotations of the polarizer at 40° · s^{-1}: a counterclockwise rotation of the polarizer, which was discarded to exclude artifacts from phasic light-on responses, and one clockwise and another counterclockwise rotation, which were averaged to calculate the preferred AoP. Testing all stimulus positions took roughly 40 min; in some cases, not all 33 positions could be tested due to instability of recordings.

Data Evaluation.

Calculating preferred AoP. Action potentials were assigned the orientation of the polarizer at the respective timing; the resulting angles were multiplied by 2 for axial correction, averaged using the *CircStat* toolbox (58), and divided by 2, yielding the preferred AoP during this rotation. Averaging multiple rotations was done by pooling all angles and then averaging them as above. To statistically assess a response, we binned the data in 10° bins and tested the resulting bin counts for correlation with bin angles using linear-circular correlation analysis (58), yielding a P value, correlation coefficient, and coefficient of determination (R^2). Neuronal activity was considered to be significantly modulated by the presented AoP if P was < 0.05. Circular histograms were created with the *CircHist* package (59).

Calculating the best-matching polarization pattern. The same procedure was applied as previously described (32), with minor differences, and is summarized conceptually here (see *SI Appendix, Methods* and Figs. S5 and S6, for extended information). Briefly, we compared the pattern of preferred AoPs in the dorsal hemisphere with polarization patterns that would arise from specific solar positions to obtain one best-matching pattern. The azimuthal component of the solar position that belonged to this pattern was considered to be the preferred solar azimuth of the recorded cell. Solar polarization patterns were generated from 32,760 (360 × 91) virtually equally spaced solar positions on a dense hemispherical Fibonacci grid (60) with a spacing of 0.022° ± (8.7×10^{-5})° (average angle ±95% confidence interval) distance to the nearest neighbor. For each solar position, the AoP and degree of polarization were calculated at those positions that the animal was stimulated from, based on the single-scattering Rayleigh model (61) (Fig. 1*A*). At each stimulus position, the unsigned angular difference between the measured preferred AoP and the pattern's AoP at this position was calculated. Only AoP responses with statistically significant modulation were used. Angular differences were averaged, each difference weighted by the degree of polarization, the response-correlation's R^2 value, and the normalized sum of the arc distances to the nearest 22% of stimulus positions. This yielded a solar position-specific average deviation between the polarization pattern as generated from the sun at this position and the neuron's pattern of preferred AoPs. The polarization pattern corresponding to the solar position with the lowest deviation was considered the best-matching pattern, meaning that the perception of a full polarization pattern as produced by the sun at this position should evoke the highest neuronal activity in the recorded neuron. The dependence of the azimuth of this preferred solar position on the column of neural arborization was tested using circular–linear correlation analysis (62).

Bootstrapping. To classify the magnitude of pattern deviations—whether the lowest pattern deviation is objectively low—we implemented a bootstrapping procedure that created a population of 1,000 randomized samples for each dataset. A randomized sample was obtained by randomly drawing (with replacement) stimulus responses from the pool of measured responses that showed a statistically significant activity modulation and distributing them on all stimulus positions used during this experiment. Each sample was treated as described above for real datasets, yielding a best-matching polarization pattern and its average deviation from the randomized response pattern. We then used the population of randomization-based pattern deviations to classify the minimum pattern deviation of the actual dataset by calculating a bootstrap P value with $P(D) = \frac{\sum_{k=1}^{b} [d_k \leq D]}{b}$, where D is the minimum pattern deviation of the actual dataset, k is the bootstrap sample index, b is the number of samples (1,000), and d_k is the minimum pattern deviation of the kth sample. Simply put, P equals the fraction of the number of bootstrapped minimum pattern deviations that are less than or equal to the minimum pattern deviation of the actual dataset. We considered D to be objectively low if $P(D) < 0.05$, which is equivalent to D being below the 5% percentile of the bootstrap population. From a total of 23 datasets, this was the case for 17; only these were used for further analysis of matched-filter tuning (cf. *SI Appendix*, Fig. S8, for the same analysis based on all datasets).

Estimating visual fields. We calculated the dimensions of visual fields based on the R^2 value of AoP responses. Briefly, we excluded data points for which the response's normalized (per neuron) R^2 value was below 0.75 and assigned the remaining data points to clusters based on their distance to one another (see *SI Appendix*, Fig. S2, for a detailed graphical description). First, we created a hemispherical Fibonacci grid (60) of 2,500 virtually equally distributed points. To simplify calculations, we flattened the grid and the spherical data points that referred to the stimulation positions by converting them to polar coordinates where the center (radius $\rho = 1$) corresponds to the zenith and points with $\rho = 1$ and arbitrary θ correspond to the spherical coordinate with 0° elevation and θ azimuth. To facilitate the next steps, these coordinates were further converted to planar Cartesian coordinates. We then linearly interpolated the R^2 values at the stimulation positions over the generated grid using MATLAB's *scatteredInterpolant* function. Points that were outside the convex hull built from the Delaunay-triangulated stimulation positions were discarded; this way, only the part of the visual field being enclosed by the outermost (relative to the zenith as center) stimulus positions was considered. The interpolated R^2 values were normalized to their range, and all data points where $R^2_{\text{norm}} < 0.75$ were discarded. This resulted in one or more clouds of data points on the flattened visual field of the animal where the AoP response was relatively high; we considered these clouds the receptive fields of the recorded cell. We then used a hierarchical cluster analysis approach in order to objectively separate the resulting clouds from one another and categorize them into individual receptive fields. First, the points were converted back to spherical coordinates, and their pairwise distances were calculated with the *pdist* function using the great-circle distance as the distance measure. Cluster trees were generated with the *linkage* function; to find the linkage method that resulted in a tree that described the distance relationships in the data best, we used *cophenet* to calculate the cophenetic correlation coefficient for each method and used the one with the highest coefficient. We then used *evalclusters* with the gap criterion, also called "elbow method," and the silhouette criterion to find the optimal number of clusters in the tree; separation into maximal six clusters was considered. The optimal number of clusters was chosen based on visual inspection of the raw clusters and the cluster tree and on the tree evaluation.

Data Availability. Physiological recordings, neural morphologies, and MATLAB code have been deposited in data_UMR for public access (https://dx.doi.org/10.17192/fdr/22 and https://dx.doi.org/10.17192/fdr/23) (64, 65).

ACKNOWLEDGMENTS. We thank Dr. Stephanie Wegener and Jann Goschenhofer for initial discussions on the bootstrap procedure, Dr. Naomi Takahashi for supplying additional data, Dr. Basil el Jundi for helpful discussions on the manuscript draft, and Martina Kern for maintaining locust cultures. This work was funded by DFG (Deutsche Forschungsgemeinschaft, German Research Foundation) grants HO 950/24-1 and HO 950/25-1 to U.H.

1. J. S. Taube, Head direction cells and the neurophysiological basis for a sense of direction. *Prog. Neurobiol.* **55**, 225–256 (1998).
2. J. S. Taube, The head direction signal: Origins and sensory-motor integration. *Annu. Rev. Neurosci.* **30**, 181–207 (2007).
3. D. E. Angelaki, J. Laurens, The head direction cell network: Attractor dynamics, integration within the navigation system, and three-dimensional properties. *Curr. Opin. Neurobiol.* **60**, 136–144 (2020).
4. J. D. Seelig, V. Jayaraman, Neural dynamics for landmark orientation and angular path integration. *Nature* **521**, 186–191 (2015).
5. A. G. Varga, R. E. Ritzmann, Cellular basis of head direction and contextual cues in the insect brain. *Curr. Biol.* **26**, 1816–1828 (2016).
6. J. Green, V. Vijayan, P. Mussells Pires, A. Adachi, G. Maimon, A neural heading estimate is compared with an internal goal to guide oriented navigation. *Nat. Neurosci.* **22**, 1460–1468 (2019).
7. H. M. Shiozaki, K. Ohta, H. Kazama, A multi-regional network encoding heading and steering maneuvers in *Drosophila*. *Neuron* **106**, 126–141.e5 (2020).
8. J. Green *et al.*, A neural circuit architecture for angular integration in *Drosophila*. *Nature* **546**, 101–106 (2017).
9. S. S. Kim, H. Rouault, S. Druckmann, V. Jayaraman, Ring attractor dynamics in the *Drosophila* central brain. *Science* **356**, 849–853 (2017).
10. S. S. Kim, A. M. Hermundstad, S. Romani, L. F. Abbott, V. Jayaraman, Generation of stable heading representations in diverse visual scenes. *Nature* **576**, 126–131 (2019).
11. U. Pegel, K. Pfeiffer, U. Homberg, Integration of celestial compass cues in the central complex of the locust brain. *J. Exp. Biol.* **221**, jeb171207 (2018).
12. S. Heinze, S. M. Reppert, Sun compass integration of skylight cues in migratory monarch butterflies. *Neuron* **69**, 345–358 (2011).
13. T. Stone *et al.*, An anatomically constrained model for path integration in the bee brain. *Curr. Biol.* **27**, 3069–3085.e11 (2017).
14. B. el Jundi *et al.*, Neural coding underlying the cue preference for celestial orientation. *Proc. Natl. Acad. Sci. U.S.A.* **112**, 11395–11400 (2015).
15. P. T. Weir, M. H. Dickinson, Flying *Drosophila* orient to sky polarization. *Curr. Biol.* **22**, 21–27 (2012).

16. Y. M. Giraldo *et al*., Sun navigation requires compass neurons in *Drosophila*. *Curr. Biol.* **28**, 2845–2852.e4 (2018).
17. K. Fent, Polarized skylight orientation in the desert ant *Cataglyphis*. *J. Comp. Physiol. A Neuroethol. Sens. Neural Behav. Physiol.* **158**, 145–150 (1986).
18. M. L. Brines, J. L. Gould, Bees have rules. *Science* **206**, 571–573 (1979).
19. S. M. Reppert, H. Zhu, R. H. White, Polarized light helps monarch butterflies navigate. *Curr. Biol.* **14**, 155–158 (2004).
20. B. el Jundi, J. Smolka, E. Baird, M. J. Byrne, M. Dacke, Diurnal dung beetles use the intensity gradient and the polarization pattern of the sky for orientation. *J. Exp. Biol.* **217**, 2422–2429 (2014).
21. D. Brunner, T. Labhart, Behavioural evidence for polarization vision in crickets. *Physiol. Entomol.* **12**, 1–10 (1987).
22. M. Mappes, U. Homberg, Behavioral analysis of polarization vision in tethered flying locusts. *J. Comp. Physiol. A Neuroethol. Sens. Neural Behav. Physiol.* **190**, 61–68 (2004).
23. T. L. Warren, P. T. Weir, M. H. Dickinson, Flying *Drosophila melanogaster* maintain arbitrary but stable headings relative to the angle of polarized light. *J. Exp. Biol.* **221**, jeb177550 (2018).
24. T. F. Mathejczyk, M. F. Wernet, Heading choices of flying *Drosophila* under changing angles of polarized light. *Sci. Rep.* **9**, 16773 (2019).
25. T. Labhart, E. P. Meyer, Detectors for polarized skylight in insects: A survey of ommatidial specializations in the dorsal rim area of the compound eye. *Microsc. Res. Tech.* **47**, 368–379 (1999).
26. U. Homberg, S. Heinze, K. Pfeiffer, M. Kinoshita, B. el Jundi, Central neural coding of sky polarization in insects. *Philos. Trans. R. Soc. Lond. B Biol. Sci.* **366**, 680–687 (2011).
27. K. Pfeiffer, U. Homberg, Organization and functional roles of the central complex in the insect brain. *Annu. Rev. Entomol.* **59**, 165–184 (2014).
28. S. Heinze, U. Homberg, Maplike representation of celestial *E*-vector orientations in the brain of an insect. *Science* **315**, 995–997 (2007).
29. U. Pegel, K. Pfeiffer, F. Zittrell, C. Scholtyssek, U. Homberg, Two compasses in the central complex of the locust brain. *J. Neurosci.* **39**, 3070–3080 (2019).
30. S. Rossel, R. Wehner, The bee's map of the e-vector pattern in the sky. *Proc. Natl. Acad. Sci. U.S.A.* **79**, 4451–4455 (1982).
31. S. Rossel, R. Wehner, How bees analyse the polarization patterns in the sky. *J. Comp. Physiol. A Neuroethol. Sens. Neural Behav. Physiol.* **154**, 607–615 (1984).
32. M. Bech, U. Homberg, K. Pfeiffer, Receptive fields of locust brain neurons are matched to polarization patterns of the sky. *Curr. Biol.* **24**, 2124–2129 (2014).
33. F. Schmeling, J. Tegtmeier, M. Kinoshita, U. Homberg, Photoreceptor projections and receptive fields in the dorsal rim area and main retina of the locust eye. *J. Comp. Physiol. A Neuroethol. Sens. Neural Behav. Physiol.* **201**, 427–440 (2015).
34. U. Homberg, A. Paech, Ultrastructure and orientation of ommatidia in the dorsal rim area of the locust compound eye. *Arthropod Struct. Dev.* **30**, 271–280 (2002).
35. S. Heinze, "Polarized-light processing in insect brains: Recent insights from the desert locust, the monarch butterfly, the cricket, and the fruit fly" in *Polarized Light and Polarization Vision in Animal Sciences*, G. Horváth, Ed. (Springer, 2014), pp. 61–111.
36. P. T. Weir *et al*., Anatomical reconstruction and functional imaging reveal an ordered array of skylight polarization detectors in *Drosophila*. *J. Neurosci.* **36**, 5397–5404 (2016).
37. S. Rossel, R. Wehner, Polarization vision in bees. *Nature* **323**, 128–131 (1986).
38. K. Pfeiffer, M. Negrello, U. Homberg, Conditional perception under stimulus ambiguity: Polarization- and azimuth-sensitive neurons in the locust brain are inhibited by low degrees of polarization. *J. Neurophysiol.* **105**, 28–35 (2011).
39. S. Heinze, Unraveling the neural basis of insect navigation. *Curr. Opin. Insect Sci.* **24**, 58–67 (2017).
40. B. el Jundi, E. Baird, M. J. Byrne, M. Dacke, The brain behind straight-line orientation in dung beetles. *J. Exp. Biol.* **222**, jeb192450 (2019).
41. A. G. Varga, N. D. Kathman, J. P. Martin, P. Guo, R. E. Ritzmann, Spatial navigation and the central complex: Sensory acquisition orientation and motor control. *Front. Behav. Neurosci.* **11**, 4 (2017).
42. D. B. Turner-Evans, V. Jayaraman, The insect central complex. *Curr. Biol.* **26**, R453–R457 (2016).
43. A. Honkanen, A. Adden, J. da Silva Freitas, S. Heinze, The insect central complex and the neural basis of navigational strategies. *J. Exp. Biol.* **222**, jeb188854 (2019).
44. D. Turner-Evans *et al*., Angular velocity integration in a fly heading circuit. *eLife* **6**, e23496 (2017).
45. K. S. Kakaria, B. L. de Bivort, Ring attractor dynamics emerge from a spiking model of the entire protocerebral bridge. *Front. Behav. Neurosci.* **11**, 8 (2017).
46. R. Franconville, C. Beron, V. Jayaraman, Building a functional connectome of the *Drosophila* central complex. *eLife* **7**, e37017 (2018).
47. J. Green, G. Maimon, Building a heading signal from anatomically defined neuron types in the *Drosophila* central complex. *Curr. Opin. Neurobiol.* **52**, 156–164 (2018).
48. J. J. Knierim, K. Zhang, Attractor dynamics of spatially correlated neural activity in the limbic system. *Annu. Rev. Neurosci.* **35**, 267–285 (2012).
49. B. el Jundi, K. Pfeiffer, S. Heinze, U. Homberg, Integration of polarization and chromatic cues in the insect sky compass. *J. Comp. Physiol. A Neuroethol. Sens. Neural Behav. Physiol.* **200**, 575–589 (2014).
50. B. el Jundi, J. J. Foster, M. J. Byrne, E. Baird, M. Dacke, Spectral information as an orientation cue in dung beetles. *Biol. Lett.* **11**, 20150656 (2015).
51. K. Pfeiffer, U. Homberg, Coding of azimuthal directions via time-compensated combination of celestial compass cues. *Curr. Biol.* **17**, 960–965 (2007).
52. E. Gkanias, B. Risse, M. Mangan, B. Webb, From skylight input to behavioural output: A computational model of the insect polarised light compass. *PLOS Comput. Biol.* **15**, e1007123 (2019).
53. A. N. Clements, T. E. May, Studies on locust neuromuscular physiology in relation to glutamic acid. *J. Exp. Biol.* **60**, 673–705 (1974).
54. J. Schindelin *et al*., Fiji: An open-source platform for biological-image analysis. *Nat. Methods* **9**, 676–682 (2012).
55. C. A. Schneider, W. S. Rasband, K. W. Eliceiri, NIH image to ImageJ: 25 years of image analysis. *Nat. Methods* **9**, 671–675 (2012).
56. S. Heinze, U. Homberg, Neuroarchitecture of the central complex of the desert locust: Intrinsic and columnar neurons. *J. Comp. Neurol.* **511**, 454–478 (2008).
57. M. J. Beetz, B. el Jundi, S. Heinze, U. Homberg, Topographic organization and possible function of the posterior optic tubercles in the brain of the desert locust *Schistocerca gregaria*. *J. Comp. Neurol.* **523**, 1589–1607 (2015).
58. P. Berens, CircStat: A MATLAB toolbox for circular statistics. *J. Stat. Soft.* **31**, 1–21 (2009).
59. F. Zittrell, CircHist: Circular histogram in MATLAB. https://dx.doi.org/10.5281/zenodo.3445083. Accessed 19 March 2020.
60. R. Swinbank, R. J. Purser, Fibonacci grids: A novel approach to global modelling. *Q. J. R. Meteorol. Soc.* **132**, 1769–1793 (2006).
61. J. W. Strutt, XV. On the light from the sky, its polarization and colour. *Phil. Mag.* **41**, 107–120–274–279 (1871).
62. R. Kempter, C. Leibold, G. Buzsáki, K. Diba, R. Schmidt, Quantifying circular-linear associations: Hippocampal phase precession. *J. Neurosci. Methods* **207**, 113–124 (2012).
63. A. E. Kurylas, T. Rohlfing, S. Krofczik, A. Jenett, U. Homberg, Standardized atlas of the brain of the desert locust, *Schistocerca gregaria*. *Cell Tissue Res.* **333**, 125–145 (2008).
64. F. Zittrell, MATLAB code files from "Matched-filter coding of sky polarization results in an internal sun compass in the brain of the desert locust." data_UMR. Available at https://dx.doi.org/10.17192/fdr/22. Deposited 26 June 2020.
65. F. Zittrell, Raw data: Recording files and microscope image stacks from "Matched-filter coding of sky polarization results in an internal sun compass in the brain of the desert locust." data_UMR. Available at https://dx.doi.org/10.17192/fdr/23. Deposited 26 June 2020.

Chapter 3

Receptive Field Structures for Two Celestial Compass Cues at the Input Stage of the Central Complex in the Locust Brain

Receptive field structures for two celestial compass cues at the input stage of the central complex in the locust brain

Running title: Receptive fields for celestial compass cues

Naomi Takahashi[1], Frederick Zittrell[1], Ronja Hensgen[1], Uwe Homberg[1,2*]
[1]Department of Biology, Animal Physiology, Philipps-Universität Marburg, D-35032 Marburg, Germany
[2]Center for Mind, Brain and Behavior (CMBB), University of Marburg and Justus Liebig University Giessen

*Correspondence to: Uwe Homberg, Fachbereich Biologie, Tierphysiologie, Philipps-Universität Marburg, D-35032 Marburg, Germany, Tel. +49-6421-2823402, Fax +49-6421-13 2828941, E-mail: homberg@staff.uni-marburg.de

Key words: sun compass orientation, insect brain, central complex, polarization vision, desert locust

Number of pages: 34

Number of figures and tables: 7 figures

Number of words for Abstracts: 250

Total words: 6410 (introduction 719, results 2715, discussion 1494, legends 1482)

Supplementary information: 1 PDF file (4.0 MB)

Summary Statement

GABAergic input neurons to the locust sky compass detect sky polarization and sun position but show poor matched-filter performance, suggesting that faithful heading direction signaling emerges within the central complex.

List of Symbols and Abbreviations

AoP, angle of polarization; BA, background activity; CBL, lower division of the central body; CBU, upper division of the central body; CX, central complex; GABA, γ-aminobutyric acid; PB, protocerebral bridge; TL neuron, tangential neuron of the CBL; Φ_{max} and Φ_{min}; preferred angle and anti-preferred angle

Abstract

Successful navigation depends on an animal's ability to perceive its spatial orientation relative to visual surroundings. Heading direction in insects is represented in the central complex (CX), a navigation center in the brain, to generate steering commands. In insects that navigate relative to sky compass signals, CX neurons are tuned to celestial cues indicating the location of the sun. The desert locust CX contains a compass-like representation of two related celestial cues: the direction of unpolarized direct sunlight and the pattern of polarized light, which depends on the sun position. Whether congruent tuning to these two compass cues emerges within the CX network or is inherited from CX input neurons is unclear. To address this question, we intracellularly recorded from GABA-immunoreactive TL neurons, input elements to the locust CX (corresponding to R neurons in *Drosophila*), while applying visual stimuli simulating unpolarized sunlight and polarized light across the hemisphere above the animal. We show that TL neurons have large receptive fields for both types of stimuli. However, faithful integration of polarization angles across the dorsal hemisphere, or matched-filter ability to encode particular sun positions, was found in only two out of 22 recordings. Additionally, only two neurons showed a good match in sun position coding through polarized and unpolarized light signaling, whereas 20 neurons showed substantial mismatch in signaling of the two compass cues. The data, therefore, suggest that considerable refinement of azimuth coding based on sky compass signals occurs at the synapses from TL neurons to postsynaptic CX compass neurons.

Introduction

Spatial orientation relative to visual surroundings is a crucial ability for successful navigation. Neurons representing an animal's orientation, such as the rat head direction cells (Taube et al., 1990a; Taube et al., 1990b), have been intensely studied (Cullen and Taube, 2017). Theoretical studies have proposed recurrent network models called ring attractors to explain neuronal population dynamics of heading representation (Knierim and Zhang, 2012; Skaggs et al., 1995). Theoretical and experimental data suggested that heading-direction systems are driven by internally generated self-motion cues, but most networks also use external sensory cues for feedback control, such as visual landmarks.

Insects also show physiological signatures of heading-direction coding to visual references, enabling the characterization of ring attractor elements in biological circuits that consist of a much smaller number of neurons than mammalian systems (Green and Maimon, 2018; Turner-Evans et al., 2020). Heading direction is represented in the central complex (CX), a navigation center of the insect brain, to generate appropriate motor commands. The CX is a group of midline-spanning neuropils consisting of the protocerebral bridge (PB), the upper and the lower divisions of the central body (CBU and CBL, also termed fan-shaped body and ellipsoid body), and the paired noduli. These neuropils are

subdivided into vertical slices and horizontal layers by neuronal projection patterns (Heinze and Homberg, 2008; Hulse et al., 2021; Wolff et al., 2015). In *Drosophila*, heading direction is represented as a localized bump of population activity in the so-called E-PG neurons of a ring attractor (Green et al., 2017; Seelig and Jayaraman, 2015). E-PG neurons are topographically arranged in the slices of the CBL and PB. The activity bump moves to neighboring slices when the fly turns clockwise or counterclockwise, and optogenetic manipulation of the bump position leads to flight orientation shifts following the bump (Kim et al., 2019). This heading representation works in darkness but more reliably when a visual cue is available (Turner-Evans et al., 2020).

In several insects, many neurons of the CX are tuned to visual stimuli simulating celestial cues (el Jundi et al., 2015; Hardcastle et al., 2021; Heinze and Homberg, 2007; Heinze and Reppert, 2011). Celestial cues are related to the location of the sun and include the direction of unpolarized direct sunlight as well as the products of sunlight scattering in the atmosphere, such as a coherent polarization pattern and chromatic gradient across the sky (Fig. 1A). Therefore, these neurons are suitable for heading-direction coding relative to the sun and considered a basis of orientation behavior dependent on a sky compass (Heinze, 2017; Honkanen et al., 2019).

In desert locusts, different celestial cues complement each other for robust heading-direction coding. The locust CX contains a topographic arrangement of neurons tuned to the azimuth of bright light spots, simulating direct sunlight, across the vertical slices of the PB (Pegel et al., 2019). The neurons are also tuned to the angle of polarization (AoP) of light across the entire hemisphere above the animal (Bech et al., 2014; Zittrell et al., 2020). The AoP tunings of individual neurons are coherently arranged across the dorsal hemisphere and match the sky polarization pattern produced by a particular position of the sun (Bech et al., 2014; Zittrell et al., 2020). This polarization-based solar azimuth is topographically arranged consistent with the direct sunlight compass (Zittrell et al., 2020).

The polarization-vision pathway is largely conserved across insects (el Jundi et al., 2014; Hardcastle et al., 2021; Homberg et al., 2011). It originates from the dorsal rim area of the compound eye, where specialized, homochromatic photoreceptors detect polarized light, and runs through the optic lobe, anterior optic tubercle, and bulb to finally enter the CBL via tangential neurons (TL neurons, corresponding to R neurons in *Drosophila*). Tuning of TL neurons to the AoP in the zenith above the animal and to the azimuth of light spots shows a 90°-angular difference (Pegel et al., 2018) corresponding to the natural relationship between the zenithal AoP and the solar azimuth in the sky (Fig. 1A). To elucidate whether the matching AoP- and direct sunlight signaling in postsynaptic CX compass neurons studied by Zittrell et al. (2020) is inherited from TL neurons, or emerges through integration of TL inputs to postsynaptic CX compass neurons, we studied the receptive field structures of TL neurons by applying light stimuli simulating polarization and direct sunlight across the sky.

Materials and Methods

Animals and preparation

Adult male and female desert locusts (*Schistocerca gregaria*) were reared under crowded conditions at 28°C in a 12/12 h light/dark cycle. After removing legs and wings, animals were mounted on a metal holder with dental wax. The head capsule was opened frontally; ocelli and antennae were removed. Fat, tracheal tissues, and muscles were partially removed to expose the brain. We also removed the esophagus and gut through the abdomen to reduce peristaltic movements. A twisted metal wire was placed under the brain to stabilize it. A small part of the neural sheath was removed with fine tweezers to allow brain penetration by the recording electrode. During dissection and intracellular recording, the brain was immersed in locust saline (Clements and May, 1974).

Intracellular recording

Sharp glass microelectrodes were drawn from borosilicate capillaries (Hilgenberg, Malsfeld, Germany) by a Flaming/Brown horizontal puller (P-97, Sutter Instruments, Novato, CA, USA). We filled electrode tips with 4% Neurobiotin (Vector Laboratories, Burlingame, CA, USA) in 1 mol l^{-1} KCl and shanks with 1 mol l^{-1} KCl. Neural signals were amplified (×10) and filtered (20 kHz low-pass) by an amplifier (SEC 05L, npi electronic, Tamm, Germany). The signals were digitized at 20 kHz and stored on a PC by an A/D converter and associated software (Power1401-mkII and Spike2 version 7.06, Cambridge Electronic Design [CED], Cambridge, UK).

Visual stimulation

We used three types of light for visual stimulation: linearly polarized blue light, unpolarized green light, and unpolarized blue light. They were switchable during recording. Polarized blue light was used to test AoP sensitivity of single cells. Blue LED light (ELJ-465-627, Roithner LaserTechnik, Vienna, Austria) was passed through a diffuser and a polarizer (HN38S, Polaroid, Cambridge, MA, USA). The light covered a visual angle of 5.2°, and the light intensity was 8.4×10^{13} photons cm^{-2} s^{-1} with a peak at 461 nm. A single AoP stimulus was a full rotation of the polarizer at an angular velocity of 40°/s clockwise or counterclockwise. We started rotating the polarizer several seconds after the light was turned on to exclude phasic responses to lights on. The initial orientation of the polarizer was always 0°, which is parallel to the animal's anterior-posterior body axis when the light was positioned at the animal's zenith. An unpolarized green light was used to test sensitivity to direct sunlight, reported previously in TL neurons by Pegel et al. (2018, 2019). An unpolarized blue light was used for comparison. The light sources were green and blue LEDs (green: Nichia NCSE119A, Lumitronix, Hechingen, Germany; blue: OSLON SSL 80 LD CQ7P, OSRAM Opto Semiconductors, Regensburg, Germany). Both lights covered a visual angle of 1.05°. The green light intensity was 1.7×10^{14} photons cm^{-2} s^{-1} with a peak at 518 nm, and the blue one was 1.2×10^{15} photons cm^{-2} s^{-1} with a peak at 440 nm.

The stimulus setup was modified from that described by Bech et al. (2014) and Zittrell et al. (2020). The animal was positioned in the center of the setup with its anterior-posterior body axis oriented vertically (Fig. 1B). A stimulation device containing the three lights was mounted on a perimeter apparatus. After stimulating the animal from the zenith, we shifted the light device in left-right directions along the perimeter and tilted the whole perimeter in anterior-posterior directions (arrows in Fig. 1B). This allowed stimulating the animal from various positions in its dorsal visual field.

Histology

We injected Neurobiotin into the recorded cell by applying a positive current of up to 1 nA for 0.5–4 min. The brains were dissected out and submerged overnight at 4°C in fixative containing 4% paraformaldehyde (PFA), 0.25% glutaraldehyde, and 0.2% saturated picric acid in 0.1 mol l^{-1} phosphate buffered saline (PBS, 0.15 mol l^{-1} NaCl in 0.1 mol l^{-1} sodium phosphate buffer, pH 7.4). Optionally, the fixed brains were stored at 4°C in sodium phosphate buffer until further processing. After the fixation, the brains were rinsed in PBS and then incubated in Cy3-conjugated streptavidin (Dianova, Hamburg, Germany; 1:1000 in PBS with 0.3% Triton X-100) for 3 d at 4°C. The incubated brains were rinsed in PBS with 0.3% Triton X-100 followed by PBS, dehydrated in an ascending ethanol series (30%, 50%, 70%, 90%, 95%, 2 × 100%; 15 min each), and cleared in a 1:1 mixture of 100% ethanol and methyl salicylate for 20 min, followed by pure methyl salicylate for 35 min. Finally, we embedded the brains between two coverslips in Permount (Fisher Scientific, Waltham, MA, USA).

For double labeling of the recorded cells combined with GABA immunostaining, the staining method was modified from a previous study (Takahashi et al., 2017). Neurobiotin-injected brains were submerged overnight at 4°C in 4% PFA in 0.1 mol l^{-1} sodium phosphate buffer (pH 7.4). Immediately after fixation, the brains were rinsed in PBS, embedded in albumin-gelatin (4.8% gelatin and 12% ovalbumin in demineralized water), and fixed overnight at 4°C in 8% formaldehyde diluted in 0.1 mol l^{-1} sodium phosphate buffer. The brains in the gelatin block were cut into 80–130 µm sections by a vibrating-blade microtome (VT 1000S, Leica Microsystems, Wetzlar, Germany). Brain sections were rinsed in PBS with 1% Triton X-100 (PBST) and then blocked for 1 h at room temperature in 2% normal goat serum diluted in PBST with 0.25% bovine serum albumin (PBST-BSA). Afterward, the sections were incubated for 5 d at 4°C in a mixture of anti-synapsin monoclonal antibody (provided by Drs. Erich Buchner and Christian Wegener, University of Würzburg, Germany; 1:50) and anti-GABA polyclonal antibody generated in rabbit (A2052, RRID: AB_2315425, Sigma, Steinheim, Germany; 1:1000) diluted in PBST-BSA. Following the incubation, the sections were rinsed in PBST-BSA and incubated for 5 d at 4°C in a mixture of goat-anti-mouse-Cy5 (Dianova, 1:300), goat-anti-rabbit-Cy2 (Dianova, 1:300), and streptavidin-Cy3 (1:1,000) in PBST-BSA. After incubation, the sections were rinsed, dehydrated, cleared, and embedded in Permount.

Image acquisition and processing

We scanned preparations with a confocal laser scanning microscope (TCS SP5, Leica Microsystems). Cy3 signals were detected with a diode-pumped solid-state laser (561 nm). In GABA- and synapsin-labeled sections, Cy2 and Cy5 signals were detected with an argon laser (458 nm) and a helium-neon laser (633 nm), respectively. Spatial resolution (pixel size) in the xy-plane was about 0.51 µm x 0.51 µm for the morphology of whole neurons and approximately 0.13 µm x 0.13 µm for magnified cell bodies. Step size was 1.5–3.0 µm along the z-axis. Scanned images were stacked two-dimensionally in an image-processing software (ImageJ version 1.52a, NIH, Bethesda, MD, USA; Schneider et al., 2012). Input levels of the image stacks were uniformly adjusted in photo-editing software (GNU Image Manipulation Program version 2.10.22, GIMP Development Team). We deduced innervation layers of neurons from the position of their arborizations within neuropils, identifiable through tissue autofluorescence or visualized synapsin (Fig. 2C).

Data pre-processing

Physiological data were analyzed when the recorded neuron was successfully labeled. More than one neuron was stained in some preparations, probably due to leakage of Neurobiotin into neighboring cells. We included these cases in the analyses if we identified the recorded neuron based on Neurobiotin (Cy3) signal intensity (e.g., a TL3b neuron in Fig. 2C) or if all stained cells belonged to the same cell type and had cell bodies in the same brain hemisphere.

For pre-processing of recorded data, action potentials were detected in Spike2 by a threshold-based feature detection script (FeatureDetect.s2s, downloaded from the CED website). Detection quality was verified by visual inspection. We performed all subsequent analyses in MATLAB version 2021b (The MathWorks, Natick, MA, USA) and R version 4.1.1 (R Core Team, 2021). The significance level for statistical tests was $\alpha = 0.05$.

Data plots

Data were plotted as boxplots in the following way. Boxes range from the 25th (Q1) to 75th (Q3) percentile of the data. Horizontal lines in the boxes indicate the median. Whiskers extend to the adjacent value that is the most extreme data point, which is not less than $Q3 - 1.5\times(Q3 - Q1)$ and greater than $Q3 + 1.5\times(Q3 - Q1)$. Numerals of x-axis labels represent sample numbers.

Spherical coordinates of the dorsal visual field (Fig. 1B,C) were transformed on a polar-coordinate grid to show the data on a flattened hemisphere from above (Fig. 1D) following Zittrell et al. (2020). The center (pole) of the grid corresponds to the zenith (elevation = 90°). The radius from the pole (ρ) is defined as 1 – elevation/90° ($0 \leq \rho \leq 1$) and the angle (θ) equals the spherical azimuth ($0° \leq \theta < 360°$). Elevation and azimuth are indicated relative to the animal's head.

Response to AoP: sensitivity

Spike times during stimulation were transformed into the orientation of the polarizer (spike angles) based on angular velocity (40°/s) and direction (clockwise or counterclockwise) of polarizer rotation. Spike angles were used to calculate spike rates per 10°-bin (36 bins from 0° to 360°, Fig. 3A–C). For spike rate calculations, we pooled spike activities to equal numbers of clockwise and counterclockwise rotations to avoid spike angle shifts due to rotation direction.

To judge neural responses to the AoP orientation, we calculated the square of the circular-linear correlation coefficient ($0 \leq r_{cl}^2 \leq 1$) between bin center angles and spike rates per bin using the function "circ_corrcl" in the "Circular Statistics Toolbox" of MATLAB (Berens, 2009) (see Supplementary Materials and Methods). Bin center angles were doubled for the calculation because the AoP is axial data: 0° = 180° (Batschelet, 1981). Spike activities were considered an AoP response when the p value of $r_{cl}^2 < 0.05$. Because the p value of r_{cl}^2 depends on the sample number used for the calculation (Berens, 2009), and we always used spike rates of 36 bins, $p < 0.05$ is equivalent to $r_{cl}^2 > 0.1664$.

Response to AoP: tuning properties

To yield a tuning curve of AoP responses, we fitted von Mises distributions to spike angle data (Fig. 3C). The von Mises distribution is known as a circular normal distribution, commonly used for circular data analysis. In a von Mises distribution, the probability of angles θ depends on two parameters: peak position μ and concentration κ. Increasing values of κ represent increased probability of angles around μ, whereas $\kappa = 0$ results in the uniform distribution.

To describe our bimodal AoP response data, we mixed two von Mises distributions as described in Fitak and Johnsen (2017) and Schnute and Groot (1992):

$$\lambda M(\theta \mid \mu, \kappa) + \lambda M(\theta \mid \mu + \pi, \kappa) \qquad (1)$$

where $M(\theta \mid \mu, \kappa)$ denotes a von Mises distribution with peak μ and concentration κ. The mixed von Mises distribution represented by equation (1) possesses bimodal peaks of the same height (λ) and width (κ) in symmetric positions (μ and $\mu + \pi$). The best-fit parameters λ, μ, and κ for a tuning curve of the data were found by the maximum likelihood method; the likelihood was calculated by the function "circ_mle" in the "CircMLE" package of R (Fitak and Johnsen, 2017). The best-fit peak position μ ($0° \leq \mu < 180°$) was termed Φ_{max} (preferred angle), and Φ_{min} (anti-preferred angle) was defined as 90° distant from Φ_{max}. The half width at the half amplitude of the peak was used as tuning width (horizontal line segment in Fig. 3C). Tuning width was measured with increments of 1° to simplify the calculation.

Further, we quantified excitatory and inhibitory modulations of spike rate caused by AoP presentation based on the tuning curve and the background activity (BA). The BA level for this analysis was the averaged firing rate (spikes/s) calculated from one or several 1-s bins before the polarized light was turned on (horizontal line in Fig. 3C). We defined $\Phi_{max\,(min)}$ activity as the difference between the spike rate at $\Phi_{max\,(min)}$ and the BA (left and center arrows in Fig. 3C). These values indicate excitatory (upward arrow) or

inhibitory (downward arrow) modulation from the BA. In the example of Fig. 3C, Φ_{max} and Φ_{min} activities were excitatory and inhibitory, respectively. However, both Φ_{max} and Φ_{min} activities can be excitatory or inhibitory, depending on the tuning curve position relative to the BA. To compare modulation strengths and direction between individuals, we scaled Φ_{max} activities by the amplitudes of the individual tuning curves (Φ_{max} activity/amplitude). The amplitude of a tuning curve is defined as the difference of Φ_{max} and Φ_{min} activities (right upward arrow in Fig. 3C). Here, we did not use the BA for scaling because some individuals had no background spiking before the stimulus.

Response to AoP: receptive fields

To visualize neural receptive fields to AoP, we plotted surface heatmaps based on AoP sensitivity (r_{cl}^2) (Fig. 4A). The r_{cl}^2 values of tested positions were linearly interpolated in between on the flattened hemispheres (Fig. 1D) using the function "scatteredInterpolant" in MATLAB.

Further, we determined highly AoP sensitive parts of the receptive fields in each cell (black boundary lines in Fig. 4A) for comparison with downstream CX neurons analyzed in Zittrell et al. (2020), in which AoP receptive fields were defined as the regions with 75% or more r_{cl}^2 value to the response maxima of individual recordings. To find the corresponding regions, we followed the procedures of Zittrell et al. (2020). Normalized r_{cl}^2 values of tested positions were linearly interpolated to the points distributed over the surface of the dorsal visual field, and boundary lines were drawn to enclose all points with normalized $r_{cl}^2 \geq 0.75$.

A detailed description is provided by Zittrell et al. (2020). Briefly, first, we distributed 2,500 points evenly over the surface of a spherical dorsal visual field hemisphere using a hemispherical Fibonacci grid proposed by Swinbank and Purser (2006). The spherical coordinates for the 2,500 points were transformed to two-dimensional coordinates on a flattened hemisphere (Fig. 1D) to simplify the following calculations. Out of the 2,500 points, we only used the points inside the convex hull of the positions tested in individual recordings; the convex hull was built by the Delaunay triangulation method in the same way as surface heatmaps (e.g., Fig. 4A).

Next, the r_{cl}^2 values at the tested positions were normalized to the response maxima of individual recordings and linearly interpolated over the generated points using the function "scatteredInterpolant" in MATLAB. We picked up the points with normalized $r_{cl}^2 \geq 0.75$, which resulted in one or more clouds of data points. To categorize those clouds into individual fields, we used an agglomerative hierarchical clustering approach. This clustering method successfully merges pairs of the closest or most similar data point sets (clusters) into single clusters. In the first step, each data point was considered its own cluster. The distances or similarities between pairs of clusters are defined by a linkage criterion. In the current study, the linkage criterion "minimum distance (single-linkage) method" was applied to all recordings, defining the clusters' distance as the minimum distance between a data point in one cluster and a data point in the other cluster. The

great-circle distance was adopted as a distance measure, and the original spherical coordinates of data points were used to calculate the distances here (see Supplementary Materials and Methods). The clusters were split (not merged) when their distance was greater than the visual angle covered by the polarized light of the stimulus setup ($5.2° \times \pi/180$). Finally, we drew a boundary line to enclose all data points of each cluster to mark the higher AoP sensitivity regions corresponding to the study by Zittrell et al. (2020).

Response to AoP: best-matching polarization patterns

Many neurons of the locust CX show coherent arrangements of preferred AoP orientations across the dorsal visual field (Bech et al., 2014; Zittrell et al., 2020). These tuning arrangements act as filters that match the sky polarization pattern generated by particular solar coordinates relative to the animal (Bech et al., 2014; Zittrell et al., 2020). We defined the best-matching polarization pattern as the sky polarization pattern that would evoke the highest neuronal activity in a cell. We also defined the preferred sun encoded by AoP responses as the solar coordinates that generate the best-matching polarization pattern.

To find the preferred sun encoded by AoP responses (Fig. 5A), we used the procedure described in Zittrell et al. (2020), which was adapted from the original of Bech et al. (2014). This procedure calculates deviations between a neural response pattern (Φ_{max} angles) and various model sky polarization patterns. The model pattern with the minimum deviation from the neural responses is considered the best-matching pattern, and the corresponding solar coordinates are the position of the preferred sun.

A detailed description of the procedures is provided in Zittrell et al. (2020). Briefly, first, we generated sky polarization patterns (angles and degrees of polarization) based on the single-scattering Rayleigh model (Strutt, 1871) (Fig. 1A and see Supplemental Materials and Methods). We prepared 32,760 model patterns from equally spaced solar positions (azimuth 360 ways × elevation 91 ways). Next, for each model pattern, we calculated the absolute angular differences (from 0° to 90°) between the Φ_{max} angles of AoP responses ($r_{cl}^2 > 0.1664$) and the model angles of polarization. Finally, we averaged the absolute angular differences to yield the deviation of the model pattern.

Before the averaging process, the absolute angular differences were weighted in each position; weighting factors were (1) response r_{cl}^2 value, (2) model degree of polarization, and (3) the normalized sum of the great-circle distances to the nearest 22% of tested positions. The third weighting factor was introduced to counterbalance the overrepresentation of values from densely sampled areas. The value of 22% was chosen in accordance with the original procedure (Bech et al., 2014), where every data set contained AoP responses from 37 positions, and the nearest eight positions were used to calculate the weighting factor. In the current study and the study of Zittrell et al. (2020), the total number of tested positions varied due to the instability of intracellular recordings. Hence, we chose $8/37 \approx 22\%$ of the total number of tested positions of each data set as the number of nearest positions to calculate the weighting factor.

Response to AoP: evaluation of pattern matching results

Neural AoP responses can encode unambiguous solar coordinates when the minimum deviation between the response pattern and the best-matching polarization pattern is small enough. To evaluate the minimum deviation and, thus, the matched-filter quality of a neuron, Zittrell et al. (2020) performed a bootstrap procedure. In this procedure, the *p* value of the minimum deviation of the best matching pattern is calculated as the probability that a lower value is observed in a population of the minimum deviations of randomized response patterns. When $p < 0.05$, the neuron is considered as a reliable matched filter encoding unambiguous solar coordinates based on the sky polarization pattern.

A detailed description of the procedures is provided in Zittrell et al. (2020). Briefly, first, we generated 5,000 randomized response patterns from an actual neural response pattern; a randomized pattern was generated by randomly drawing (with replacement) AoP responses from the pool of the actual neural responses ($r_{cl}^2 > 0.1664$) and distributing them on all neural response positions. Next, for each randomized response pattern, we calculated the best-matching polarization pattern and its deviation in the same way as described in the previous section, yielding a bootstrap population of the minimum deviations. Finally, the *p* value of the minimum deviation for the actual neural response pattern was calculated as follows:

$$p = \left(\sum_{k=1}^{b} [d_k \leq D]\right)/b \qquad (2)$$

where *D* is the minimum deviation of the actual data, *k* is the bootstrap sample index, *b* is the number of randomized samples (5,000), and d_k is the minimum deviation of the *k*th sample. Recordings were excluded from the analysis if there were only one or two AoP responses because the number of possible randomized sample variations was too small ($\leq 2^2$).

In this procedure, the *p* value tends to be large when the preferred sun encoded by the actual AoP responses is near the elevation of 0° in anterior (azimuth 0°), left (90°), posterior (180°), and right (270°) directions from the animal (Fig. 1D). That is because all Φ_{max} angles are approximately 0° or 90° in these cases, resulting in a small difference between the actual neural response pattern and the randomized patterns (e.g. TL2a_18 in Fig. S2). However, for comparison to the results of downstream CX neurons analyzed in Zittrell et al. (2020), we did not add any modification to the procedure.

Response to stationary light spots

To analyze neural responses caused by light spots, we counted spikes during 1-s intervals before and after the light was turned on (control and post-ON in Fig. 6A) and estimated a 68% confidence interval (CI) of the mean of post-ON spike counts (examples in Fig. 6B). A 68% CI equivalents to mean ± s.d. of normal distribution data. Spike activities during a post-ON interval were considered an inhibitory response when the CI was on the left to the mean of control spike counts (left column in Fig. 6B), while they were consid-

ered an excitatory response when the CI was on the right to the control mean (right column in Fig. 6B). When the CI contained the control mean, spike activities were considered no response.

We estimated a 68% CI of spike counts by the χ^2 distribution method (Sahai and Khurshid, 1993), because the simple mean ± s.d. method is inappropriate to estimate a CI of count data when the mean value is small. The χ^2 distribution method estimates lower and upper 68% confidence limits of mean λ separately as follows:

$$\frac{1}{2n}\,\chi^2_{(2k)}\,(0.16) \leq\ \lambda\ \leq \frac{1}{2n}\,\chi^2_{2(k+1)}\,(0.84) \qquad (3)$$

where $\chi^2_{(k)}\,(\alpha)$ denotes the 100α percentile of the χ^2 distribution with k degrees of freedom, n is the sample number, and k is the sample sum (Sahai and Khurshid, 1993).

To visualize neural receptive fields to light spots (Fig. 6C), we plotted surface heatmaps based on spike count modulation (Δspikes/s) in the same way as the AoP receptive fields. Spike count modulation was defined as the difference from the mean of control spike counts to the nearest 68% confidence limit of the mean of post-ON spike counts: the upper limit in inhibitory responses and the lower limit in excitatory responses (horizontal arrows in Fig. 6B). Spike count modulation of no response was defined as 0 independent of the control and post-ON spike count means.

Results

Morphology of AoP-sensitive TL neurons

We recorded intracellularly from 59 tangential neurons of the CBL in the locust CX (Fig. 2A). All neurons were sensitive to the AoP. First, we determined their cell types. The locust CBL consists of six horizontal layers (Fig. 2B,C) (Müller et al., 1997), and six types of tangential neurons termed TL1–TL5 (Müller et al., 1997; von Hadeln et al., 2020) and TL7 (Hensgen et al., 2021) have been distinguished based on the location of their input arborizations and cell bodies. All of our recordings were from TL2 and TL3 neurons (N = 38 and 21, respectively).

Each of TL2 and TL3 populations was estimated to consist of up to 40 individuals per brain hemisphere (Homberg et al., 1999). TL2 neurons are defined by their cell body along the ventro-medial face of the lateral complex and ramifications in small areas of the lateral bulb (Müller et al., 1997; von Hadeln et al., 2020). Two subtypes of TL2 neurons have been distinguished: TL2a and TL2b (Pegel et al., 2019). TL2a neurons arborize in dorsal parts of the lateral bulb and invade layer 2 of the CBL, while TL2b neurons arborize in ventral parts of the lateral bulb and invade layer 3 (orange neuron in Fig. 2A). Based on these criteria, we recorded from 34 TL2a neurons and four TL2b neurons (Fig. 2D).

TL3 neurons share a common cell body position with TL2 neurons, but their dendrites ramify in the medial bulb (Müller et al., 1997; von Hadeln et al., 2020). Three subtypes of TL3 neurons have been distinguished, termed TL3a, TL3b (von Hadeln et al.,

2020), and TL3c (Hensgen et al., 2021). We recorded from four TL3a and 17 TL3b neurons but no TL3c neurons (Fig. 2D). TL3a neurons exclusively ramify in the medial bulb, while TL3b neurons have additional ramifications in the lateral bulb or along the isthmus tract (blue neuron in Fig. 2A). All TL3a and TL3b neurons recorded in this study innervated layer 5. Pegel et al. (2019) reported three AoP-sensitive TL3 neurons innervating layers 4 and 5 of the CBL. We reanalyzed those neurons and concluded that their innervation was confined to layer 5 as in all TL3 neurons studied here. We found symmetric and asymmetric branching patterns (von Hadeln et al., 2020) in both TL3a and TL3b neurons.

Based on morphological criteria, TL2 neurons likely correspond to R2 cells, and TL3 neurons to R3 cells in *Drosophila* (Omoto et al., 2017). R2 and R3 cells are thought to be GABAergic (Hanesch et al., 1989). Homberg et al. (1999) reported GABA immunoreactivity of single TL2 and TL3 neurons but did not distinguish between the different subtypes. Therefore, we tested GABA immunoreactivity of 22 TL neurons (Fig. 2E). We found that the cell bodies of all examined TL2 and TL3 neurons were GABA-immunoreactive: TL2a (N = 10 [recorded] and 6 [staining only]), TL2b (N = 1 and 2), and TL3b (N = 2 and 1) neurons. Unfortunately, we could not perform double labeling of TL3a neurons, but our data support similar ring attractor architectures in the locust and the fly.

Response to zenithal AoP

TL neuron data presented previously (Pegel et al., 2018, 2019) were included in our analysis hereafter: seven recordings in which the polarizer was rotated at the same angular velocity (40°/s) as in our stimulus setup. First, we investigated neural sensitivity and tuning properties to zenithal AoP (Fig. 3A) tested at the beginning of the recordings (~ 100 s) to exclude effects of stimulus position and fluctuations of background activity (BA) (Supplementary Materials and Methods, Fig. S1). To judge neural responses to the AoP orientation, we used the square of circular-linear correlation coefficient (r_{cl}^2) between spike rate and the polarizer orientation (Fig. 3B,C). Out of 66 neurons, five TL2a and two TL2b neurons were not sensitive to the zenithal AoP (Fig. 3D, $r_{cl}^2 < 0.1664$), although they responded to the AoP at other stimulus positions. All TL3a and TL3b neurons were sensitive to the zenithal AoP. In the TL2a population, individual r_{cl}^2 values were widely distributed, ranging from 0.00935 to 0.787 with the median 0.611, while the TL2b population showed lower AoP sensitivity (median = 0.341) than the other cell types. The r_{cl}^2 values of TL3a and TL3b neurons were higher (medians = 0.847 and 0.7888, respectively) than those of TL2 neurons (Fig. 3D).

We analyzed tuning properties of AoP responses by fitting mixed von Mises distributions to spike activities (Fig. 3C). Tuning width (horizontal line segment in Fig. 3C) was largest in TL2b neurons and smallest in TL3a neurons (Fig. 3E). TL2a and TL3b neurons shared similar intermediate tuning widths (Fig. 3E).

$\Phi_{max\ (min)}$ activity (left and center arrows in Fig. 3C) indicates spike rate modulations from the BA (horizontal line in Fig. 3C) at $\Phi_{max\ (min)}$. Positive (upward arrow) and negative

(downward arrow) $\Phi_{max\ (min)}$ activities are excitatory and inhibitory modulations, respectively. Figure 3F shows Φ_{max} activities scaled by the amplitudes of individual tuning curves (Φ_{max} activity/amplitude); here, the amplitude of a tuning curve is the difference of Φ_{max} and Φ_{min} activities (right arrow in Fig. 3C). Φ_{max} activity/amplitude between 0 and 1 means excitatory modulation at Φ_{max} and inhibitory modulation at Φ_{min}. When the tuning curve is below the BA, inhibitory modulations occur both at Φ_{max} and Φ_{min}, resulting in Φ_{max} activity/amplitude values < 0. When the tuning curve is above the BA, the neuron was excited both at Φ_{max} and Φ_{min}, resulting in values > 1 because, in this case, Φ_{max} activity is larger than the amplitude of the tuning curve. In our data set, Φ_{max} activity/amplitude of most individuals was between 0 and 1 independent of cell type, which means that the zenithal AoP usually induced excitation at Φ_{max} and inhibition at Φ_{min} in AoP-sensitive TL neurons.

Finally, Fig. 3G shows Φ_{max} histograms for each cell type. The Φ_{max} distribution of TL2a neurons was uniform (Rayleigh test of uniformity to doubled Φ_{max}, $Z = 0.0804$, $p = 0.784$), while that of TL3b neurons had a gap around 90° ($Z = 0.487$, $p = 0.00925$). We did not test the distribution of TL2b and TL3a neurons due to the small sample size. In summary, TL2a neurons cover the full range of zenithal AoP orientations (from 0° to 180°) with various sensitivity levels (r_{cl}^2). On the other hand, TL3 neurons have higher AoP sensitivity, but their activities do not code zenithal AoP orientation around 90°.

Receptive fields of AoP responses

Next, we investigated the receptive fields of the neurons to the AoP (Fig. 4). Following zenithal AoP stimulation, we stimulated from various positions within the dorsal visual hemisphere of the animal, which yielded an AoP sensitivity (r_{cl}^2) map for each neuron (examples in Fig. 4A). Recordings from 27 individual neurons were used for the analysis in which the AoP sensitivity was measured at least at five positions: at the zenith and at elevations of 30° in anterior (azimuth 0°), left (90°), posterior (180°), and right (270°) directions from the animal (inset in Fig. 4C). No TL3a neuron was available for this analysis.

To compare the receptive field organizations for AoP sensitivity of TL neurons with those in downstream neurons of the CX (Zittrell et al. 2020), we defined the receptive fields as those areas that had r_{cl}^2 values of at least 75% of the response maxima of each cell (inside black boundary line in Fig. 4A; see Fig. S2 for all 27 individuals) as done by Zittrell et al. (2020). Similar to the results of the downstream CX neurons, the receptive fields for AoP sensitivity generally varied in size, shape, and position in individuals, however with some cell type specific trends. In TL2a/2b neurons, the r_{cl}^2 values tended to be highly affected by stimulus position, resulting in relatively small susceptible parts (Figs. 4A,B, S2). In contrast, the r_{cl}^2 values of most TL3b neurons were high across the dorsal visual field, resulting in larger sizes of receptive fields (Figs. 4A,B, S2).

We superimposed the boundaries of the 75%-r_{cl}^2 fields of all 27 neurons (Fig. 4C) in the same way as done by Zittrell et al. (2020). Similar to the downstream CX

neurons, the overlap of the receptive fields was nearly bilaterally symmetrical to the midline and maximal around the zenith (Fig. 4C), suggesting that the AoP receptive field structures are conveyed from TL populations to the downstream CX network.

Matched-filter properties of AoP sensitivity

The preferred AoP orientations of TL neurons were coherently arranged across the dorsal visual field (Figs. 5, S2), similar to those of CX neurons investigated in previous studies (Bech et al., 2014; Zittrell et al., 2020). In postsynaptic CX compass neurons, these tuning arrangements likely act as filters matched to the sky polarization pattern generated by particular solar coordinates. We estimated the sun positions encoded by AoP responses by calculating the best-matching sky polarization pattern with the minimum deviation from the neural response pattern (pattern matching procedure; Bech et al., 2014; Zittrell et al., 2020) and quantitatively assessed the matched filter qualities of the neurons by calculating the *p* value of the minimum deviation using a bootstrap procedure (Zittrell et al., 2020).

Figure 5A shows examples of the AoP response patterns measured in single neurons (orange and gray bars). On each response pattern, we superimposed the best-matching sky polarization pattern (black bars) calculated by the single-scattering Rayleigh model and its corresponding sun position (crossed yellow circle). We estimated best matching sun coordinates in 22 individuals out of 27 used in the receptive field analysis in the previous section; five recordings were excluded because of low number of AoP responses (≤ 2).

To assess the matched filter quality of individual neurons, we applied a bootstrap procedure that evaluates the minimum deviation of the best matching polarization pattern. Fig. 5B shows the distributions of the sun positions encoded by AoP responses for all analyzed neurons. Data points are color-coded by the *p* value of the minimum deviation of the best-matching pattern with increments of 0.1. Only two neurons passed the criterion, $p < 0.05$, and, thus, are considered a reliable matched filter of the sky polarization patterns (yellow circles with bold outline in Fig. 5B; TL2a_05: minimum pattern deviation = 1.84°, $p = 0.0192$; TL2b_01: minimum pattern deviation = 7.63°, $p = 0.0296$). Therefore, the proportion of reliable matched filter coding in TL neurons (2 out of 22 recordings) is considerably lower than in downstream CX neurons (17 of 23 neurons; Zittrell et al., 2020). This proportion was not affected (proportion: 1 out of 10 recordings) by including only recordings with at least nine tested stimulus positions, the requirements equal to those of Zittrell et al. (2020).

Receptive fields for stationary light spots

Besides sensitivity to AoP, TL2 and TL3 neurons are sensitive to the azimuth of an unpolarized green light spot rotating around the animal's head, suited to code for solar azimuth (Pegel et al., 2018, 2019). Our data, based on stationary green and blue light spots presented at different positions across the dorsal visual field, confirm these results.

In addition, we investigated whether the preferred azimuth of the light spot corresponded to the preferred sun encoded by AoP responses in individual TL neurons. To judge neural responses to light spots, we counted spikes during 1-s intervals before and after the light was turned on (control and post-ON in Fig. 6A). When the mean of the control spike counts was outside of the 68% CI of the mean of the post-ON spike counts, post-ON spike activities were considered inhibitory or excitatory responses to a light spot presentation (Fig. 6B). Otherwise, spike activities were considered no response. To plot surface heatmaps of receptive fields, we then calculated spike count modulation values (Δspikes/s) as the difference from the mean of control spike counts to the nearest 68% confidence limit of the mean of post-ON spike counts (horizontal arrows in Fig. 6B). In no response spike activities, Δspikes/s value was defined as 0 independent of the control and post-ON spike count means.

In most neurons (13 recordings), the receptive fields for stationary unpolarized green light spots comprised spatially distinct excitatory and inhibitory subfields (Figs. 6C, S2). Six recordings, however, showed only excitatory, five only inhibitory responses, and one TL2 neuron was completely unresponsive (Fig. S2). Overall, the receptive field organization for blue light spots was similar to that for green light stimuli (Fig. S2), but when presenting blue spots, purely inhibitory responses (6 recordings) occurred more frequently than mixed excitatory/inhibitory fields (5 recordings) and purely excitatory responses (3 recordings). TL2b neurons (2 recordings) were only excited, and TL3b neurons (3 recordings) were only inhibited to blue light throughout their receptive fields.

Figure 6C shows examples of receptive fields for unpolarized green light stimulation together with the sun positions encoded by AoP responses estimated in the previous section. These examples were chosen because their *p* values of the minimum deviations from a particular sky polarization pattern (see in the previous section) were smaller than 0.2 (see Fig. S2 for all individuals). In the two TL2 neurons with a faithful polarization-matched filter quality (TL2a_05 and TL2b_01, $p < 0.05$), the preferred sun encoded by AoP responses and the excitatory fields defined by green light responses were located in close proximity, suggesting integration of the two related celestial cues that match the situation in the sky. However, in three other TL2a neurons and a TL3b neuron (TL2a_07, TL2a_08, TL2a_09, and TL3b_02), the sun coordinates encoded by AoP responses were near the inhibitory fields. In the remaining cases shown in Fig. 6C, the preferred sun encoded by AoP responses was far away from the receptive fields for the green light responses. These examples illustrate striking mismatches in coding of the two celestial cues in neurons at the input stage of the CX.

Receptive fields defined by unpolarized blue light are shown in Fig. S2. The excitatory subfield structures differ from those of green light. As a result, the preferred sun encoded by AoP responses was far away from the excitatory fields in all recordings.

Changes in response properties

Finally, we investigated changes in response properties that occurred in some neurons during the recording. Particularly prominent changes, including a response reversal, were

observed in a TL2a neuron (TL2a_09 in Fig. 7 and Table S1). Responses to zenithal visual stimuli were tested twice, at the beginning of the recording and roughly 30 min later. The neuron showed an AoP response during the first test period, while no AoP response was observed during the second testing (top traces in Fig. 7, $r_{cl}^2 = 0.791$ in Test #1 and $r_{cl}^2 = 0.133$ in Test #2). The lack of AoP response during the second test was likely caused by the disappearance of inhibition at Φ_{min} (Table S1, the first Φ_{max} activity/amplitude = 0.973 and the second Φ_{max} activity/amplitude = 1.45). Similarly, the inhibitory response to unpolarized blue light spots changed to an excitatory response (bottom in Fig. 7, Δspikes/s = −4.90 in Test #1 and Δspikes/s = 2.29 in Test #2). No response was observed during both test periods to unpolarized green light spot presentation (middle in Fig. 7).

In the recording of another TL2a neuron (TL2a_31), we tested zenithal AoP responses seven times (results of first, fourth, and last testing in Table S1). AoP responses were stable during the first three test periods (~ 10 min) but were not present during tests four and five. AoP response returned in tests six and seven, roughly 5 min after the no response activities. Similar to the TL2a_09 neuron, inhibition at Φ_{min} angle was not observed during tests four and five (Φ_{max} activity/amplitude = 3.53 and 2.28). Responses to stationary light spots were not tested in this neuron.

Zenithal responses were, likewise, tested twice with a time interval > 10 min in six other TL2a neurons and two TL3b neurons. AoP response properties of one TL2a neuron (TL2a_38) and the two TL3b neurons were stable over time, while those of five TL2a neurons differed between the first and the second test of stimuli (summarized in Table S1). Especially in the second test of a TL2a neuron (TL2a_20), we observed no AoP response due to the disappearance of inhibition at Φ_{min}, similar to the examples described above. Some unknown factors may have modulated the balance of excitation and inhibition in these neurons during the recording.

Discussion

In the insect brain, TL/R neurons constitute the input to a ring attractor network in the CX, resulting in heading direction coding and steering commands transmitted to thoracic motor centers (Green et al., 2019; Heinze and Homberg, 2007; Heinze and Homberg, 2009; Nguyen et al., 2021; Omoto et al., 2017; Rayshubskiy et al., 2020; Seelig and Jayaraman, 2013; Seelig and Jayaraman, 2015; Shiozaki and Kazama, 2017; Sun et al., 2017; Vitzthum et al., 2002). We have characterized receptive field properties of two subtypes of these neurons, TL2 and TL3, in the locust by using visual stimuli simulating celestial compass cues across the sky. These neurons have large receptive fields for skylight polarization. However, unlike postsynaptic compass neurons of the CX (Zittrell et al., 2020), only a minority of the recorded neurons showed coding for polarization angles that match sky polarization patterns for particular sun positions. TL2 and 3 neurons, in addition, have complex, spatially partitioned excitatory and inhibitory subfields for small

light spots. In most cases, these subfields were not located in line with the polarization tuning, revealing substantial mismatch in compass coding through both sky compass cues.

Input neurons to the CX network

TL/R neurons convey multiple cues to different layers of the CBL. These cues help to establish the animal's spatial orientation, including sky compass signals, object and visual panorama information, and wind direction (el Jundi et al., 2015; Hardcastle et al., 2021; Heinze and Reppert, 2011; Kim et al., 2019; Okubo et al., 2020; Pegel et al., 2018). A connectome analysis of the *Drosophila* CX suggests hierarchical competition between R neuron subtypes, in which different cues influence heading direction coding to various degrees (Hulse et al., 2021).

Our recordings were confined to TL2a, TL2b, and TL3 neurons innervating layers 2, 3, and 5 of the locust CBL, respectively (Fig. 2). Based on morphological criteria, TL2 neurons likely correspond to R2 cells and TL3 neurons to R3 cells in *Drosophila* (Omoto et al., 2017). Like R2 and R3 cells, all TL2 and TL3 neurons appear to be GABAergic, further supporting similar ring attractor architectures in both species. However, in contrast to TL3 neurons, R3 cells in the fly are not sensitive to the orientation of polarized light and thus might have lost sensitivity to the polarization pattern in the sky (Hardcastle et al., 2021).

Cell-type specific responses to sky compass signals

All TL subtypes were responsive to light stimuli simulating polarization and direct sunlight across the sky but differed in physiological properties (Figs. 3–5, S1, S2). Similar cell-type specific trends were reported previously (Bockhorst and Homberg, 2015; Heinze et al., 2009; Pegel et al., 2018; Pegel et al., 2019; Vitzthum et al., 2002) but were not systematically analyzed. The different inputs to the different CBL layers may allow for dynamic head direction coding depending on sky conditions. The AoP sensitivity of TL2 neurons was highly dependent on stimulus position, which corresponds to the highly varying degree of polarization in the sky and should result in relatively good performance in matching sky polarization patterns (Fig. 5). Therefore, signals from TL2 neurons might be particularly useful under clear sky conditions. In contrast, TL3 neurons do not cover the full range of AoP orientations at the zenith (Fig. 3G), disadvantageous to matching sky polarization patterns. However, most TL3 neurons showed uniform high AoP sensitivity across large parts of the dorsal visual field, and thus, their signals may be robust even under cloudy or hazy sky conditions.

Comparison to the postsynaptic network

The large size and position of receptive fields for AoP sensitivity of TL neurons (Figs. 4, S2) were similar to those of downstream neurons studied in Zittrell et al. (2020). Heinze et al. (2009) reported that TL2 neurons have medium-sized, ipsilaterally-biased receptive fields relative to other CX neurons, but this conclusion is based on only a few tested stimulus positions. Vitzthum et al. (2002) and Heinze et al. (2009) showed that AoP responses in TL3 neurons are mediated by the ipsilateral eye only (monocular input) but

did not distinguish between TL3a and TL3b subtypes. We reanalyzed the morphology of those neurons and found that at least two of their recordings were from TL3b neurons. As shown here, most TL3b neurons were equally sensitive to AoP from ipsi- and contralateral directions, suggesting that their monocular input source did not limit their receptive field sizes within the range tested.

The preferred AoP of TL neurons changed gradually within the 120° range around the zenith (Figs. 5, S2), again similar to downstream neurons of the CX (Zittrell et al., 2020). Pattern matching between the AoP responses and sky polarization model yielded best matches to particular sun positions. However, judged by *p* values obtained from bootstrapping procedure, the quality of the best match was good in only 10% of the cells compared to 74% in downstream neurons (Zittrell et al., 2020). Therefore, the matched filter properties in postsynaptic columnar neurons, such as CL1 or CPU types of the CX, are likely considerably refined by convergence and integration of synaptic input from appropriate TL neurons. In fact, E-PG neurons in *Drosophila* (equivalents to CL1 neurons) receive synaptic input from nearly all visually tuned R neurons (Hulse et al., 2021).

Responsiveness to unpolarized light spots

The receptive fields for stationary unpolarized light spots comprised spatially distinct excitatory and inhibitory subfields in most neurons (Figs. 6, S2). This receptive field organization for visual stimuli is similar to that of R2 and R4d ring neurons in *Drosophila* (Seelig and Jayaraman, 2013). In the fly, inhibitory subfields are usually in close proximity to an excitatory area and partly surround an excitatory center, suggesting contrast enhancement for object detection similar to mechanisms in the mammalian visual cortex (Bonin et al., 2011). In the locust, however, both subfields were often spatially far apart and suggest spatial excitatory-inhibitory opponency across the sky, likely used to evaluate brightness contrast (Pegel et al., 2018; Pegel et al., 2019).

Some TL neurons possessed only excitatory or inhibitory fields for stationary light spots, and one TL2 neuron was completely unresponsive. In contrast, Pegel et al. (2018) found pronounced spatial opponency responses to rotating light spots in all TL2 neurons (7 recordings) compared to weaker responses in two TL3 neurons. A primary reason for this discrepancy may be the coarse grid of tested stimulus positions in our study. In addition, we used unpolarized light spots of 1.05° visual angle, which is closer to the apparent size of the sun (about 0.5°) but smaller than 16.3° light spots used by Pegel et al. (2018).

We found some differences between receptive field structures for unpolarized green and blue light. This difference may be critical for compass integration because the excitatory fields for blue light, in contrast to those for green light, were often far from the sun position estimated from AoP responses (Fig. S2). The response to green light originates from the main retina, while unpolarized blue light is detected by both the main retina and the dorsal rim area. In the main retina most photoreceptors co-express two types of opsins, a long wavelength (green)-absorbing type and a blue-absorbing type, while in the

dorsal rim area, all photoreceptors express only a blue-absorbing opsin (Schmeling et al., 2014). It remains an open question how this receptive field difference affects solar azimuth detection.

Changes in response properties

We observed response property changes in seven recordings out of ten in which the response to zenithal stimuli was tested repeatedly over the course of the recording (Fig. 7 and Table S1). In three individuals, the AoP responses during the initial test were comprised of excitation at Φ_{max} and inhibition at Φ_{min}, but inhibition at Φ_{min} was no longer detected during the following test. In one TL neuron, even a reverse response to unpolarized light spots was found. The balance of excitation and inhibition may have been modulated in these neurons by changes in the internal state of the animal, suggesting state-dependent processing of visual information in these neurons. Similar activity changes were found in *Drosophila* R neurons as epochs of elevated calcium activity visualized in glomeruli of the bulb, which were restricted to neurons in a specific glomerulus but not correlated with the activities of the upstream neuron in the same glomerulus (Sun et al., 2017). However, fluctuation in calcium activity was not reported when the activities to AoP stimuli were recorded as ensemble responses of R neuron populations (Hardcastle et al., 2021). Therefore, activity fluctuations may affect the dominance of TL/R neurons relative to others in the same layer and thereby control the output of the CBL/ellipsoid body to select visual features in a specific location.

Visual features of the sky are reliable compass cues owing to their persistent presence during navigation. Parallel channels for celestial cues as inputs to the CX are likely combined and refined by the compass network in the CX to yield a robust heading signal based on a combination of sky compass cues that eventually leads to accurate spatial orientation.

Acknowledgments

We thank Dr. Uta Pegel for providing data for reanalysis, Drs. Christian Wegener and Erich Buchner for supplying anti-synapsin antibodies, and Martina Kern for maintaining locust cultures.

Competing interests

No competing interests declared.

Funding

This work was supported by JSPS Overseas Challenge Program for Young Researchers and JSPS Overseas Research Fellowships from Japan Society for the Promotion of Science (No. 201780130 and No. 201960238 to N.T.) and the Deutsche Forschungsgemeinschaft (HO 950/28-1 to U.H.).

References

Batschelet, E. (1981). *Circular statistics in biology*. London, UK; New York, NY, USA: Academic Press.

Bech, M., Homberg, U. and Pfeiffer, K. (2014). Receptive fields of locust brain neurons are matched to polarization patterns of the sky. *Curr. Biol.* **24**, 2124–2129.

Berens, P. (2009). CircStat: a MATLAB toolbox for circular statistics. *J. Stat. Softw.* **31**, 1–21.

Bockhorst, T. and Homberg, U. (2015). Amplitude and dynamics of polarization-plane signaling in the central complex of the locust brain. *J. Neurophysiol.* **113**, 3291–3311.

Bonin, V., Histed, M. H., Yurgenson, S. and Reid, R. C. (2011). Local diversity and fine-scale organization of receptive fields in mouse visual cortex. *J. Neurosci.* **31**, 18506–18521.

Clements, A. N. and May, T. E. (1974). Studies on locust neuromuscular physiology in relation to glutamic acid. *J. Exp. Biol.* **60**, 673–705.

Cullen, K. E. and Taube, J. S. (2017). Our sense of direction: progress, controversies and challenges. *Nat. Neurosci.* **20**, 1465–1473.

el Jundi, B., Pfeiffer, K., Heinze, S. and Homberg, U. (2014). Integration of polarization and chromatic cues in the insect sky compass. *J. Comp. Physiol. A* **200**, 575–589.

el Jundi, B., Warrant, E. J., Byrne, M. J., Khaldy, L., Baird, E., Smolka, J. and Dacke, M. (2015). Neural coding underlying the cue preference for celestial orientation. *Proc. Natl. Acad. Sci. USA* **112**, 11395–11400.

Fitak, R. R. and Johnsen, S. (2017). Bringing the analysis of animal orientation data full circle: model-based approaches with maximum likelihood. *J. Exp. Biol.* **220**, 3878–3882.

Green, J. and Maimon, G. (2018). Building a heading signal from anatomically defined neuron types in the *Drosophila* central complex. *Curr. Opin. Neurobiol.* **52**, 156–164.

Green, J., Adachi, A., Shah, K. K., Hirokawa, J. D., Magani, P. S. and Maimon, G. (2017). A neural circuit architecture for angular integration in *Drosophila*. *Nature* **546**, 101–106.

Green, J., Vijayan, V., Mussells Pires, P., Adachi, A. and Maimon, G. (2019). A neural heading estimate is compared with an internal goal to guide oriented navigation. *Nat. Neurosci.* **22**, 1460–1468.

Hanesch, U., Fischbach, K. F. and Heisenberg, M. (1989). Neuronal architecture of the central complex in *Drosophila melanogaster*. *Cell Tissue Res.* **257**, 343–366.

Hardcastle, B. J., Omoto, J. J., Kandimalla, P., Nguyen, B.-C. M., Keleş, M. F., Boyd, N. K., Hartenstein, V. and Frye, M. A. (2021). A visual pathway for skylight polarization processing in *Drosophila*. *eLife* **10**, e63225.

Heinze, S. (2017). Unraveling the neural basis of insect navigation. *Curr. Opin. Insect Sci.* **24**, 58–67.

Heinze, S. and Homberg, U. (2007). Maplike representation of celestial *E*-vector orientations in the brain of an insect. *Science* **315**, 995–997.

Heinze, S. and Homberg, U. (2008). Neuroarchitecture of the central complex of the desert locust: intrinsic and columnar neurons. *J. Comp. Neurol.* **511**, 454–478.

Heinze, S. and Homberg, U. (2009). Linking the input to the output: new sets of neurons complement the polarization vision network in the locust central complex. *J. Neurosci.* **29**, 4911–21.

Heinze, S. and Reppert, S. M. (2011). Sun compass integration of skylight cues in migratory monarch butterflies. *Neuron* **69**, 345–358.

Heinze, S., Gotthardt, S. and Homberg, U. (2009). Transformation of polarized light information in the central complex of the locust. *J. Neurosci.* **29**, 11783–11793.

Hensgen, R., Göthe, J., Jahn, S., Hümmert, S., Schneider, K. L., Takahashi, N., Pegel, U., Gotthardt, S. and Homberg, U. (2021). Organization and neural connections of the lateral complex in the brain of the desert locust. *J. Comp. Neurol.* **529**, 3533–3560.

Homberg, U., Vitzthum, H., Müller, M. and Binkle, U. (1999). Immunocytochemistry of GABA in the central complex of the locust *Schistocerca gregaria*: identification of immunoreactive neurons and colocalization with neuropeptides. *J. Comp. Neurol.* **409**, 495–507.

Homberg, U., Heinze, S., Pfeiffer, K., Kinoshita, M. and el Jundi, B. (2011). Central neural coding of sky polarization in insects. *Philos. Trans. R. Soc. B* **366**, 680–687.

Honkanen, A., Adden, A., da Silva Freitas, J. and Heinze, S. (2019). The insect central complex and the neural basis of navigational strategies. *J. Exp. Biol.* **222**, jeb188854.

Hulse, B. K., Haberkern, H., Franconville, R., Turner-Evans, D. B., Takemura, S., Wolff, T., Noorman, M., Dreher, M., Dan, C., Parekh, R., Hermundstad, A. M., Rubin, G. M., Jayaraman, V. (2021). A connectome of the *Drosophila* central complex reveals network motifs suitable for flexible navigation and context-dependent action selection. *eLife* **10**, e66039.

Kim, S. S., Hermundstad, A. M., Romani, S., Abbott, L. F. and Jayaraman, V. (2019). Generation of stable heading representations in diverse visual scenes. *Nature* **576**, 126–131.

Knierim, J. J. and Zhang, K. (2012). Attractor dynamics of spatially correlated neural activity in the limbic system. *Annu. Rev. Neurosci.* **35**, 267–285.

Müller, M., Homberg, U. and Kühn, A. (1997). Neuroarchitecture of the lower division of the central body in the brain of the locust (*Schistocerca gregaria*). *Cell Tissue Res.* **288**, 159–176.

Nguyen, T. A. T., Beetz, M. J., Merlin, C. and el Jundi, B. (2021). Sun compass neurons are tuned to migratory orientation in monarch butterflies. *Proc. R. Soc. B* **288**, 20202988.

Okubo, T. S., Patella, P., D'Alessandro, I. and Wilson, R. I. (2020). A neural network for wind-guided compass navigation. *Neuron* **107**, 924–940.

Omoto, J. J., Keleş, M. F., Nguyen, B. C. M., Bolanos, C., Lovick, J. K., Frye, M. A. and Hartenstein, V. (2017). Visual input to the *Drosophila* central complex by developmentally and functionally distinct neuronal populations. *Curr. Biol.* **27**, 1098–1110.

Pegel, U., Pfeiffer, K. and Homberg, U. (2018). Integration of celestial compass cues in the central complex of the locust brain. *J. Exp. Biol.* **221**, jeb171207.

Pegel, U., Pfeiffer, K., Zittrell, F., Scholtyssek, C. and Homberg, U. (2019). Two compasses in the central complex of the locust brain. *J. Neurosci.* **39**, 3070–3080.

R Core Team (2021). R: a language and environment for statistical computing. R Foundation for Statistical Computing, Vienna, Austria. https://www.R892project.org/.

Rayshubskiy, A., Holtz, S. L., D'Alessandro, I., Li, A. A., Vanderbeck, Q. X., Haber, I. S., Gibb, P. W. and Wilson, R. I. (2020). Neural circuit mechanisms for steering control in walking *Drosophila*. *bioRxiv* 10.1101/2020.04.04.024703.

Sahai, H. and Khurshid, A. (1993). Confidence intervals for the mean of a Poisson distribution: a review. *Biometrical J.* **35**, 857–867.

Schmeling, F., Wakakuwa, M., Tegtmeier, J., Kinoshita, M., Bockhorst, T., Arikawa, K. and Homberg, U. (2014). Opsin expression, physiological characterization and identification of photoreceptor cells in the dorsal rim area and main retina of the desert locust, *Schistocerca gregaria*. *J. Exp. Biol.* **217**, 3557–3568.

Schneider, C. A., Rasband, W. S. and Eliceiri, K. W. (2012). NIH Image to ImageJ: 25 years of image analysis. *Nat. Methods* **9**, 671–675.

Schnute, J. T. and Groot, K. (1992). Statistical analysis of animal orientation data. *Anim. Behav.* **43**, 15–33.

Seelig, J. D. and Jayaraman, V. (2013). Feature detection and orientation tuning in the *Drosophila* central complex. *Nature* **503**, 262–266.

Seelig, J. D. and Jayaraman, V. (2015). Neural dynamics for landmark orientation and angular path integration. *Nature* **521**, 186–191.

Shiozaki, H. M. and Kazama, H. (2017). Parallel encoding of recent visual experience and self-motion during navigation in *Drosophila*. *Nat. Neurosci.* **20**, 1395–1403.

Skaggs, W. E., Knierim, J. J., Kudrimoti, H. S. and McNaughton, B. L. (1995). A model of the neural basis of the rat's sense of direction. *Adv. Neural Inf. Process. Syst.* **7**, 173–80.

Strutt, H. J. W. (1871). XV. On the light from the sky, its polarization and colour. *London, Edinburgh, Dublin Philos. Mag. J. Sci.* **41**, 107–120.

Sun, Y., Nern, A., Franconville, R., Dana, H., Schreiter, E. R., Looger, L. L., Svoboda, K., Kim, D. S., Hermundstad, A. M. and Jayaraman, V. (2017). Neural signatures of dynamic stimulus selection in *Drosophila*. *Nat. Neurosci.* **20**, 1104–1113.

Swinbank, R. and Purser, R. J. (2006). Fibonacci grids: a novel approach to global modelling. *Q. J. R. Meteorol. Soc.* **132**, 1769–1793.

Takahashi, N., Katoh, K., Watanabe, H., Nakayama, Y., Iwasaki, M., Mizunami, M. and Nishino, H. (2017). Complete identification of four giant interneurons supplying mushroom body calyces in the cockroach *Periplaneta americana*. *J. Comp. Neurol.* **525**, 204–230.

Taube, J. S., Muller, R. U. and Ranck Jr, J. B. (1990a). Head-direction cells recorded from the postsubiculum in freely moving rats. I. Description and quantitative analysis. *J. Neurosci.* **10**, 420–435.

Taube, J. S., Muller, R. U. and Ranck Jr, J. B. (1990b). Head-direction cells recorded from the postsubiculum in freely moving rats. II. Effects of environmental manipulations. *J. Neurosci.* **10**, 436–447.

Turner-Evans, D. B., Jensen, K. T., Ali, S., Paterson, T., Sheridan, A., Ray, R. P., Wolff, T., Lauritzen, J. S., Rubin, G. M., Bock, D. D., et al. (2020). The neuroanatomical ultrastructure and function of a biological ring attractor. *Neuron* **108**, 145–163.

Vitzthum, H., Müller, M. and Homberg, U. (2002). Neurons of the central complex of the locust *Schistocerca gregaria* are sensitive to polarized light. *J. Neurosci.* **22**, 1114–1125.

von Hadeln, J., Hensgen, R., Bockhorst, T., Rosner, R., Heidasch, R., Pegel, U., Quintero Pérez, M. and Homberg, U. (2020). Neuroarchitecture of the central complex of the desert locust: tangential neurons. *J. Comp. Neurol.* **528**, 906–934.

Wolff, T., Iyer, N. A. and Rubin, G. M. (2015). Neuroarchitecture and neuroanatomy of the *Drosophila* central complex: A GAL4-based dissection of protocerebral bridge neurons and circuits. *J. Comp. Neurol.* **523**, 997–1037.

Zittrell, F., Pfeiffer, K. and Homberg, U. (2020). Matched-filter coding of sky polarization results in an internal sun compass in the brain of the desert locust. *Proc. Natl. Acad. Sci. USA* **117**, 25810–25817.

Figure Legends

Figure 1. Celestial compass cues and visual stimulation.

(A) Schematic illustration of the polarization pattern and color gradient in the sky. The AoP (black bar orientation) is arranged tangentially along concentric circles around the sun. The degree of polarization (black bar thickness) reaches its maximum at a given point of the sky when the great-circle distance is 90° from the sun. The chromatic gradient is the product of a gradient of long-wavelength light intensity (left, green) and a uniform distribution of short-wavelength light (right, UV).

(B) Stimulus setup modified from Bech et al. (2014) and Zittrell et al. (2020). The light stimulus could be switched between polarized blue, unpolarized green, and unpolarized blue during recording. After stimulation from the animal's zenith, the light device was shifted along the perimeter that could be tilted as indicated by blue arrows. It allowed stimulating the animal from directions in the entire dorsal visual field.

(C) Frontal view of the spherical dorsal visual field of the animal.

(D) Top view of the spherical dorsal visual field flattened on a polar-coordinate grid. The radius (ρ) is defined as 1 – elevation/90° ($0 \leq \rho \leq 1$) and the angle (θ) equals the spherical azimuth ($0° \leq \theta < 360°$). The elevation and azimuth are indicated relative to the animal's head.

Figure 2. CBL layers and TL neuron subtypes.

(A) Schematic drawing of the locust CX and TL neurons investigated in this study, modified from Pegel et al. (2019). Inset shows a frontal diagram of the locust brain with the CX and its bilateral structures (lateral complex) in yellow. Dots in the lower division of the central body (CBL) represent varicose arborizations and thus likely presynaptic output regions. The filled lateral and medial bulbs (LBU, MBU) indicate input synapses arranged in microglomerular complexes.

(B,C) CBL layers numbered 1–6. Sagittal diagram (B) and frontal confocal image stack (C), in which TL2a and TL3b neurons (layers 2 and 5) were stained by Cy3-labeled streptavidin-Neurobiotin.

(D) Confocal image stacks of all TL neuron types investigated in this study: TL2a, TL2b, TL3a, and TL3b neurons with soma in the left hemisphere. Insets show sagittal views of the innervated CBL layer. Arrowheads point to input synapses in the lateral (white) and medial (black) bulbs.
(E) GABA immunoreactivity of TL neuron subtypes. Arrowheads point to cell bodies of double-labeled neurons.
Scale bars = 400 μm in the inset of A, 50 μm in C, 100 μm in D, and 20 μm in E. CBU, upper division of the central body; LAL, lateral accessory lobe; PB, protocerebral bridge.

Figure 3. Response to zenithal AoP.
(A) Spike activities of a TL2a neuron (TL2a_19) during a 360° clockwise (CW) and counterclockwise (CCW) rotation of the polarizer. Spike rasters are aligned to the time of rotation represented above.
(B,C) Spike trains represented in A shown as spike rate histograms with 10° bins presented as polar and linear plots, respectively. The response showed a strong correlation with the orientation of the polarizer (the square of circular-linear correlation coefficient $r_{cl}^2 = 0.93$, $p = 5.37 \times 10^{-8}$). The best-fit tuning curve (mixed von Mises distributions) and the BA level before the stimulus (horizontal line) are superimposed on the histogram in C.
(D–G) Tuning properties of AoP responses. (D) The square of circular-linear correlation coefficient ($0 \leq r_{cl}^2 \leq 1$) between spike rate and polarizer orientation as AoP sensitivity. Values of $r_{cl}^2 > 0.1664$ (horizontal dotted line), equivalent to $p < 0.05$, are considered as AoP responses. Individuals with $r_{cl}^2 \leq 0.1664$ (N = 7) are excluded from other plots. (E) Tuning width (°) of the tuning curve. (F) Φ_{max} activity/amplitude of the tuning curve. The amplitude of the tuning curve (right arrow in C) indicates the difference of Φ_{max} and Φ_{min} activities. Φ_{max} and Φ_{min} activities (left and center arrows in C) indicate spike rate modulation from the BA (horizontal line in C); positive and negative values are excitatory and inhibitory modulation, respectively. Values of Φ_{max} activity/amplitude range from 0 to 1 when the spike rate at Φ_{max} is higher than the BA and the spike rate at Φ_{min} lower than the BA. When the spike rates at Φ_{max} and Φ_{min} are lower than the BA, the plot value < 0, and when the spike rates at Φ_{max} and Φ_{min} are higher than the BA, the plot value > 1. In one TL3 neuron, the BA before the stimulus was not available due to recording noise, and thus it was excluded from the analysis.
(G) Peak position of the tuning curve ($0° \leq \Phi_{max} < 180°$) shown in histograms with 10° bins. The *p* values of Rayleigh test of uniformity are given for the Φ_{max} distributions of TL2a and TL3b neurons.

Figure 4. Receptive fields for AoP.
(A) Polarization sensitivity maps of three recordings (top view on flattened hemispheres; see inset in C and Fig. 1D for clarification of the coordinate system). The sensitivity to polarization angle (r_{cl}^2 value) is color-coded at each tested position (circles) and linearly

interpolated in between. The fields with $r_{cl}^2 \leq 0.1664$ (dark blue) are considered no AoP response parts. Black lines are smoothed 75% isolines of the normalized r_{cl}^2 values.
(B,C) Superimposed boundary lines of 75% fields of each cell type in B and all analyzed neurons in C with a color-coded degree of overlap. N indicates number of neurons. Inset in C shows the minimum requirement of stimulus positions (circles) for the receptive field analysis: the anterior, left, posterior, and right direction at an elevation of 30° relative to the animal's head as well as the zenith (elevation 90°). See Fig. S2 for sensitivity maps of all individuals.

Figure 5. AoP response patterns and best-matching polarization patterns.
(A) Pattern fitting results of three individual neurons (top view on flattened hemispheres). The same individuals are shown as those in Fig. 4A. The Φ_{max} of the tuning curve is shown by orange ($r_{cl}^2 > 0.1664$) or gray ($r_{cl}^2 \leq 0.1664$) bar orientation at each tested position. The best-matching sky polarization patterns (black bars) are superimposed on the responses. The bar length was scaled by r_{cl}^2 value (response pattern) and degree of polarization (polarization pattern). A crossed yellow circle indicates the solar position used to generate the polarization pattern. The *p* values are the results of the bootstrap test of the minimum deviation.
(B) The solar positions with the minimum deviations of single cells. Data points are color-coded by *p* value of the minimum deviations with increments of 0.1. Bold outlines of data points indicate $p < 0.05$. N indicates the number of neurons. See Fig. S2 for response patterns of all individuals.

Figure 6. Response to stationary light stimuli in the dorsal visual field.
(A) Spike activities of a TL2a neuron during presentation of an unpolarized green light from the zenith (square wave above activities).
(B) Examples of responses to stationary light and spike count modulation. A TL2a neuron (TL2a_08 shown in C) showed an inhibitory response (left column) and an excitatory response (right column) to the green light spot presented from the anterior and posterior directions, respectively. The upper panels are spike rasters during 1-s control and post-ON intervals, aligned to the time of the light turned on (vertical dotted lines). A mean value of spike counts (/s) is represented at the bottom of a raster series of each interval. On the lower panels, Poisson distributions of spike counts are plotted with 68% CI of the post-ON mean (shaded areas). The blue CI was on the left to the mean of control spike counts, and thus, the post-ON spike activities were considered an inhibitory response. In contrast, the red CI was on the right to the control mean, and thus, the post-ON spike activities were considered an excitatory response. Spike count modulation (Δspikes/s) to plot surface heatmaps in C was defined as the difference from the mean of control spike counts to the nearest 68% confidence limit of the mean of post-ON spike counts (horizontal arrows): −4.73 for the inhibitory response and 7.93 for the excitatory response in these examples.

(C) Spike count modulation maps of single neurons to stationary unpolarized green light spots (top view on flattened hemispheres). The three individuals in the first row are the same as those shown in Figs. 4A and 5A. The spike count modulation (Δspikes/s value) is color-coded at each tested position (circles) and linearly interpolated in between. The preferred suns encoded by AoP responses are also shown (crossed yellow circle) with *p* values of the minimum pattern deviation. See Fig. S2 for receptive fields of all individuals.

Figure 7. Plasticity of neural responses in a TL2a neuron.
Spike rasters are aligned to the onset of the zenithal light stimuli (straight line or square wave above the respective rasters). Waveforms were high-pass filtered for display purpose. Test #1 was performed at the beginning of the recording, and test #2 responses were recorded roughly 30 min later.

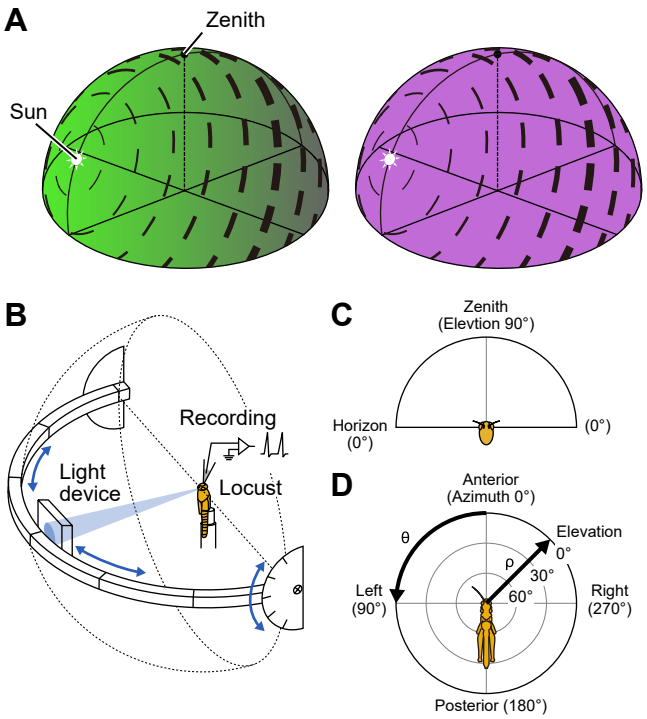

FIGURE 1

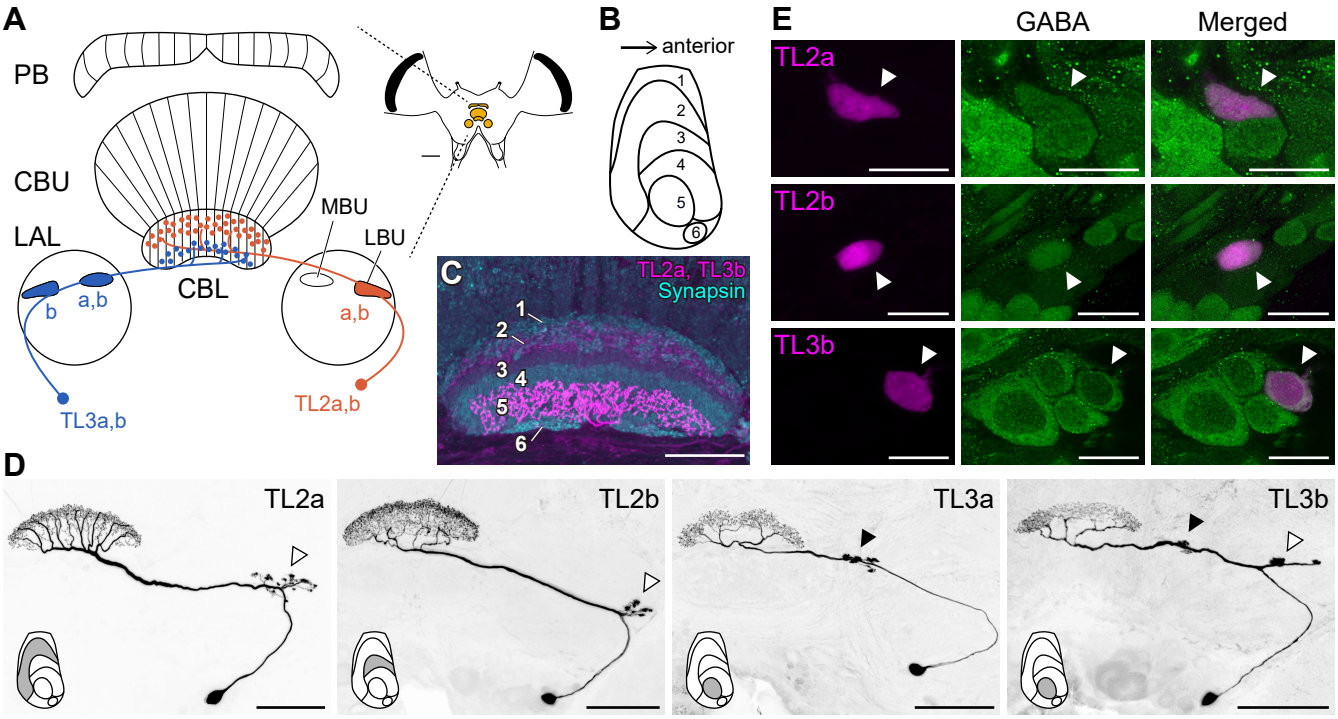

FIGURE 2

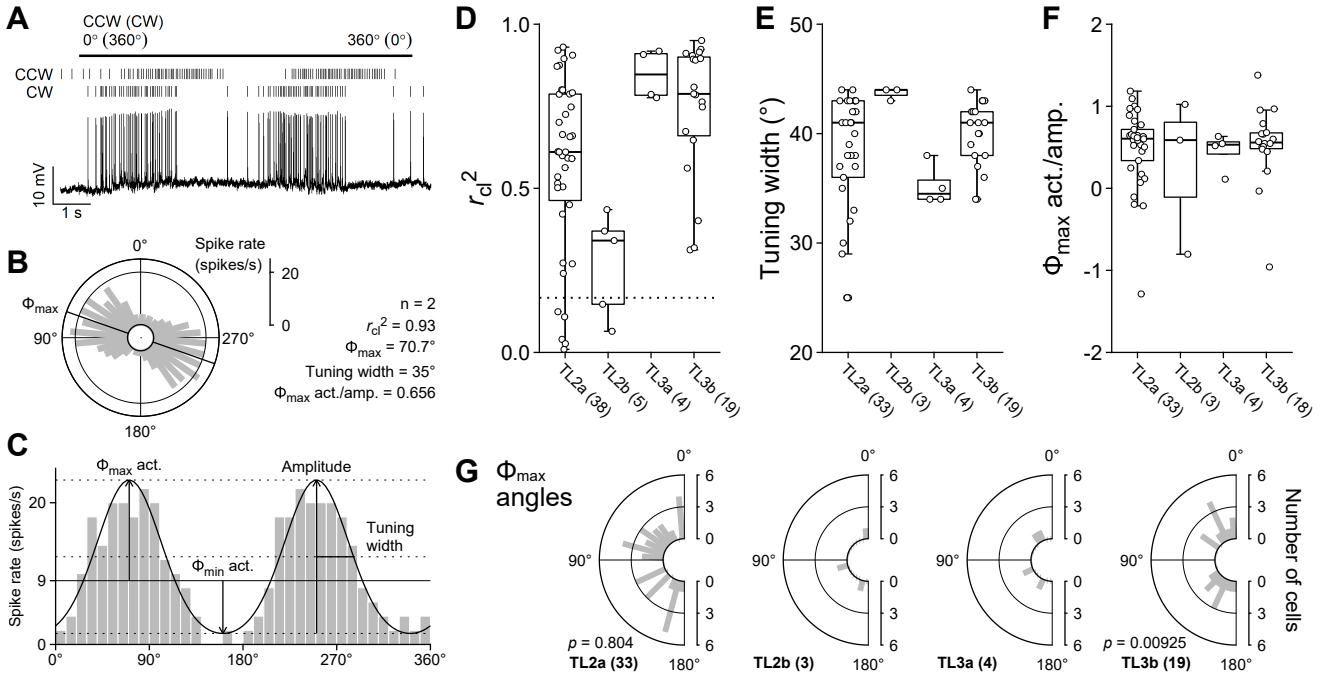

FIGURE 3

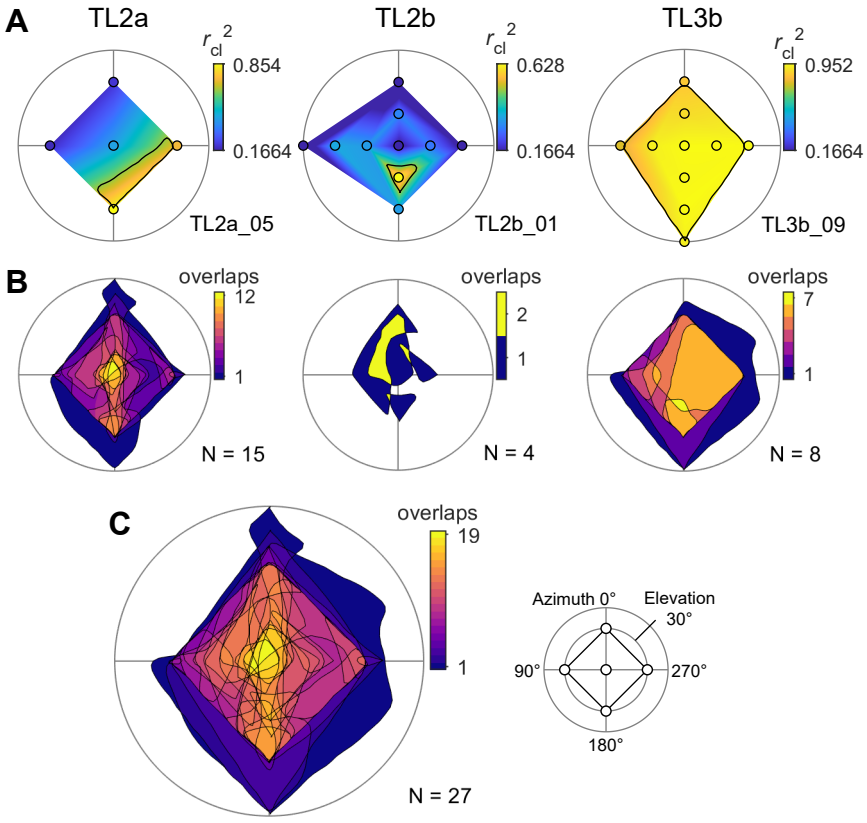

FIGURE 4

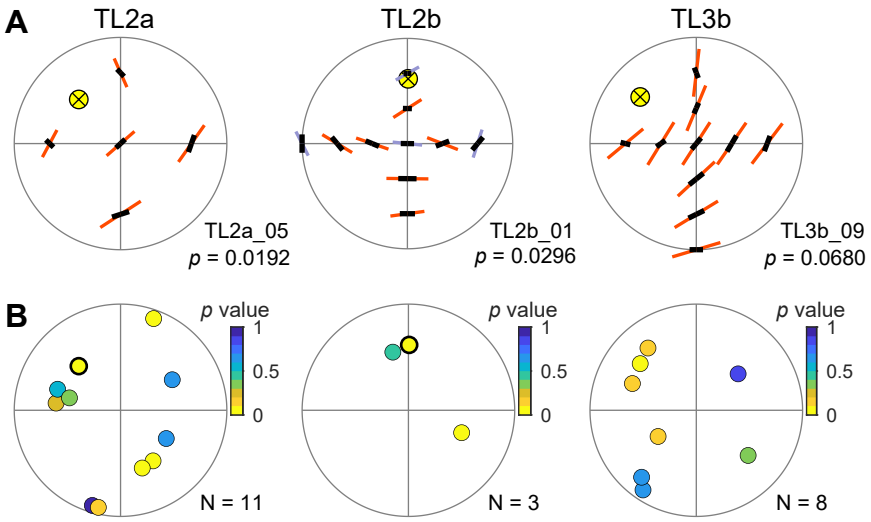
A
TL2a
TL2b
TL3b
TL2a_05
p = 0.0192
TL2b_01
p = 0.0296
TL3b_09
p = 0.0680
B
p value
1
0.5
0
N = 11
p value
1
0.5
0
N = 3
p value
1
0.5
0
N = 8

FIGURE 5

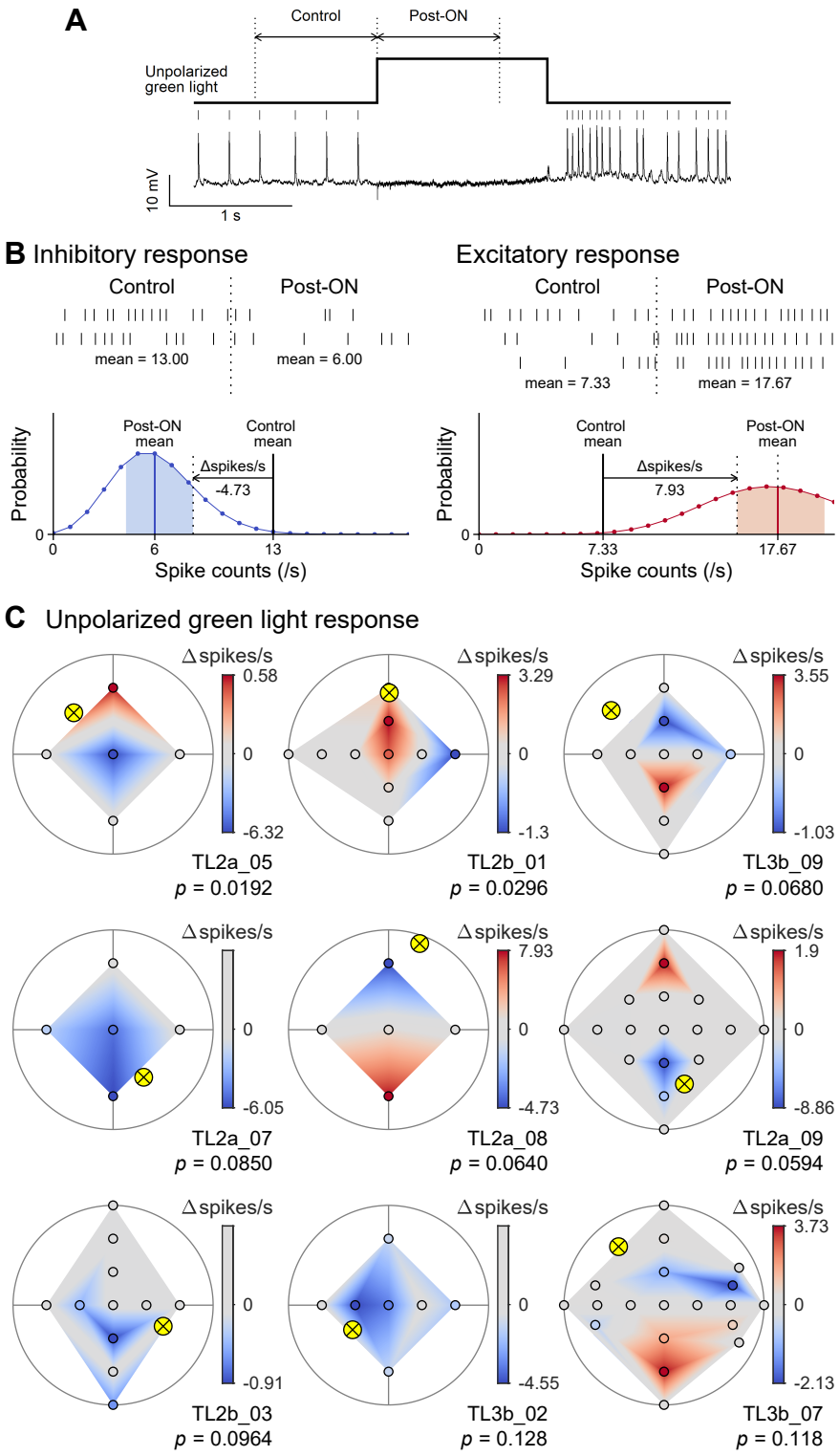
A
Control
Post-ON
Unpolarized green light
10 mV
1 s
B Inhibitory response
Control
Post-ON
mean = 13.00
mean = 6.00
Post-ON mean
Control mean
Δspikes/s
-4.73
Probability
0
6
13
Spike counts (/s)
Excitatory response
Control
Post-ON
mean = 7.33
mean = 17.67
Control mean
Post-ON mean
Δspikes/s
7.93
Probability
0
7.33
17.67
Spike counts (/s)
C Unpolarized green light response
Δspikes/s
0.58
0
-6.32
TL2a_05
p = 0.0192
Δspikes/s
3.29
0
-1.3
TL2b_01
p = 0.0296
Δspikes/s
3.55
0
-1.03
TL3b_09
p = 0.0680
Δspikes/s
0
-6.05
TL2a_07
p = 0.0850
Δspikes/s
7.93
0
-4.73
TL2a_08
p = 0.0640
Δspikes/s
1.9
0
-8.86
TL2a_09
p = 0.0594
Δspikes/s
0
-0.91
TL2b_03
p = 0.0964
Δspikes/s
0
-4.55
TL3b_02
p = 0.128
Δspikes/s
3.73
0
-2.13
TL3b_07
p = 0.118

FIGURE 6

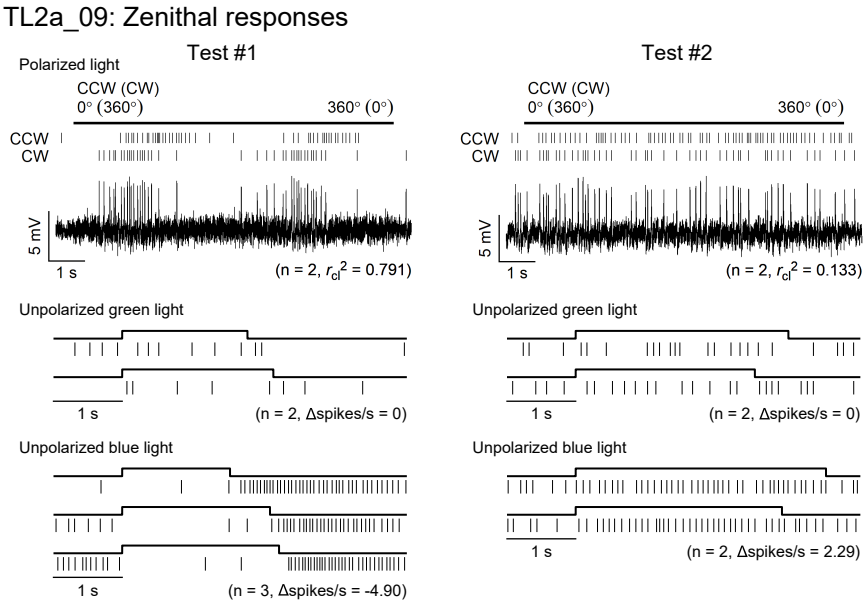
TL2a_09: Zenithal responses
Test #1
Test #2
Polarized light
CCW (CW)
0° (360°)
360° (0°)
CCW
CW
5 mV
1 s
(n = 2, r_{cl}^2 = 0.791)
(n = 2, r_{cl}^2 = 0.133)
Unpolarized green light
(n = 2, Δspikes/s = 0)
Unpolarized blue light
(n = 3, Δspikes/s = -4.90)
(n = 2, Δspikes/s = 2.29)

FIGURE 7

Supplementary Materials and Methods

Circular-linear correlation

To calculate the circular-linear correlation coefficient (r_{cl}), we used the function "circ_corrcl" in the "Circular Statistics Toolbox" of MATLAB (Berens, 2009). When a circular variable is α and a linear variable is x, this function defines the correlation coefficients $r_{sx} = c(\sin\alpha, x)$, $r_{cx} = c(\cos\alpha, x)$ and $r_{cs} = c(\sin\alpha, \cos\alpha)$, where $c(x, y)$ is the Pearson correlation coefficient. Then the circular-linear correlation coefficient r_{cl} is computed as follows;

$$r_{\mathrm{cl}} = \sqrt{\frac{r_{cx}^2 + r_{sx}^2 - 2r_{cx}r_{sx}r_{cs}}{1 - r_{cs}^2}} \qquad (1)$$

To judge AoP responses, we used the square value of the coefficient (r_{cl}^2) because it follows a χ^2 distribution with two degrees of freedom (Berens, 2009).

Great-circle distance

Generally, for spherical coordinates of a given point α (azimuth α_1, elevation α_2) with $0° \le \alpha_1 < 360°$ and $0° \le \alpha_2 \le 90°$ (Fig. 1A,C), the position vector $\vec{\alpha}$ is

$$\vec{\alpha} = \begin{pmatrix} \cos\alpha_1 \cdot \cos\alpha_2 \\ \cos\alpha_1 \cdot \sin\alpha_2 \\ \sin\alpha_1 \end{pmatrix} \qquad (2)$$

The great-circle distance θ between the points α and β is calculated using vector products as follows;

$$\theta = arccos\left(\vec{\alpha} \cdot \vec{\beta}\right) = arctan\frac{\left|\vec{\alpha} \times \vec{\beta}\right|}{\vec{\alpha} \cdot \vec{\beta}} \qquad (3)$$

Single-scattering Rayleigh model

We generated sky polarization patterns (angles and degrees of polarization) based on the single-scattering Rayleigh model (Strutt, 1871). The angle of polarization (AoP) at a given point of the sky is perpendicular to a great circle passing through the sun and the subject point. Thus, the vector of AoP is calculated as the cross vector product;

$$\overrightarrow{AoP} = \vec{s} \times \vec{p} \qquad (4)$$

where $\vec{s}$ and $\vec{p}$ are the position vectors of the sun and the subject point, respectively. The degree of polarization (DoP), or percent polarization, varies between 0 (for unpolarized light) and 1 (for completely polarized light). In the single-scattering Rayleigh model, the DoP is calculated as a function of the great-circle distance between the sun and the subject point;

$$DoP = \frac{1 - \cos^2\theta}{1 + \cos^2\theta} \qquad (5)$$

where θ is the great-circle distance between $\vec{s}$ and $\vec{p}$. The DoP reaches its maximum (= 1) when the great-circle distance is 90°.

Background activity (BA).

Spikes were counted per 1-s bins as background activity (BA) of the neurons (Fig. S1). We used all bins during the absence of stimulation and current injection for the analysis, except during 5 s after the light was turned off to exclude rebound responses. We sometimes observed spike rate changes lasting after light stimuli were turned off. Such long-lasting aftereffects were more frequently observed in TL3 than in TL2 neurons. However, as we did not have objective means to isolate these effects from spontaneous changes in BA, we used the whole recording fulfilling the criteria to avoid arbitrary omission of parts of the recording.

To evaluate BA characteristics of each cell type, we calculated the mean and Fano factor of spike counts per bin. Fano factor is the variance to mean ratio (variance/mean) of count data, commonly used to evaluate variability (Fano, 1947; Rajdl et al., 2020). That is because ideal count data follow a Poisson-distributed process where mean equals variance. When the Fano factor > 1 or < 1, BA is considered more fluctuating or more constant through the whole recording, respectively.

For statistical comparison of BA mean levels between cell types, we constructed a generalized linear model (GLM) of a gamma distribution by function “glm” in the “stats” package of R (R Core Team, 2021). The link function of GLM was “identity.” Response variables were BA mean of individuals, and fixed effects were cell types. The statistical significance of a fixed effect was tested by Wald test of an estimated coefficient (Faraway, 2016). In this method, the test static z is obtained by dividing the coefficient value by its s.e.. The distribution of z is approximated by a normal distribution to calculate the p value under the null hypothesis that the coefficient = 0.

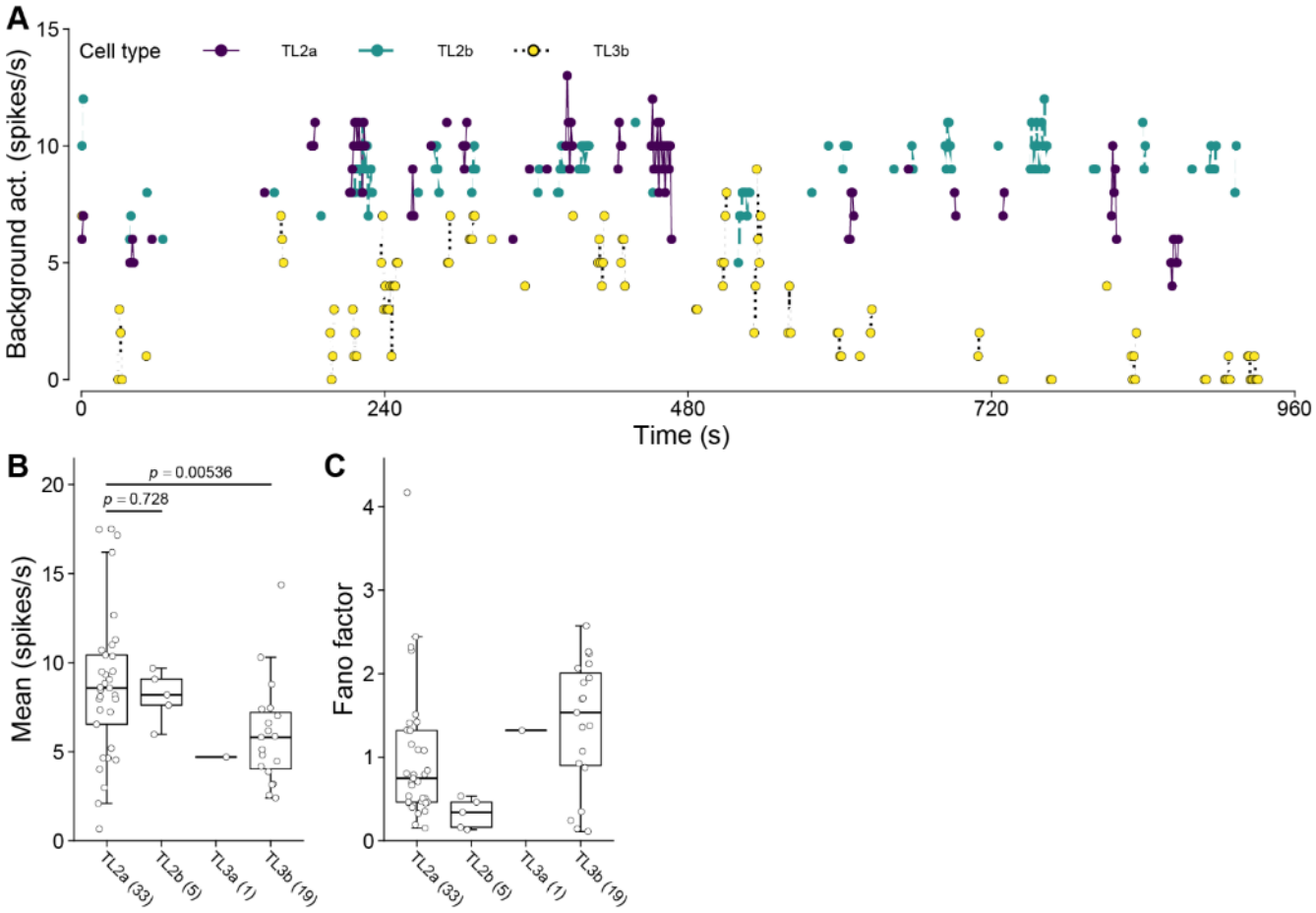

Figure S1. Background activity (BA).

(A) BA examples of three single neurons: TL2a_03 (dark purple), TL2b_01 (green), and TL3b_04 (yellow) throughout the recordings (~ 16 min). Data points indicate spike counts per 1-s bins. Line-connected points are consecutive bins not interrupted by a stimulus or current injection.

(B,C) Box plots showing group data for each cell type. (A) variation of mean BA levels; (B) distribution of Fano factor (variance/mean) throughout the recordings. Eight recordings were excluded because only short parts (< 30 s) were available for BA analysis. The *p* values of Wald test of fixed effect coefficients are shown in A. TL2a cell type was defined as the baseline (control) to estimate the fixed effect coefficients of the GLM because the sample number was the largest. The only TL3a cell was excluded from the statistical test. The BA of each cell type showed several characteristics. TL2a and TL2b neurons shared similar BA levels (A), with median group activities of 8.6 and 8.2 spikes/s, respectively, and a significant difference was not detected (Wald test, coefficient = −0.0640, z = −0.349, $p = 0.728$). In contrast, the median BA level of TL3b neurons was 5.8 spikes/s, which was significantly lower than that of TL2a neurons (coefficient = −2.77, z = −2.90,

p = 0.00536). The only TL3a neuron showed a TL3b-like BA level (4.7 spikes/s). We also investigated the variability of BA throughout the recordings by calculating Fano factor, or variance to mean ratio, of spike counts per bin (B). The BA of TL2b neurons was highly constant throughout the recordings (group median of Fano factor < 0.5), in contrast to that of TL3b neurons whose BA fluctuated more strongly (group median of Fano factor > 1.5). Naturally, there were outliers from the general trend for each cell type. Especially in TL2a neurons, BA levels were more dependent on the individually recorded cell (A).

Figure S2. Receptive fields and AoP pattern fitting results of all 27 neurons studied (related to Figs. 4–6).

Figure parts are on the following pages. Each row shows the data from a single neuron. The information of cell type, ID, and brain hemisphere of its soma is indicated on the upper left corner of each row. All plots are top views on flattened sky hemispheres (see Fig. 1D for the coordinate system). Plots in column 1 indicate best matching sky polarization patterns and the corresponding sun positions, as shown in Fig. 5A. Plots in column 2 are related to the pattern matching analysis (Fig. 5), showing linearly interpolated pattern deviations between the AoP response pattern and sky polarization patterns generated by various solar coordinates. Values at the bottom indicate the minimum pattern deviations (best match) yielded from the solar coordinates indicated by a crossed yellow circle. Plots of column 3 indicate polarization sensitivity as shown in Fig. 4A, and plots of columns 4 and 5 indicate the receptive field organizations to unpolarized green light as in Fig. 6C and unpolarized blue light, respectively. Blank spaces are properties that were not measured in the respective neurons.

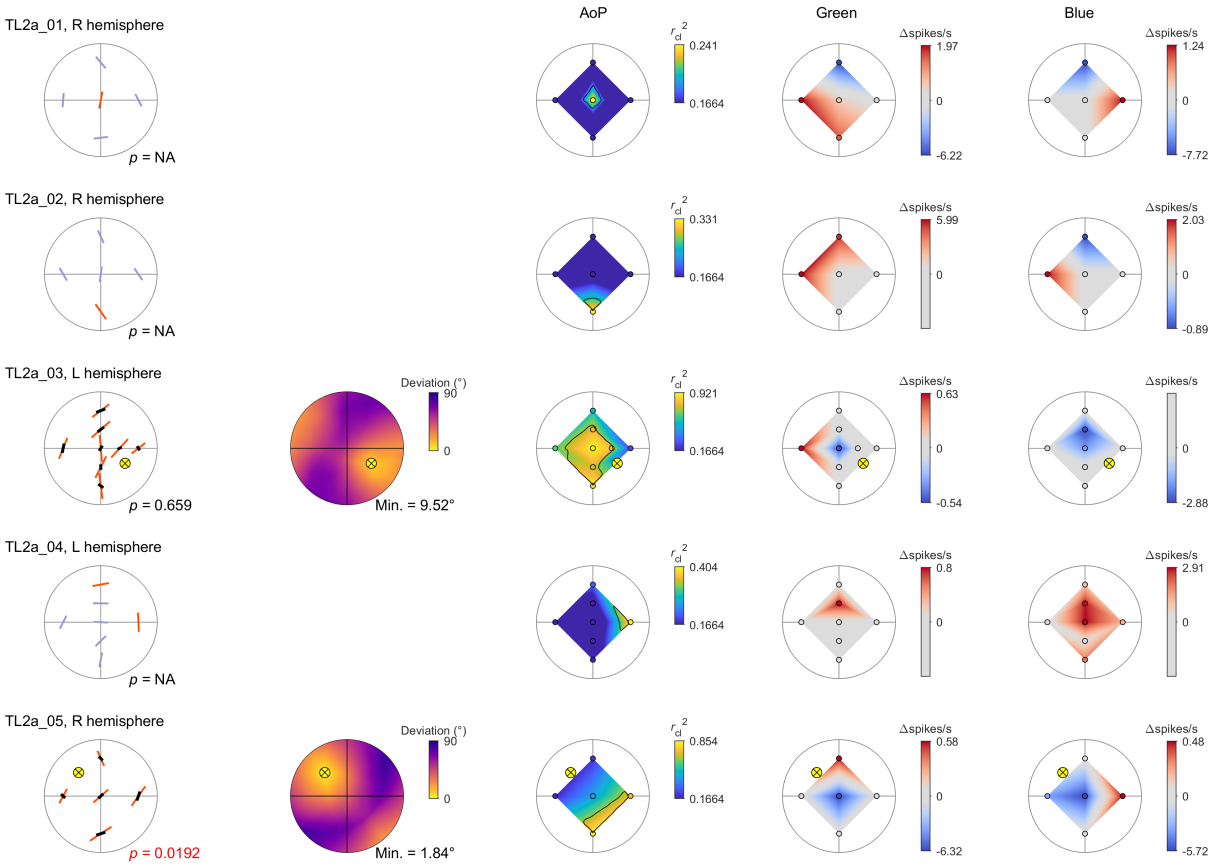

FIGURE S2 (PART 1/6)

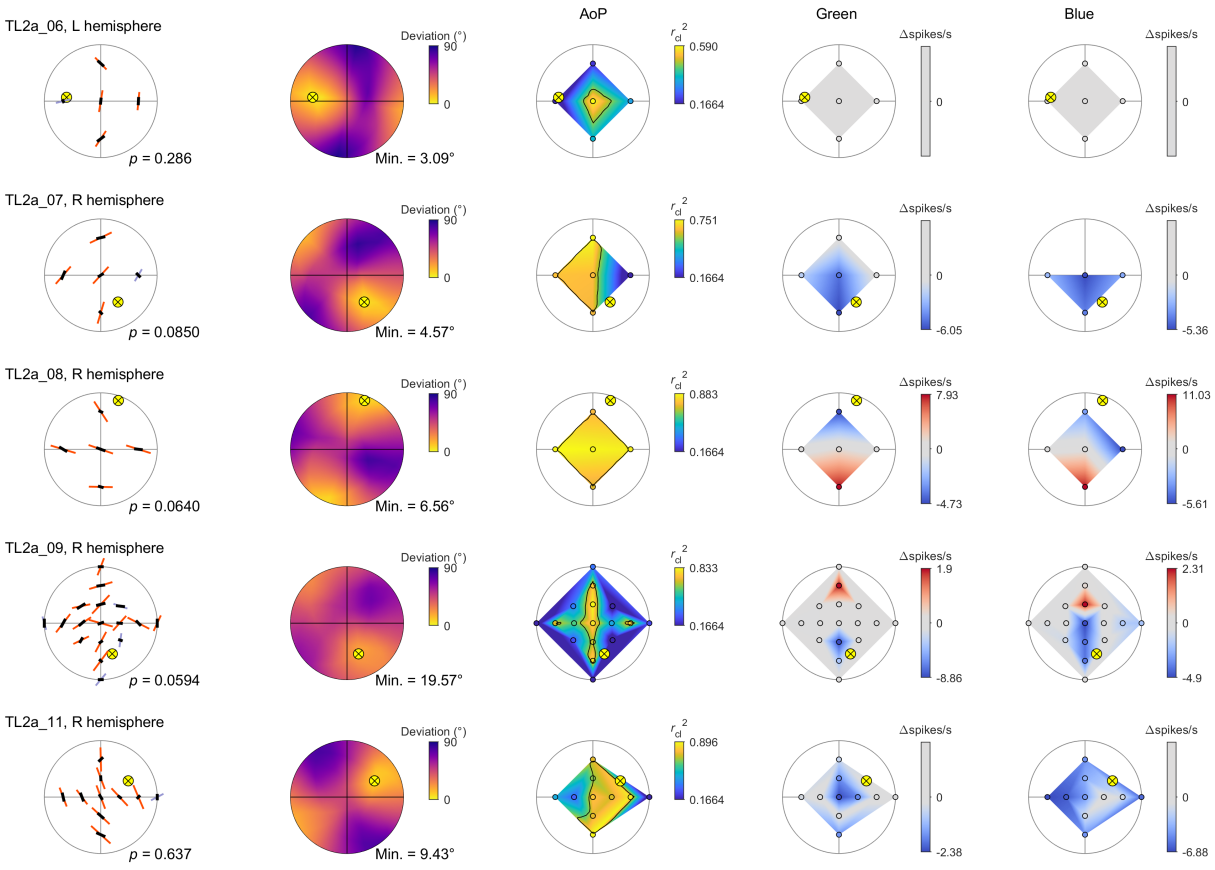

FIGURE S2 (PART 2/6)

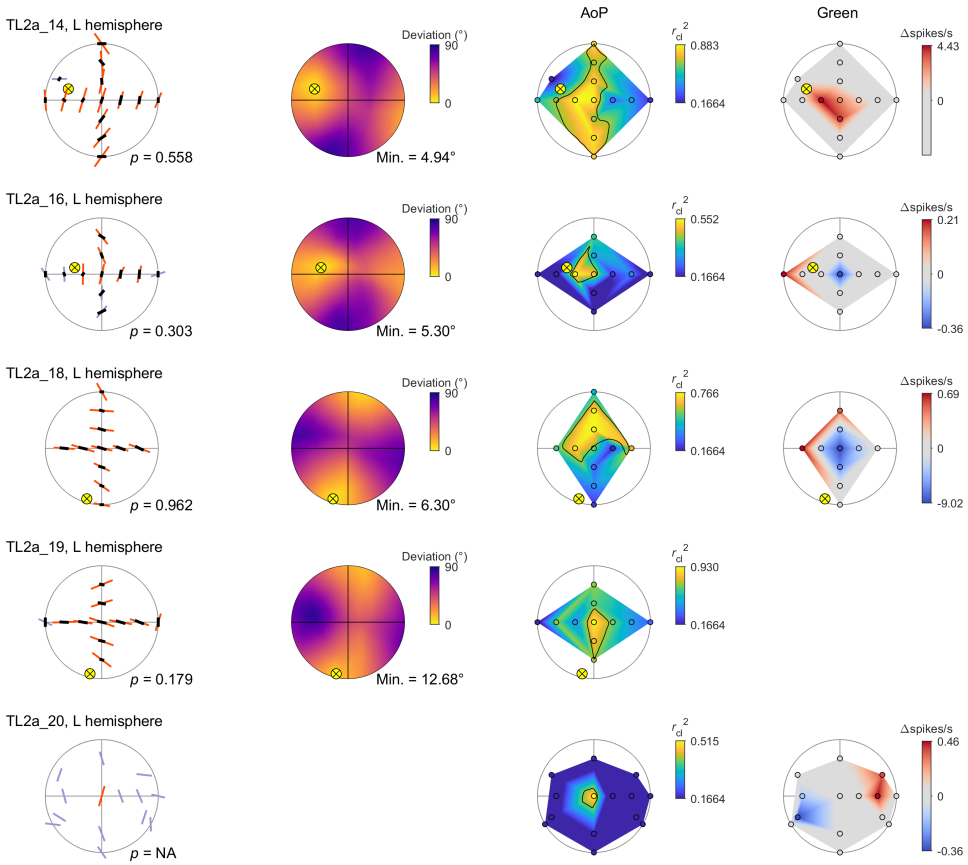

FIGURE S2 (PART 3/6)

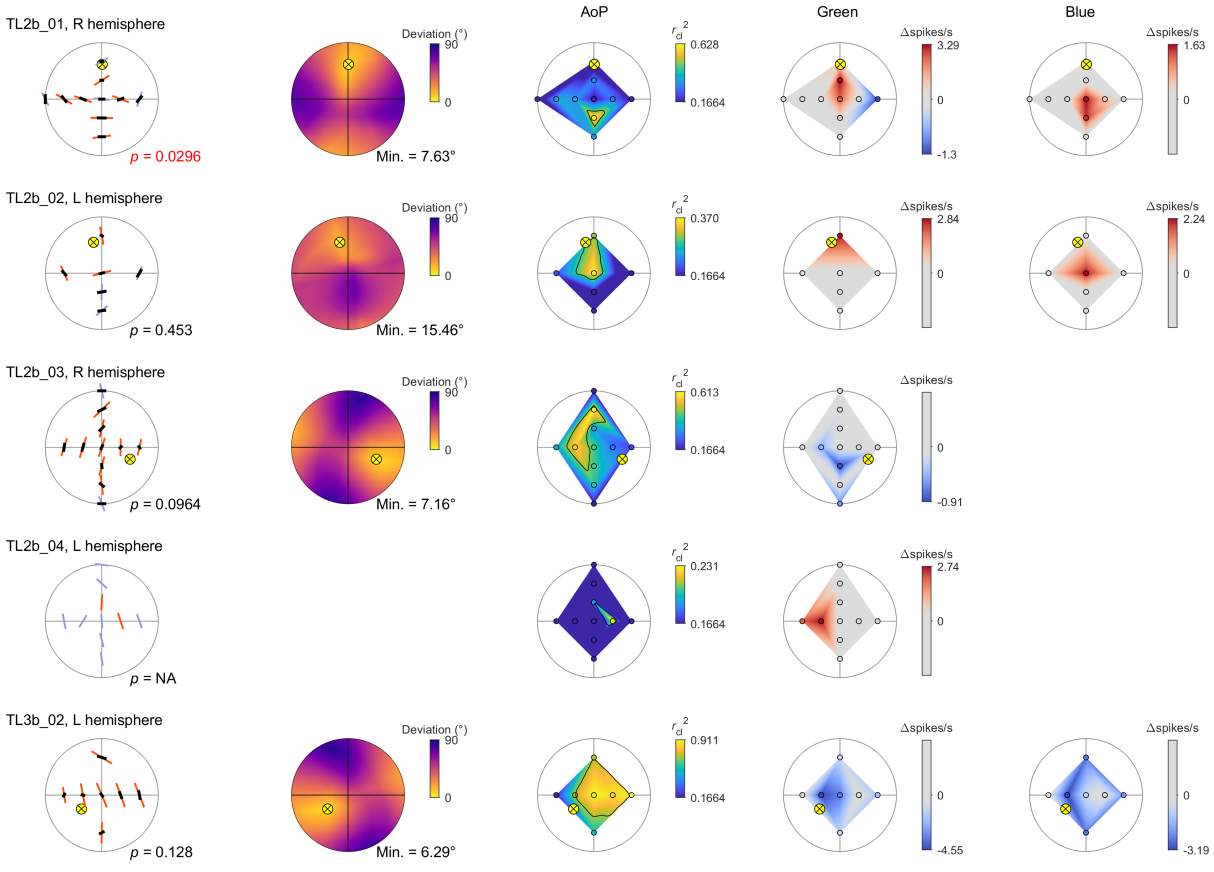

FIGURE S2 (PART 4/6)

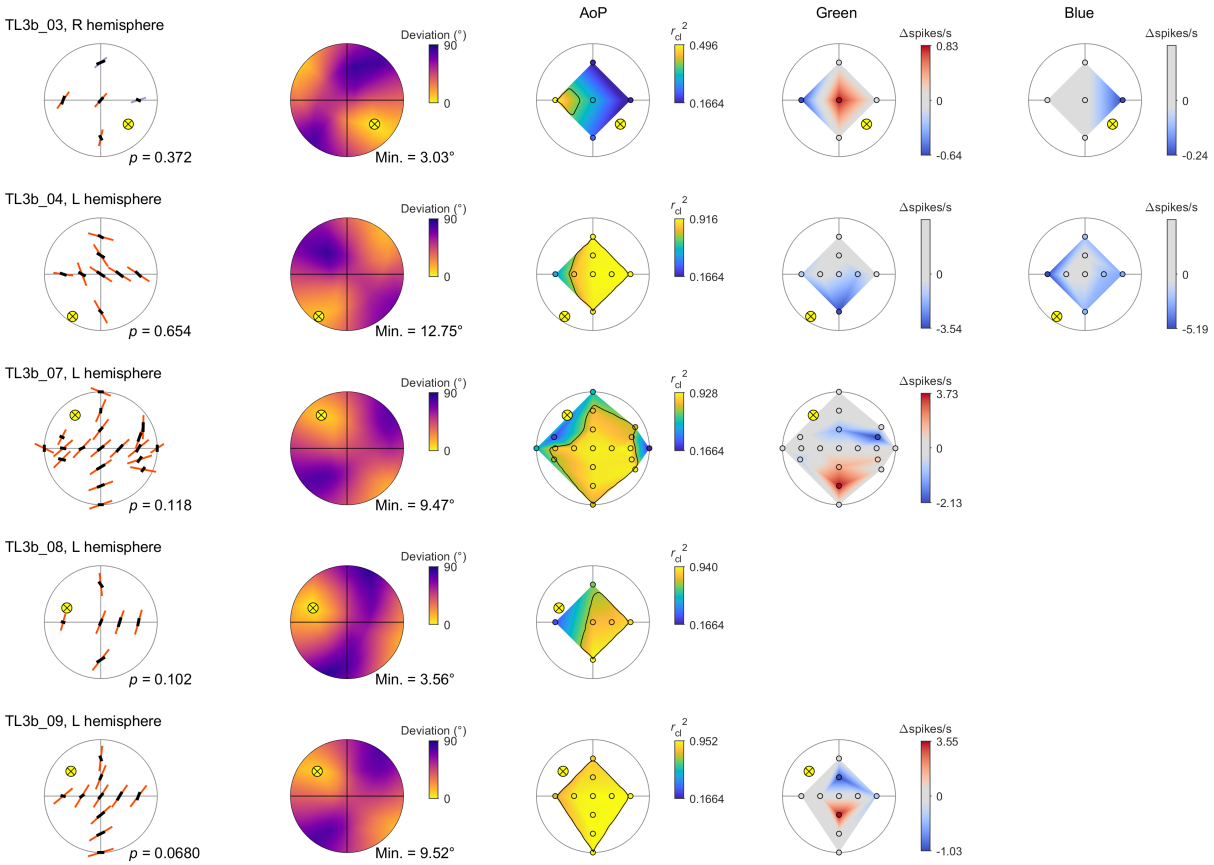

FIGURE S2 (PART 5/6)

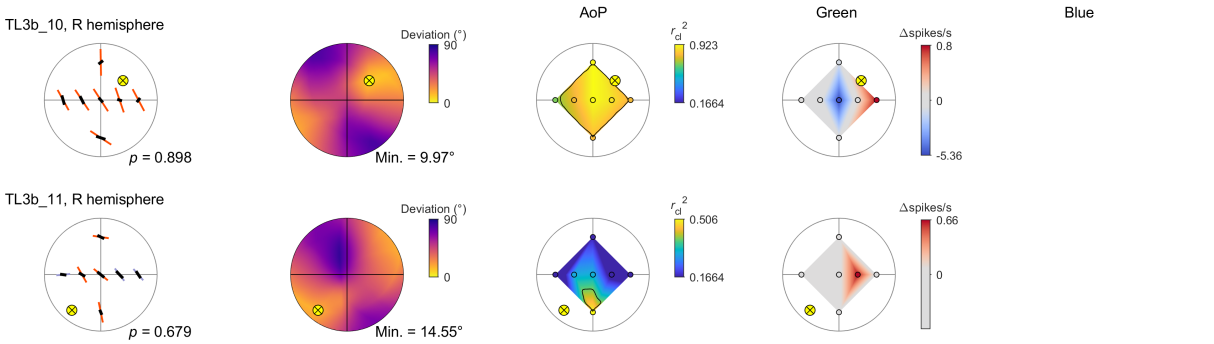

FIGURE S2 (PART 6/6)

Table S1. Changes in response properties to zenithal stimulation in TL neurons.

				AoP			Light spot (Δspikes/s)	
ID	Test #	Interval (s)	BA level (spikes/s)	r_{cl}^2	Φ_{max} (°)	Φ_{max} act./amp.	Green	Blue
TL2a_03	1	0	6.50	0.921	4.7	0.718	-0.54	-1.88
	2	610	7.00	0.612	150.4	0.638	NA	NA
TL2a_09	1	0	0.50	0.791	74.3	0.973	0.00	-4.90
	2	1720	4.00	0.133	75.5	1.446	0.00	2.29
TL2a_11	1	0	9.00	0.800	20.3	0.590	-2.38	-4.54
	2	990	11.67	0.748	43.2	0.255	-2.12	-1.02
TL2a_16	1	0	1.25	0.502	166.8	0.625	-0.36	NA
	2	910	0.00	NA	NA	NA	0.16	NA
TL2a_20	1	0	2.50	0.515	164.4	0.819	0.00	NA
	2	1470	9.08	0.013	78.9	3.375	NA	NA
TL2a_31	1	0	12.25	0.895	59.9	0.630	NA	NA
	4	660	9.43	0.051	133.8	3.533	NA	NA
	7	1060	15.41	0.828	58.6	0.587	NA	NA
TL2a_33	1	0	3.60	0.270	114.6	0.889	NA	NA
	2	850	2.15	0.772	98.9	1.023	NA	NA
TL2a_38	1	0	14.00	0.611	41.1	0.503	NA	NA
	2	680	6.75	0.868	39.3	0.700	NA	NA
TL3b_07	1	0	8.11	0.904	130.8	0.599	0.00	NA
	2	1050	6.00	0.892	133.3	0.769	0.11	NA
TL3b_19	1	0	6.00	0.895	27.6	0.665	NA	NA
	2	650	4.21	0.832	30.3	0.741	NA	NA

Mixed von Mises distributions were fitted to the spike activities during the AoP stimuli even if they were considered no response to AoP ($r_{cl}^2 < 0.1664$) in the same way as to AoP responses, to investigate Φ_{max} (°) and Φ_{max} activities/amplitude. Interval (s), measured from the last AoP stimulus in test #1 to the first AoP stimulus in test #2 (or #4, #7); BA level (spikes/s), BA mean used to calculate Φ_{max} act./amp.; NA, properties that were not calculated (AoP) or tested (light spot).

References

Fano, U. (1947). Ionization yield of radiations. II. The fluctuations of the number of ions. *Phys. Rev.* **72**, 26–29.

Faraway, J. J. (2016). *Extending the linear model with R: generalized linear, mixed effects and nonparametric regression models*. 2nd ed. Boca Raton, FL, USA; London; New York, NY, USA: CRC Press.

Rajdl, K., Lansky, P. and Kostal, L. (2020). Fano factor: a potentially useful information. *Front. Comput. Neurosci.* **14**, 569049.

Chapter 4

Performance of Polarization-Sensitive Neurons of the Locust Central Complex at Different Degrees of Polarization

Performance of polarization-sensitive neurons of the locust central complex at different degrees of polarization

Ronja Hensgen[1], ORCID: 0000-002-4876-9084,

Frederick Zittrell[1], ORCID: 0000-0001-7878-4325,

Keram Pfeiffer[2], ORCID: 0000-0001-5348-2304,

Uwe Homberg[1*], ORCID: 0000-0002-8229-7236

[1]Department of Biology, Animal Physiology & Center for Mind Brain and Behavior (CMBB), Philipps-University of Marburg and Justus Liebig University of Giessen, D-35032 Marburg, Germany

[2]Behavioral Physiology and Sociobiology (Zoology II), Biocenter, University of Würzburg, D-97074 Würzburg, Germany

[*]Correspondence to: Uwe Homberg, Department of Biology, Animal Physiology, Philipps-University of Marburg, D-35032 Marburg, Germany

Email: homberg@biologie.uni-marburg.de

Acknowledgements We are grateful to Martina Kern for maintaining laboratory cultures of desert locusts.

ABBREVIATIONS: AoP, angle of polarization; CBL, lower division of the central body; CBU, upper division of the central body; CX, central complex; DRA, dorsal rim area; DoP, degree of polarization

ABSTRACT

The polarization pattern of the sky is exploited by many insects for spatial orientation and navigation. It derives from Rayleigh scattering in the atmosphere and depends directly on the position of the sun. In the insect brain the central complex (CX) houses neurons tuned to the angle of polarization (AoP), that together constitute an internal compass for celestial navigation. Polarized light is not only characterized by the AoP, but also by the degree of polarization (DoP), which can be highly variable, depending on sky conditions. Under a clear sky the DoP of polarized sky light may reach up to 0.75 but is usually much lower especially when light is scattered by clouds or haze. To investigate how the polarization-processing network of the CX copes with low DoPs, we recorded intracellularly from neurons of the locust CX at different stages of processing, while stimulating with light of different DoPs. Significant responses to polarized light occurred down to DoPs of 0.05 indicating reliable coding of the AoP even at unfavorable sky conditions. Moreover, we found that the activity of neurons at the CX input stage may be strongly influenced by nearly unpolarized light, while the activity of downstream neurons appears less affected.

Keywords polarization vision, central complex, sky compass coding, intracellular recordings, desert locust

INTRODUCTION

Spatial orientation and navigation require the perception and integration of environmental stimuli. For estimating spatial directions, many animals rely on sky compass cues, including celestial bodies such as the sun or moon, the chromatic gradient and the polarization pattern of the sky. Linear polarization of skylight mainly derives from Rayleigh scattering in the atmosphere (Strutt 1871) and results in a polarization pattern across the sky that directly depends on the position of the sun or moon (Fig. 1a). Orientation to polarized light has been demonstrated for several insect species in the field (honey bees, *Apis mellifera*: von Frisch 1949; Evangelista et al. 2014; desert ants, *Cataglyphis fortis*: Sommer and Wehner 2005; dung beetles, *Scarabaeus satyrus*: Dacke et al. 2013) and in the laboratory (desert locusts, *Schistocerca gregaria*: Mappes and Homberg 2004; field crickets, *Gryllus campestris*: Brunner and Labhart 1987; monarch butterflies, *Danaus plexippus*: Reppert et al. 2004). The neural pathways that mediate transmission of polarization information from the eye to the central brain have been studied particularly well in locusts (Homberg et al. 2003, 2011; Kinoshita et al. 2007), crickets (Labhart 1988; Labhart et al. 2001; Sakura et al. 2007) and fruit flies (Hardcastle et al. 2021) but also in other insects including monarch butterflies (Heinze and Reppert 2011) and dung beetles (el Jundi et al. 2015). Specialized photoreceptors of a small, dorsal region of the compound eye, the dorsal rim area (DRA) are particularly sensitive to the oscillation angle of polarized light (Labhart and Meyer 1999). Signals from dorsal rim photoreceptors are transmitted via the

optic lobe, the anterior optic tubercle, and the bulb of the lateral complex to the central complex (CX) of the brain. The CX is an assembly of midline spanning neuropils, including the protocerebral bridge, the lower (CBL) and upper (CBU) division of the central body, and the paired noduli. The CX houses a neural network signaling head-direction (Seelig and Jayaraman 2015; Green and Maimon 2018; Pisokas et al. 2020; Green et al. 2019; Hulse and Jayaraman 2020; Shiozaki et al. 2020) and as such integrates various sensory cues to generate appropriate behavioral output and guidance during navigation (Varga et al. 2017; Honkanen et al. 2021). The architecture of the CX is characterized by the projections of tangential and columnar neurons (Fig. 1b,c) that provide connectivity within the CX and between the CX and other brain regions (Hanesch et al. 1989; Hulse et al. 2021; Heinze and Homberg 2008; von Hadeln et al. 2019; Heinze and Reppert 2013).

As in other insects, many neurons of the CX of the locust *S. gregaria* are sensitive to the angle of polarization (AoP) of light from the sky. Physiological studies revealed a putative processing hierarchy for polarized light information in the CX (Heinze and Homberg 2009; Bockhorst and Homberg 2015): Tangential neurons of the CBL (TL neurons) provide input from the bulbs of the lateral complex to the CX (Fig. 1b). Columnar neurons of the CBL (CL1 neurons) transmit the signals to tangential neurons of the protocerebral bridge (TB neurons) that signal onto columnar neurons of the CBU (CPU neurons). The latter provide output from the CX to the lateral accessory lobes (Fig. 1c). Consistent with the role of the CX as an internal compass, the orientation of the pattern of AoPs across the sky and the azimuth of a simulated sun are represented topographically in the neuronal activity across the protocerebral bridge (Heinze and Homberg 2007; Pegel et al. 2019; Zittrell et al. 2020).

Linearly polarized light is characterized, in addition to its AoP, by the degree of polarization (DoP) which indicates the percentage of polarized light within a light beam. The DoP depends on the angular distance from the sun and is lowest for direct sunlight (DoP = 0) and highest at 90° from the sun (DoP = 0.75 under optimal sky conditions; Fig. 1a). The DoP decreases under haze or clouds resulting in lower values. Several behavioral studies accounted for the natural occurrence of low DoPs by testing the performance of animals under matching conditions. For *A. mellifera* a detection threshold was proposed at a DoP between 0.07 and 0.1 (von Frisch 1967), and field crickets (*Gryllus campestris*) showed behavioral responses at DoPs even lower than 0.07 (Henze and Labhart 2007). Findings for the nocturnal dung beetle (*Scarabaeus satyrus*) indicated a behavioral threshold for polarized lunar skylight between 0.04 and 0.32 (Foster et al. 2019). These studies show that certain insect species can utilize polarization information for orientation even under highly unfavorable conditions. However, the majority of physiological experiments on neuronal responses to polarized light has been conducted with substantially higher DoPs (of 0.99). Only few studies examined the influence of low DoPs on neuronal responses. Among these are experiments performed in *G. campestris* that revealed a threshold DoP of 0.05 for polarization-opponent interneurons of the optic lobes (Labhart

1996) and an insensitivity of CX neurons of *G. bimaculatus* to changes in the DoP between 0.99 and 0.18 (Sakura et al. 2007). These findings fit the results from behavioral experiments. In contrast, neuronal responses of interneurons of the anterior optic tubercle of *S. gregaria* indicated a much higher DoP threshold of 0.3 and additionally demonstrated increasing neuronal inhibition upon stimulation with decreasing DoPs (Pfeiffer et al. 2011).

In this study, we investigated how different DoPs affect the responses of CX neurons of *S. gregaria* to polarized blue light. We show that reliable coding of AoPs is present in certain cell types down to DoPs of 0.05. Moreover, the activity of some neurons of the CX input is strongly affected by nearly unpolarized blue light, and this response is also mediated by the DRA.

MATERIALS AND METHODS

Animals and Preparation

Male and female gregarious desert locusts were obtained from colonies reared at Philipps-Universität Marburg. Animals were kept at a constant temperature of 28°C under a 12h:12h light/dark cycle. Animals were mounted onto a metal holder and legs and wings were cut off. A window was cut frontally into the head capsule, and fat tissue and air sacs were removed to get access to the brain. The esophagus was cut and the gut was removed via the abdomen, which was sealed afterwards with dental wax. The brain was stabilized from posterior with a small twisted metal wire inserted into the window of the head. Finally, the neural sheath of the brain was partly removed to allow penetration of the recording electrode. The brain was kept submerged in locust saline (Clements and May 1974) during preparation, recording and dissection.

Electrophysiology

Intracellular recordings were performed with sharp microelectrodes drawn from borosilicate capillaries (Hilgenberg, Malsfeld, Germany), with a Flaming/Brown horizontal puller (P-97, Sutter Instrument, Novato, CA). The tip of the electrodes was loaded with 4% Neurobiotin (Vector Laboratories, Burlingame, CA) in 1 mol l^{-1} KCl and the shanks were loaded with 1 mol l^{-1} KCl. Signals were amplified 10x with a BA-01X amplifier (npi electronic instruments, Tamm, Germany), and monitored with a custom-built audio monitor (University of Marburg) and an oscilloscope (Hameg, Frankfurt/Main, Germany). Data was digitized with a Power1401-mkII (Cambridge Electronic Design, Cambridge, GB) and stored on a PC using Spike2 (Cambridge Electronic Design, Cambridge, UK) with a sampling rate of 20 kHz. After the recording, Neurobiotin was injected into the cell by application of a positive current of 0.5-2 nA for at least 2 min.

Histology and image acquisition

Brains were dissected and fixed in 4% paraformaldehyde, 0.25% glutaraldehyde, and 2% saturated picric acid diluted in 0.1 mol l^{-1} phosphate buffered saline (PBS) at 4°C overnight. Following rinses in PBS (4 x 15 min) brains were incubated in Cy3-conjugated

streptavidin (1:1,000) in PBS containing 0.3% Triton X-100 (PBT) at 4°C for 3 d. Following rinses in PBT (2 x 20 min) and PBS (3 x 20 min) brains were dehydrated in an ascending ethanol series (30%, 50%, 70%, 90%, 95%, 100%, 15 min each) and cleared in a 1:1 mixture of 100% ethanol and methyl salicylate (Merck, Darmstadt, Germany) for 15 min and in pure methyl salicylate for 1 h. Finally, they were mounted in Permount (Fisher Scientific, Pittsburgh, PA) between two coverslips. Samples were scanned with a confocal laser scanning microscope (Leica, TCS SP5, Leica Microsystems, Wetzlar, Germany) with a 20x immersion objective (HC PL APO 20x/0.75 Imm Corr CS2, Leica). A diode pumped solid state laser (561 nm) was used to excite Cy3. Scanning frequency was 400 Hz and the voxel size was 0.54 x 0.54 x 2.0 µm.

Stimulation

Animals were stimulated from the zenith by light from a blue light emitting diode (LED; Oslon SSL 80, LDCQ7P, 452 nm, Osram Opto Semiconductors GmbH, Regensburg, Germany). The light was linearly polarized by a dichroic polarizer sheet (HNP'B, Polaroid, Cambridge, MA). To generate degrees of polarization between 0.002 and 0.9, diffusor sheets were placed in different combinations between the LED and the polarizer or between the animal and the polarizer (Fig. 2a). At the highest degree of polarization, all four diffusor sheets were placed between the LED and the polarizer, while at the lowest degree of polarization, the four diffusor sheets were placed between the animal and the polarizer. With the different arrangements, five stimuli could be tested: DoP = 0.99 (maximally polarized light, 1.9 x 10^{13} photons cm^{-2} s^{-1}), DoP = 0.35 (1.6 x 10^{13} photons cm^{-2} s^{-1}), DoP = 0.1 and DoP = 0.05 (1.5 x 10^{13} photons cm^{-2} s^{-1}), and DoP = 0.002 (1.7 x 10^{13} photons cm^{-2} s^{-1}). The stimuli covered a visual angle of 12.6°. To monitor the angle and the degree of polarization, a HNP'B polarization filter was placed in front of an OPT101 photodiode/transimpedance amplifier (Texas Instruments, Dallas, TX) positioned close to the animal's head (Fig. 2a). The output of the OPT101 was continuously recorded via the digitizer. The stimulation device rotated 360° clockwise and counterclockwise at 40 °/s. In some experiments we painted both DRAs of the animal with acrylic black paint.

Data evaluation

Physiological data were preprocessed using Spike2 and exported as mat-files for further analysis in MATLAB (Version 2020a, The MathWorks, Natick, MA, USA) using custom scripts. Circular histograms were created with the CircHist package (Zittrell 2019). Confocal image stacks were processed in Amira 5.6 (ThermoFisher Scientific, Waltham, MA; RRID:SCR_007353). Images showing raw data were exported from Spike2 and processed with Affinity photo and Affinity Designer (Serif, Nottingham, UK; RRID:SCR_016951). Diagrams were generated with Microsoft Excel or MATLAB and were exported to Affinity photo to create figure panels.

Background activity. Owing to fluctuations of background activity (BA) in some neurons we calculated the BA for comparison with firing activity during stimulation within a time window of 5 s preceding the respective stimulus. Spikes were binned in 1 s bins

and these spike counts were used to calculate the median and the 2.5th and 97.5th percentile of BA.

Stimulus responsiveness. We used linear-circular correlation analysis (*CircStat*; Berens 2009) to determine whether the modulation of spike rate was correlated to changes in AoP. Time points of action potentials during each 360° rotation were assigned to the respective orientation of the polarizer and these angles were doubled to allow using circular statistics on these axial data (Zar 1999). The resulting angles were averaged and the result was halved, yielding the preferred AoP (Φ_{max}) in circular space. At least one clockwise and one counterclockwise rotation of the polarizer were included to measure the responsiveness to a stimulus with a particular DoP. To determine a correlation between firing rate and AoP, spike angles were binned in 10° bins and counts were tested for correlation with bin angles. A resulting P value < 0.05 indicated significant modulation by AoP. To specify properties of significant responses, we calculated the mean resultant vector length r and the response amplitude A. The vector length r describes the directedness of the response and ranges from 0 to unity, with unity indicating that all vectors are of the same direction (Batschelet 1981). It was calculated with the *CircStat* toolbox (Berens 2009). A describes the absolute amplitude of spike frequency modulation during stimulation, with higher A values indicating stronger modulation. A was calculated as follows according to Labhart (1996) and Pfeiffer et al. (2011):

$A = \sum_{i=1}^{i=18} |n_i - \overline{n}|,$

where n_i is the number of spikes in bin i and $\overline{n}$ is the number of spikes during the 360° rotation divided by the number of bins.

Firing rates at Φ_{max} and Φ_{min} were estimated by fitting a bimodal von Mises distribution model to the binned data (Fitak and Johnsen 2017) and taking the model's firing rate at the respective angles.

Regression analysis. To test whether modulation amplitude A, length of the mean vector r, and mean spiking activity were dependent on the DoP, respective data were pooled and tested for linear regression. If the resulting residuals were not normally distributed (based on the Lilliefors test), the data were logarithmically transformed and the regression was done again. If the residuals of this regression were not normally distributed, the two linear models were compared regarding their R^2 values and the one with the higher value was chosen.

Threshold for reliable coding of the AoP. To estimate the DoP threshold for reliable coding of the AoP we compared the mean resultant vector length r obtained during the stimulus with the upper 95% confidence limit of r obtained without stimulation (Pfeiffer et al. 2011). We defined the threshold as the lowest DoP at which the r values of all responses exceeded the upper 95% confidence limit of the estimated average r value of the no-stimulus controls.

RESULTS

We recorded intracellularly from 49 AoP-sensitive neurons in the CX, including 8 TL2 neurons, 5 TL3 neurons, 14 CL1a neurons, 10 TB1 neurons, 8 CPU1 neurons, and 4 CPU2 neurons. We investigated the influence of blue light with different DoPs on the mean vector length *r*, the response amplitude *A*, and the firing activity of the neurons. Based on the data we determined a DoP threshold for reliable AoP signaling.

The recorded neurons showed characteristic sinusoidal modulation of activity during 360° rotation of the polarizer (Fig. 2b). The AoP that results in maximal activity during stimulus presentation is referred to as preferred AoP (or preferred *E*-vector orientation, Φ_{max}). The AoP perpendicular to the Φ_{max} is called anti-preferred AoP (Φ_{min}).

Threshold for reliably signaling the angle of polarization

All recordings (N = 49) included stimulation with blue light of the highest DoP (0.99). Depending on recording stability and duration additional stimuli were tested (DoP = 0.35, N = 41; DoP = 0.1, N = 34; DoP = 0.05, N = 33; DoP = 0.002, N = 45). Figure 3 illustrates the responses of a CL1a neuron that was tested with all five stimuli.

All neurons (TL2 = 5, TL3 = 5, CL1a = 11, TB1 = 10, CPU = 11) tested with polarized blue light at a DoP of 0.35 showed a significant modulation of firing activity by AoP. All three TL2 neurons and all four TL3 neurons tested with a DoP of 0.1 still responded significantly to the stimulus. Most of the CL1a neurons (6 out of 8), TB1 neurons (6 out of 8), and CPU neurons (9 out of 11) also showed significant responses at 0.1 DoP. At a DoP of 0.05 less than half of the tested neurons responded significantly to the stimulus (TL2, 3 out of 4; TL3, 1 out of 5; CL1, 2 out of 6; TB1, 3 out of 7; CPU, 4 out of 11). The lowest DoP of 0.002, which should equal unpolarized light, did not elicit a significant response in any of the neurons tested. These results (summarized in Fig. 4a) point to a threshold for reliable coding of the AoP between a DoP of 0.1 and 0.05.

Pfeiffer et al. (2011) used the mean vector length *r* to calculate the threshold for reliable AoP coding (see Materials and Methods). In TL2 neurons all *r* values at DoP values ≥0.05 exceeded the upper 95% confidence level. TB1 neurons showed reliable coding at DoP values ≥0.1. In all other cell types stimuli with a DoP ≥0.35 resulted in reliable coding of the AoP (Fig. 4b).

Response amplitude and firing activity at different degrees of polarization

The response amplitude *A* was positively correlated with increasing DoPs in all types of neuron tested (Fig. 5). Testing for linear regression revealed that the dependence of *A* on the DoP in TL2 neurons was best described when using non-logarithmically transformed data, whereas the dependence of *A* on the DoP in all other neurons was best described by a linear model based on logarithmically transformed data (see Materials and Methods, Fig. 5). This indicates that the relationship between the response amplitude *A* and the DoP is linear in TL2 neurons but logarithmic in the remaining cell types. However, individual neurons of each type could show an either linear or logarithmic relationship between the

response amplitude *A* and the DoP (not shown). Similar to Pfeiffer et al. (2011) we calculated whether the mean spiking activity during a 360° rotation of the polarizer was influenced by the presented DoP. We found that the mean spiking activity was positively correlated with increasing DoPs in TL2 neurons, negatively correlated in CL1 neurons and not linearly correlated in TL3-, TB1- and CPU neurons (Fig. 6). To further explore the cell-type specific results, we calculated the minimum and maximum activity of neurons at Φ_{max} and Φ_{min} for different DoPs (Fig. 7). The results show that both, inhibition and excitation, increased in all types of neuron with an increase in DoP, and that activity during low DoPs was clustered around background activity in TL3, TB1 and CPU neurons (Fig. 7). In contrast, activity of CL1 neurons at Φ_{max} and Φ_{min} at low DoPs was increased above background activity, whereas in TL2 neurons activity at low DoPs was lower than background activity, except for one cell (Fig. 7, TL2, Fig. 8).

Influence of unpolarized blue light on firing activity

The activity of some neurons was strongly affected by unpolarized blue light. Reducing the DoP revealed an overall inhibition or excitation of the neurons during stimulus presentation with strongest effects at the lowest DoP of 0.002 (Figs. 8, 9). Excitatory and inhibitory responses were followed by rebound inhibition or excitation, respectively, at stimulus offset. These effects were observed primarily in TL neurons, especially TL2 cells, but could also be observed, however to a lesser extent, in CL1-, TB1- and CPU neurons.

Out of eight TL2 neurons five were inhibited and two were excited at 0.002 DoP, among four TL3 neurons one was inhibited. The strength of inhibition and excitation varied between individual cells and could be very pronounced or rather mild. The remaining TL2 and TL3 neurons did not show obvious changes in firing activity upon stimulation with unpolarized blue light.

The strong excitatory response of a TL2 neuron to stimulation with the lowest DoP as well as the responses to higher degrees of polarization were followed by strong inhibition upon stimulus offset which lasted up to 20 s (Fig. 8, arrowheads). These inhibitions at lights off were abolished after the DRAs were covered with black paint (Fig. 8) but were restored when uncovering the DRAs again (Fig. 8). Painting the DRAs resulted, in addition, in higher overall activity of the neuron, perhaps owing to the lack of inhibition following each stimulus. The opposite response, again in a TL2 neuron, is illustrated in Fig. 9. Here the TL2 neuron responded to low DoPs with inhibition and rebound excitation at lights off. Both responses were abolished when the DRAs were covered (Fig. 9). Uncovering the DRAs restored the polarization response at high DoPs, the inhibition at low DoPs (unpolarized blue light) and the excitation at lights off (Fig. 9).

In 12 out of 13 CL1 neurons we observed phasic inhibition after stimulus offset (lights off) that varied in strength. Nine of these neurons displayed phasic inhibition also at stimulus onset (lights on) that gave way to slightly elevated activity (Fig. 10a). Three neurons did not show phasic lights on inhibition but only excitation during stimulation with the lowest DoP (Fig. 10b). Although the strength and duration of phasic inhibition at lights

on, the following sustained excitation, and the rebound inhibition upon lights off varied between individual neurons, only one CL1 neuron showed a completely different response characterized by phasic excitation upon lights on (Fig. 10c).

The ten TB1 neurons showed more variable responses. One neuron showed slight excitation followed by rebound inhibition (Fig. 11a). Two neurons showed slight excitation during stimulation but lacked rebound inhibition. Two neurons showed no change in activity upon stimulation with the lowest DoP (Fig. 11b), three neurons only showed excitation upon stimulus offset (Fig. 11c), and one neuron only showed slight inhibition after stimulus offset.

Four out of twelve CPU neurons showed inhibition during stimulation with a DoP = 0.002 and rebound excitation upon stimulus offset (Fig. 12a). Rebound excitation without obvious inhibition was displayed by one CPU neuron. One neuron showed phasic excitation upon stimulus onset and rebound excitation upon stimulus offset (Fig. 12b). Rebound inhibition and slight excitation during stimulus presentation were observed in one CPU neuron, respectively. The remaining four CPU neurons showed no obvious change in activity during stimulation (Fig. 12c).

DISCUSSION

Threshold for reliable AoP signaling

Intracellular recordings from AoP-sensitive neurons of the locust CX revealed that AoP signaling in these neurons is reliable down to DoPs of 0.35 in TL3-, CL1-, and CPU neurons, 0.1 in TB1 neurons and 0.05 in TL2 neurons. Because our estimation of reliable coding does not account for DoPs between the discrete values that were tested (0.3, 0.1 and 0.5), and based on the significance of responses of individual neurons, we assume that at least for TL3-, CL1- and CPU neurons the actual threshold for AoP coding might be lower than the estimated threshold and might lie between 0.35 and 0.1. The low thresholds found in TL2 and TB1 neurons are similar to thresholds that have been determined for polarotactic behavior in honeybees, crickets, and dung beetles (von Frisch 1967; Henze and Labhart 2007; Foster et al. 2019) and for neuronal responses of polarization-opponent interneurons in the optic lobes of crickets (Labhart 1996). Prior to this study, neurons of the CX have been tested with different DoPs only in crickets (CNL neurons, Sakura et al. 2007). Those neurons are homologous to TL2/TL3 neurons in locusts. They showed responses to polarized light with modulation amplitudes independent of the DoP, ranging from 0.99 to 0.18. Lower DoPs, however, were not tested. In contrast to the data in crickets, the modulation amplitude in all types of locust CX neurons increased with increasing DoP (Fig. 5). In general, response amplitudes measured here were relatively high for all cell types, compared to response amplitudes described by Heinze and Homberg (2009).

For two cell types of the anterior optic tubercle of the locust (LoTu- and TuTu neurons), Pfeiffer et al. (2011) determined a DoP threshold for reliable AoP signaling of 0.3. While

the anterior optic tubercle is a prominent part of the polarization vision pathway to the CX, dominant input to CX neurons is, however, likely provided by transmedulla neurons contacting tubercle-bulb neurons in the anterior optic tubercle, while LoTu and TuTu neurons are not directly involved in the polarization vision pathway to the CX, but rather provide integration between the right and left tubercle in the locust brain.

Effect of unpolarized blue light on polarization-sensitive neurons

Pfeiffer et al. (2011) found that dorsally presented blue light with low DoPs inhibited the activity of LoTu- and TuTu neurons. Inhibition of LoTu neurons by dorsally presented unpolarized blue light and of TuTu neurons by contralaterally presented unpolarized blue light was also demonstrated by Kinoshita et al. (2007). The authors argued that suppression of activity in these neurons might prevent signaling of ambiguous information deriving from low DoPs (Pfeiffer et al. 2011). We found similar, but also opposite responses in TL neurons, with pronounced inhibition upon presentation of unpolarized blue light (Fig. 9) in most cells, but also pronounced excitation upon stimulation with unpolarized blue light (Fig. 8) in some other cells. Similar but less prominent effects were also observed in the downstream cell types of the CX. Especially in CL1 neurons consistent rebound inhibition after stimulus offset corresponded to an increase in firing rate during stimulus presentation. Responses in TB1- and CPU neurons were more variable. Slight inhibition observed in several CPU neurons might point to inhibitory input from CL1 neurons.

Pfeiffer et al. (2011) plotted the average firing rate of LoTu- and TuTu neurons over the DoP to illustrate the increase in average firing rate with increasing DoPs. As we observed mostly inhibition in TL neurons when presented with low DoPs, we expected a similar trend in these types of neuron. For TL2 neurons our results met the expectations (Fig. 6), but for TL3 neurons we found no correlation (Fig. 6). In CL1 neurons the average firing activity was negatively correlated with an increase in the DoP, which is in line with the assumption that CL1 neurons are inhibited by the GABAergic TL neurons and, therefore, show an opposite correlation between average firing rate and DoP compared to TL2 neurons. In TB1- and CPU neurons average firing activity appeared to be independent of the DoP. TL2 and TL3 neurons show polarization opponency, i.e. they receive inhibitory input at Φ_{min} and excitatory input at Φ_{max} (Bockhorst and Homberg 2015; Pegel et al. 2018). Pronounced inhibition or excitation at low DoP values in TL neurons might, therefore, result from unbalanced inhibitory and excitatory inputs leading to an overall excitation or inhibition when reducing the DoP. As unpolarized light consists of all possible angles of polarization, neurons would get inhibited when the inhibitory input outweighs the excitatory input and vice versa. Balanced inhibitory and excitatory input would result in unaltered neuronal activity upon presentation of low DoPs. As activity of CL1 neurons is likely modulated by global inhibition from TL neurons, inhibition or excitation as a result of unbalanced inhibitory and excitatory input is less pronounced in these neurons and is even weaker in the downstream TB1- and CPU neurons, possibly by convergent input to these neurons from many TL neurons. A likely mechanism for the reoccurrence

of polarization opponency in TB1- and CPU neurons was outlined by Bockhorst et al. (2015). The authors suggest that polarization opponency in these neurons arises from mutual inhibition of TB1 neurons that receive excitatory input from opponently tuned CL1 neurons. Unbalanced input to TL neurons that results in either pronounced excitation or inhibition might serve to modulate the TL network activity according to available stimuli, i.e. silencing the polarization-processing pathway when respective stimuli are absent, clearing the way for other navigational relevant stimuli, such as wind (Okubo et al. 2020) or proprioceptive feedback.

Pfeiffer et al. (2011) assumed that the observed inhibition by low DoP in neurons of the anterior optic tubercle is caused by the same set of polarization-sensitive photoreceptors that signal relevant AoP stimuli. Here, we demonstrate that photoreceptors of the DRA, indeed, mediate the inhibitory and excitatory responses to dorsally presented unpolarized blue light in TL neurons (Figs. 8, 9), whereas other eye regions have only a marginal, if any, effect.

The data show that the CX in desert locusts is capable of reliable AoP coding and thus sky-compass dependent head-direction signaling even under highly unfavorable sky conditions. As our stimulus device only covered a visual angle of 12.5°, even lower effective degrees of polarization in the sky may suffice to generate head-direction signals by integration of inputs across the full sky as shown by Zittrell et al. (2020). This might allow to still exploit skylight polarization at a sky fully overcast by thin clouds showing effective degrees of polarization just above 0.05 (Labhart 1996, 1999).

DECLARATIONS

Funding This work was supported by the Deutsche Forschungsgemeinschaft, Grant number HO 950/24-1 and HO 950/28-1.

Conflict of interests The authors declare no conflict of interest.

Availability of data and materials All data that support the findings of this study are available from the corresponding author.

Code availability MATLAB analysis code is available upon request.

Author`s contributions Study concept and design: UH, KP, RH; acquisition of data: RH; data analysis and interpretation: RH, FZ; analysis code: FZ; drafting the manuscript: RH; review and editing: UH, RH, KP.

REFERENCES

Batschelet E (1981) Circular statistics in biology. New York: Academic Press

Berens P (2009) CircStat: A MATLAB toolbox for circular statistics. J Stat Soft 31:1-21.

Bockhorst T, Homberg U (2015) Amplitude and dynamics of polarization-plane signaling in the central complex of the locust brain. J Neurophysiol 113:3291-3311. https://doi.org/10.1152/jn.00742.2014

Brunner D, Labhart T (1987) Behavioral evidence for polarization vision in crickets. Physiol Entomol 12:1-10. https://doi.org/10.1111/j.1365-3032.1987.tb00718.x

Clements AN, May TE (1974) Studies on locust neuromuscular physiology in relation to glutamic acid. J Exp Biol 60:6730-705. https://doi.org/10.1242/jeb.60.3.673

Dacke M, Baird E, Byrne M, Scholtz CH, Warrant EJ (2013) Dung beetles use the milky way for orientation. Curr Biol 23:298-300. https://doi.org/10.1016/j.cub.2012.12.034

el Jundi B, Homberg U (2012) Receptive field properties and intensity-response functions of polarization-sensitive neurons of the optic tubercle in gregarious and solitarious locusts. J Neruophysiol 108:1695-1710.

el Jundi B, Warrant EJ, Byrne, MJ, Khaldy L, Baird E, Smolka J, Dacke M (2015) Neural coding underlying the cue preference for celestial orientation. Proc Natl Acad Sci USA 112:11395-11400. https://doi.org/10.1073/pnas.1501272112

Evangelista C, Kraft P, Dacke M, Labhart T (2014) Honeybee navigation: critically examining the role of the polarization compass. Phil Trans R Soc B 369:20130037. https://doi.org/10.1098/rstb.2013.0037

Fitak RR, Johnsen S (2017) Bringing the analysis of animal orientation data full circle: model-based approaches with maximum likelihood. J Exp Biol 220:3878–3882. https://doi.org/10.1242/jeb.167056

Foster JJ, Kirwan JD, el Jundi B, Smolka J, Khaldy L, Baird E, Byrne MJ et al. (2019) Orienting to polarized light at night – matching lunar skylight to performance in a nocturnal dung beetle. J Exp Biol 222:jeb188532. https://doi.org/10.1242/jeb.188532

Green J, Maimon G (2018) Building a heading signal from anatomically defined neuron types in the *Drosophila* central complex. Curr Opin Neurobiol 52:156-164. https://doi.org/10.1016/j.conb.2018.06.010

Hanesch U, Fischbach KF, Heisenberg M (1989) Neuronal architecture of the central complex in *Drosophila melanogaster*. Cell Tissue Res 257:343-366. https://doi.org/10.1007/BF00261838

Hardcastle BJ, Omoto JJ, Kandimalla P, Nguyen BCM, Keleş MF, Boyd NK, Hartenstein V, Frye MA (2021) A visual pathway for skylight polarization processing in *Drosophila*. eLife 10:e63225. https://doi.org/10.7554/eLife.63225

Heinze S, Homberg U (2007) Maplike representation of celestial *E*-vector orientations in the brain of an insect. Science 315:995-997. https://doi.org/10.1126/science.1135531

Heinze S, Homberg U (2008) Neuroarchitecture of the central complex of the desert locust: intrinsic and columnar neurons. J Comp Neurol 511:454-478. https://doi.org/10.1002/cne.21842

Heinze S, Homberg U (2009) Linking the input to the output: New sets of neurons complement the polarization vision network in the locust central complex. J Neurosci 29:4911-4921. https://doi.org/10.1523/JNEUROSCI.0332-09.2009

Heinze S, Reppert M (2011) Sun compass integration of skylight cues in migratory

monarch butterflies. Neuron 69:345-358. https://doi.org/10.1016/j.neuron.2010.12.025

Heinze S, Florman J, Asokaraj A, el Jundi B, Reppert SM (2013) Anatomical basis of sun compass navigation II: the neuronal composition of the central complex of the monarch butterfly. J Comp Neurol 521:267-298. https://doi.org/10.1002/cne.23214

Henze MJ, Labhart T (2007) Haze, clouds and limited sky visibility: polarotactic orientation of crickets under difficult stimulus conditions. J Exp Biol 210:3266-3276. https://doi.org/10.1242/jeb.007831

Homberg U, Hofer S, Pfeiffer K, Gebhardt S (2003) Organization and neural connections of the anterior optic tubercle in the brain of the locust, *Schistocerca gregaria*. J Comp Neurol 468:415-430. https://doi.org/10.1002/cne.10771

Homberg U, Heinze S, Pfeiffer K, Kinoshita M, el Jundi B (2011) Central neural coding of sky polarization in insects. Phil Trans R Soc B 366:680-687. https://doi.org/10.1098/rstb.2010.0199

Honkanen AE, Adden A, da Silva Freitas J, Heinze S (2021) The insect central complex and the neural basis of navigational strategies. J Exp Biol 222:jeb188854. https://doi.org/10.1242/jeb.188854.

Hulse BK, Haberkern H, Franconville R, Turner-Evans DB, Takemura S, Wolff T et al. (2021) A connectome of the *Drosophila* central complex reveals network motifs suitable for flexible navigation and context-dependent action selection. BioRxiv 2020.12.08.413955. https://doi.org/10.1101/2020.12.08.413955

Kinoshita M, Pfeiffer K, Homberg U (2007) Spectral properties of identified polarized-light sensitive interneurons in the brain of the desert locust *Schistocerca gregaria*. J Exp Biol 210:1350-1361. https://doi.org/10.1242/jeb.02744

Labhart T (1988) Polarization-opponent interneurons in the insect visual system. Nature 331:435-437. https://doi.org/10.1038/331435a0

Labhart T (1996) How polarization-sensitive interneurones of crickets perform at low degrees of polarization. J Exp Biol 199:1467-1475. https://doi.org/10.1242/jeb.199.7.1467

Labhart T (1999) How polarization-sensitive interneurons of crickets see the polarization pattern of the sky: A field study with an opto-electronic model neurone. J Exp Biol 201:757-770.

Labhart T, Meyer EP (1999) Detectors for polarized skylight in insects: a survey of ommatidial specializations in the dorsal rim area of the compound eye. Microsc Res Tech 47:368-379. https://doi.org/10.1002/(SICI)1097-0029(19991215)47:6<368::AID-JEMT2>3.0.CO;2-Q

Labhart T, Petzold J, Helbling H (2001) Spatial integration in polarization-sensitive interneurones of crickets: a survey of evidence, mechanisms and benefits. J Exp Biol 204:2423-2430. https://doi.org/10.1242/jeb.204.14.2423

Mappes M, Homberg U (2004) Behavioral analysis of polarization vision in tethered flying locusts. J Comp Physiol A 190:61-68. https://doi.org/10.1007/s00359-003-0473-4

Okubo TS, Patella P, D'Alessandro I, Wilson RI (2020) A neural network for wind-guided compass navigation. Neuron 107:924-940.e18. https://doi.org/10.1016/j.neuron.2020.06.022

Pegel U, Pfeiffer K, Zittrell F, Scholtyssek C, Homberg U (2019) Two compasses in the central complex of the locust brain. J Neurosci 39:3070-3080. https://doi.org/10.1523/JNEUROSCI.0940-18.2019

Pfeiffer K, Negrello M, Homberg U (2011) Conditional perception under stimulus ambiguity: polarization- and azimuth-sensitive neurons in the locust brain are inhibited by low degrees of polarization. J Neurophysiol 105:28-35. https://doi.org/10.1152/jn.00480.2010

Pisokas I, Heinze S, Webb B (2020) The head direction circuit of two insect species. eLife 9:e53985. https://doi.org/10.7554/eLife.53985

Reppert SM, Zhu H, White RH (2004) Polarized light helps monarch butterflies to navigate. Curr Biol 14:155-158. https://doi.org/10.1016/j.cub.2003.12.034

Sakura M, Lambrinos D, Labhart T (2007) Polarized skylight navigation in insects: model and electrophysiology of e-vector coding by neurons in the central complex. J Neurophysiol 99:667-682. https://doi.org/10.1152/jn.00784.2007

Seelig JD, Jayaraman V (2015) Neural dynamics for landmark orientation and angular path integration. Nature 521:186-191. https://doi.org/10.1038/nature14446

Sommer S, Wehner R, (2005) Vector navigation in desert ants, *Cataglyphis fortis*: celestial compass cues are essential for the proper use of distance information. Naturwissenschaften 92:468-471. https://doi.org/10.1007/s00114-005-0020-y

Stalleicken J, Mukhida M, Labhart T, Wehner R, Frost B, Mouritsen H (2005) Do monarch butterflies use polarized skylight for migratory orientation? J Exp Biol 208:2399-2408. https://doi.org/10.1242/jeb.01613

Strutt, JW (1871) XV. On the light from the sky, its polarization and colour. Phil Mag 41:107–120 & 274-279.

Varga AG, Kathman ND, Martin JP, Guo P, Ritzmann RE (2017) Spatial navigation and the central complex: sensory acquisition, orientation, and motor control. Front Behav Neurosci 11:4. https://doi.org/10.3389/fnbeh.2017.00004

von Frisch K (1949) Die Polarisation des Himmelslichtes als orientierender Faktor bei den Tänzen der Bienen. Experientia 5:142-148. http://dx.doi.org/10.1007/bf02174424

von Frisch K (1967) The dance language and orientation of bees. Cambridge, MA, USA, Harvard University Press.

von Hadeln J, Hensgen R, Bockhorst T, Rosner R, Heidasch R, Pegel U, Pérez MQ, Homberg U (2020) Neuroarchitecture of the central complex of the desert locust: Tangential neurons. J Comp Neurol 528:906-934. https://doi.org/10.1002/cne.24796

Zar JH (1999) Biostatistical analysis, 4th ed. Upper Saddle River, N.J.: Prentice Hall.

Zittrell F (2019) CircHist: Circular histogram in MATLAB. Available at: https://github.com/zifredder/CircHist.

Zittrell F, Pfeiffer K, Homberg U (2020) Matched-filter coding of sky polarization results in an internal sun compass in the brain of the desert locust. Proc Natl Acad Sci USA 117:25810-25817. https://doi.org/10.1073/pnas.2005192117

FIGURE LEGENDS

Fig 1 a Schematic representation of the polarization pattern of the sky as seen from the center of the sphere (orange) at a solar elevation of 40°. Double arrows indicate angles of polarization (AoP) that are arranged tangentially along concentric circles around the sun (yellow). Numbers indicate the degree of polarization (DoP). Under optimal atmospheric conditions the DoP increases with angular distance from the sun up to a maximum value of 0.75 at 90° from the sun. **b, c** Schematic illustration of tangential neurons (b) and columnar neurons (c) of the locust central complex. Fine branches indicate dendritic arborizations and small dots indicate axonal terminals. CBL, lower division of the central body; CBU, upper division of the central body; GA, gall; LAL, lateral accessory lobe; LBU, lateral bulb; MBU, medial bulb; PB, protocerebral bridge; POTU, posterior optic tubercle. **a** from Homberg et al. (2011) and Pfeiffer et al. (2011), **b, c** modified from Pegel et al. (2019) and Zittrell et al. (2020).

Fig 2 a Schematic illustration of the stimulus setup. Unpolarized light emitted by a light-emitting diode (LED) was linearly polarized by a polarizer. Diffusors were placed between the LED and the polarizer or between the polarizer and the animal to achieve different degrees of polarization (DoPs). With four diffusors between the LED and the polarizer (small image inset) maximally polarized light (DoP = 0.99) was generated. The degree and angle of polarization were measured via a photodiode/transimpedance amplifier placed behind a polarization filter. **b** Spike train showing the response of a CL1a neuron to two full rotations of the polarizer in clockwise and counterclockwise direction (0°-360°, 360°-0°). The blue bar indicates the time window during which polarized blue light was presented. The mean spiking frequency is indicated as moving average with a window size of 1 s above the spike train.

Fig 3 a Spike trains of a CL1a neuron in response to full clockwise- and counterclockwise polarizer rotations when stimulated with different degrees of polarization (DoP). The duration of the light stimulus is indicated by the blue bars. Ramps indicate 360° rotations of the polarizer, the angle of polarization (AoP) is not indicated by the ramps, as it is shifted depending on the arrangement of diffusors. **b** Circular histograms showing the firing rate (blue bars) during two polarizer rotations at five different DoPs. Black bars indicate standard deviations. If the firing rate was statistically significantly correlated with the AoP, the orange line indicates the preferred angle of polarization with the black portion indicating the resultant vector length. Black circles indicate median background activity (solid line) and the lower and upper 2.5 percentile (dashed lines) of the background activity. **c** Projection view of the CL1a neuron with arborizations in the protocerebral bridge (PB), the lower division (CBL) of the central body and the gall (GA). CBU, upper division of the central body. Scale bar = 50 µm.

Fig 4 a Summary of significant (grey portion of bars) versus non-significant (white portion of bars) responses of different cell types at different degrees of polarization (DoP). All neurons responded significantly at DoPs of 0.99 and 0.35. At DoPs of 0.1 and 0.05 some neurons of each cell type showed significant responses, whereas others did not respond. At a DoP of 0.002 no neuron showed a significant response. **b** The mean vector length *r*, i.e. the directedness of responses increased with increasing DoP in all cell types. The regression lines are shown in red. The solid blue lines indicate the means of the no-stimulus data, the dashed blue lines indicate the respective lower and the upper 95% confidence limits. Vertical black lines mark the stimulus at which the *r*-values of all responses exceed the upper 95% confidence limit of the estimated average *r*-value of the no-stimulus controls. Blue dots are no-stimulus data points, grey dots are non-significant responses, grey dots with blue outline indicate non-significant responses that lie within the confident limits of the no-stimulus data. Black dots are significant-responses. Black dots with blue outline indicate significant-responses that lie within the confident limits of the no-stimulus data.

Fig 5 The absolute response amplitude *A* increases with increasing degree of polarization in all cell types. The regression lines are shown in red. The solid blue lines indicate the mean of the no-stimulus data, the dashed blue lines indicate the respective lower and the upper 95% confidence limits. Blue dots are no-stimulus data points, grey dots are non-significant responses, grey dots with blue outline indicate non-significant responses that lie within the confident limits of the no-stimulus data. Black dots are significant-responses. Black dots with blue outline indicate significant-responses that lie within the confident limits of the no-stimulus data. Vertical black lines mark the stimulus at which the *A*-values of all responses exceed the upper 95% confidence limit of the estimated average *A*-value of the no-stimulus controls.

Fig 6 The average firing activity during stimulation with a rotating polarizer was positively correlated with the degree of polarization (DoP) in TL2 neurons and negatively correlated with the DoP in CL1 neurons. In TL3, TB1 and CPU neurons the average firing activity was not correlated with the DoP. The regression lines are shown in red. The solid blue lines indicate the mean of the no-stimulus data, the dashed blue lines indicate the respective lower and the upper 95% confidence limits. Blue dots are no-stimulus data points, grey dots are non-significant responses, grey dots with blue outline indicate non-significant responses that lie below the upper confidence limit of the no-stimulus data. Black dots are significant-responses. Black dots with blue outline indicate significant-responses that lie below the upper confident limit of the no-stimulus data.

Fig 7 Activity of individual neurons at Φ_{max} (orange) and Φ_{min} (blue) during responses to a rotating polarizer at different degrees of polarization (DoP). Activity is normalized to background activity of a 5 s interval (median value of 1-s-binned spike rate averages) preceding each stimulus. The grey lines indicate background activity. Dots indicate significant responses, whereas circles indicate non-significant responses. The bold lines indicate the averaged activity of all neurons at Φ_{max} and Φ_{min}, respectively.

Fig 8 Responses of a TL2 neuron to polarizer rotations with the lowest degree of polarization (DoP = 0.002) and the highest degree of polarization (DoP = 0.99). The blue bars indicate the time windows during which polarized blue light was presented. Ramps indicate 360° rotations of the polarizer. Covering the DRA of both eyes abolished the polarization response, the excitation during low DoPs, and the inhibitory rebound at lights off (arrowheads). Uncovering the DRAs restored the responses.

Fig 9 Responses of a TL2 neuron to polarizer rotations with the lowest degree of polarization (DoP = 0.002) and highest degree of polarization (DoP = 0.99). The blue bars indicate the time windows during which polarized blue light was presented. Ramps indicate 360° rotations of the polarizer. Covering the DRA of both eyes abolished the polarization response, the inhibition during low DoPs and the excitatory rebound after the stimulus (arrowheads). Uncovering the DRAs restored the responses.

Fig 10 Responses of three different CL1 neurons to the lowest degree of polarization (DoP = 0.002). The blue bars indicate the time windows during which polarized blue light was presented. Ramps indicate 360° rotations of the polarizer. **a** This CL1 neuron responded with slightly elevated activity preceded by phasic inhibition at lights on. Phasic rebound inhibition occurs at lights off. **b** This CL1 neuron responded with excitation to the stimulus, followed by rebound inhibition at lights off. **c** This CL1 neuron displayed phasic excitation at lights on.

Fig 11 Responses of three different TB1 neurons to the lowest degree of polarization (DoP = 0.002). The blue bars indicate the time windows during which polarized blue light was presented. Ramps indicate 360° rotations of the polarizer. **a** This TB1 neurons showed slight excitation during stimulus presentation and rebound inhibition at lights off. **b** This TB1 neuron showed no change in activity during stimulus presentation. **c** This TB1 neurons displayed phasic excitation at lights off.

Fig 12 Responses of three different CPU neurons to the lowest degree of polarization (DoP = 0.002). The blue bars indicate the time windows during which polarized blue light was presented. Ramps indicate 360° rotations of the polarizer. **a** This CPU neuron was slightly inhibited during stimulus presentation, and rebound excitation occurred at lights off. **b** This CPU neuron displayed phasic excitation at lights on and at lights off. **c** This CPU neuron showed no change in activity during stimulus presentation.

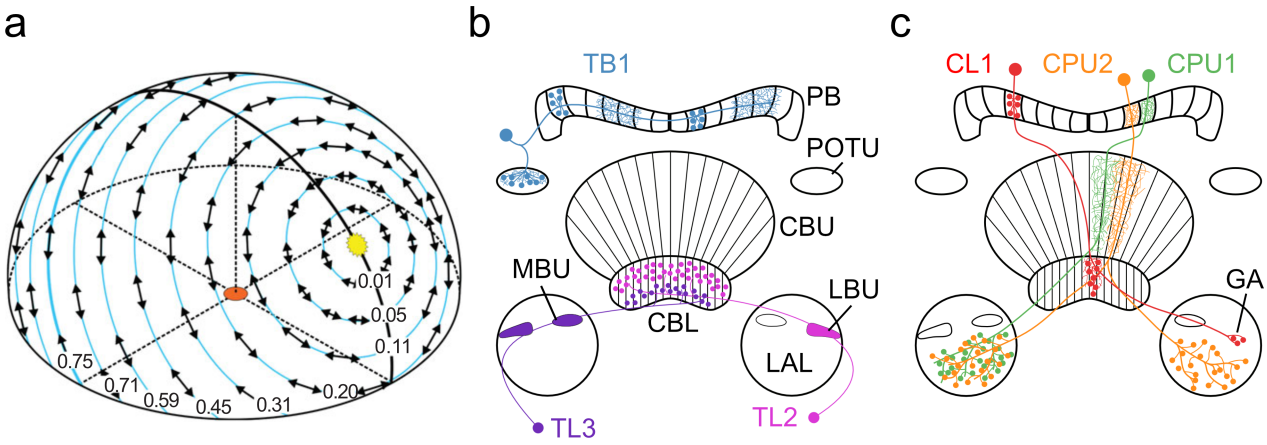

FIGURE 1

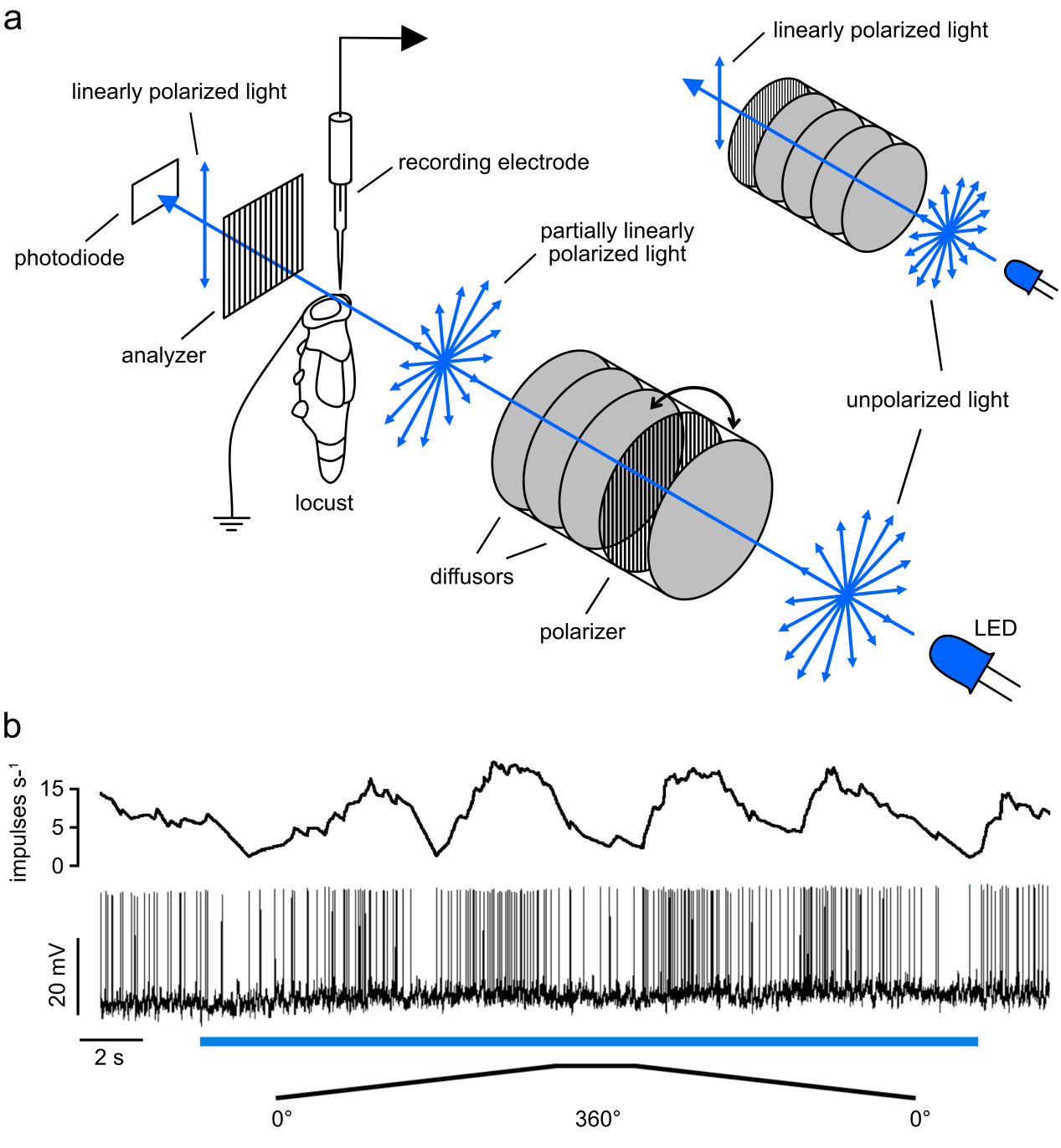

FIGURE 2

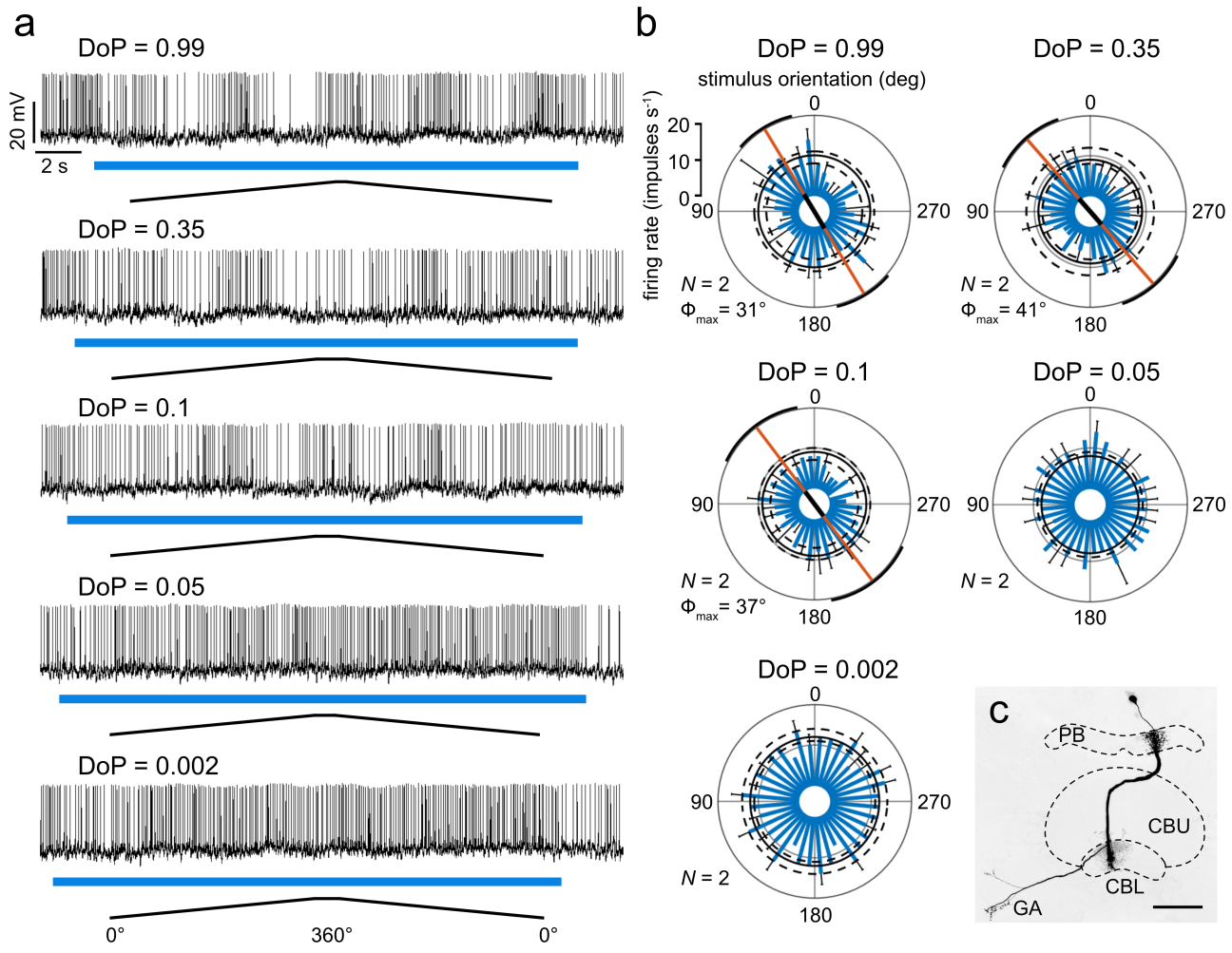
a
DoP = 0.99
20 mV
2 s
DoP = 0.35
DoP = 0.1
DoP = 0.05
DoP = 0.002
0°
360°
0°
b
DoP = 0.99
stimulus orientation (deg)
firing rate (impulses s⁻¹)
20
10
0
0
90
270
180
N = 2
Φmax = 31°
DoP = 0.35
N = 2
Φmax = 41°
DoP = 0.1
N = 2
Φmax = 37°
DoP = 0.05
N = 2
DoP = 0.002
N = 2
c
PB
CBU
CBL
GA

FIGURE 3

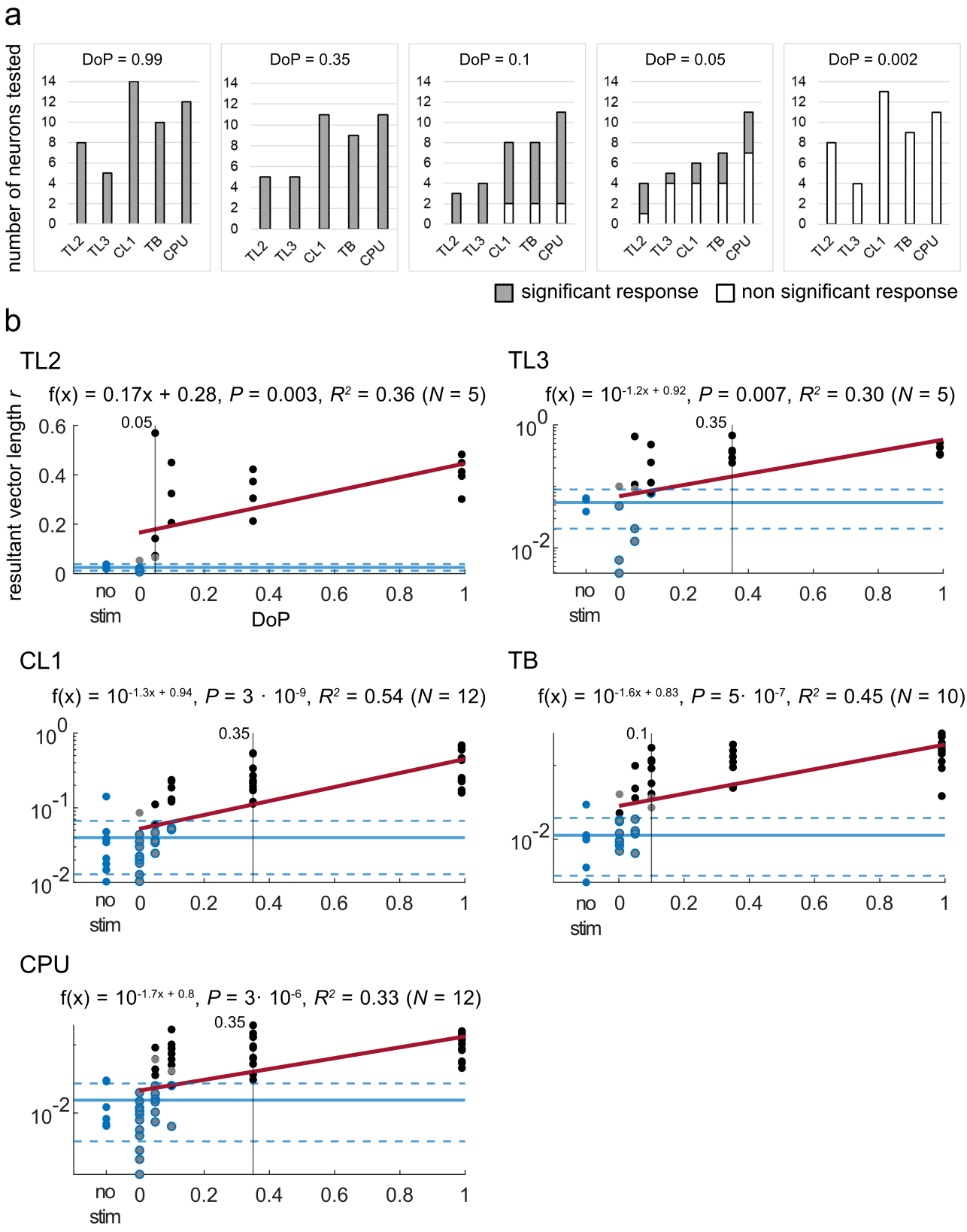
a
number of neurons tested
DoP = 0.99
DoP = 0.35
DoP = 0.1
DoP = 0.05
DoP = 0.002
TL2
TL3
CL1
TB
CPU
significant response
non significant response
b
TL2
f(x) = 0.17x + 0.28, P = 0.003, R² = 0.36 (N = 5)
resultant vector length r
TL3
f(x) = 10^-1.2x + 0.92, P = 0.007, R² = 0.30 (N = 5)
CL1
f(x) = 10^-1.3x + 0.94, P = 3 · 10^-9, R² = 0.54 (N = 12)
TB
f(x) = 10^-1.6x + 0.83, P = 5· 10^-7, R² = 0.45 (N = 10)
CPU
f(x) = 10^-1.7x + 0.8, P = 3· 10^-6, R² = 0.33 (N = 12)
no stim
DoP

FIGURE 4

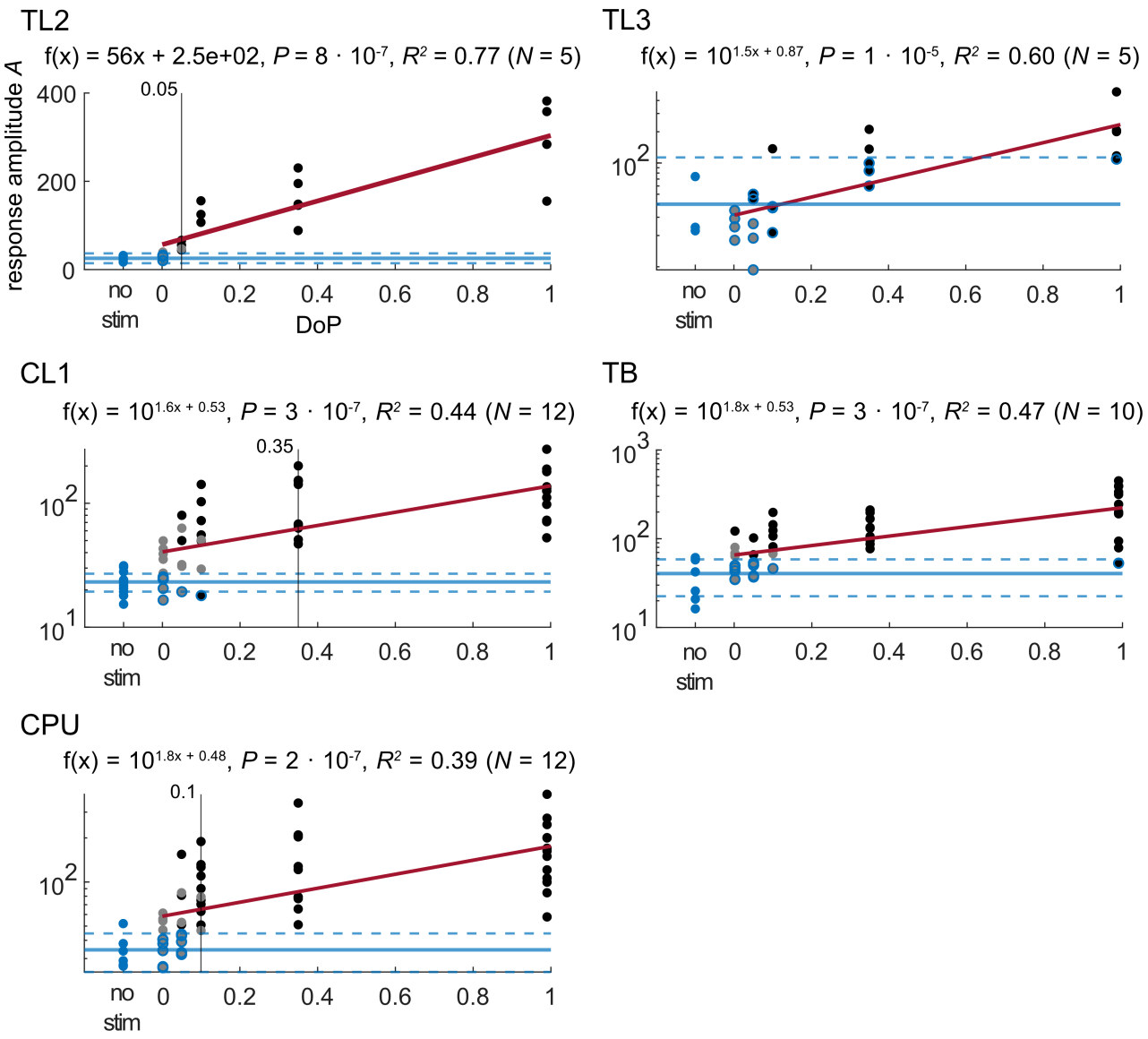
TL2
f(x) = 56x + 2.5e+02, P = 8 · 10^-7, R^2 = 0.77 (N = 5)
response amplitude A
400
200
0
0.05
no stim
0
0.2
0.4
0.6
0.8
1
DoP
TL3
f(x) = 10^1.5x + 0.87, P = 1 · 10^-5, R^2 = 0.60 (N = 5)
10^2
CL1
f(x) = 10^1.6x + 0.53, P = 3 · 10^-7, R^2 = 0.44 (N = 12)
0.35
10^2
10^1
TB
f(x) = 10^1.8x + 0.53, P = 3 · 10^-7, R^2 = 0.47 (N = 10)
10^3
10^2
10^1
CPU
f(x) = 10^1.8x + 0.48, P = 2 · 10^-7, R^2 = 0.39 (N = 12)
0.1
10^2

FIGURE 5

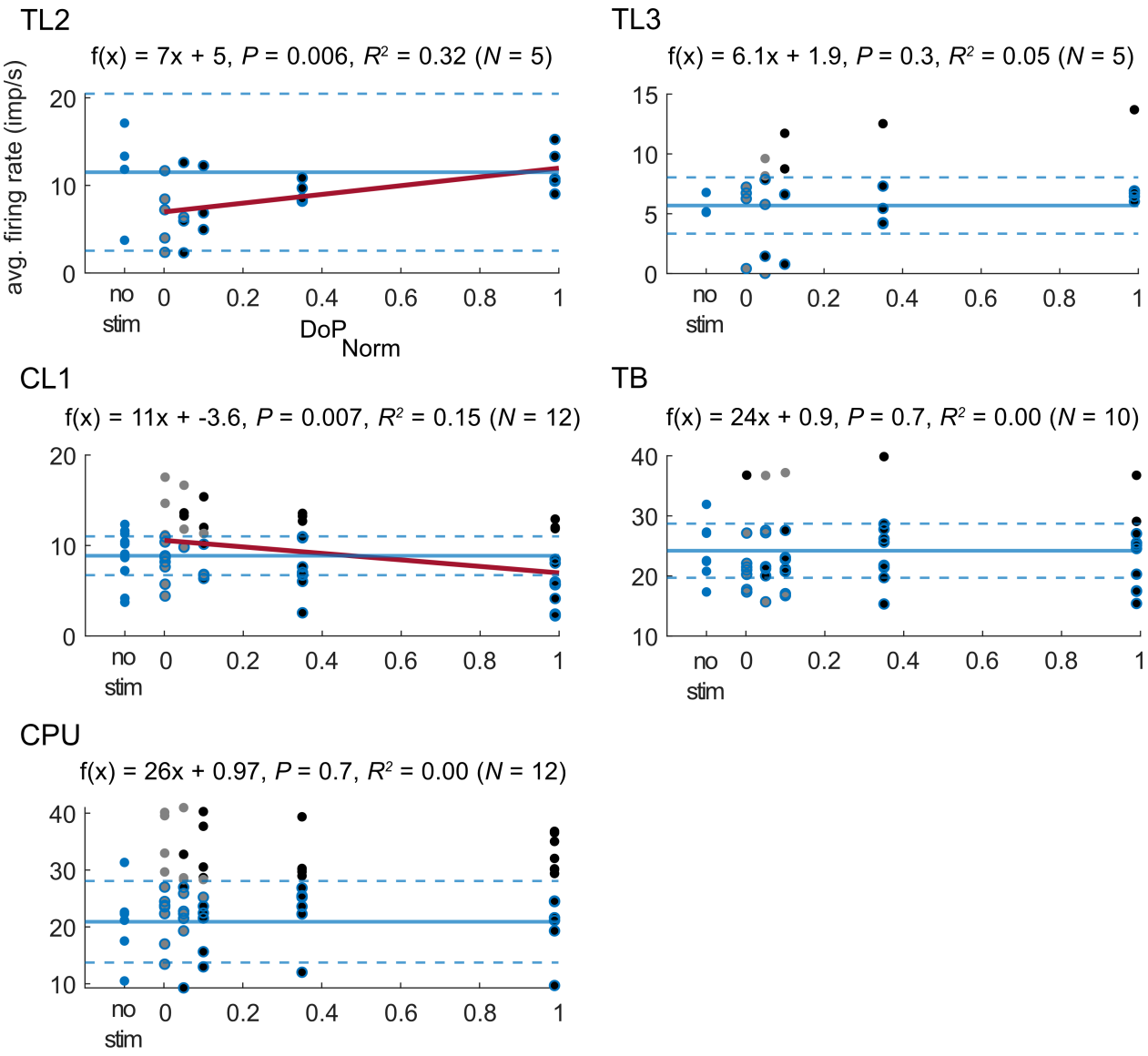
TL2
f(x) = 7x + 5, P = 0.006, R² = 0.32 (N = 5)
avg. firing rate (imp/s)
20
10
0
no stim
0
0.2
0.4
0.6
0.8
1
DoP Norm
TL3
f(x) = 6.1x + 1.9, P = 0.3, R² = 0.05 (N = 5)
15
10
5
0
CL1
f(x) = 11x + -3.6, P = 0.007, R² = 0.15 (N = 12)
TB
f(x) = 24x + 0.9, P = 0.7, R² = 0.00 (N = 10)
40
30
20
10
CPU
f(x) = 26x + 0.97, P = 0.7, R² = 0.00 (N = 12)

FIGURE 6

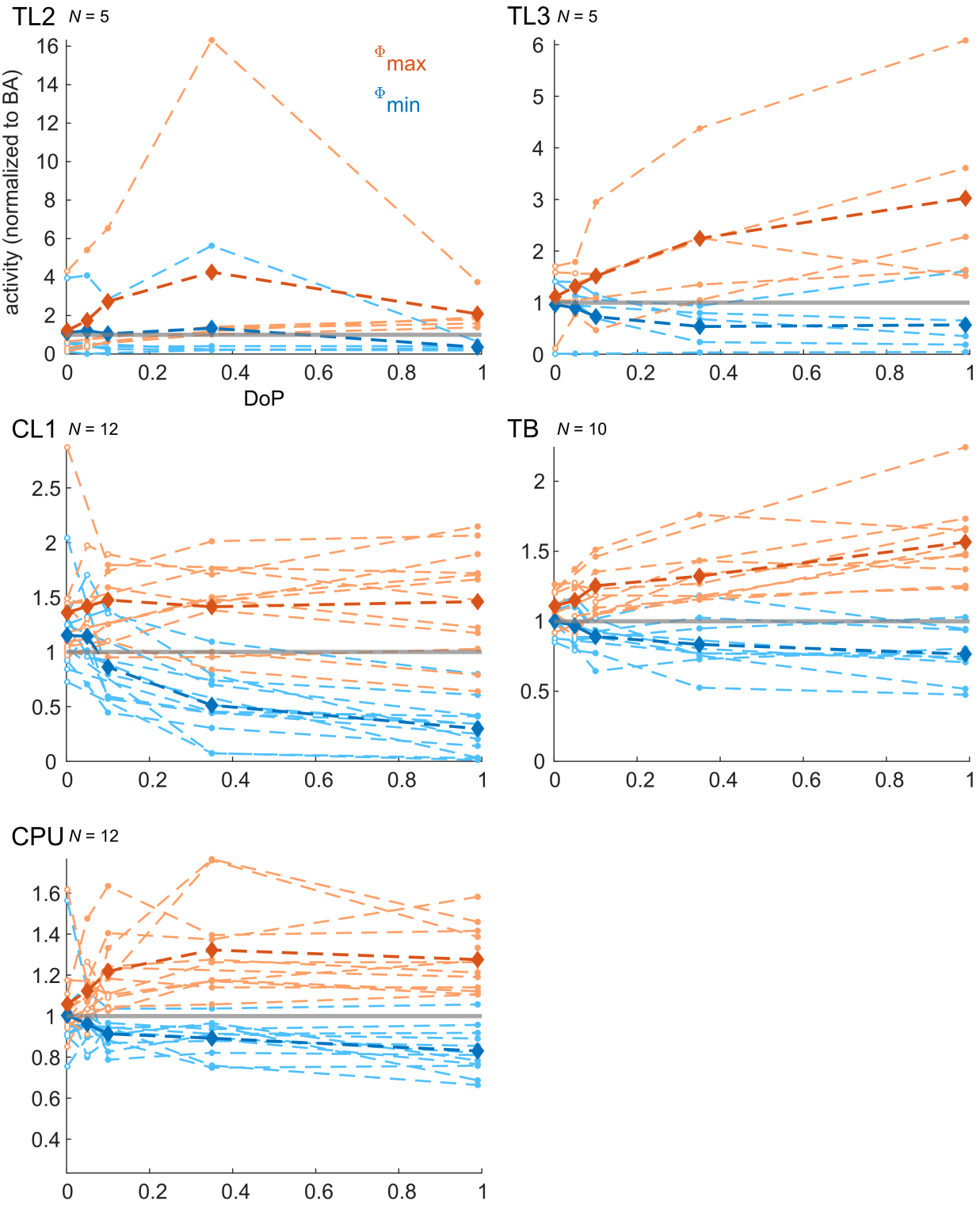
TL2 N = 5
TL3 N = 5
CL1 N = 12
TB N = 10
CPU N = 12
Φmax
Φmin
activity (normalized to BA)
DoP

FIGURE 7

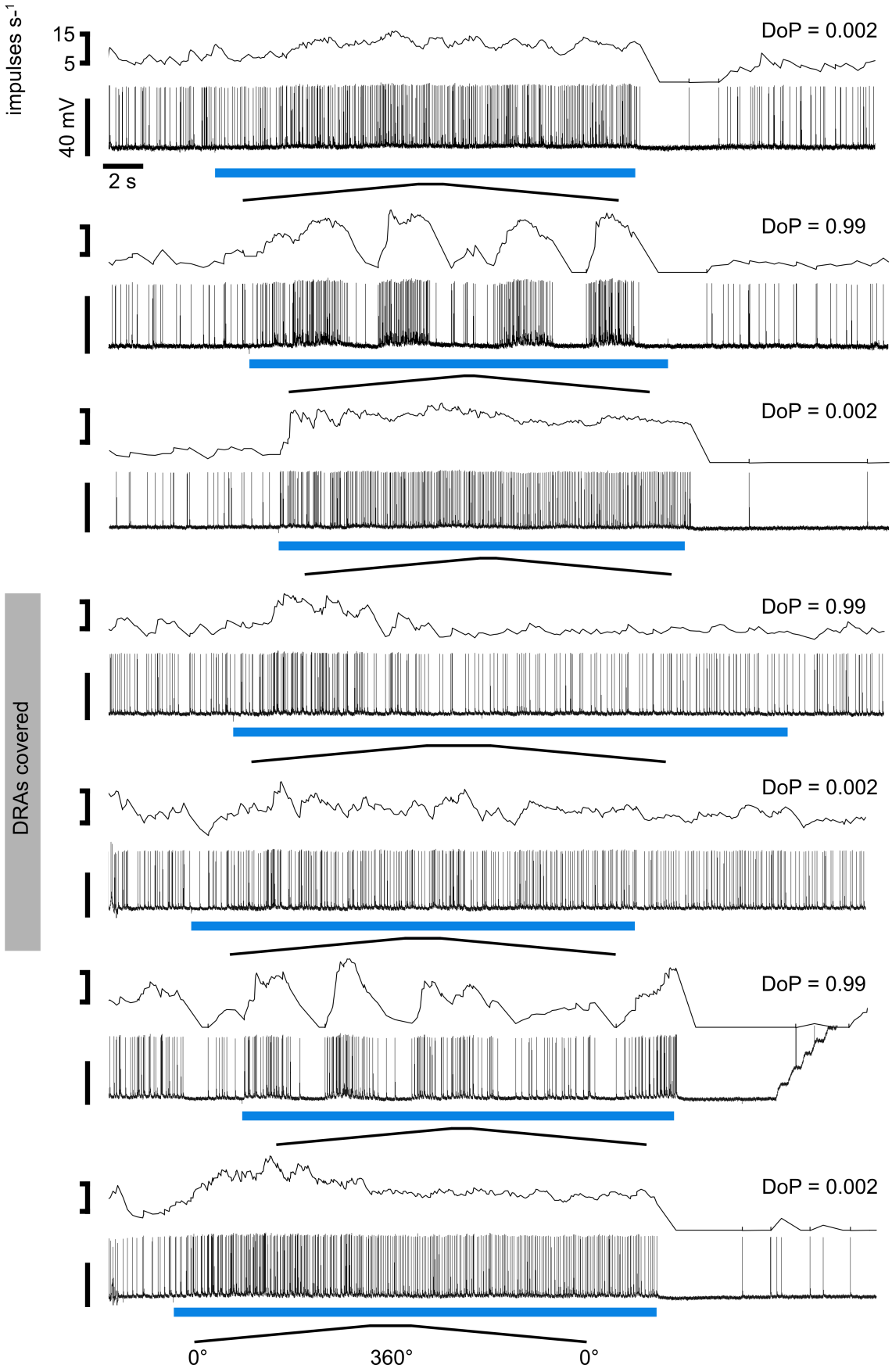
impulses s-1
15
5
40 mV
2 s
DoP = 0.002
DoP = 0.99
DoP = 0.002
DRAs covered
DoP = 0.99
DoP = 0.002
DoP = 0.99
DoP = 0.002
0°
360°
0°

FIGURE 8

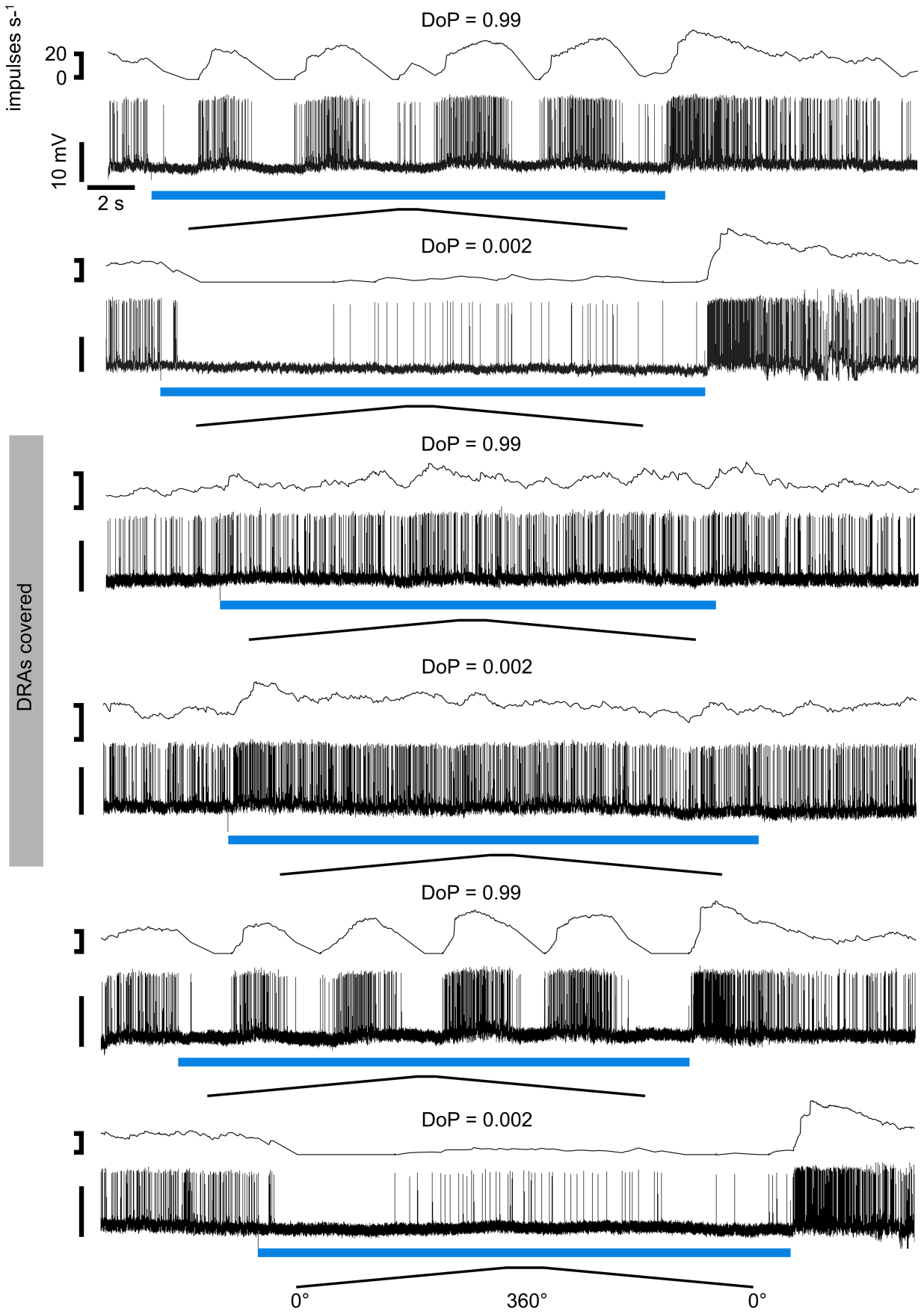
impulses s-1
20
0
10 mV
2 s
DoP = 0.99
DoP = 0.002
DoP = 0.99
DoP = 0.002
DRAs covered
DoP = 0.99
DoP = 0.002
0°
360°
0°

FIGURE 9

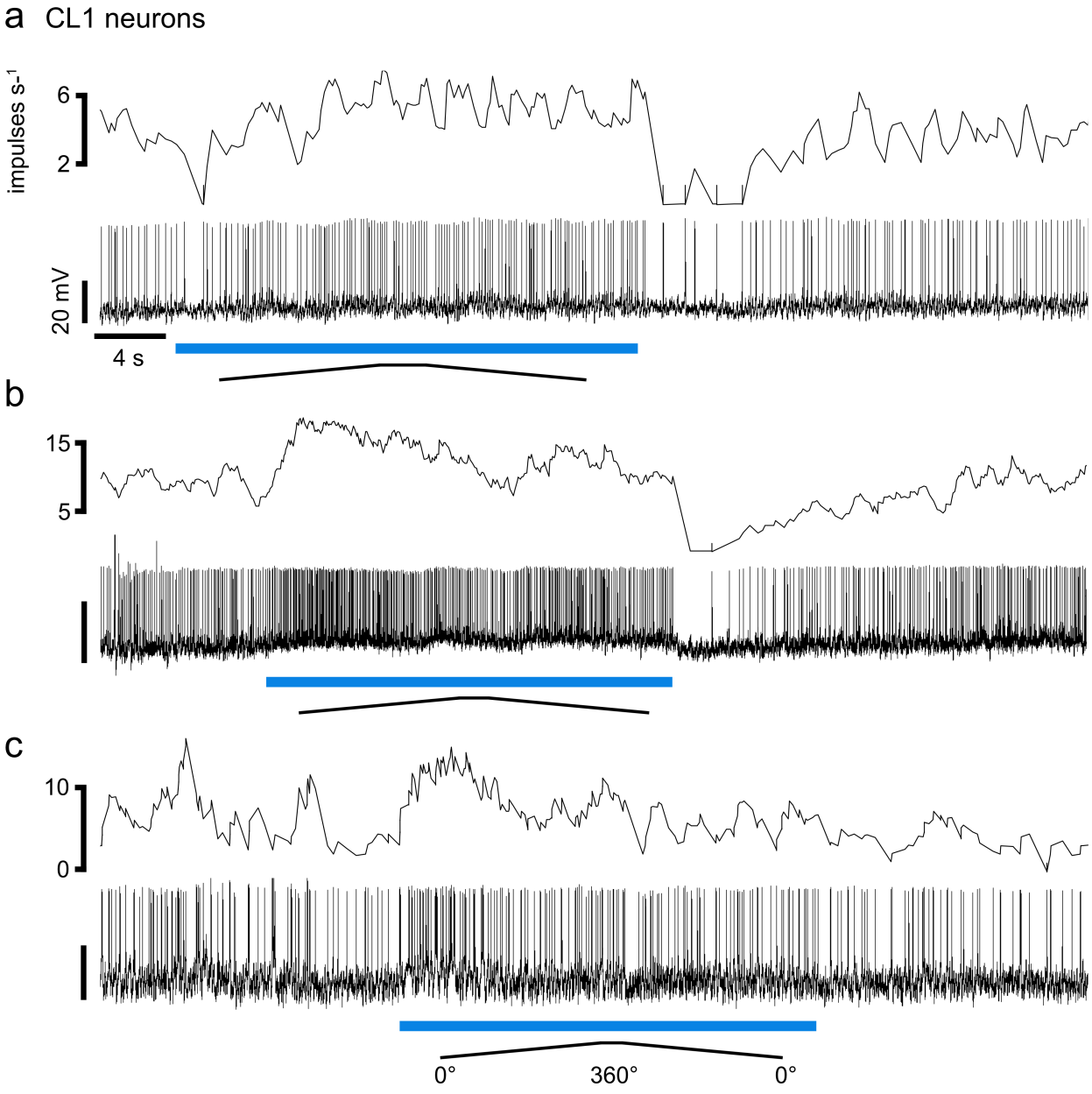

FIGURE 10

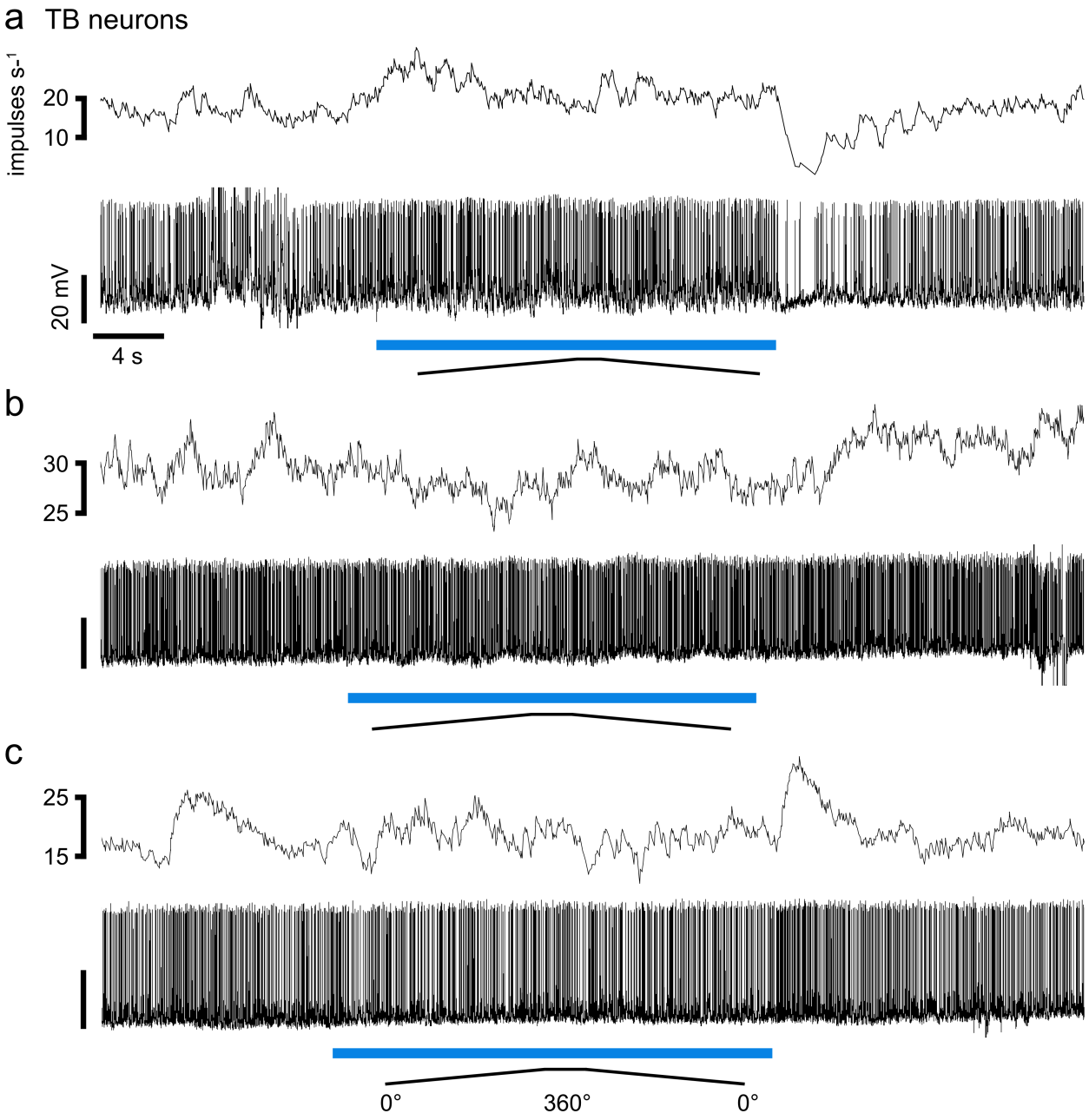

FIGURE 11

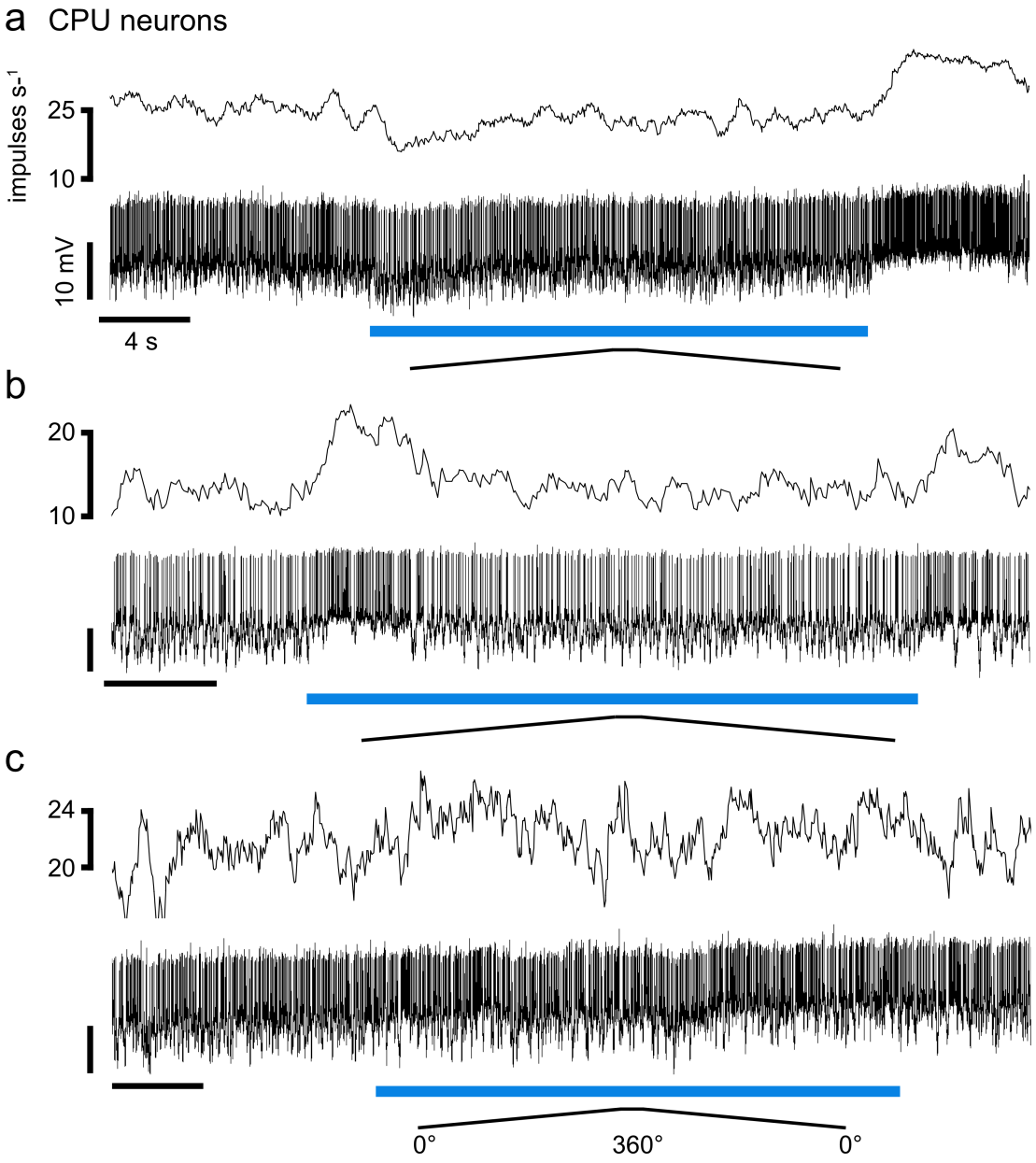

FIGURE 12

Chapter 5

Flexible Integration of Visual Self-Motion Cues in Locust Central Complex Neurons

Flexible integration of visual self-motion cues in locust central-complex neurons

Abbreviated title: Integration of visual self-motion

Frederick Zittrell[1,2], Elena Carlomagno[1], Kathrin Pabst[2,3], Ronny Rosner[1], Dominik Endres[2,3], Uwe Homberg[1,2]*

[1]Department of Biology, Animal Physiology, Philipps-Universität Marburg, D-35032 Marburg, Germany

[2]Center for Mind, Brain and Behavior (CMBB), University of Marburg and Justus Liebig University Giessen

[3]Department of Psychology, Theoretical Cognitive Science, Philipps-Universität Marburg, D-35032 Marburg, Germany

*Corresponding author: Uwe Homberg, Fachbereich Biologie, Tierphysiologie, Philipps-Universität Marburg, D-35032 Marburg, Germany, Tel. +49-6421-2823402, E-mail: homberg@staff.uni-marburg.de

Number of pages: 25

Number of figures: 9

Number of tables: 2

Number of words for abstract: 250

Number of words for introduction: 570

Number of words for discussion: 1483

Conflict of interest: The authors declare no competing financial interests.

Acknowledgements: This work was supported by Deutsche Forschungsgemeinschaft (HO 950/28-1 to U. H. and EN 1152/3-1 to D. E.). We thank Dr. Uta Pegel for providing data and Martina Kern for maintaining locust cultures. Current affiliation of E. C.: Department of Psychiatry, Philipps-Universität Marburg, Marburg, Germany.

Abstract

Flexible orientation through any environment requires a sense of current relative heading that is updated based on self-movement. Global external cues originating from the sky or the earth`s magnetic field and local cues provide a reference frame for the sense of direction. Locally, optic flow may inform about turning maneuvers, travel speed and covered distance. The central complex in the insect brain is associated with orientation behavior and largely acts as a navigation center. Visual information from global celestial cues and local landmarks are integrated in the central complex to form an internal representation of current heading. However, it is still unclear which neurons integrate optic flow in the central-complex network. We recorded intracellularly from neurons in the locust central complex while presenting lateral grating patterns that simulated translational and rotational motion in order to identify these sites of integration. Central-complex neurons of various type were sensitive to visual self-motion independent of the type and direction of simulated motion. Sensitivity to visual self-motion was widely uncoupled from celestial cue sensitivity, showing that central-complex neurons can flexibly integrate different cues. Columnar neurons innervating the noduli, paired central-complex substructures, were tuned to the direction of simulated horizontal turns. Modelling the connectivity of these neurons with a system of proposed compass neurons can account for rotation-direction specific shifts in the activity profile in the central complex corresponding to turn direction. Our model is similar but not identical to the mechanisms proposed for angular velocity integration in the navigation compass of the fly *Drosophila*.

Significance statement

For successful navigation, animals need to combine allothetic cues like the solar azimuth with idiothetic cues like optic flow. The navigation center in the insect brain, the central complex (CX), computes current heading direction and initiates movement. To examine where optic flow is integrated in the CX, we recorded intracellularly from various neurons of the locust CX and stimulated with visually simulated self-motion and celestial cues. We found high variability in visual self-motion sensitivity, widely uncoupled from skylight cue sensitivity, suggesting flexible integration. Specific neurons were tuned to the direction of simulated horizontal turns. Modelling the connectivity of these neurons with proposed compass neurons resulted in a network that is suited to integrate angular rotation into the internal compass.

Introduction

Animals navigate in order to feed, escape, migrate, and reproduce. Any navigational task requires a sense of current travel direction, which must be anchored to external cues and updated by internal cues, self-generated by movement. Celestial cues are used as external cues by many insects, such as bees (von Frisch, 1946), ants (Fent, 1986), butterflies (Perez et al., 1997), dung beetles (Byrne et al., 2003), fruit flies (Weir and Dickinson, 2012) and caterpillars (Uemura et al., 2021): The sun and the skylight polarization pattern provide a

reliable reference for dead reckoning (Gould, 1998). Internal cues, such as proprioceptive feedback (Wittlinger et al., 2006) and optic flow (Srinivasan, 2015; Stone et al., 2017), provide information about traveling speed and covered distance and may update the inner sense of direction in the absence of external cues. Only the flexible combination of information from external and internal cues enables robust and efficient navigation behavior, such as path integration (Heinze et al., 2018).

The central complex (CX), a midline spanning group of neuropils, houses the internal sense of direction in the brain of insects. It consists of the protocerebral bridge (PB), the lower (CBL) and upper (CBU) division of the central body, also termed ellipsoid- and fan-shaped body, and a pair of layered noduli (NO), and is associated with learning, memory and, importantly, spatial orientation (Pfeiffer and Homberg, 2014). CX neurons in various insect species are tuned to celestial cues (Heinze, 2017; Honkanen et al., 2019) and encode the solar azimuth in a compass-like manner in the locust (Pegel et al., 2019; Zittrell et al., 2020). Silencing compass neurons in the CX impairs navigation behavior in the fruit fly (Giraldo et al., 2018), showing the necessity of the CX for behavior. Like mammalian head direction cells (Taube, 1998, 2007), specific CX neuron populations are tuned to the animal's current heading (Seelig and Jayaraman, 2015; Hulse and Jayaraman, 2020). This internal heading estimate is multimodally tethered to environmental cues, such as visual compass cues and wind direction (Okubo et al., 2020), but also operates without external cues, because internal cues from self-movement are likewise integrated (Green et al., 2017; Turner-Evans et al., 2017; Green and Maimon, 2018).

Although the understanding of the CX network has made considerable progress, mainly owing to fruit fly research, and plausible models explaining network computations for navigation have been proposed (Stone et al., 2017), it is yet unclear at which network stages optic flow input is integrated with celestial cues. In order to investigate this, we recorded intracellularly from various CX neurons in the desert locust (Schistocerca gregaria), a long-distance migratory insect, while stimulating laterally with wide-field visual motion that simulated self-movement to the animal. We analyzed general motion sensitivity for translational and rotational self-motion directions and asked whether the neural responses to opposing motion directions were discriminated (direction selectivity). Additionally, we tested the neurons for sensitivity to celestial cues, namely azimuthal preference for a green or UV light spot that simulated the sun and angular preference for the polarization angle of blue light, simulating skylight polarization, in order to examine the association between celestial cue sensitivity and visual motion sensitivity. Guided by data on a particular type of neuron sensitive to the direction of simulated horizontal turns we implemented an algorithmic model (in the sense of Marr, 1982) of the central complex circuit which integrates visual self-motion cues with head direction representation and tested it in an agent simulation.

Materials and Methods

Animals and preparation

Desert locusts (*Schistocerca gregaria*) were kept and dissected as described previously (Zittrell et al., 2020). Animals were reared in large groups (gregarious state) at 28 °C with a 12 h / 12 h light / dark cycle; adult locusts from either sex were used for experiments. Limbs and wings were cut off, the animals were fixed on a metal holder with dental wax, and the head capsule was opened frontally, providing access to the brain. The esophagus was cut inside the head, close to the mandibles, and the abdomen's end was cut off in order to take out the whole gut through this opening. The brain was freed of fat, trachea and muscle tissue and was stabilized with a small metal platform that was fixed to the head capsule. Shortly before recording, the brain sheath was removed at the target site with forceps, permitting penetration with sharp glass electrodes. The brain was kept moist with locust saline (Clements and May, 1974) throughout the experiment.

Intracellular recording and histology

Sharp microelectrodes were drawn with a Flaming/Brown filament puller (P-97; Sutter Instrument), their tips filled with Neurobiotin tracer (Vector Laboratories; 4 % in 1 mol · l^{-1} KCl) and their shanks filled with 1 mol · l^{-1} KCl. Intracellular recordings were amplified with a custom-built amplifier and digitized with a 1401plus (Cambridge Electronic Device, CED) analog-digital converter (ADC) or amplified with a BA-01X (npi electronic GmbH) and digitized with a Micro1401 mkII with an ADC12 expansion unit (CED). Signals were monitored with a custom-built audio monitor and recorded with Spike2 (CED). Neurons were traced by electrically injecting Neurobiotin (~1 nA positive current for several minutes). Each neuron presented in this study originates from a different specimen. Brains were dissected and immersed in fixative (4 % paraformaldehyde, 0.25 % glutaraldehyde and 0.2 % saturated picric acid, diluted in 0.1 mol · l^{-1} phosphate buffered saline [PBS]) over night, followed by optional storage at 4 °C in sodium phosphate buffer until further processing. Brains were rinsed in PBS (4 × 15 min) and incubated with Cy3-conjugated streptavidin (Dianova; 1:1,000 in PBS with 0.3 % Triton X-100 [PBT]) for 3 d at 4 °C. After rinsing in PBT (2 × 30 min) and PBS (3 × 30 min), they were dehydrated in an ascending ethanol series (30 %, 50 %, 70 %, 90 %, 95 %, and 2 × 100 %, 15 min each) and cleared in a 1:1 solution of ethanol (100 %) and methyl salicylate for 20 min and in pure methyl salicylate for 35 min, to finally mount them in Permount (Fisher Scientific) between two coverslips. For anatomical analysis, brains were scanned with a confocal laser-scanning microscope (Leica TCS SP5; Leica Microsystems). Cy3 fluorescence was elicited with a diode-pumped solid-state laser at 561 nm wavelength. The resulting image stacks were processed with Fiji (Schindelin et al., 2012) and GIMP (gimp.org). The chirality of some neurons could not be determined because multiple neurons of the same neuron class but on both brain sides were stained in these cases.

Experimental Design and Statistical Analysis

Visual self-motion

We used two monitors (FT10TMB, 10“, 1024x768 px at 60 Hz, Faytech, Shenzhen, China) that were placed 12.7 cm apart on the left and right side of the animal. They were mounted vertically to present sinusoidal grayscale grating patterns (Fig. 1A). The displays were covered with diffuser sheets to eliminate light polarization inherent to LCD monitors. The patterns were drawn on the inner center-square (15.35 cm edge length) of the displays, covering 62.3° of the visual field on each side. The monitor brightness amounted to 1.12 · 1011 photons · cm-2 · s-1 when displaying a black area and 7.09 · 1013 photons · cm-2 · s-1 displaying a white area. Monitor brightness was measured using a digital spectrometer (USB2000; Ocean Optics) placed at the position of the locust head.

The grating patterns were animated in order to simulate self-motion to the animal. We tested translational (forward and backward) motion, yaw rotation (left and right turning), lift (upward and downward), and roll (counter clockwise and clockwise). Throughout this study, these direction labels refer to simulated self-motion directions and not absolute motion of the displayed patterns. Thus, “forward motion” means that both monitors displayed a grating pattern with horizontal bands (perpendicular to the locust’s body axis, cf. Fig. 1A), and both patterns continually moved from top to bottom. For the sake of readability, we use “visual motion” for this wide-field visual motion stimulation, although this term includes diverse visual stimulation types, such as looming objects, small moving targets or full-panoramic optic flow, neither of which we presented to the animals.

Each motion direction was tested in a series of trials; each trial consisted of two phases, a motion phase and an immediately following stationary phase. All phases in the same recording lasted for five or six seconds. Each series consisted of two to five trials; each trial was immediately followed by the next one, unless it was the last of the series. Neurons typically responded strongly to the pattern display switch between series. Therefore, each series of a given motion direction was preceded by an adaptation phase which was discarded; this phase was a single stationary phase of the same pattern used during the upcoming series, immediately followed by the first motion phase of the series. If the same motion direction was tested in more than one series, all trials were treated as if they belonged to the same series. Not all neurons could be tested for all motion directions due to recording instability.

A separate PC running MATLAB (R2019, MathWorks) with the Psychophysics toolbox (Brainard, 1997) was used to generate the grating patterns (Fig. 1). The sine gratings had a spatial resolution of 0.005 cycles · px^{-1} (one sine cycle spanned 200 px) and were shifted with 2 cycles · s^{-1} during the motion phases. This PC was USB-connected to an Arduino Uno (Arduino) via which TTL pulses were sent to the ADC, recorded at 500 Hz. These pulses indicated grating pattern animation and onset of stimulation phases. Two squares with 30 px edge length in the top left corner of each display were used to indicate the presented motion type by flashing them white: Each motion type was assigned a distinct

number of flashes (20 ms duration) that were generated at the end of the adaptation phase of each series. Each square was covered by a photo diode that picked up the white flashes and whose signal was recorded by the ADC at 200 Hz. This allowed for encoding the motion type of each stimulation series in the data file. The generation of each rectangle flash was also recorded via the Arduino as a TTL rectangle pulse of the same duration, which allowed for measuring the precise timing of stimulus display by cross correlating diode signal and TTL signal.

Celestial cues

We simulated celestial cues with LEDs that were mounted on a rotatable holder in the animal's dorsal field of view (Fig. 1A). The holder and LEDs were controlled in Spike2 via the ADC's sequencer and custom-built hardware. A blue LED (LXML-PR01-0500, Philips Lumileds, 447.5 nm, brightness $1.7 \cdot 10^{13}$ photons · cm-2 · s-1, visual angle 32.5°) with a polarization filter (HNP'B, Polaroid) in the animal's zenith (90° elevation) was used to test the recorded neuron for polarization sensitivity, which indicates whether it may take part in sky light polarization processing (el Jundi et al., 2014; Pegel et al., 2018). A full rotation of the polarizer resulted in a linear modulation of the presented angle of polarization (AoP) by 360°. A 0° AoP was defined as being parallel to the animal's longitudinal body axis.

A green (Oslon SSL 80 LT CP7P, Osram Opto Semiconductors, 527 nm, brightness 1 · 1014 photons · cm-2 · s-1, visual angle 16.3°) and a UV (NCSU033B(T), Nichia, 365 nm, brightness 1 · 1014 photons · cm-2 · s-1, visual angle 16.3°) LED were mounted at 45° elevation in the animal's dorsal visual field. A full rotation of the stimulation device resulted in a linear 360° modulation of the azimuthal angle of the light spot at constant elevation, 0° azimuth defined as directly in front of the animal. An angular preference of a neuron for a green or UV light spot suggests a role in sun compass coding (el Jundi et al., 2014; Pegel et al., 2018).

Celestial cues were tested separately from one another and with the lateral monitors showing black screens. Cue preference was tested in sets of at least three consecutive rotations of the same cue with alternating rotation directions, all at the same rotation velocity (40° · s^{-1} or 60° · s^{-1}). The first rotation of a set was discarded, because cue onset often provoked a phasic response. Equal numbers of both rotation directions were used per cue. Sets of control rotations were done with all LEDs switched off. Not all neurons could be tested for all cues due to recording instability.

Data evaluation

All visualization and analysis were done with custom written MATLAB scripts (R2019 onward, MathWorks). Circular histograms were created with the `CircHist` package (Zittrell, 2019).

Visual motion

Spikes were detected by median filtering (500 ms window width) the voltage signal and applying a manually chosen threshold. Spikes were binned in 250 ms intervals for rate

estimation and all rates with the same relative time within their trial were averaged, resulting in a single average firing rate trace during motion phase and stationary phase, per tested motion direction and experiment.

We analyzed motion sensitivity for each tested motion direction by directly comparing the binned firing rate values during the motion phase with those during the stationary phase using the Wilcoxon signed-rank test (MATLAB's `signrank`, $\alpha = 5\,\%$) with the relative bin time as pairing factor (Fig. 1C,D). We assigned a response score to each tested motion direction based on this firing rate comparison:

$$\text{Response score} = \begin{cases} -1 & \text{if } P_{A,B} < 0.05 \text{ and } FR_A < FR_B \\ +1 & \text{if } P_{A,B} < 0.05 \text{ and } FR_A > FR_B \\ 0 & \text{otherwise} \end{cases}, \quad (1)$$

where *A* and *B* are the phases to be compared, in this case the motion (*A*) and stationary (*B*) phase. *P* is the Wilcoxon signed-rank test's *P* value resulting from the statistical comparison and $FR_{A|B}$ is the median firing rate during the respective phase. Simply put: If there was a significant activity difference between phases *A* and *B*, the response score is `+1` if the activity was higher in *A* and `-1` if it was higher in *B*; non-significant differences are scored with `0`. Therefore, response scores for motion sensitivity indicate whether a single neuron responded to a specific motion direction and allow for comparison between neurons by indicating whether different neurons responded in the same manner.

We analyzed direction selectivity in four categories, each comprised of two opposing motion directions: translational motion (forward vs. backward direction), yaw rotation (left vs. right turning), lift (upward vs. downward), and roll (counter clockwise vs. clockwise). In order to compare firing rates of opposing directions, we needed to correct for potential drift in the neurons' baseline firing rate, because opposing directions were often tested several minutes apart in the course of the recording session. To this end we estimated the median firing rate from the averaged rates during the stationary phase and used this value as a baseline-correction coefficient by simply subtracting it from the firing rate trace values during the motion phase. This yielded baseline-corrected motion-response firing rates that clustered around 0 spikes/s if the neuron's activity was similar during the motion phase compared to the stationary phase; values >0 indicate that the activity was relatively higher during the motion phase and vice versa for values <0. Thus, these baseline-corrected firing rates represent a neuron's response to the presented pattern motion independent of slow baseline-activity drift and side effects caused by varying alignment and starting angle of the grating patterns.

Finally, we scored direction selectivity per motion category by statistically comparing the baseline-corrected firing rates of opposing motion directions (Fig. 1E,F). We calculated response scores with the same formula as above (eq. 1) but using baseline-corrected firing rates and with *A* and *B* referring to the motion phases of opposing motion directions, namely forward and backward for translational, left turn and right turn for yaw rotation, upward and downward for lift, and counter clockwise and clockwise for roll rotation,

respectively. Therefore, response scores of `±1` for direction selectivity indicate directionally selective responses, while `0` may result from highly similar responses to opposing motion directions or from the lack of a response to both directions.

We calculated average response scores for each morphological neuron class in order to investigate whether neurons of the same class responded consistently with an increase or decrease in firing rate with respect to a given motion direction and whether they consistently discriminated between opposing directions. Averaged motion response scores lie in the interval [-1,+1], where values near the ends of this interval indicate a consistent motion response across neurons. However, a value around 0 may both mean that no neuron responded significantly or that equal numbers of neurons had a response score of +1 as had -1. Therefore, we also examined the average of the absolute motion response score, which lies in [0,+1] and indicates whether neurons were responsive or selective, respectively, regarding a given motion category irrespective of the response tendency.

Celestial cues

Cue rotation periods were cropped from the voltage trace, spikes were detected as described above and each spike was assigned the cue angle (AoP or light spot azimuth, respectively) at the time of occurrence. Spike angles were pooled per cue type and the firing rate was estimated in 10° bins. The firing rate was then tested for correlation with the cue angle using `circ_corrcl` from the circular statistics toolbox (Berens, 2009), yielding a P and R^2 value, which we used as a metric of sensitivity. In case of statistical significance ($P < 5$ %), the average angle from the spike angles was calculated using `circ_mean`. AoP data are axial, hence for this cue the spike angles were doubled before calculation and the result was halved, returning the average angle in axial space (Zar, 1999); likewise, bin angles were doubled before testing for correlation. Control rotations were treated as axial data, because the LED holder is of axial symmetric geometry. If the spike rate was significantly correlated with holder rotation, the responses to all cues were discarded as potentially being artifacts. This was frequently encountered in neurons with arborizations in the optic lobes or the posterior protocerebrum, but in none of the recorded central-complex neurons, albeit only 30 % were tested for it.

Computational Model

The model and simulations and the related figures were implemented in the Python programming language (Van Rossum and Drake Jr, 1995) with the PyTorch (Paszke et al., 2019), numpy (Harris et al., 2020), and matplotlib (Hunter, 2007) external libraries.

We would like to emphasize that the model described here is, in the sense of Marr (1982), algorithmic, not implementational. In other words, it is designed with the aim to understand how the compass system represents and processes information. Our model does not aim to be a 1:1 representation of the neural hardware involved in this input-output transformation.

Our model features two tangential inputs to the lower units of the NO (TN units), 16 Loop units, and 16 columnar neurons connecting the CBL to the PB (CL1a units). Together, the

TN units represent the entire TN neuron population. The Loop units subsume the computational effects of sets consisting of a type 2 columnar neuron connecting the NO and PB to the CBL (CL2 neuron) in hemisphere A, a CL1a neuron it innervates in hemisphere B, and a CL2 neuron in hemisphere B that this same CL1a neuron projects onto (see Fig. 8C, the neurons described here are colored in orange, dark green, and brown, respectively). While TN and Loop units are rather abstract representations of the neuronal architecture of the locust's compass system, the CL1a units can be interpreted in terms of single CL1a neurons distributed across the PB.

Neural activity of the CL1a and CL2 neuron populations was modelled as vectors of average firing rate at a time point t_n, $\vec{r}(\text{CL1a}, t_n)$ for the CL1 units and $\vec{r}(\text{Loop}, t_n)$ for the Loop units. We would like to emphasize that the Loop units' activities are computational abstractions of the joint activities of the neurons involved in a loop. The properties of their activities are constrained by the hypothesis that the TN inputs shift the CL1a activities according to the direction in which the visual input turns. Further, the firing rates obtained via the following equations cannot be interpreted in terms of absolute firing rates but instead in terms of deviations from a working point or baseline activity.

We assume that the optic flow is represented in the TN inputs. To allow for a shift of the activation maximum of the CL1a units according to the TN input, Loop and CL1a unit activations are hypothesized to represent linearly independent vectors in the same space. By linear combination of these vectors, a rotation of both activation vectors is accomplished. This rotation gives rise to the observable CL1a activation maximum shift. Specifically, the firing rates of the CL1a units were initialized based on the normalized cosine of the CL1a neurons' azimuthal preferences across the PB:

$$\vec{r}(\text{CL1a}, t_0) = cos\left(\vec{\phi}_{\text{CL1a}} + \vec{\phi}\right) / \left\| cos\left(\vec{\phi}_{\text{CL1a}} + \vec{\phi}\right) \right\|_F, \quad (2)$$

where $\| \quad \|_F$ denotes the Frobenius norm and $\vec{\phi}_{\text{CL1a}}$ is the vector of preferred azimuths of the CL1a neurons, approximated to be evenly distributed across the PB from left to right in a range $[0,2\pi]$ (see Fig. 8D–D''). $\vec{\phi} = (\phi, \cdots, \phi)$ is the vector representing the phase of the CL1a activity bump that corresponds to the azimuth ϕ of an environmental cue, such as the solar azimuth. Trigonometric functions of vectors are evaluated component-wise. Inspired by the finding reported by Turner-Evans et al. (2017) that in the PB of *Drosophila*, the P-EN activity bump lags behind the E-PG bump by approximately one glomerulus, we initialized the Loop activity shifting the CL1a activity by a phase $\vec{\theta} = (\theta, \cdots, \theta)$, where $\theta = -\frac{2\pi}{16}$, which is the equivalent of one PB column in the locust:

$$\vec{r}(\text{Loop}, t_0) = cos\left(\vec{\phi}_{\text{CL1a}} + \vec{\phi}\right) / \left\| cos\left(\vec{\phi}_{\text{CL1a}} + \vec{\phi} + \vec{\theta}\right) \right\|_F. \quad (3)$$

The circuit's activity at a time point t_n with $n > 0$ is obtained from the activity at the previous time point t_{n-1}:

$$\vec{r}(\text{CL1a}, t_n) = \overrightarrow{w}_{\text{CL1a}\to\text{CL1a}} \times \vec{r}(\text{CL1a}, t_{n-1}) + \overrightarrow{w}_{\text{Loop}\to\text{CL1a}} \times \vec{r}(\text{Loop}, t_{n-1}), \quad (4)$$

$$\vec{r}(\text{Loop}, t_n) = \overrightarrow{w}_{\text{CL1a}\to\text{Loop}} \times \vec{r}(\text{CL1a}, t_{n-1}) + \overrightarrow{w}_{\text{Loop}\to\text{Loop}} \times \vec{r}(\text{Loop}, t_{n-1}), \quad (5)$$

where × denotes the matrix-vector product and $\vec{w}_{\mathrm{CL1a}\to\mathrm{Loop}}$ and $\vec{w}_{\mathrm{Loop}\to\mathrm{CL1a}}$ are the vectors of weights for connections from CL1a onto Loop units and vice versa. $\vec{w}_{\mathrm{CL1a}\to\mathrm{CL1a}}$ and $\vec{w}_{\mathrm{Loop}\to\mathrm{Loop}}$ are the vectors of weights for recurrent connections from CL1a and Loop units onto themselves.

We assume that the influence of angular movement on the compass circuit is mediated by a modulatory impact of the TN neurons on the synapses between CL1a and CL2 neurons. This is reflected in the way the TN units encode motion direction and modulate the weights of connections between and among CL1a and Loop units. In this first model, we abstract angular velocity and only employ a ternary direction representation: straightforward, left and right. The TN units encode the turn direction $d(t_{n-1} \to t_n)$ during the time step between time points t_{n-1} and t_n as follows:

$$\mathrm{TN_L}(t_n) = \begin{cases} 0 & \text{if } d(t_{n-1} \to t_n) = \text{straightforward} \\ 1 & \text{if } d(t_{n-1} \to t_n) = \text{left} \\ 0 & \text{if } d(t_{n-1} \to t_n) = \text{right} \end{cases}, \tag{6}$$

$$\mathrm{TN_R}(t_n) = \begin{cases} 0 & \text{if } d(t_{n-1} \to t_n) = \text{straightforward} \\ 0 & \text{if } d(t_{n-1} \to t_n) = \text{left} \\ 1 & \text{if } d(t_{n-1} \to t_n) = \text{right} \end{cases}. \tag{7}$$

The weights of connections between and among CL1a and Loop units are modulated by the TN units according to

$$\begin{pmatrix} \vec{w}_{\mathrm{CL1}a\to\mathrm{CL1a}} & \vec{w}_{\mathrm{CL1}a\to\mathrm{Loop}} \\ \vec{w}_{\mathrm{Loop}\to\mathrm{CL1a}} & \vec{w}_{\mathrm{Loop}\to\mathrm{Loop}} \end{pmatrix} = (1 - [\mathrm{TN_L}(t_n) + \mathrm{TN_R}(t_n)]) * w_S + \mathrm{TN_L}(t_n) * w_L + \mathrm{TN_R} * (t_n) w_R, \tag{8}$$

such that

$$\begin{pmatrix} \vec{w}_{\mathrm{CL1}a\to\mathrm{CL1a}} & \vec{w}_{\mathrm{CL1}a\to\mathrm{CL2}} \\ \vec{w}_{\mathrm{CL2}\to\mathrm{CL1a}} & \vec{w}_{\mathrm{CL2}\to\mathrm{CL2}} \end{pmatrix} = \begin{cases} w_S & \text{if } d(t_{n-1} \to t_n) = \text{straightforward} \\ w_L & \text{if } d(t_{n-1} \to t_n) = \text{left} \\ w_R & \text{if } d(t_{n-1} \to t_n) = \text{right} \end{cases}. \tag{9}$$

Here, $w_S = I_2$ is the identity matrix of size 2, such that the circuit activity is stable during straightforward motion. w_L and w_R are given by

$$w_L = T^{-1} \times \left(R_{-\Delta_\phi} \times T\right), \tag{10}$$

$$w_R = T^{-1} \times \left(R_{\Delta_\phi} \times T\right), \tag{11}$$

where $R_{\pm\Delta_\phi}$ is a 2-dimensional orthogonal matrix that rotates the coordinate system by Δ_ϕ. $T = \begin{pmatrix} 1 & cos(\theta) \\ 0 & \sin(\theta) \end{pmatrix}$ is a transformation matrix from a 2-dimensional affine coordinate system to a 2-dimensional orthogonal coordinate system, where the first axes of the coordinate systems coincide, and the second axis of the affine system is slanted by θ. T^{-1} is the inverse of T. These weights produce a shift of the CL1a and Loop units' activity patterns by the magnitude of a turn performed during one time step which we denote by $\pm\Delta_\phi$. The magnitude of Δ_ϕ is arbitrary and was set to $\frac{\pi}{10}$ for simulations.

As not all units can be interpreted in terms of individual neurons, their connections do not translate to synapses and the weights of their connections cannot be understood as synaptic weights or conductances. Instead, connections and their weights indicate more abstract principles of influence between parts of the circuit: All connections are unidirectional, with a sending and a receiving unit. Weights $w < 0$ correspond to the sending unit inhibiting, and weights $w > 0$ correspond to it exciting the receiving unit, while weights $w = 0$ indicate no influence. Fig. 9A shows the general scheme of connections among the different unit types and Fig. 9B shows the connectivity itemized for the individual units. The connectivity matrices result from substituting the values ofw_S and w_L, respectively, into equations 4 and 5. Substituting w_R into these equations results in the same matrix as does w_L, but it is rotated by 180°.

Agent Simulation

To test whether the circuit can both maintain and shift the head direction representation manifested in the CL1a activity pattern, we simulated movement tracks and fed them into the network via the TN units. As the model is deterministic and currently supports a single fixed magnitude of yaw angle change, a single simulation of each straightforward motion, rightward, and leftward yaw-rotation was sufficient.

Code and data accessibility

MATLAB analysis code, python modelling code, and physiological and morphological data have been deposited in data_UMR (http://dx.doi.org/10.17192/fdr/76).

Results

We surveyed CX neurons at different integration stages for sensitivity to visually simulated self-motion (Fig. 1) and celestial cues (Fig. 2). We found that visual motion sensitivity and direction selectivity is wide spread, but very variable, in the CX network and may occur together with celestial cue sensitivity.

Visual self-motion sensitivity and direction selectivity in the central complex

Neurons in almost all morphological classes (Fig. 3A–C) were sensitive to the moving gratings in at least one motion direction (motion sensitivity) and responded differently to opposing motion directions (direction selectivity) (Fig. 3D). Response scores, indicating the sign of the firing rate change due to visual self-motion perception, were likewise inconsistently distributed within the same neuron class (Fig. 3E). We explored the possibility that this inconsistency might originate from anatomy: The CX is an unpaired yet bilaterally symmetric brain structure, hence CX neurons from the same morphological class occur in two mirror-symmetric sets, one in each hemisphere. Therefore, neurons from different brain sides might process turning motion antagonistically, leading to a balanced integration across the CX. If so, neurons from different brain sides should have responded with inverted response scores to the same yaw rotation and roll motion directions or should show inverted direction selectivity. However, we found no indications for this

hypothesis in the distribution of response scores after grouping neurons by their brain side of origin (Fig. 3F). Additional separation by neuron class was not reasonable due to the low sample size per class. Overall, within a given neuron class, individual neurons responded with excitation, inhibition or not at all to the same stimulus, independent of their brain side of origin.

Fig. 4A and Fig. 5A provide a more detailed view on the distribution of response scores. The average motion response scores per motion direction and selectivity category illustrate that neuronal responses and directional selectivity in a given neuron class were very variable and inconsistent. Considering absolute response score, which indicates whether neurons generally responded to a given motion direction (Fig. 4B) or were selectively direction sensitive (Fig. 5B), irrespective of the direction of the neuronal response, roughly as many neurons were responsive as were unresponsive. TB1 and CP2 neurons make a notable exception. They were consistently unselectively sensitive to the direction of translational and yaw-rotational motion (Fig. 5), while one CP2 and two TB1 neurons showed motion sensitivity (Fig. 4).

Visual self-motion sensitivity and celestial-cue sensitivity are independent

Neurons in almost all morphological classes were both sensitive to visual self-motion and simulated celestial cues (Fig. 3D). Most TU neurons, however, were unresponsive to celestial cues, with only one out of seven neurons sensitive to a single celestial cue. Neurons within a given class did not respond consistently to the same stimulation, which likewise applies to motion sensitivity, direction selectivity, and celestial cues. Hence, we investigated whether there is a connection between these response properties, hypothesizing that when neurons were sensitive to visual motion, they were likely also sensitive to celestial cues. We tested this hypothesis for both motion sensitivity and direction selectivity: As a metric of visual-motion sensitivity, we used the absolute difference in firing rate between motion phase and stationary phase (e. g., Y-axis difference between the triangle markers in Fig. 1D). Analogously, we used the absolute difference in baseline-corrected firing rate between opposing motion directions as a measure of direction selectivity (e. g., Fig. 1F). As a metric of celestial-cue sensitivity, we used the R^2 value of the circular-linear correlation (cf. Fig. 2). Each motion and direction sensitivity metric was tested for linear correlation with each celestial cue sensitivity metric. A statistically significant positive correlation between response metrics would mean that susceptibility to different cues is positively linked, implying concurrent integration of both cues; negative correlation would suggest a rather strict separation of different cue channels.

We found significant positive correlations for 8 out of 24 motion directions (Fig. 6; Table 1). This inconsistency suggests that cue sensitivity is largely independent, but may indeed be flexibly coupled. Strikingly, for forward and backward translation, motion sensitivity was significantly correlated with all types of celestial cue sensitivity, except for one sensitivity pair (AoP sensitivity and forward motion). Although we did not test cues simultaneously, this could mean that desert locusts mainly process celestial cues during translational movement while comparing the current travel direction with the desired one.

During turning, other cues such as proprioceptive feedback might be more informative to quickly update the internal travel direction.

We found no significant linear correlation between the sensitivity metrics for direction selectivity and celestial cue sensitivity (Fig. 7; Table 2). Grouping data by response significance had no effect on this finding. This seems counterintuitive for the translation category because forward and backward motion sensitivity were correlated with celestial cue sensitivity (Fig. 6). However, motion sensitivity need not lead to directional selectivity in the same motion category (e. g. see Fig. 1).

In conclusion, the data suggest that neurons that are currently sensitive to celestial cues are more likely to also respond to translational visual motion, either progressive or regressive, which possibly helps stabilizing straight-line navigation. Otherwise, visual motion processing seems to be largely independent of celestial cue sensitivity, illustrating that different information streams are flexibly integrated in the CX.

Yaw-rotation is processed by CL2 neurons

We recorded from two mirror-symmetric CL2 neurons, i. e., one neuron having postsynaptic arborizations in the left NO and right half of the PB and the other one in the right NO and left half of the PB. Both neurons were directionally selective for visual motion that simulated yaw rotation, but with opposite polarity (Fig. 8A–B'). CL2 neurons are part of the internal compass system in the locust CX (Pegel et al., 2018) and like homologous neurons in Drosophila (P-EN) apparently signal rotational self-motion, updating the internal heading representation when the animal turns (Fig. 8C–D'').

Two entry sites into the CX network for information on rotational self-motion have been proposed so far, based on work in the fruit fly: i) The PB, where neurons are asymmetrically excited depending on turning direction, conveyed via SpsP neurons (TB7 neurons in the locust) (Green and Maimon, 2018; Lu et al., 2020). These neurons connect to the head-direction system, specifically to P-EN neurons (CL2 neurons in the locust). ii) The NOs, where neurons innervating one NO are excited depending on turning direction, conveyed via LNO neurons (TN neurons in the locust) that receive input in the lateral complexes. P-EN neurons convey these asymmetric inputs to E-PG neurons via synapses in the ellipsoid body, leading to a shift of the internal heading representation according to turning (Green et al., 2017; Turner-Evans et al., 2017).

Our data support the idea that the locust internal compass signal is also shifted during turns via asymmetric excitation and inhibition of CL2 neurons (Fig. 8). The site of this interaction may be the NOs (via TN neurons), as TN neurons are tuned to turning motion in *Drosophila* (Lu et al., 2020) and are morphologically suited to provide asymmetric input to the CL2 population. Like in *Drosophila* P-EN neurons, the projections of locust CL2 neurons in the CBL are shifted by one column relative to the projections of CL1 neurons (Fig. 8C,D). A notable difference between compass representation in the locust and the *Drosophila* compass system is that the E-PG population activity peak in the EB results in two activity peaks with a fixed offset along the PB, while available data in the

locust suggest a single peak along the PB that results from azimuthal tuning to celestial cues (Pegel et al., 2019; Zittrell et al., 2020). If so, locust CL2 neurons should have inhibitory connections to CL1a neurons (Fig. 8C); however, these connections and their polarity are hypothetical as there are no data on functional connectivity in the locust CX.

We tested this hypothetic heading compass system by implementing it as a simple algorithmic model. The model maintains an initial bump of activity when no yaw-rotation is simulated. The activity bump is shifted to the left (right) by $\Delta_\phi * n$ when a right (left) turn over n time steps is simulated, tracking the change in the agent's heading direction (see Fig. 9C).

Discussion

We analyzed the sensitivity to visually simulated self-motion in different neuron classes in the locust CX network, from input-providing neurons (TL [R neurons in *Drosophila*] and TU neurons) to output neurons (CPU1 [P-F-R] and CPU2) and at intermediate stages (e. g. CL1a [E-PG] and TB1 [Δ7]). Neurons in nearly all investigated classes were sensitive to visual self-motion and discriminated between opposite motion directions. However, we seldom encountered consistent responses within the same neuron class, suggesting that single cells flexibly switch their cue sensitivity based on the internal state of the animal and environmental conditions. An exception may be CL2 neurons, which mirror-symmetrically encoded yaw rotation direction, depending on the brain hemisphere in which they arborized, suggesting a role in keeping the internal compass system up to date during turning.

TL neurons form a large group of neurons that have in common that they provide input to all columns of the CBL (Omoto et al., 2018). TL neurons take part in sensory processing of diverse environmental cues: Visual-landmark detection (Seelig and Jayaraman, 2013; Sun et al., 2017), thermosensation (Buhl et al., 2021), polarization vision (fruit fly: Hardcastle et al., 2021; monarch butterfly: Heinze and Reppert, 2011; Nguyen et al., 2021; locust: Pegel et al., 2018; dung beetle: el Jundi et al., 2015), and perception of wind direction (Okubo et al., 2020). This makes TL neurons candidates for visual motion processing, possibly feeding self-motion information into the CX navigation system.

The four TL neurons we recorded (three TL2 and one TL3a neuron) showed mixed responses regarding both motion sensitivity (Fig. 4) and direction selectivity (Fig. 5), while individual neurons responded consistently to repetitive stimulation. This coincides with a previous study (Rosner et al., 2019) and suggests that TL neurons may be involved in visual-motion processing depending on the current behavioral context and even recent visual experience (Shiozaki and Kazama, 2017), which is plausible considering the plethora of sensory processing that this neuron class is involved in. The two direction selective neurons (Fig. 5) had their postsynaptic arborizations on the same side (the animal's left) and responded in a highly similar way, i. e., both were inhibited by forward-motion and excited by right-turn motion compared to the respective opposite direction (Fig. 5A),

which implies a fixed role, provided that the neuron is currently engaged in visual-motion processing.

CL1a/E-PG neurons carry the internal heading signal in the fly brain (Seelig and Jayaraman, 2015). At any time, several neighboring neurons along the ellipsoid body are exclusively active, representing the fly's current heading relative to external cues as the phase angle along this neuropil. This activity peak persists during inactivity and is shifted by turning movements, thereby tracking the current heading. We assume that locust CL1a neurons are, likewise, involved in head direction tracking, although the underlying network organization appears to be different from that of the fruit fly. Assuming that CL1a neurons code for head direction as a population, a single neuron should respond to turning motion based on whether it is currently part of the population activity peak. If it was in the peak's center, a turning-induced peak shift should decrease neural activity; if the peak was close to it and driven towards it, activity should increase; if the peak was far away, activity should be little affected.

We indeed found CL1a neurons to be highly variable: Half of the recorded neurons were sensitive to yaw-rotational visual motion and discriminated between turning directions (Fig. 3D); out of those, some were inhibited by left turning and some were excited, with a tendency to inhibition (Fig. 3E). Although this is in line with the expectations formulated above for turning motion, we found the same response variability for all other visual-motion directions (Fig. 3D,E). This in turn is contradicting, because the internal heading signal should be influenced strongest by yaw rotation and not by translational motion. However, natural movement may often be a combination of different types of body axis transformations: E. g., turning may be a combination of rotational, forward and sideways movement, leading to rather complex arrangement of optic flow vectors in the visual field, which might be represented in the recorded neurons by mixed sensitivity to different motion directions. Similar to TL neurons, CL1a neurons might flexibly process visual motion in order to update the internal compass based on the current behavioral context.

Δ7 neurons are an integral part of the internal heading system in the fruit fly. They constitute an inhibitory anti-phase peak along the PB that stabilizes the E-PG head-direction peak (Turner-Evans et al., 2020). Their axons connect to E-PG neurons (Hulse et al., 2021) and they receive input from SpsP neurons, which are tuned to lateral velocity (Lu et al., 2020). This strong involvement in the head direction system suggests that Δ7 neurons are sensitive to visual self-motion cues, although the origin of sensory input—visual or mechanosensory—driving SpsP neurons is as yet unknown.

In the locust, TB1 neurons are part of the sky compass system (Heinze and Homberg, 2007; Pegel et al., 2019; Zittrell et al., 2020). SpsP analogues are TB7 neurons, which provide input from the superior posterior slope to all slices of one PB half (von Hadeln et al., 2020). Our data (Fig. 3D,E) suggest that TB1 neurons are not involved in visual motion processing and rather take part only in sky compass signaling. Rosner et al. (2019),

however, found TB1 neurons to variably respond to visual motion, suggesting state-dependent processing.

TU neurons are a diverse group of tangential neurons of the CBU (fan shaped body in *Drosophila*), that provide input from various brain areas to the CBU (von Hadeln et al., 2020). Generally, neurons of the CBU (PoU, CPU1 and CPU2) were unresponsive or at most inconsistently sensitive to visual self-motion. This coincides with studies on *Drosophila* that found CBU neuron activity to highly depend on whether the animals were actively engaged in flight (Weir and Dickinson, 2015; Shiozaki et al., 2020). It is therefore possible that neurons at this integration stage are silent in locusts under the constrained conditions of our experiments. PoU neurons (hΔb in *Drosophila*) integrate external and internal self-motion cues in order to transform egocentric directions into world-centric coordinates (Lu et al., 2020; Lyu et al., 2020). The lack of mechanosensory feedback under our experimental conditions might explain why most PoU neurons did not respond to purely visual self-motion cues. Under such conditions, PoU neurons strongly respond to looming objects (Rosner and Homberg, 2013), thus they might rather be involved in escape reactions when quiescence is signaled by the body. In general, physiological activity of locust CX neurons is considerably affected by active leg movement (Rosner et al., 2019), an influence that was excluded in the current study.

CPU4 neurons (PFN in Drosophila) were hypothesized to be “integration cells” based on data from sweat bees (Stone et al., 2017). In fruit flies they indeed integrate current heading and travel speed (Lu et al., 2020; Lyu et al., 2020). We recorded from a CPU5 neuron, a similar cell type that is suited to integrate information from the NOs and the PB (Fig. 3C). This neuron was sensitive to yaw-rotation and directionally selective for translational visual motion (Fig. 4; Fig. 5), which suggests that locust CPU5 neurons as well encode egocentric travel direction, at least forward and backward travel, inferred from visual motion. This cue is possibly fed in by TN neurons (von Hadeln et al., 2020) and is then combined with compass information from the PB, as the neuron was also sensitive to simulated celestial cues (Fig. 3D).

The computational model of the CL1a-CL2 network accounting for turning-direction dependent shifts in CL1 compass neurons is similar to the recurrent loop connectivity between P-EN and E-PG neurons in Drosophila accounting for angular velocity integration into the CX compass (Turner-Evans et al., 2017; Turner-Evans et al., 2020; Hulse et al., 2021). However, distinct differences exist, based on the 360° angular representation in the locust PB (Pegel et al., 2019; Zittrell et al., 2020) versus the 2 × 360° representation of space in the *Drosophila* PB. As a consequence, inhibitory synaptic connections from CL2 to CL1a neurons are required in the locust, whereas in *Drosophila* P-EN and E-PG neurons are connected by recurrent excitatory loops. While in *Drosophila* E-PG neurons form a 360° representation of space in the ellipsoid body, two opposite 180° representations of space would be topographically intercalated in the CBL of the locust (Fig. 8D). The linear model and binary concept of movement employed here are still quite abstract representations of the neuronal and behavioral characteristics of the locust. In particular,

our model is not dynamic; it switches between stable states but does not make the dynamics underlying the transitions explicit. We aim to increase the model's biological plausibility by implementing velocity dependence in future work, but expect the general principles of maintaining and updating the compass bump to hold independently of the level of analysis.

References

Beetz MJ, el Jundi B, Heinze S, Homberg U (2015) Topographic organization and possible function of the posterior optic tubercles in the brain of the desert locust *Schistocerca gregaria*. J Comp Neurol 523:1589–1607.

Berens P (2009) CircStat: A MATLAB toolbox for circular statistics. J Stat Soft 31:1–21.

Brainard DH (1997) The psychophysics toolbox. Spatial Vis 10:433–436.

Buhl E, Kottler B, Hodge JJL, Hirth F (2021) Thermoresponsive motor behavior is mediated by ring neuron circuits in the central complex of *Drosophila*. Sci Rep 11:155.

Byrne M, Dacke M, Nordström P, Scholtz C, Warrant E (2003) Visual cues used by ball-rolling dung beetles for orientation. J Comp Physiol A 189:411–418.

Clements AN, May TE (1974) Studies on locust neuromuscular physiology in relation to glutamic acid. J Exp Biol 60:673–705.

el Jundi B, Homberg U (2010) Evidence for the possible existence of a second polarization-vision pathway in the locust brain. J Insect Physiol 56:971–979.

el Jundi B, Pfeiffer K, Heinze S, Homberg U (2014) Integration of polarization and chromatic cues in the insect sky compass. J Comp Physiol A 200:575–589.

el Jundi B, Warrant EJ, Byrne MJ, Khaldy L, Baird E, Smolka J, Dacke M (2015) Neural coding underlying the cue preference for celestial orientation. Proc Natl Acad Sci USA 112:11395–11400.

Fent K (1986) Polarized skylight orientation in the desert ant *Cataglyphis*. J Comp Physiol A 158:145–150.

Giraldo YM, Leitch KJ, Ros IG, Warren TL, Weir PT, Dickinson MH (2018) Sun navigation requires compass neurons in *Drosophila*. Curr Biol 28:2845–2852.

Gould JL (1998) Sensory bases of navigation. Curr Biol 8:731–738.

Green J, Adachi A, Shah KK, Hirokawa JD, Magani PS, Maimon G (2017) A neural circuit architecture for angular integration in *Drosophila*. Nature 546:101–106.

Green J, Maimon G (2018) Building a heading signal from anatomically defined neuron types in the *Drosophila* central complex. Curr Opin Neurobiol 52:156–164.

Hardcastle BJ, Omoto JJ, Kandimalla P, Nguyen B-CM, Keleş MF, Boyd NK, Hartenstein V, Frye MA (2021) A visual pathway for skylight polarization processing in *Drosophila*. eLife 10:e63225.

Harris CR et al. (2020) Array programming with NumPy. Nature 585:357–362.

Heinze S (2017) Unraveling the neural basis of insect navigation. Curr Opin Insect Sci 24:58–67.

Heinze S, Homberg U (2007) Maplike representation of celestial *E*-vector orientations in the brain of an insect. Science 315:995–997.

Heinze S, Homberg U (2008) Neuroarchitecture of the central complex of the desert locust: Intrinsic and columnar neurons. J Comp Neurol 511:454–478.

Heinze S, Narendra A, Cheung A (2018) Principles of insect path integration. Curr Biol 28:1043–1058.

Heinze S, Reppert SM (2011) Sun compass integration of skylight cues in migratory monarch butterflies. Neuron 69:345–358.

Honkanen A, Adden A, da Silva Freitas J, Heinze S (2019) The insect central complex and the neural basis of navigational strategies. J Exp Biol 222:jeb188854.

Hulse BK, Haberkern H, Franconville R, Turner-Evans DB, Takemura S, Wolff T, Noorman M, Dreher M, Dan C, Parekh R, Hermundstad AM, Rubin GM, Jayaraman V (2021) A connectome of the *Drosophila* central complex reveals network motifs suitable for flexible navigation and context-dependent action selection. bioRxiv:2020.12.08.413955; https://doi.org/10.1101/2020.12.08.413955.

Hulse BK, Jayaraman V (2020) Mechanisms underlying the neural computation of head direction. Annu Rev Neurosci 43:31–54.

Hunter JD (2007) Matplotlib: A 2D graphics environment. Comput Sci Eng 9:90–95.

Lu J, Westeinde EA, Hamburg L, Dawson PM, Lyu C, Maimon G, Druckmann S, Wilson RI (2020) Transforming representations of movement from body- to world-centric space. bioRxiv:2020.12.22.424001; https://doi.org/10.1101/2020.12.22.424001.

Lyu C, Abbott LF, Maimon G (2020) A neuronal circuit for vector computation builds an allocentric traveling-direction signal in the *Drosophila* fan-shaped body. bioRxiv:2020.12.22.423967; https://doi.org/10.1101/2020.12.22.423967.

Marr D (1982) Vision: A computational investigation into the human representation and processing of visual information. New York: Henry Hold and Co.

Nguyen TAT, Beetz MJ, Merlin C, el Jundi B (2021) Sun compass neurons are tuned to migratory orientation in monarch butterflies. Proc R Soc B 288:20202988.

Okubo TS, Patella P, D'Alessandro I, Wilson RI (2020) A neural network for wind-guided compass navigation. Neuron 107:924–940.

Omoto JJ, Nguyen B-CM, Kandimalla P, Lovick JK, Donlea JM, Hartenstein V (2018) Neuronal constituents and putative interactions within the *Drosophila* ellipsoid body neuropil. Front Neural Circuits 12:449.

Paszke A et al. (2019) PyTorch: An imperative style, high-performance deep learning library. Adv Neural Inf Process Syst 32:8026–8037.

Pegel U, Pfeiffer K, Homberg U (2018) Integration of celestial compass cues in the central complex of the locust brain. J Exp Biol 221:jeb171207.

Pegel U, Pfeiffer K, Zittrell F, Scholtyssek C, Homberg U (2019) Two compasses in the central complex of the locust brain. J Neurosci 39:3070–3080.

Perez SM, Taylor OR, Jander R (1997) A sun compass in monarch butterflies. Nature 387:29.

Pfeiffer K, Homberg U (2014) Organization and functional roles of the central complex in the insect brain. Annu Rev Entomol 59:165–184.

Rosner R, Homberg U (2013) Widespread sensitivity to looming stimuli and small moving objects in the central complex of an insect brain. J Neurosci 33:8122–8133.

Rosner R, Pegel U, Homberg U (2019) Responses of compass neurons in the locust brain to visual motion and leg motor activity. J Exp Biol 222:jeb196261.

Schindelin J, Arganda-Carreras I, Frise E, Kaynig V, Longair M, Pietzsch T, Preibisch S, Rueden C, Saalfeld S, Schmid B, Tinevez J-Y, White DJ, Hartenstein V, Eliceiri K, Tomancak P, Cardona A (2012) Fiji: An open-source platform for biological-image analysis. Nat Methods 9:676–682.

Seelig JD, Jayaraman V (2013) Feature detection and orientation tuning in the *Drosophila* central complex. Nature 503:262–266.

Seelig JD, Jayaraman V (2015) Neural dynamics for landmark orientation and angular path integration. Nature 521:186–191.

Shiozaki HM, Kazama H (2017) Parallel encoding of recent visual experience and self-motion during navigation in *Drosophila*. Nat Neurosci 20:1395–1403.

Shiozaki HM, Ohta K, Kazama H (2020) A multi-regional network encoding heading and steering maneuvers in *Drosophila*. Neuron 106:126–1415.

Srinivasan MV (2015) Where paths meet and cross: navigation by path integration in the desert ant and the honeybee. J Comp Physiol A 201:533–546.

Stone T, Webb B, Adden A, Weddig NB, Honkanen A, Templin R, Wcislo W, Scimeca L, Warrant E, Heinze S (2017) An anatomically constrained model for path integration in the bee brain. Curr Biol 27:3069–308511.

Sun Y, Nern A, Franconville R, Dana H, Schreiter ER, Looger LL, Svoboda K, Kim DS, Hermundstad AM, Jayaraman V (2017) Neural signatures of dynamic stimulus selection in *Drosophila*. Nat Neurosci 20:1104–1113.

Taube JS (1998) Head direction cells and the neurophysiological basis for a sense of direction. Prog Neurobiol 55:225–256.

Taube JS (2007) The head direction signal: origins and sensory-motor integration. Annu Rev Neurosci 30:181–207.

Turner-Evans D, Wegener S, Rouault H, Franconville R, Wolff T, Seelig JD, Druckmann S, Jayaraman V (2017) Angular velocity integration in a fly heading circuit. eLife 6:23496.

Turner-Evans DB, Jensen KT, Ali S, Paterson T, Sheridan A, Ray RP, Wolff T, Lauritzen JS, Rubin GM, Bock DD, Jayaraman V (2020) The neuroanatomical ultrastructure and function of a biological ring attractor. Neuron 108:145–163.

Uemura M, Meglič A, Zalucki MP, Battisti A, Belušič G (2021) Spatial orientation of social caterpillars is influenced by polarized light. Biol Lett 17:rsbl20200736.

Van Rossum G, Drake Jr FL (1995) Python tutorial. Amsterdam: Centrum voor Wiskunde en Informatica Amsterdam.

von Frisch K (1946) Die Tänze der Bienen. Österr Zool Z 1:1–148.

von Hadeln J, Hensgen R, Bockhorst T, Rosner R, Heidasch R, Pegel U, Quintero Pérez M, Homberg U (2020) Neuroarchitecture of the central complex of the desert locust: Tangential neurons. J Comp Neurol 528:906–934.

Weir PT, Dickinson MH (2012) Flying *Drosophila* orient to sky polarization. Curr Biol 22:21–27.

Weir PT, Dickinson MH (2015) Functional divisions for visual processing in the central brain of flying *Drosophila*. Proc Natl Acad Sci USA 112:E5523–E5532.

Wittlinger M, Wehner R, Wolf H (2006) The ant odometer: Stepping on stilts and stumps. Science 312:1965–1967.

Zar JH (1999) Biostatistical analysis, 4th ed. Upper Saddle River, N.J.: Prentice Hall.

Zittrell F (2019) CircHist: Circular histogram in MATLAB. Available at: https://github.com/zifredder/CircHist.

Zittrell F, Pfeiffer K, Homberg U (2020) Matched-filter coding of sky polarization results in an internal sun compass in the brain of the desert locust. Proc Natl Acad Sci USA 117:25810–25817.

Figures

Fig. 1: Experimental setup, visual-motion response of a CL1a neuron, and response analysis. (A) Schematic of the experimental setup (not to scale). Animals were mounted vertically and stimulated with motion of sinusoidal grating patterns on two laterally placed monitors, a blue polarized light spot in the animals' zenith, and a green or UV light spot at 45° elevation. Rotation of the LED mount resulted in modulation of the angle of polarization (AoP) or light spot azimuth, respectively. All stimuli were tested separately. (B) Response of a CL1a neuron to wide-field visual motion that simulated horizontal left turning. Raw data (top), detected spikes (middle) and smoothed firing rate estimate (bottom). Vertical lines indicate onset of stimulation phases: Pattern motion (Mot.) and standstill (Stat.) were alternated, each pair constituting one stimulation trial. (B') Same as B but for simulation of horizontal right turn motion. (C,D) Data evaluation steps for motion sensitivity, leftward turning. (C) Raster plot (top) of all left-turn trials (cf. B) and estimated firing rate, averaged in 250 ms bins (dots, bottom). The blue line is the smoothed firing rate during the motion phase (for illustration only), the red horizontal line indicates the median firing rate during all standstill phases (grey dots); the dot colors of bin values code for relative bin time during the motion phase, error bars denote standard deviation of bin averages. (D) Statistic comparison of firing rates. Data points correspond to the binned firing rates during motion and standstill phase. The color codes for relative bin time in each phase, which was used as a pairing factor for statistical comparison (Wilcoxon signed-rank test, *P* value indicated above the diagram), i. e., the first (leftmost) bin value in the motion phase was paired with the first value in the standstill phase, the second motion value with the second standstill value etc. Triangles denote total median of bin values during motion (colored) and standstill (grey). This response is assigned a response score of `-1`, because the neural activity during the motion phase (Mot.) was significantly lower than during the standstill phase (Stat.). (C',D'–C''',D''') Same as C,D but for forward, right yaw and backward motion; all responses are assigned a response score of `-1`. (E,F) Comparison of responses to opposite turning motion in order to score direction selectivity for yaw-rotation direction. (E) Baseline-corrected firing rates: The median firing rate during the respective stationary phase was subtracted from the binned firing rates of

the respective motion phase (cf. C,C''), yielding baseline-corrected firing rates suitable for comparison. The lines are smoothed (for illustration only) baseline-corrected firing rates and are colored as in C and C''. (F) Statistic comparison as in D, but here data points correspond to the binned baseline-corrected firing rates during the motion phase of the opposite directions. This comparison is assigned a response score of `+1`, because the baseline-corrected neural activity during left-yaw stimulation was significantly higher than during right-yaw stimulation. (E'–F') Same as E,F but for translational motion (forward vs. backward motion); response score of `0`, because the baseline-corrected neural activities were statistically equal.

Fig. 2: Celestial-cue response of a single CL1a neuron (same neuron as in Fig. 1) and response analysis. (A) Response to 360° rotation (decreasing angle) of presented AoP. Raw data (top), detected spikes (middle), and smoothed firing rate estimate (bottom). Vertical lines indicate start and end of the rotation. (B) Circular histogram of all presented rotations. Histogram bars indicate the average firing rate per 10° bin, error bars indicate standard deviation; orange line with black circle segments indicate average angle (Φ_{max}) and circular standard deviation, respectively. *P* and R^2 value refer to circular-linear correlation of firing rate with bin angle; *N* is the number of rotations. (A',B'–A''',B''') Same as A and B but for presentation of a green light spot, UV light spot and control rotations (no LED active), respectively.

Fig. 3: Morphology of neuron classes presented in this study and overview of motion sensitivity and direction selectivity of all recorded neurons. (A–C) Schematics of the locust central complex and associated neuropils with individual neurons from different classes superimposed. Large dots indicate somata, small dots indicate axonal (presynaptic) arborizations, and fine lines indicate dendritic (postsynaptic) arborizations. (A) Tangential neurons. We classified TU neurons as a group of diverse neurons that only have in common that they have large presynaptic arborizations in the CBU and input regions outside the central complex. Wiring schematics based on von Hadeln et al. (2020). (B–C) Columnar neurons. Wiring schematics based on Heinze and Homberg (2008). (D) Numbers of neurons per neuron class that showed statistically significant responses for the presented stimuli: Neurons were considered motion sensitive if they had an absolute response score of `+1` for at least one motion direction in a given motion category. Direction selective neurons had an absolute response score of `+1` for the comparison of opposite motion directions. A statistically significant average angle for a given LED stimulus indicated celestial cue sensitivity. Numbers are given as fraction of responsive neurons out of the total number of tested neurons; this fraction is also indicated by the background color. The total number of recorded neurons for each neuron class is indicated in parentheses. Empty cells mean that no neuron was tested with the respective stimulus. (E) Distribution of response score per neuron class and motion direction (left) and direction category (right), respectively. Each cell holds the total number of neurons with a given response score for a given direction or category; cell shading codes for the fraction of this number from the number of all neurons in the same class that were tested with the same

stimulus. The total number of recorded neurons for each neuron class is indicated in parentheses. Empty rows mean that no neuron was tested with the respective stimulus. (F) Distribution of response score for motion sensitivity and direction selectivity for turning-related motion directions; neuron classes pooled and separated by brain side of soma position. Abbreviations: CBL, lower division of the central body; CBU, upper division of the central body; LX, lateral complex; NO, nodulus; PB, protocerebral bridge; POTU, posterior optic tubercle.

Fig. 4: Individual motion sensitivity: Response scores per motion direction and neuron class. (A) False-color matrices showing individual response scores for motion sensitivity, indicating whether neurons responded to a given motion direction. Individual response scores are `-1` (statistically significant inhibition compared to standstill, solid blue), `+1` (excitation, solid green) or `0` (non-significant response, solid black). The bottom row of each matrix holds the average response score per column (values inside `[-1,+1]`, color coded as a shade of blue or green), indicating whether neurons in the respective group tended to respond consistently. Average values were omitted if the number of underlying values was smaller than four. Rows are sorted for average response score; row numbers denote neuron ID, superscripts denote the brain side of the soma position. Empty fields indicate that the neuron was not tested with the respective stimulus; these fields did not contribute to the column average. (B) Same as A but for absolute response score, which can be `+1` (statistically significant activity change, solid orange) or `0` (non-significant response, solid black). Thus, the column average indicates whether neurons responded consistently disregarding the direction of firing rate change. Fig. 1 shows raw data of neuron 550 (CL1a).

Fig. 5: Individual direction selectivity: Response scores per direction category and neuron class. (A,B) Analogous to Fig. 4A,B, but showing response scores for direction selectivity, indicating whether neurons were differently tuned to opposite motion directions.

Fig. 6: Celestial-cue sensitivity and visual-motion sensitivity of central-complex neurons are partly correlated. Scatter plots of celestial-cue sensitivity (R^2 values of cue-angle vs. firing-rate correlation) vs. visual-motion response magnitude ($|\Delta Act|$, absolute difference between median firing rates during visual motion and standstill) for each combination of visual motion direction (columns) and type of celestial cue (rows). Each data point corresponds to a single neuron that was tested for both the visual motion direction and the celestial cue type. Data points are visually grouped by statistical significance of the responses, which refers to the firing rate difference between opposing motion directions for visual motion (cf. Fig. 1F) and to the correlation of cue-angle vs. firing-rate for celestial cues (cf. Fig. 2). *N* indicates the total number of data points per plot. Black lines are linear regression lines, indicating a statistically significant correlation between the response parameters based on all plotted data points. The purple line (bottom right) indicates a statistically significant correlation based on the data subset only including neurons with a

significant UV response. See Table 1 for numeric regression results. Subsets with N < 8 were excluded from regression analysis. n. s., statistically not significant.

Fig. 7: Scatter plots of celestial cue sensitivity (R^2 values) vs. directional selectivity, which is reflected by the absolute difference between the median firing rates during opposite motion directions (|ΔAct|). There is no significant linear correlation for any data population and subset (cf. Table 2).

Fig. 8: Rotational visual motion processing by CL2 neurons updates the heading compass. (A,A') Physiological response to yaw rotation of CL2 neurons arborizing in the right (A) and left (A') NO, respectively (recordings from different locusts). Both neurons responded directionally selective to visual turning motion, but with different polarity of the activity change (see Fig. 1 for plot explanations). (B) Posterior view of a frontal-plane maximum projection of a recorded CL2 neuron (response shown in A'). Scale bar: 100 µm. (B') Sagittal-plane maximum projection of the same staining. (C) Schematic wiring diagram of the CX with a subset of the involved neuron types: CL1a (E-PG in *Drosophila*) and CL2 (P-EN) neurons are connected to one another in the protocerebral bridge (PB) and lower division of the central body (CBL), while CL2 neurons also have postsynaptic arborizations in the noduli (NOs). CL1a neurons are topographically tuned to solar azimuth along the PB (black arrows). (D–D'') Hypothetical shift mechanism of the internal heading signal in the PB. (D) Full population of CL1a and CL2 neurons and initial activity state in the network: With an environmental cue 90° left of the locust (bottom), the CL1a population activity (top) has a distinct maximum according to the neural tuning (highlighted arrows in PB and CBL). (D') When the locust turns right, CL2 neurons are excited or inhibited depending on their brain side. Neurons that innervate the left (right) NO are excited (inhibited) by tangential neurons (TN) from the lateral complexes and relay onto CL1a neurons from the left (right) half of the PB. This asymmetric input may analogously be conveyed in the PB by tangential neurons (TB7) from the superior posterior slope. (D'') After turning, the CL1a population activity maximum is shifted so that the neural heading estimate accordingly represents the new heading relative to the external cue. Wiring schemes from Heinze and Homberg (2008), topographic tuning in the PB and CBL based on Zittrell et al. (2020).

Fig. 9: Computational model of a circuit integrating self-motion inputs and a localized maximum of activity to update head-direction representation. (A) Schematic of information passing between the TN, CL1a, and Loop units. Gray plates designate time points. At each time point, the CL1a and Loop units receive recurrent inputs from the previous time point (solid arrows). During turns, they also receive inputs from units of the respective other type (dashed arrows). Both types of connections are modulated by the TN units, as indicated by the arrows pointing from the TN units to the arrows connecting CL1a and Loop units. (B) Connectivity matrices for the CL1a and Loop units. Each connection is unidirectional with a sending and a receiving unit. Connection weights $\begin{pmatrix} w_{\mathrm{CL1}a\rightarrow\mathrm{CL1a}} & w_{\mathrm{CL1}a\rightarrow\mathrm{Loop}} \\ w_{\mathrm{Loop}\rightarrow\mathrm{CL1a}} & w_{\mathrm{Loop}\rightarrow\mathrm{Loop}} \end{pmatrix}$ are modulated by movement direction. Left: w_S for forward

motion, the framed off-diagonal connections have weights equal to zero for w_S but not for w_L and w_R. Right: w_L for left turn. w_R for right turn is the same as w_L but rotated by 180°. Units are indexed with PB columns. (C) CL1a activity bump in an agent simulation over $n = 3$ time steps. The left panel shows the pattern of CL1a activity at the first time point, encoding the initial heading direction with respect to an external stimulus. The right panel shows the updated patterns at the fourth time point for the different conditions: When the agent does not perform any turns (blue), the initial activity maximum is maintained. When it turns left (orange) or right (green), the activity bump is shifted in the opposite direction, representing the new relative heading direction.

Table 1: Pearson's correlation statistics per data population and subset shown in Fig. 6. "All pooled" refers to the whole data population for a given motion category and celestial cue type; "LED resp. sign." refers to the subset of data showing statistically significant responses to the respective LED stimulus, irrespective of visual-motion sensitivity; "Visual-motion resp. sign." refers to the subset showing statistically significant responses to the respective motion category, irrespective of celestial-cue sensitivity; "Both sign." refers to the intersection of these sets, i. e., neurons that were statistically significantly sensitive to both visual motion and celestial cue. Subsets with $N < 8$ were excluded from regression analysis.

Table 2: Same as Table 1 but referring to Fig. 7.

TABLE 1

	Subset	Forward	Backward	Left turn	Right turn
Angle of polarization	All pooled	P=0.85 R^2=0.00066 N=59	P=0.041 R^2=0.076 N=55	P=0.96 R^2=5e-05 N=52	P=0.81 R^2=0.0011 N=53
	LED resp. sign.	P=0.89 R^2=0.0007 N=31	P=0.33 R^2=0.035 N=29	P=0.63 R^2=0.0089 N=28	P=0.61 R^2=0.0097 N=29
	Visual-motion resp. sign.	P=0.2 R^2=0.08 N=22	P=0.54 R^2=0.029 N=15	P=0.69 R^2=0.014 N=14	P=0.33 R^2=0.069 N=16
	Both sign.	P=0.18 R^2=0.14 N=14	P=0.92 R^2=0.0013 N=10	P=0.47 R^2=0.089 N=8	P=0.43 R^2=0.079 N=10
Green azimuth	All pooled	P=0.033 R^2=0.11 N=43	P=0.0048 R^2=0.2 N=39	P=0.32 R^2=0.027 N=38	P=0.65 R^2=0.0058 N=39
	LED resp. sign.	P=0.79 R^2=0.0036 N=23	P=0.16 R^2=0.094 N=22	P=0.96 R^2=0.00013 N=20	P=0.77 R^2=0.0045 N=21
	Visual-motion resp. sign.	P=0.77 R^2=0.0065 N=16	P=0.78 R^2=0.01 N=10	P=0.75 R^2=0.018 N=8	N=7
	Both sign.	P=0.69 R^2=0.015 N=13	P=0.29 R^2=0.18 N=8	N=6	N=5
UV azimuth	All pooled	P=0.0094 R^2=0.16 N=40	P=0.0078 R^2=0.19 N=36	P=0.12 R^2=0.073 N=35	P=0.13 R^2=0.065 N=36
	LED resp. sign.	P=0.51 R^2=0.023 N=21	P=0.26 R^2=0.071 N=20	P=0.73 R^2=0.0079 N=18	P=0.36 R^2=0.05 N=19
	Visual-motion resp. sign.	P=0.32 R^2=0.072 N=16	P=0.42 R^2=0.081 N=10	P=0.59 R^2=0.051 N=8	N=7
	Both sign.	P=0.36 R^2=0.07 N=14	P=0.84 R^2=0.0069 N=8	N=6	N=5
		Up	**Down**	**Left roll**	**Right roll**
Angle of polarization	All pooled	P=0.2 R^2=0.059 N=29	P=0.033 R^2=0.18 N=26	P=0.0071 R^2=0.32 N=21	P=0.12 R^2=0.12 N=22
	LED resp. sign.	P=0.67 R^2=0.014 N=16	P=0.31 R^2=0.079 N=15	P=0.2 R^2=0.15 N=13	P=0.79 R^2=0.006 N=14
	Visual-motion resp. sign.	N=4	N=2	N=3	N=7
	Both sign.	N=4	N=2	N=2	N=6
Green azimuth	All pooled	P=0.25 R^2=0.056 N=25	P=0.91 R^2=0.00063 N=24	P=0.35 R^2=0.051 N=19	P=0.76 R^2=0.0054 N=20
	LED resp. sign.	P=0.96 R^2=0.0002 N=13	P=0.24 R^2=0.12 N=13	P=0.097 R^2=0.25 N=12	P=0.9 R^2=0.0015 N=13
	Visual-motion resp. sign.	N=4	N=2	N=2	N=7
	Both sign.	N=3	N=1	N=2	N=4
UV azimuth	All pooled	P=0.43 R^2=0.03 N=23	P=0.59 R^2=0.014 N=22	P=0.25 R^2=0.083 N=18	P=0.81 R^2=0.0034 N=19
	LED resp. sign.	P=0.71 R^2=0.015 N=12	P=0.51 R^2=0.044 N=12	P=0.015 R^2=0.55 N=10	P=0.93 R^2=0.00095 N=11
	Visual-motion resp. sign.	N=4	N=2	N=2	N=7
	Both sign.	N=3	N=1	N=2	N=3

TABLE 2

	Subset	Translation	Yaw	Lift	Roll
Angle of polarization	All pooled	P=0.6 R^2=0.0051 N=55	P=0.31 R^2=0.021 N=51	P=0.71 R^2=0.0058 N=26	P=0.085 R^2=0.15 N=21
	LED resp. sign.	P=0.74 R^2=0.0041 N=29	P=0.78 R^2=0.0033 N=27	P=0.4 R^2=0.054 N=15	P=0.33 R^2=0.086 N=13
	Visual-motion resp. sign.	P=0.85 R^2=0.0033 N=13	P=0.71 R^2=0.0099 N=16	P=0.99 R^2=1e-05 N=8	N=5
	Both sign.	N=7	P=0.48 R^2=0.056 N=11	N=6	N=4
Green azimuth	All pooled	P=0.71 R^2=0.0038 N=39	P=0.85 R^2=0.001 N=37	P=0.84 R^2=0.0019 N=24	P=0.24 R^2=0.08 N=19
	LED resp. sign.	P=0.35 R^2=0.044 N=22	P=0.53 R^2=0.023 N=19	P=0.42 R^2=0.061 N=13	P=0.71 R^2=0.014 N=12
	Visual-motion resp. sign.	P=0.53 R^2=0.06 N=9	P=0.25 R^2=0.18 N=9	P=0.97 R^2=0.00029 N=8	N=5
	Both sign.	N=7	N=4	N=5	N=4
UV azimuth	All pooled	P=0.39 R^2=0.022 N=36	P=0.58 R^2=0.0097 N=34	P=0.99 R^2=1e-05 N=22	P=0.15 R^2=0.13 N=18
	LED resp. sign.	P=0.81 R^2=0.0033 N=20	P=0.8 R^2=0.0045 N=17	P=0.23 R^2=0.14 N=12	P=0.53 R^2=0.05 N=10
	Visual-motion resp. sign.	P=0.14 R^2=0.29 N=9	P=0.13 R^2=0.3 N=9	N=7	N=5
	Both sign.	N=7	N=5	N=4	N=3

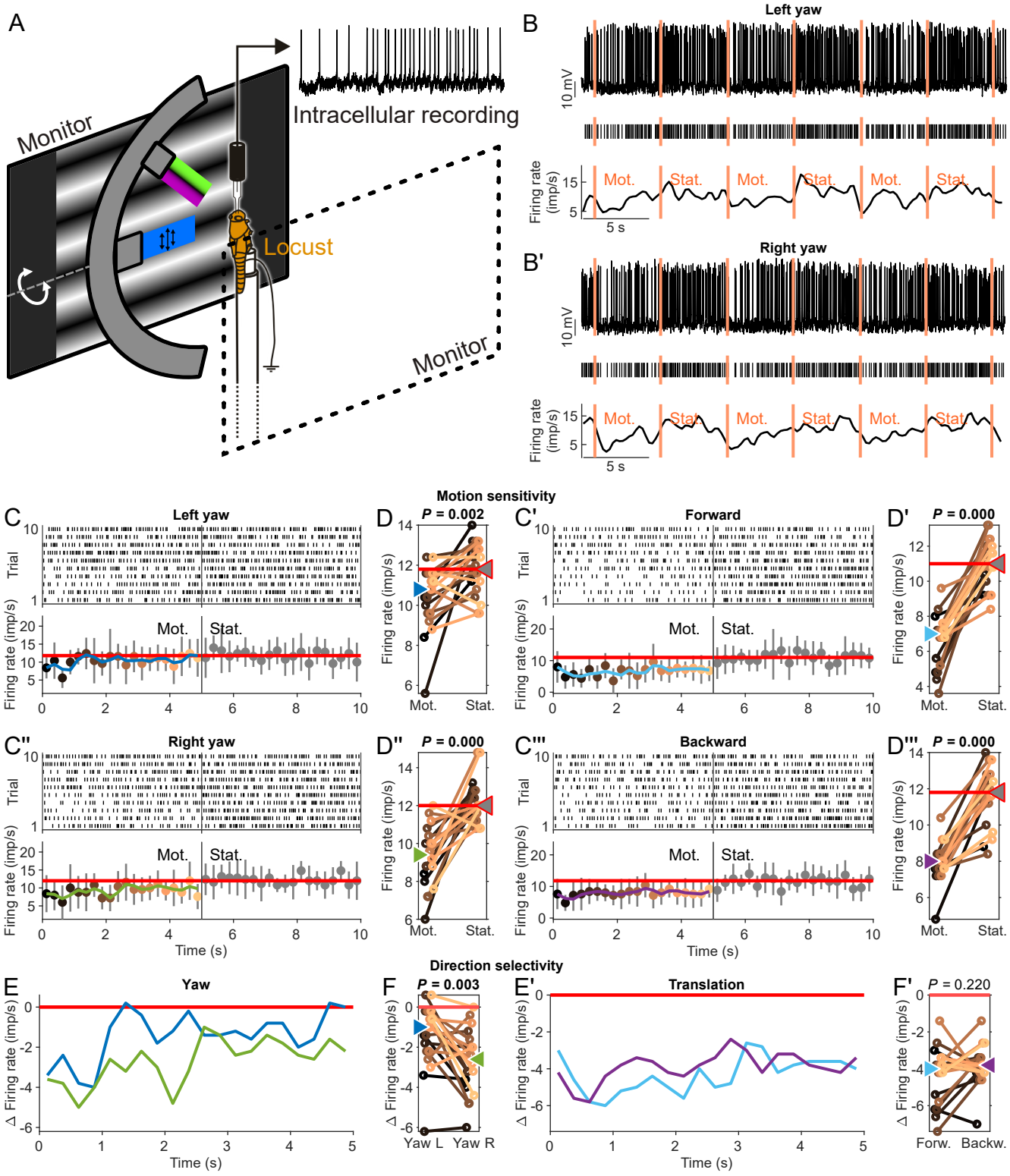
A
Monitor
Intracellular recording
Locust
Monitor
B
Left yaw
10 mV
Firing rate (imp/s)
Mot.
Stat.
5 s
B'
Right yaw
Motion sensitivity
C
Left yaw
Trial
Firing rate (imp/s)
D
P = 0.002
C'
Forward
D'
P = 0.000
C''
Right yaw
D''
C'''
Backward
D'''
Time (s)
Direction selectivity
E
Yaw
Δ Firing rate (imp/s)
F
P = 0.003
Yaw L
Yaw R
E'
Translation
F'
P = 0.220
Forw.
Backw.

FIGURE 1

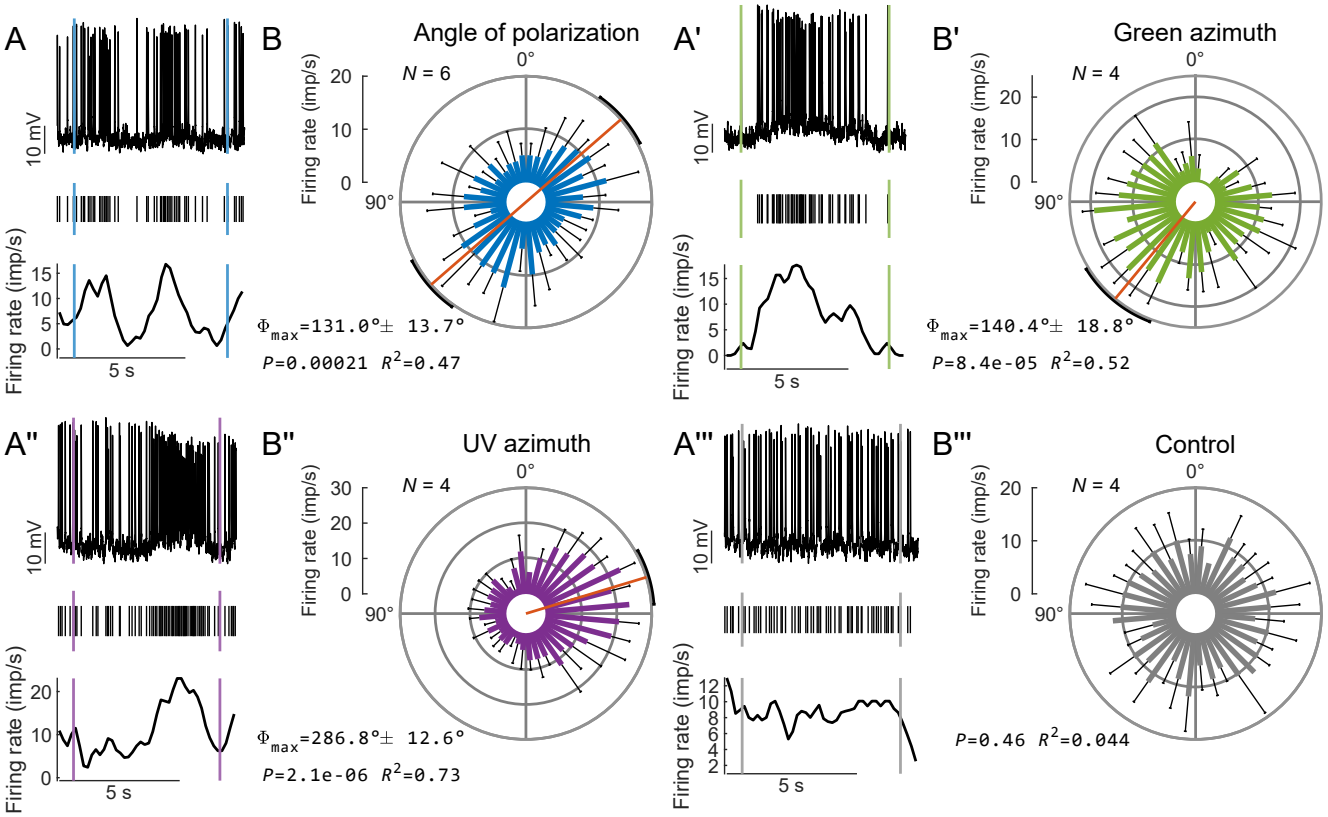
A
10 mV
Firing rate (imp/s)
5 s
B
Angle of polarization
N = 6
Firing rate (imp/s)
0°
90°
Φmax=131.0°± 13.7°
P=0.00021 R2=0.47
A'
B'
Green azimuth
N = 4
Φmax=140.4°± 18.8°
P=8.4e-05 R2=0.52
A''
B''
UV azimuth
N = 4
Φmax=286.8°± 12.6°
P=2.1e-06 R2=0.73
A'''
B'''
Control
N = 4
P=0.46 R2=0.044

FIGURE 2

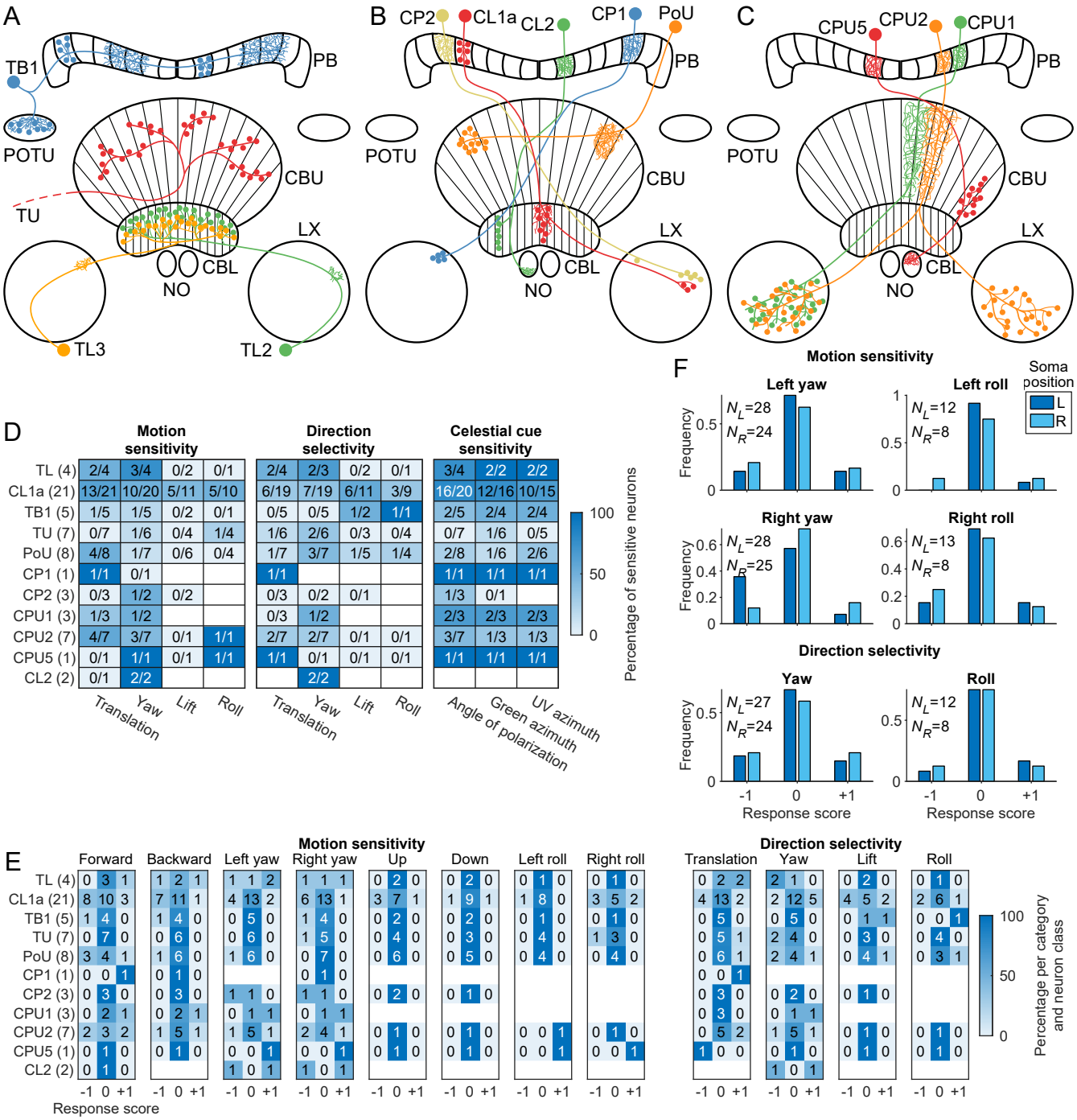
A
TB1
PB
POTU
CBU
TU
LX
CBL
NO
TL3
TL2
B
CP2
CL1a
CL2
CP1
PoU
C
CPU5
CPU2
CPU1
D
Motion sensitivity
Direction selectivity
Celestial cue sensitivity
TL (4) 2/4 3/4 0/2 0/1 2/4 2/3 0/2 0/1 3/4 2/2 2/2
CL1a (21) 13/21 10/20 5/11 5/10 6/19 7/19 6/11 3/9 16/20 12/16 10/15
TB1 (5) 1/5 1/5 0/2 0/1 0/5 0/5 1/2 1/1 2/5 2/4 2/4
TU (7) 0/7 1/6 0/4 1/4 1/6 2/6 0/3 0/4 0/7 1/6 0/5
PoU (8) 4/8 1/7 0/6 0/4 1/7 3/7 1/5 1/4 2/8 1/6 2/6
CP1 (1) 1/1 0/1 1/1 1/1 1/1
CP2 (3) 0/3 1/2 0/2 0/3 0/2 0/1 1/3 0/1
CPU1 (3) 1/3 1/2 0/3 1/2 2/3 2/3 2/3
CPU2 (7) 4/7 3/7 0/1 1/1 2/7 2/7 0/1 0/1 3/7 1/3 1/3
CPU5 (1) 0/1 1/1 0/1 1/1 1/1 0/1 0/1 0/1 1/1 1/1 1/1
CL2 (2) 0/1 2/2 2/2
Translation Yaw Lift Roll Translation Yaw Lift Roll Angle of polarization Green azimuth UV azimuth
100 50 0
Percentage of sensitive neurons
F
Motion sensitivity
Left yaw
Left roll
Right yaw
Right roll
Soma position
L
R
Frequency
N_L=28 N_R=24
N_L=12 N_R=8
N_L=28 N_R=25
N_L=13 N_R=8
Direction selectivity
Yaw
Roll
N_L=27 N_R=24
N_L=12 N_R=8
-1 0 +1
Response score
E
Motion sensitivity
Forward Backward Left yaw Right yaw Up Down Left roll Right roll
TL (4) 0 3 1 1 2 1 1 1 2 1 1 1 0 2 0 0 2 0 0 1 0 0 1 0
CL1a (21) 8 10 3 7 11 1 4 13 2 6 13 1 3 7 1 1 9 1 1 8 0 3 5 2
TB1 (5) 1 4 0 1 4 0 0 5 0 1 4 0 0 2 0 0 2 0 0 1 0 0 1 0
TU (7) 0 7 0 0 6 0 0 6 0 1 5 0 0 4 0 0 3 0 0 4 0 1 3 0
PoU (8) 3 4 1 1 6 0 1 6 0 0 7 0 0 6 0 0 5 0 0 4 0 0 4 0
CP1 (1) 0 0 1 0 1 0 0 1 0
CP2 (3) 0 3 0 0 3 0 1 1 0 1 1 0 0 2 0 0 1 0
CPU1 (3) 0 2 1 0 2 1 0 1 1 0 1 1
CPU2 (7) 2 3 2 1 5 1 1 5 1 2 4 1 0 1 0 0 1 0 0 0 1 0 1 0
CPU5 (1) 0 1 0 0 1 0 0 0 1 0 0 1 1 0 1 0 1 0 0 0 1 0 0 1
CL2 (2) 0 1 0 1 0 1
-1 0 +1
Response score
Direction selectivity
Translation Yaw Lift Roll
0 2 2 2 1 0 0 2 0 0 1 0
4 13 2 2 12 5 4 5 2 2 6 1
0 5 0 0 5 0 0 1 1 0 0 1
0 5 1 2 4 0 0 3 0 0 4 0
0 6 1 2 4 1 0 4 1 0 3 1
0 0 1
0 3 0 0 2 0 0 1 0
0 3 0 0 1 1
0 5 2 1 5 1 0 1 0 0 1 0
1 0 0 1 0 1 0 0 1 0 0 1
100 50 0
Percentage per category and neuron class

FIGURE 3

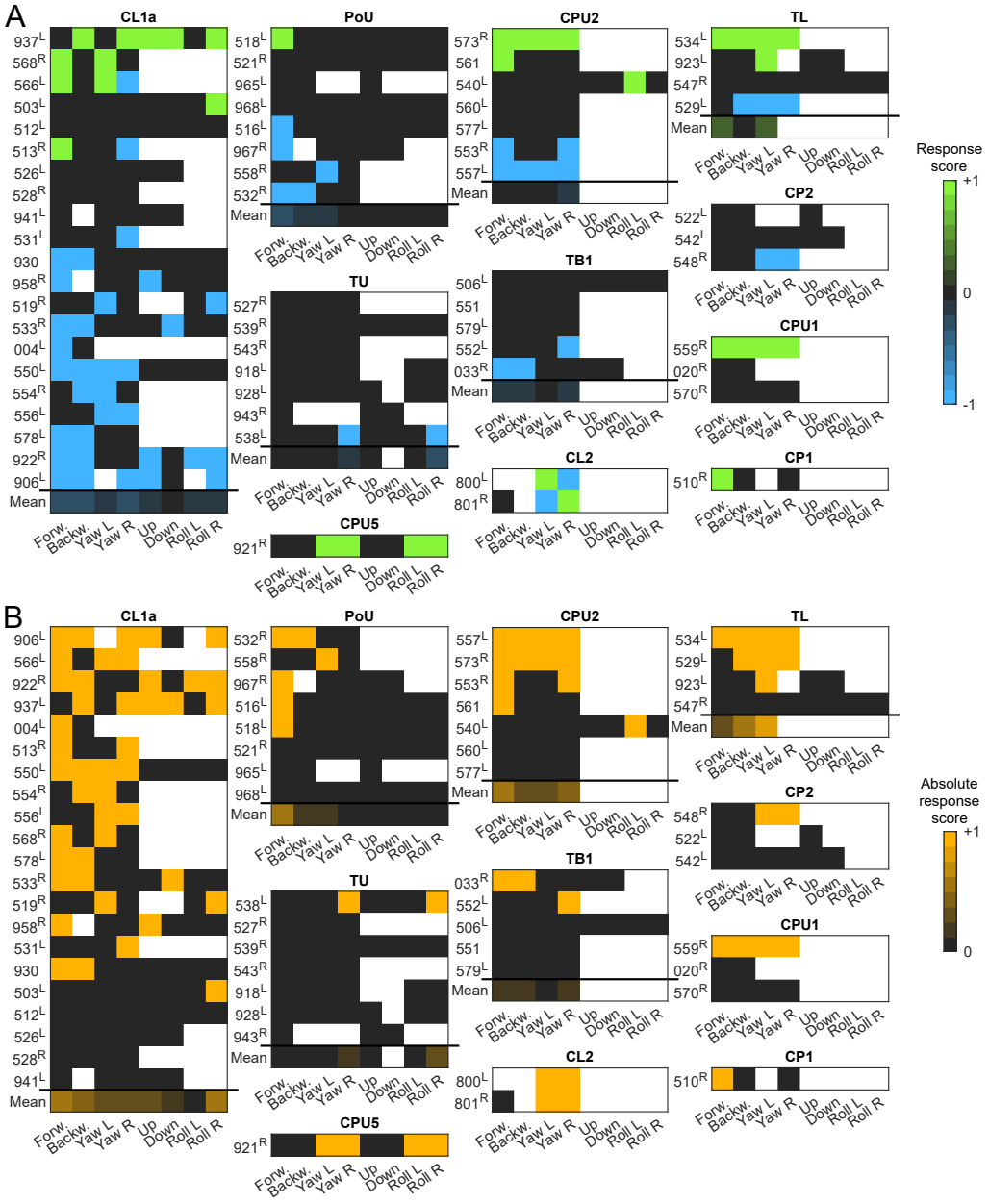
A
CL1a
937L
568R
566L
503L
512L
513R
526L
528R
941L
531L
930
958R
519R
533R
004L
550L
554R
556L
578L
922R
906L
Mean
PoU
518L
521R
965L
968L
516L
967R
558R
532R
Mean
CPU2
573R
561
540L
560L
577L
553R
557L
Mean
TL
534L
923L
547R
529L
Mean
CP2
522L
542L
548R
TB1
506L
551
579L
552L
033R
Mean
CPU1
559R
020R
570R
TU
527R
539R
543R
918L
928L
943R
538L
Mean
CL2
800L
801R
CP1
510R
CPU5
921R
Forw.
Backw.
Yaw L
Yaw R
Up
Down
Roll L
Roll R
Response score
+1
0
-1
B
CL1a
906L
566L
922R
937L
004L
513R
550L
554R
556L
568R
578L
533R
519R
958R
531L
930
503L
512L
526L
528R
941L
Mean
PoU
532R
558R
967R
516L
518L
521R
965L
968L
Mean
CPU2
557L
573R
553R
561
540L
560L
577L
Mean
TL
534L
529L
923L
547R
Mean
CP2
548R
522L
542L
TB1
033R
552L
506L
551
579L
Mean
CPU1
559R
020R
570R
TU
538L
527R
539R
543R
918L
928L
943R
Mean
CL2
800L
801R
CP1
510R
CPU5
921R
Absolute response score
+1
0

FIGURE 4

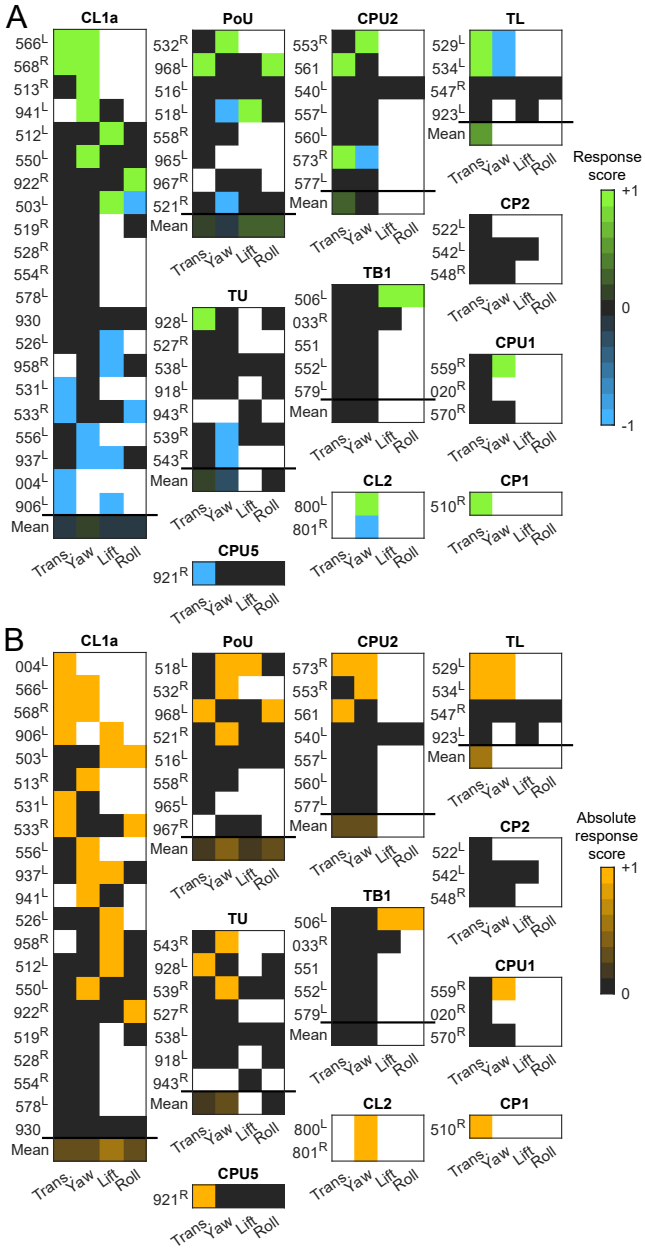
A
CL1a
566L
568R
513R
941L
512L
550L
922R
503L
519R
528R
554R
578L
930
526L
958R
531L
533R
556L
937L
004L
906L
Mean
Trans Yaw Lift Roll
PoU
532R
968L
516L
518L
558R
965L
967R
521R
Mean
Trans Yaw Lift Roll
CPU2
553R
561
540L
557L
560L
573R
577L
Mean
Trans Yaw Lift Roll
TL
529L
534L
547R
923L
Mean
Trans Yaw Lift Roll
Response score
+1
0
-1
CP2
522L
542L
548R
Trans Yaw Lift Roll
TU
928L
527R
538L
918L
943R
539R
543R
Mean
Trans Yaw Lift Roll
TB1
506L
033R
551
552L
579L
Mean
Trans Yaw Lift Roll
CPU1
559R
020R
570R
Trans Yaw Lift Roll
CL2
800L
801R
Trans Yaw Lift Roll
CP1
510R
Trans Yaw Lift Roll
CPU5
921R
Trans Yaw Lift Roll
B
CL1a
004L
566L
568R
906L
503L
513R
531L
533R
556L
937L
941L
526L
958R
512L
550L
922R
519R
528R
554R
578L
930
Mean
Trans Yaw Lift Roll
PoU
518L
532R
968L
521R
516L
558R
965L
967R
Mean
Trans Yaw Lift Roll
CPU2
573R
553R
561
540L
557L
560L
577L
Mean
Trans Yaw Lift Roll
TL
529L
534L
547R
923L
Mean
Trans Yaw Lift Roll
Absolute response score
+1
0
CP2
522L
542L
548R
Trans Yaw Lift Roll
TU
543R
928L
539R
527R
538L
918L
943R
Mean
Trans Yaw Lift Roll
TB1
506L
033R
551
552L
579L
Mean
Trans Yaw Lift Roll
CPU1
559R
020R
570R
Trans Yaw Lift Roll
CL2
800L
801R
Trans Yaw Lift Roll
CP1
510R
Trans Yaw Lift Roll
CPU5
921R
Trans Yaw Lift Roll

FIGURE 5

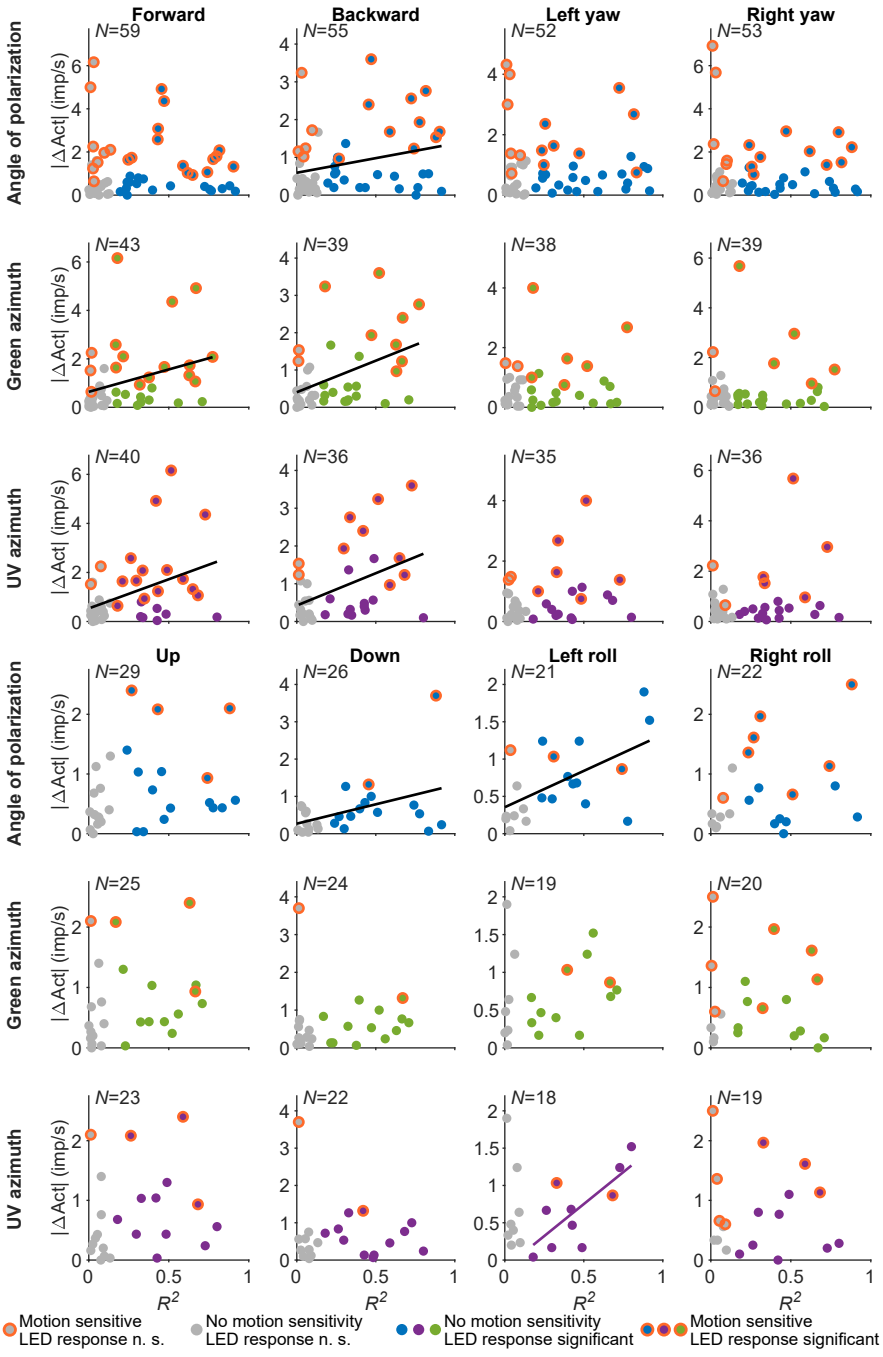
Forward
Backward
Left yaw
Right yaw
Up
Down
Left roll
Right roll
Angle of polarization
Green azimuth
UV azimuth
|ΔAct| (imp/s)
R^2
N=59
N=55
N=52
N=53
N=43
N=39
N=38
N=39
N=40
N=36
N=35
N=36
N=29
N=26
N=21
N=22
N=25
N=24
N=19
N=20
N=23
N=22
N=18
N=19
Motion sensitive
LED response n. s.
No motion sensitivity
LED response n. s.
No motion sensitivity
LED response significant
Motion sensitive
LED response significant

FIGURE 6

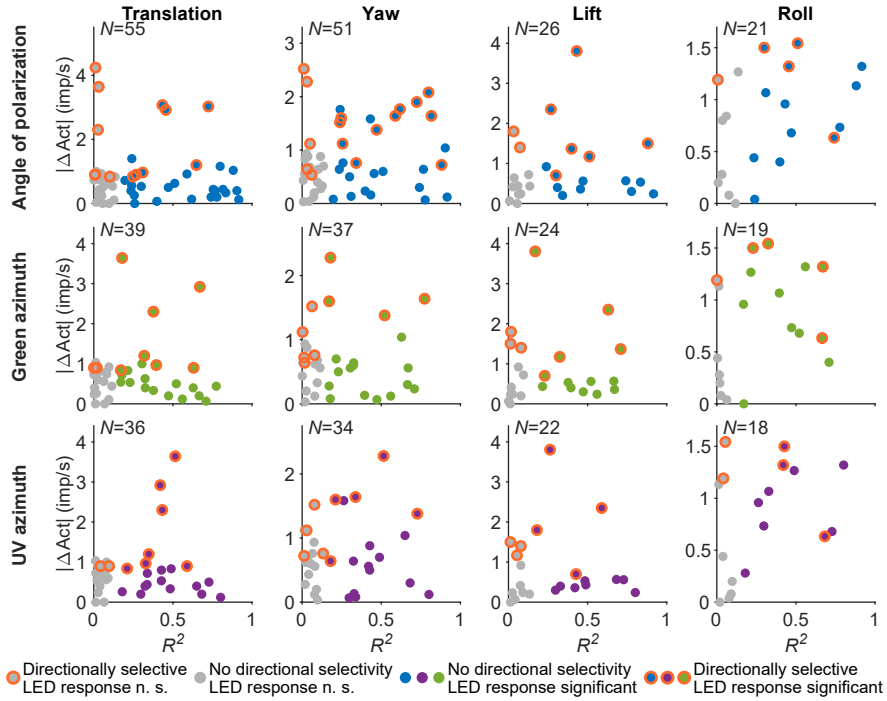

FIGURE 7

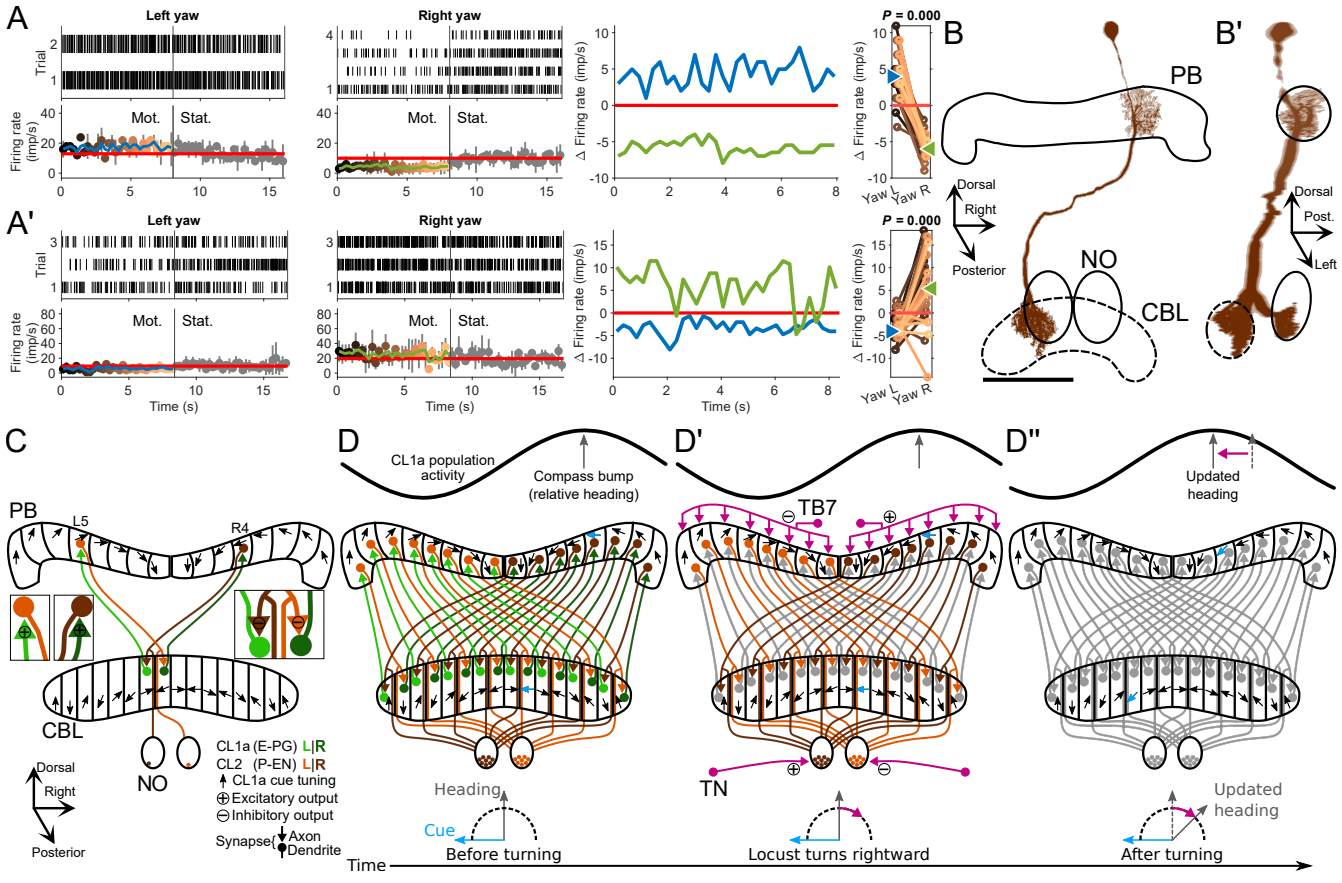

FIGURE 8

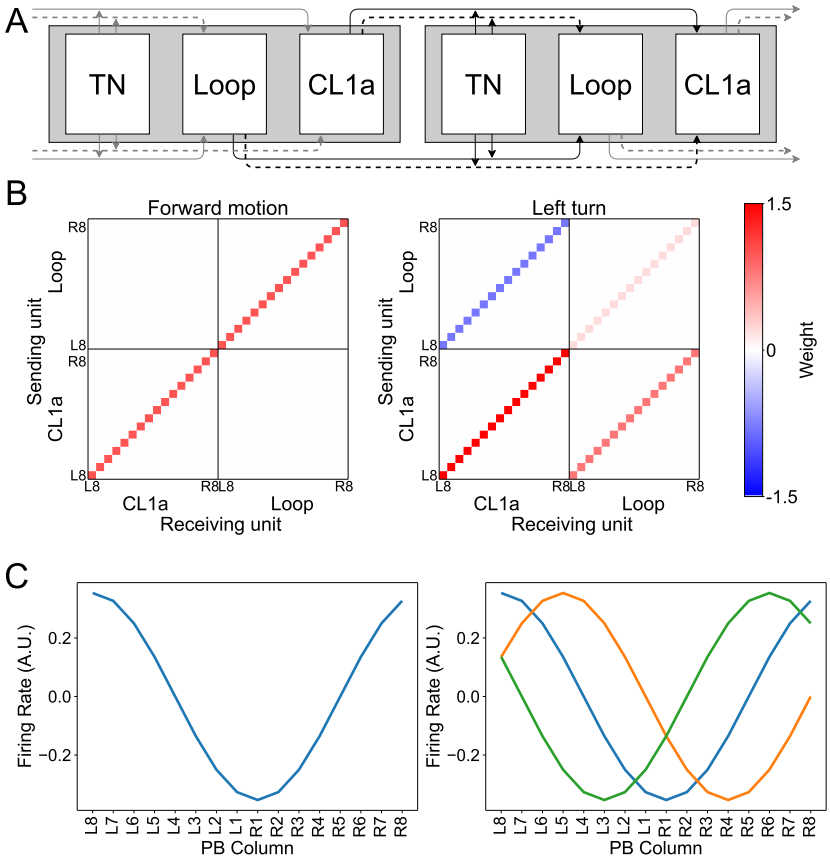
A
TN
Loop
CL1a
TN
Loop
CL1a
B
Forward motion
Left turn
Sending unit
CL1a
Loop
Receiving unit
R8
L8
1.5
0
-1.5
Weight
C
Firing Rate (A.U.)
0.2
0.0
−0.2
L8 L7 L6 L5 L4 L3 L2 L1 R1 R2 R3 R4 R5 R6 R7 R8
PB Column

FIGURE 9

Chapter 6

A Unified Platform To Manage, Share, and Archive Morphological and Functional Data in Insect Neuroscience

eLife

TOOLS AND RESOURCES

A unified platform to manage, share, and archive morphological and functional data in insect neuroscience

Stanley Heinze[1,2]*, Basil el Jundi[3], Bente G Berg[4], Uwe Homberg[5], Randolf Menzel[6], Keram Pfeiffer[3], Ronja Hensgen[5], Frederick Zittrell[5], Marie Dacke[1], Eric Warrant[7], Gerit Pfuhl[4,8], Jürgen Rybak[9], Kevin Tedore[1]

[1]Department of Biology, Lund University, Lund, Sweden; [2]NanoLund, Lund University, Lund, Sweden; [3]Biocenter, Behavioral Physiology and Sociobiology, University of Würzburg, Würzburg, Germany; [4]Department of Psychology, Chemosensory lab, Norwegian University of Science and Technology, Trondheim, Norway; [5]Fachbereich Biologie, Tierphysiologie, and Center for Mind Brain and Behavior (CMBB), University of Marburg and Justus Liebig University Giessen, Marburg, Germany; [6]Institut für Biologie - Neurobiologie, Free University, Berlin, Germany; [7]Research School of Biology, Australian National University, Canberra, Australia; [8]Department of Psychology, UiT The Arctic University of Norway, Tromso, Norway; [9]Department of Evolutionary Neuroethology, Max Planck Institute for Chemical Ecology, Jena, Germany

Abstract Insect neuroscience generates vast amounts of highly diverse data, of which only a small fraction are findable, accessible and reusable. To promote an open data culture, we have therefore developed the InsectBrainDatabase (*IBdb*), a free online platform for insect neuroanatomical and functional data. The *IBdb* facilitates biological insight by enabling effective cross-species comparisons, by linking neural structure with function, and by serving as general information hub for insect neuroscience. The *IBdb* allows users to not only effectively locate and visualize data, but to make them widely available for easy, automated reuse via an application programming interface. A unique private mode of the database expands the *IBdb* functionality beyond public data deposition, additionally providing the means for managing, visualizing, and sharing of unpublished data. This dual function creates an incentive for data contribution early in data management workflows and eliminates the additional effort normally associated with publicly depositing research data.

***For correspondence:** stanley.heinze@biol.lu.se

Competing interest: See page 22

Funding: See page 22

Preprinted: 01 December 2020
Received: 02 December 2020
Accepted: 21 August 2021
Published: 24 August 2021

Reviewing editor: Ronald L Calabrese, Emory University, United States

Introduction

Data are the essence of what science delivers - to society, to researchers, to engineers, to entrepreneurs. These data enable progress, as they provide the basis on which new experiments are designed, new machines are developed, and from which new ideas emerge. Independent of the research field, many terabytes of data are produced every year, yet only a small fraction of these data become openly available to other researchers, with even less penetrating the invisible wall between the scientific community and the public (***Mayernik, 2017***). While research papers report conclusions that are based on data and present summaries and analyses, the underlying data most often remain unavailable, despite their value beyond the original context. Whereas this is changing in many fields and the use of open data repositories becomes increasingly mandatory upon publication of a research paper, this is not ubiquitous and older data remain inaccessible in most instances.

eLife digest Insect neuroscience, like any field in the natural sciences, generates vast amounts of data. Currently, only a fraction are publicly available, and even less are reusable. This is because insect neuroscience data come in many formats and from many species. Some experiments focus on what insect brains look like (morphology), while others focus on how insect brains work (function). Some data come in the form of high-speed video, while other data contain voltage traces from individual neurons. Sharing is not as simple as uploading the raw files to the internet.

To get a clear picture of how insect brains work, researchers need a way to cross-reference and connect different experiments. But, as it stands, there is no dedicated place for insect neuroscientists to share and explore such a diverse body of work. The community needs an open data repository that can link different types of data across many species, and can evolve as more data become available. Above all, this repository needs to be easy for researchers to use.

To meet these specifications, Heinze et al. developed the Insect Brain Database. The database organizes data into three categories: species, brain structures, and neuron types. Within these categories, each entry has its own profile page. These pages bring different experiments together under one heading, allowing researchers to combine and compare data of different types. As researchers add more experiments, the profile pages will grow and evolve. To make the data easy to navigate, Heinze et al. developed a visual search tool. A combination of 2D and 3D images allow users to explore the data by anatomical location, without the need for expert knowledge. Researchers also have the option to upload their work in private mode, allowing them to securely share unpublished data.

The Insect Brain Database brings data together in a way that is accessible not only to researchers, but also to students, and non-scientists. It will help researchers to find related work, to reuse existing data, and to build an open data culture. This has the potential to drive new discoveries combining research across the whole of the insect neuroscience field.

Additionally, merely meeting the data deposition requirement by 'dumping' poorly annotated raw files on an internet platform does not aid transparency or reuse of the data. To ensure common standards for data repositories and the datasets to be stored in them, the FAIR principles for data deposition (Findability, Accessibility, Interoperability, and Reusability) were developed (***Wilkinson et al., 2016***). It is clear from these principles that annotation and rich metadata are essential, if a dataset is supposed to be beneficial to others. While this is relatively easily achievable for data such as gene sequences, protein sequences, or numerical datasets, the challenges are much bigger for complex morphological data, physiological observations, or behavioral studies. The difficulties result not only from large file sizes of image stacks, high-speed videos, or recorded voltage traces, but also from the heterogeneous data structure often generated by custom designed software or equipment.

Insect neuroscience is no stranger to these challenges. Particularly for research outside the genetically accessible fruit fly *Drosophila*, no universal data repository exists that allows retrieval of original observations that underlie published articles. Research groups worldwide investigate the nervous systems of a wide range of insect species, but mostly operate in isolation of each other. Data from these projects are often deposited in local backup facilities of individual institutions and thus remain inaccessible to the community. Combined with a lack of interoperability caused by independent choices of data formats this has the potential to severely hamper progress, given that interspecies comparison is one of the existential pillars on which insect neuroscience rests. The problem is amplified by the fact that much of the data are both large and heterogeneous (e.g. 2D and 3D images, models of brain regions, digital neuron reconstructions, immunostaining patterns, electrophysiological recordings, functional imaging data).

A final problem is that depositing well-annotated data takes time and effort, and little incentive is generally given to prioritize this work over acquiring new data or publishing research papers. While this is true for all research fields, the complex data in neuroscience requires an extra amount of effort to meet acceptable standards. This has made depositing data in a form that is useful to the community a relatively rare event. Early efforts were made to develop brain databases for various insect

species (e.g. honeybee [**Brandt et al., 2005**], *Manduca sexta* [**El Jundi et al., 2009a**], *Tribolium castaneum* [**Dreyer et al., 2010**], desert locust [**Kurylas et al., 2008**]), but in those cases, the anticipated interactive platforms for exchange and deposition of anatomical data were short-lived and not used beyond the laboratories that hosted them. More recently, several successful databases for anatomical data from insects were developed. Most notably, Virtual Fly Brain (VFB) (**Osumi-Sutherland et al., 2014**) now bundles most efforts in the *Drosophila* community regarding the deposition of neuroanatomical data - including single-cell morphologies from light microscopy, data from recent connectomics projects (most notably from **Scheffer et al., 2020**), as well as catalogues of GAL4 driver lines, which enable access to specific neurons with genetic methods. VFB hosts most content of older independent databases, such as FlyCircuit (**Chiang et al., 2011**) and FlyBrain (**Armstrong et al., 1995**) and is dedicated to providing smart ways of utilizing and visualizing *Drosophila* neuroanatomy. Similarly, but more focused on data visualization and connectivity modeling, the FruitFlyBrainObservatory allows access to current datasets of single neuron morphologies from *Drosophila*. Another database, founded in 2007, has grown substantially over recent years: NeuroMorpho.Org (**Ascoli et al., 2007**). It provides 3D reconstructed datasets of more than 100,000 neurons from across animal species and includes substantial numbers of single-cell data from insects. While the latter platform is comparative in nature, it does not offer dedicated tools for comparisons between species or much context for the deposited neuron skeletons. In contrast, the data on VFB are much richer and different datasets are tightly linked to each other, allowing, for example, correlation between GAL4 driver lines and electron microscopy based single neuron reconstructions. Yet, no comparison to other species is possible or intended via VFB. Additionally, no systematic information is provided about the function of the deposited neurons in either database, precluding insights into the structure-function relations that are critically important to understanding the insect brain.

To address these shortcomings we have developed the Insect Brain Database (*IBdb*), a cross-species, web-based platform designed for depositing and sharing research data that consist of morphological and functional information from insect brains. With an overall modular design, a concept for dual use as depository and data management tool, combined with widely useful visualization tools, this database yields a tool for increasing transparency, accessibility, and interoperability of insect neuroscience data. Moreover, the newly developed concepts are not only relevant to insect neuroscience, but to any scientific field that can be linked to a hierarchically organized framework. We thus hope that our conceptual design can be adopted by a range of users from across the sciences to simplify data handling and make scientific results in general more transparent.

Results

Database outline

The 'Insect Brain Database' (*IBdb*) can be found on the internet at insectbraindb.org and is freely available to everyone. It can be used with most modern web browsers with active Javascript (tested with Google Chrome, Safari, Firefox) on computers running any operating system, without the need for any additional plugins. A user account can be registered free of charge and is required for users who wish to download data and to contribute content.

The *IBdb* is divided into three main hierarchical layers: Species, brain structures, and neuron types. Each level is additionally linked to 'experiments', which is the fourth major organizational layer of the database (**Figure 1A**). At each level, a database entry is represented by profile pages, on which all relevant information is collected (**Figure 1C**). These profile pages are the core of the database. They can be reached directly by several search functions, as well as by entry lists. As profile pages are embedded in a hierarchical framework of species, brain regions, and cell types, they become automatically associated with metadata. For instance, an entry for a pontine neuron of the fan-shaped body (central body upper division) in the monarch butterfly would become linked to the brain regions 'fan-shaped body/central body upper division' and its parent region 'central complex', as well as to 'monarch butterfly' as species. The neuron can then be found, for example, by querying the brain regions associated with it, or by exploring the species of interest.

Species entries contain representative data of an insect species, with the aim of defining that species and the overall layout of its brain. Similarly, entries for brain regions and cell types contain representative examples of data that illustrate the respective entity and provide all information to

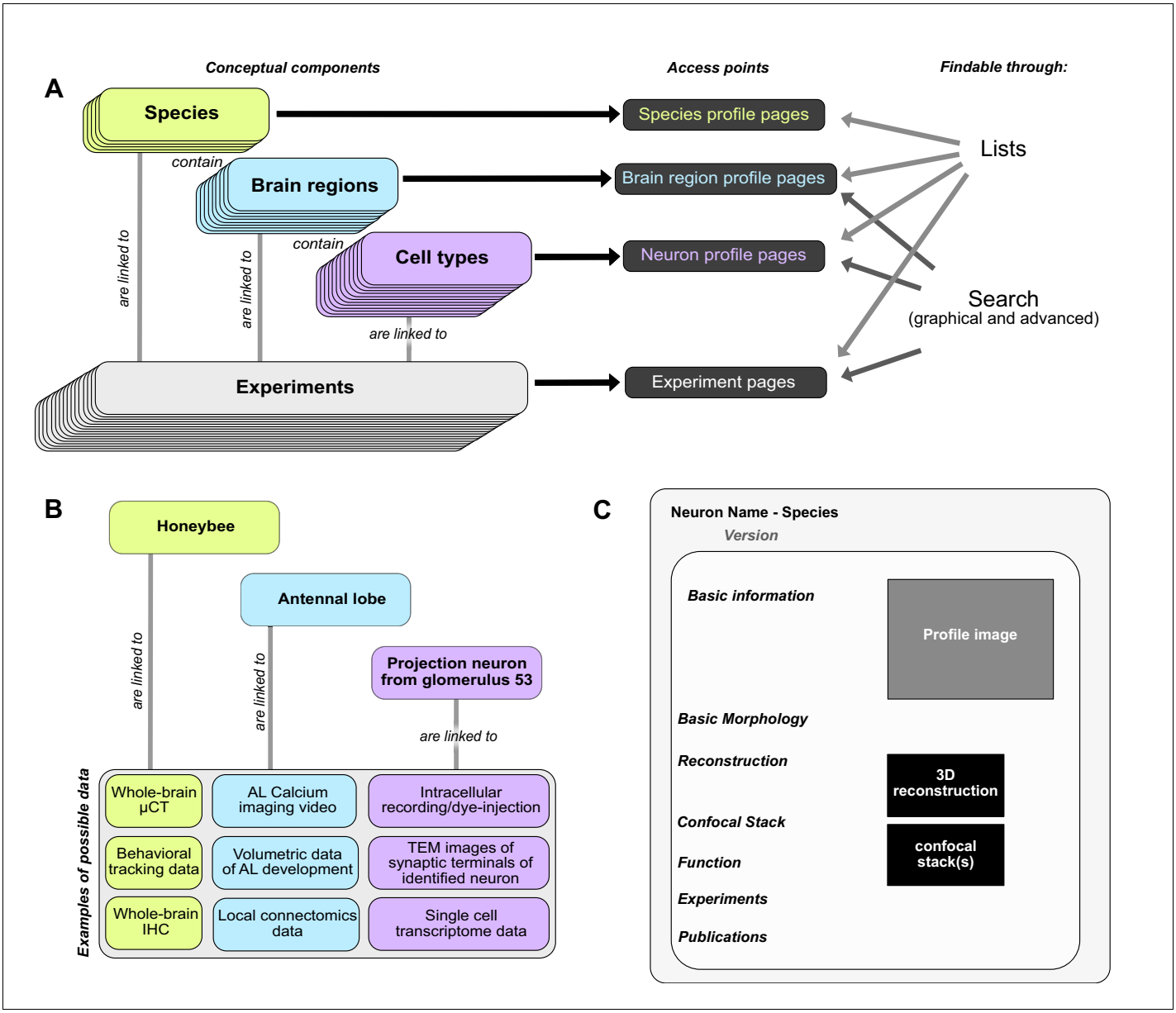

Figure 1. Basic concepts behind the Insect Brain Database. (**A**) Organizational layers of the database. Elements in each layer are represented on their respective profile pages, which can be located either through lists or search interfaces. (**B**) Examples for information that can be deposited on each level of the database, illustrating how diverse data is automatically associated with hierarchical metadata. (**C**) Schematic illustration of a neuron profile page. Detailed anatomical and functional data is available on this page, from where experiments associated with this cell type are also linked. Similar pages exist for species and brain regions. Abbreviations: AL, antennal lobe; IHC, immunohistochemistry; TEM, transmission electron microscopy; µCT, micro computed tomography.

The online version of this article includes the following figure supplement(s) for figure 1:

Figure supplement 1. Technical overview of database layout.

Figure supplement 2. Definition of cell types.

unambiguously define it, essentially providing type-specimen. While the definition of species and brain regions are straight forward in the context of this database, neuron types can theoretically be defined in many different ways, based on connectivity, function, developmental origin, morphology or neurochemical identity. Given that the database is predominantly organized according to anatomical principles, we have defined a cell type as a collection of individual neurons that are morphologically indistinguishable at the level of light microscopy. In many cases, a cell type comprises only a

single individual per brain hemisphere, but in cases where multiple identical neurons are present, a cell type is defined as the first level of similarity beyond the individual neuron. Higher levels of neuron categories group neurons according to anatomical similarities (***Figure 1—figure supplement 2***).

Contrary to the first three levels, experiment entries contain specific data from individual, defined experiments (***Figure 1B***). As research data can be obtained at the levels of species, brain regions and cell types, experiment entries exist for all three levels and are accessible via the respective profile pages (***Figure 1A***). This distinction between representative and concrete data is important, as for example only one entry for a certain columnar neuron type of the central complex exists in the database, yet, if that single cell type was subject to 30 intracellular recordings, the profile page of that cell type would list 30 experiments, each containing a unique individual neuron with its associated physiology. While an anatomical type specimen can easily be defined as the most complete example of any particular neuron's morphology, the decision of what content to depict as representative functional data is less straight forward. The functional information on the profile page should reflect the range of experimental results present in the experiment entries of any particular cell type. As those results potentially diverge, for example due to different experimental paradigms used in different research groups, the function section can contain as many entries as needed to capture the available information, without need for consensus. With new experiment entries added, this section can evolve over time.

In the context of this evolving content, it is key to ensure that entries which are cited in published work remain findable in the exact form they existed when they were cited (***Ito, 2010***). Therefore each entry receives a persistent identifier. This identifier (a 'handle') links to a version of the entry that was frozen at the time it was created (and cited). Once information is added or removed from that entry, a new handle must be generated, providing a new access link for future citations. This system is applied to multiple levels of the database (experiments, neurons, and species) and ensures that all information in the database, as well as the interrelations between entries, are truly persistent.

Interactive search interfaces

As locating specific datasets is one of the core functions of a database, we have developed a novel, more intuitive way to find specific neuron data. A graphical representation of the insect brain, resembling the overall anatomical outline of all brain regions and highlighting the regions containing neuron data (***Figure 2A***), makes it easy to search for neurons within single species and across species. This graphical interface is generated directly on the database website for each species and is adapted from a generic insect brain, that is a shared ground plan. This generic brain is the least detailed fall-back option for any cross-species search and was generated based on the insect brain nomenclature developed by ***Insect Brain Name Working Group et al., 2014***. It resembles the shared anatomical hierarchy of all brain regions in insect brains. Within this hierarchy, the entire brain is divided into 13 super-regions, which consist of individual neuropils. The latter can be further divided into sub-regions. While all super-regions exist in all species, differences become more pronounced at lower levels of the hierarchy. The generic brain therefore largely contains super-regions as well as several highly conserved neuropils (***Figure 2—figure supplement 1***, ***Figure 2—figure supplement 2***). As these categories are simply tags of brain region entries used to organize the database, the search interface does not differentiate between them, simplifying the user experience (***Figure 2A***).

If more than one species is subject to a query, a schematic brain is generated that displays the commonly shared features of the species involved. For both single and multi-species search, when selecting a specific brain region, all neurons in the *IBdb* that connect to this region become visualized by a dynamically drawn wiring diagram (***Figure 2B***). Filters can be applied to narrow down search results according to neuron polarity, functional class, etc. Individual neurons in the wiring diagram can be selected to reveal the neuron's profile page. Here, all available information for this cell type is displayed, including links to deposited experiment entries (***Figure 2C***). The schematic display of search results can visualize any neuron in the database, only requiring that a neuron is annotated with respect to the brain regions it innervates. A list of search results is additionally made available after each search and offers the possibility to also display experiment entries associated with the found neurons.

For single species queries, two more modes for visualizing search results are available: the semi-schematic view and the 3D view. The semi-schematic view mode emphasizes the natural brain

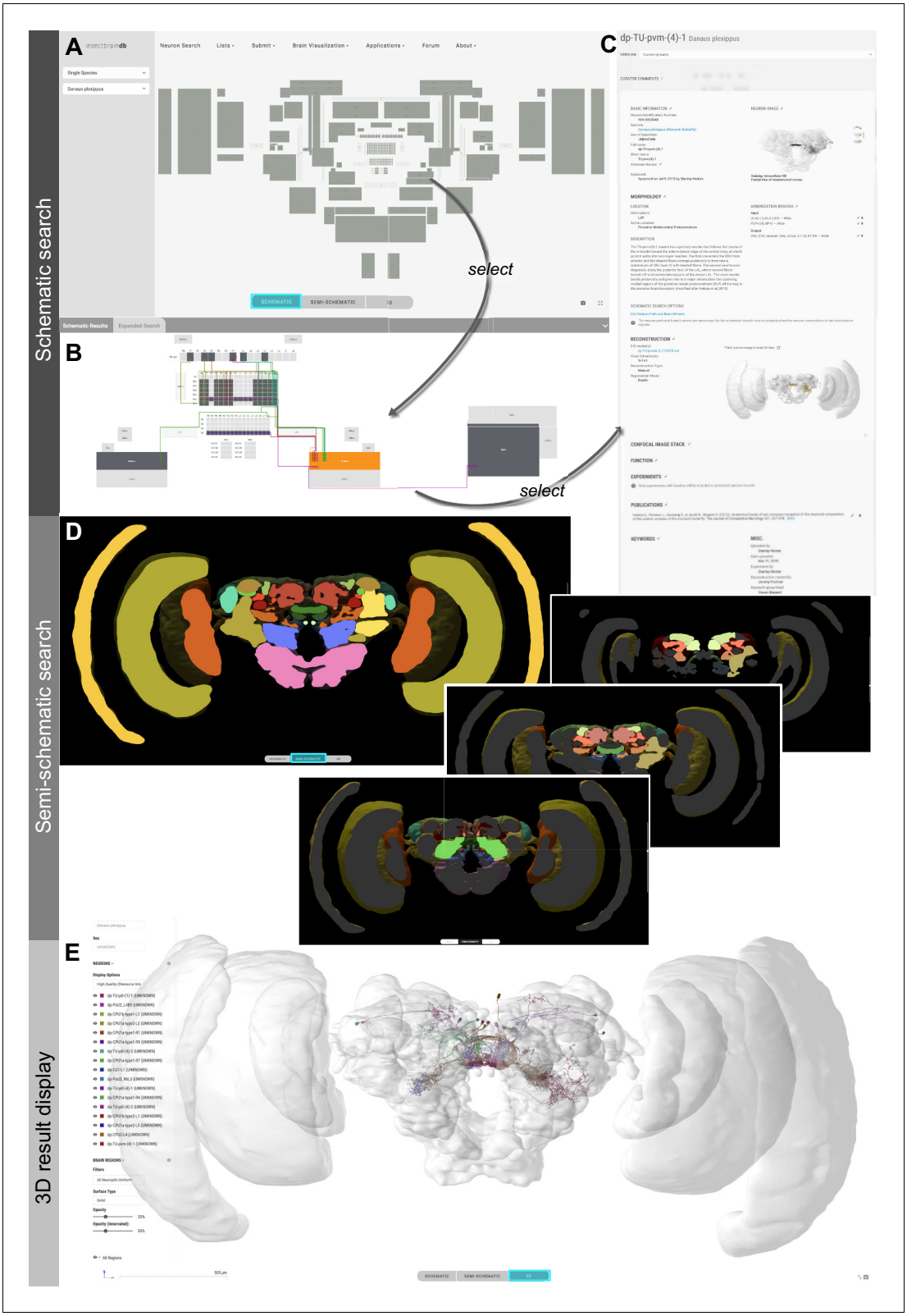

Figure 2. Neuron search in the *IBdb*. (**A**) Screenshot of the schematic brain search interface (Monarch butterfly) in single species mode. Selecting a neuropil will reveal all neurons connected to that neuropil. (**B**) Schematic wiring diagram view of the search result; orange neuropil was queried. Selecting an individual neuron will reveal the profile page of that cell type. (**C**) Example of a neuron profile page with anatomical information. Confocal image stack and functional data are not listed in this example. (**D**) Semi-schematic search interface. The section view is scrollable and allows the user to

Figure 2 continued on next page

Figure 2 continued

query individual neuropils for connected neurons by clicking the cross section. The inserts show the results view at three levels of the brain. Neuropils connected to the queried neuropil are highlighted. Switching to the schematic view will then show the neurons as wiring diagram. Switching to the 3D mode will show registered neurons in 3D. (**E**) The 3D results viewer allows one to view all neurons registered into a common reference frame; example from Monarch butterfly (data from ***Heinze and Reppert, 2012***) . The user can continuously switch between the three modes (schematic, semi-schematic, 3D). All visualizations generated with Insectbraindb.org.

The online version of this article includes the following figure supplement(s) for figure 2:

Figure supplement 1. Schematic outline of generic brain and variations across species.

Figure supplement 2. Brain structures in the database and their hierarchical organization.

organization on the level of brain regions, while also serving as interface for launching search queries. It comprises a full series of automatically generated sections through a segmented 3D brain of a species. Each brain region present in that species' 3D brain is shown as an interactive cross section that can be used to query neural connections of that region (***Figure 2D***). If a region is selected, all connected brain areas are highlighted and neurons resulting from this query can be visualized by changing to either the schematic view, the 3D view, or a list view. The advantage of the anatomically correct layout of this interface is that a brain region can be queried for a neuron, even if its name is not known to the researcher. This is particularly useful for regions with uncommon names that have only recently been introduced to the insect brain naming scheme (e.g. crepine, superior clamp, etc., see ***Insect Brain Name Working Group et al., 2014***). Launching a search for neurons in regions with unfamiliar names is made much easier when the search interface resembles the information a researcher has obtained from, for example, confocal images or physical brain slices. The semi-schematic mode of the database search function fulfills this demand and bridges the schematic wiring diagram view and the full 3D view.

The 3D view visualizes search results in an anatomically correct way and shows queried neurons in the context of a species' reference brain (given that this information was added) (***Figure 2E***). It displays interactive surface models of that brain together with neuron skeletons obtained from the neuron-type's profile page.

In the graphical search interface the search parameters are limited to anatomical information defining the neuron's location in the brain (i.e. likely input and output areas). In contrast, an additional text-based search function ('Expert Search') allows users to query all information deposited on a neuron's profile page. Individual search parameters can be logically combined to generate arbitrarily complex searches. The results are displayed as a list of neurons, which can be sent to populate a schematic wiring diagram view by a single click. Thus, this tool effectively combines complex search with the advantages of an intuitive display of results.

A different means of locating data on neurons and experiments is achieved via a publication based search function. Each neuron and experiment that is associated with a publication becomes automatically part of a dataset linked to this publication. By definition, experiments are only part of one publication, while neuron entries can be referenced by many publications. In either case, users can locate all data that has contributed to a specific piece of scientific literature.

Finally, whereas the emphasis of the database search lies on locating cell types, information on brain regions can also be found using identical interfaces. The schematic search option allows users to reveal brain region profile pages by selecting schematic neuropil representations. The same information can also be obtained by selecting brain regions in the semi-schematic neuropil search interface.

Online applications and tools

To maximize the usefulness of the database, we have implemented an integrated 3D viewer to deliver platform independent, high-quality data visualization without any additional software demands. Neuropil visibility can be independently switched on and off for each brain region, transparency can be freely adjusted, and colors of neurons can be changed (***Figure 3A***). Neurons can be shown either with diameter information or as simple backbones. The built-in screenshot function enables the user to capture any scene displayed in the 3D viewer and produces a high-resolution, publication-ready image with transparent background (***Figure 3B,C***).

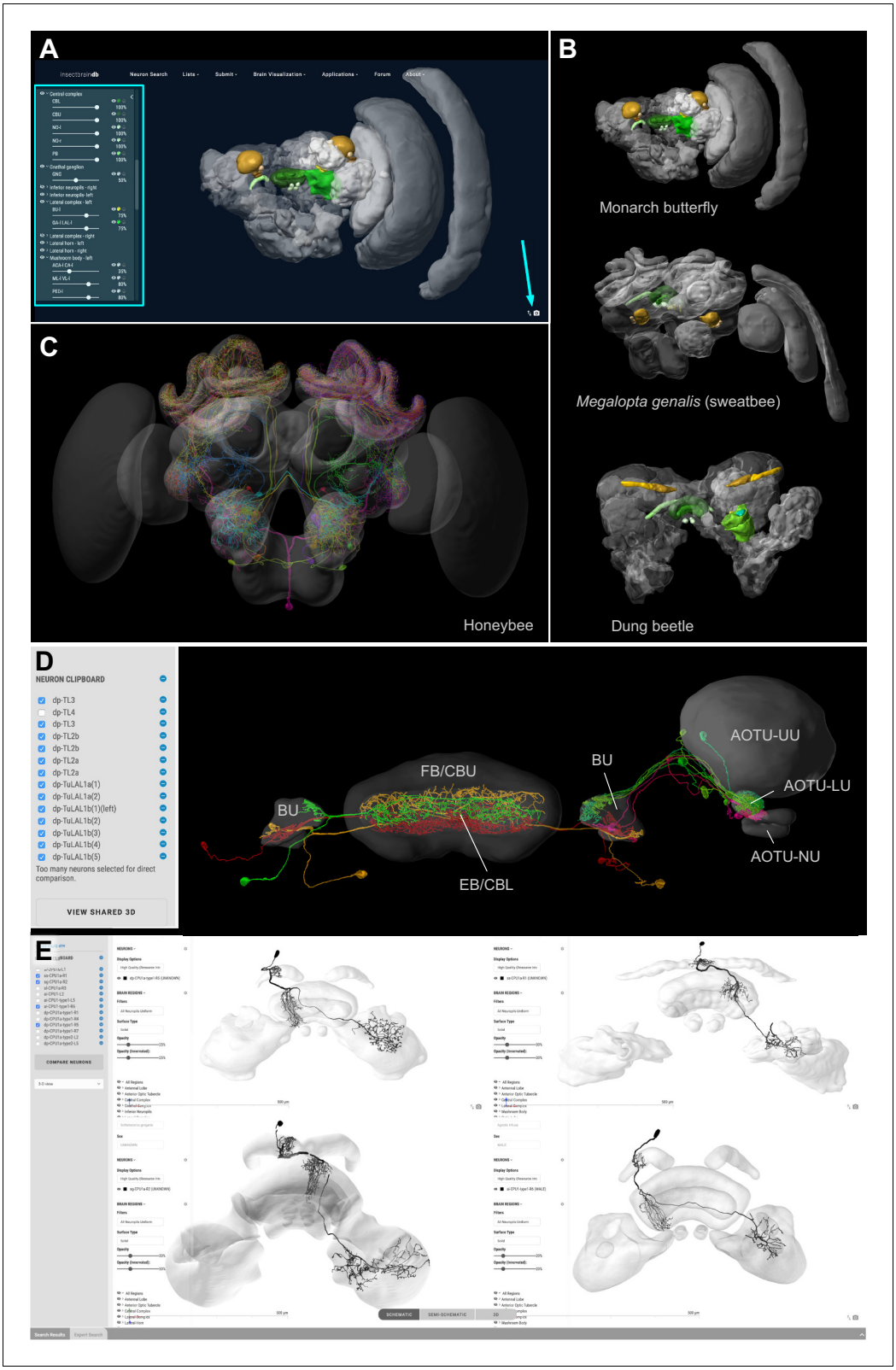

Figure 3. Visualization tools and applications. (**A**) Screenshot illustrating the functionality of the 3D viewer in the insect brain database. Cyan arrow: Screenshot button. Cyan panel: Tools for adjusting appearance of neuropils. (**B**) Examples of neuropil images generated with the *IBdb* 3D viewer, illustrating navigation relevant neuropils in three insect species (Monarch butterfly [***Heinze and Reppert, 2012***], sweat bee *Megalopta genalis* [***Stone et al., 2017***], dung beetle [***Immonen et al., 2017***]). (**C**) Neurons associated with the antennal lobe of the honeybee, generated with the *IBdb*

Figure 3 continued on next page

Figure 3 continued

3D neuron viewer (data from ***Rybak, 2012***). (**D**) Elements in the neuron clipboard (left) can be arbitrarily combined and displayed in the 3D viewer to highlight neural pathways and circuits. Shown are two parallel input pathways from the anterior optic tubercle to the ellipsoid body of the central complex in the Monarch butterfly (data from ***Heinze et al., 2013***). (**E**) Side-by-side neuron viewer. Screenshot showing comparison of 3D skeletons of CPU1 (PFL) neurons from four species (top left: Monarch butterfly [***Heinze et al., 2013***]; bottom left: desert locust [***El Jundi et al., 2009b***]; top right: Dung beetle [***el Jundi et al., 2015***]; bottom right: Bogong moth [***de Vries et al., 2017***]). All visualizations generated with Insectbraindb.org.

The *IBdb* allows users to not only locate neuronal morphologies quickly, but also to combine arbitrary neurons from any single species into a common visualization. To achieve this, we have generated a neuron clipboard, in which individual neurons from search results can be stored temporarily (***Figure 3D***). Any subset of cells in the clipboard can be sent to the 3D viewer, as long as all neurons belong to the same species, that is can be displayed using the same reference brain. The desired configuration of neurons and neuropils can be generated using the interactive tools of the viewer and the screenshot function can be used to create a high-resolution image to be used for illustration purposes (e.g. reviews, conference talks, teaching).

Additionally, we have embedded a function to directly compare up to four neurons side by side on screen. Any neuron located in the neuron clipboard can be chosen to be included in this comparison. The comparison uses the 3D view, the profile image, or the confocal stack located on the respective neurons' profile pages. This function is ideally suited to compare homologous neurons from across species to quickly assess differences and shared features of these cells. The four-window 3D viewer retains all functions of the normal full screen 3D viewer and thus also allows the capture of high resolution screen shots of each of the neurons being compared (***Figure 3E***).

The data in the database are suited for many applications, including more sophisticated ones. To provide direct access to all levels of the data in the *IBdb* we have created an API interface, specifying how to automatically draw data from the database via web-browser based apps. Applications produced by third parties that use this function can be embedded directly on the *IBdb* website, once they are approved by the site administrators. Applications envisioned are, for example, quantitative comparisons of both single neuron morphologies and neuropils between species, direct online multi-compartment modeling of neurons deposited in the database, or virtual reality interfaces that allow exploration of anatomical data in a 3D virtual reality environment. Over time, we hope that our unified platform will stimulate the insect neuroscience community to generate a collection of online tools to analyze and explore neuroanatomical and physiological data deposited in the *IBdb*, thereby allowing straight-forward meta-analysis of all raw data deposited in the database. As an offline tool, the Natverse package in R already offers the possibility to explore *IBdb* data (***Bates et al., 2020***).

Contribution of data

All data on the internet is public. This also applies to any data publicly available in the *IBdb*. Driven by the requirement to obtain data persistency and implemented by the use of handles, no data can be removed from the database once it is public (and thus citable). For all data, the contributors retain ownership and hold the copyright to their data. The publishing is performed explicitly by the owners, not by the database administrators, and the license attached to each dataset is a Creative Commons Attribution Non Commercial 4.0 International (CC BY NC 4.0). Thus, when data in the *IBdb* are downloaded for reuse, the original work that underlies these data has to be credited together with the *IBdb* as the source. When data are used to generate images with the help of the *IBdb*, these images are licensed via Creative Commons Attribution 4.0 International (CC BY 4.0), that is they can be used in any publication as long as the original data owners and the *IBdb* are credited.

Data can be contributed by registered users at all levels of the database, i.e. species, brain regions, neurons, and experiments. The process is similar on all levels but requires more expert knowledge the higher in the hierarchy the data reside. In the following sections we will briefly illustrate the main principles of how to contribute data (for full instructions see the Online User Guide).

Species

To submit a new species, a profile page has to be created, which then has to be populated with data. While photographs, bibliography, and text descriptions of the species are desirable and

strongly encouraged, the most important next step is to generate a schematic brain (***Figure 4A***). This will ensure that brain structure entries are created in the database, a prerequisite for neuropil-based search and 3D brain region identity. To generate a schematic brain, we have created the 'Brain Builder' tool on the *IBdb* website, which provides templates based on either the generic insect brain, or related species already deposited in the database. The user can simply copy an existing brain, associate it with the new species and modify it to match any unique features of the new species. Note that the ventral nerve cord (VNC), even though not part of the brain, was included as a single region as well, allowing to deposit information about VNC neurons as well and opening the possibility to expand the database beyond the actual brain in the future.

Once the profile page and the schematic brain is created, a 3D brain can be uploaded to illustrate the brain organization of the new species and to serve as reference brain for neuron display (***Figure 4A***). For all uploaded data, the database distinguishes between source files and display files. Source files contain the 3D reconstruction in a format that the researcher would like to make available for others in the field. The second set of files, the display files, are required for automatic online display and must constitute the surface models of each neuropil (.obj-format). Each brain region model is tagged with a unique neuropil identity, so that the schematic brain regions and the 3D surface models will be linked to the identical brain-structure entry. Finally, following the same principles

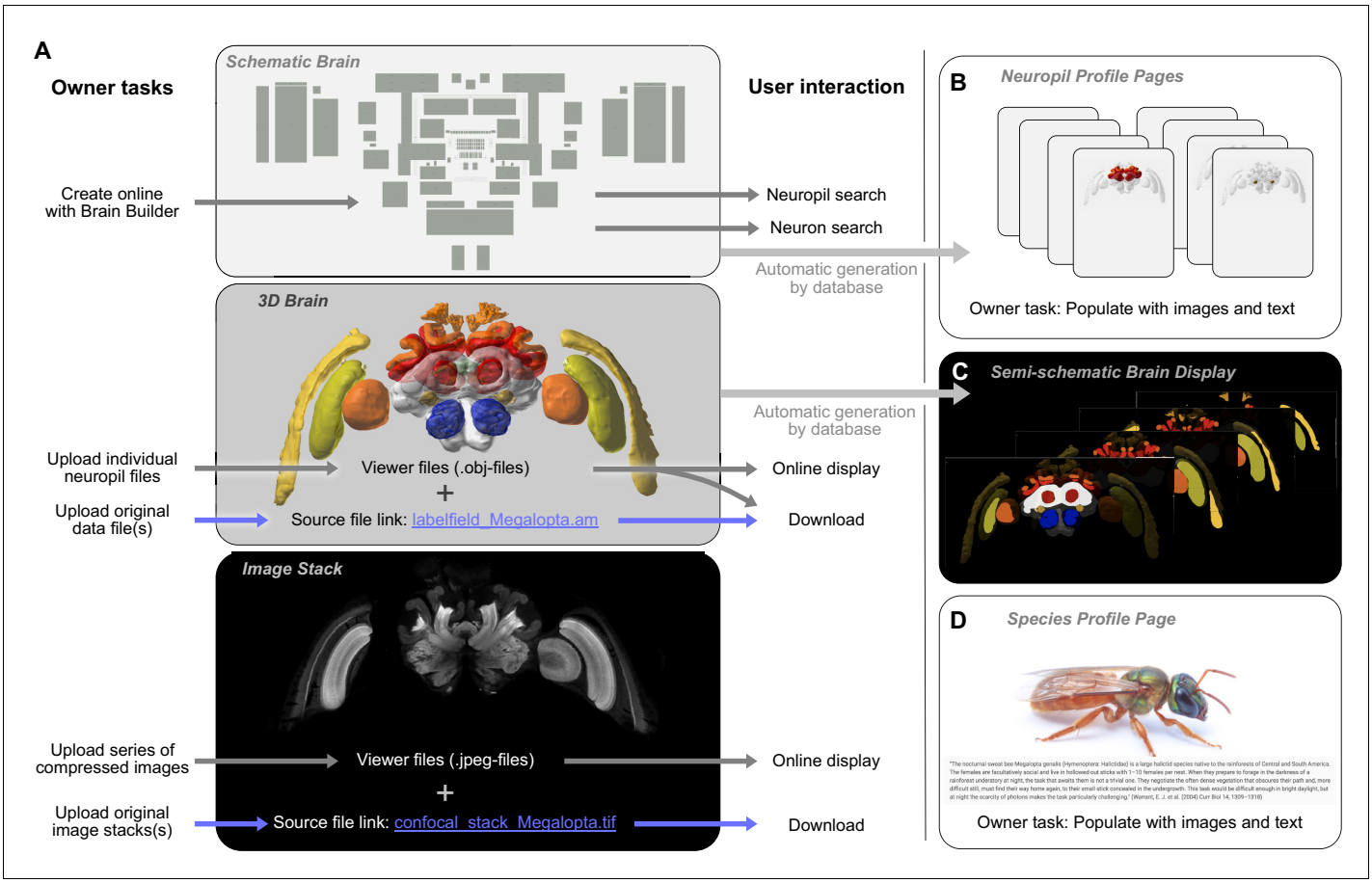

Figure 4. Contributing a species to the *IBdb*. (**A**) Three main elements have to be created for each new species: the schematic brain, the 3D brain, and an image stack. The schematic brain is generated directly on the *IBdb* website using the 'Brain Builder', while the other two elements are uploaded. For each, both source files and viewer files are needed. Viewer files are used for online display, while source files can be downloaded by users. (**B**) Neuropil profile pages are automatically generated when creating the schematic brain. They have to be populated with images and texts by the user. (**C**) The semi-schematic brain is automatically generated based on the provided 3D brain. (**D**) The species profile page must be populated with images, texts and a bibliography to provide context for the species. Visualizations in A,B,c generated with Insectbraindb.org, *Megalopta genalis* data from ***Stone et al., 2017***.

Photograph in D reproduced with permission from Ajay Narendra.

as for the 3D brain, an image stack can be uploaded to the profile page as well (***Figure 4A***). This can be any representative dataset that illustrates the layout of the species' brain (e.g. confocal stack, µCT image series, serial sections with any other technique).

Brain structures

Brain structure entries are automatically generated when defining the schematic brain search interface for a new species (***Figure 4B***). These profile pages are automatically populated by a 3D brain in which the relevant region is highlighted, a brain structure tree that reveals the relative location of the respective neuropil in the hierarchy of the species' brain, and with links to neuron entries associated with each brain region. All remaining data have to be manually added. These are mostly descriptive in nature and encompass images, text-based descriptions, and volumetric data.

Neurons

Contribution of neurons follows a similar procedure as the contribution of new species (***Figure 5***). The user creates a profile page for the new cell type that subsequently has to be populated with information. To make a neuron findable in the database, its arborization regions in the brain have to be defined (***Figure 5C***). Within a graphical user interface, these regions are chosen from the brain

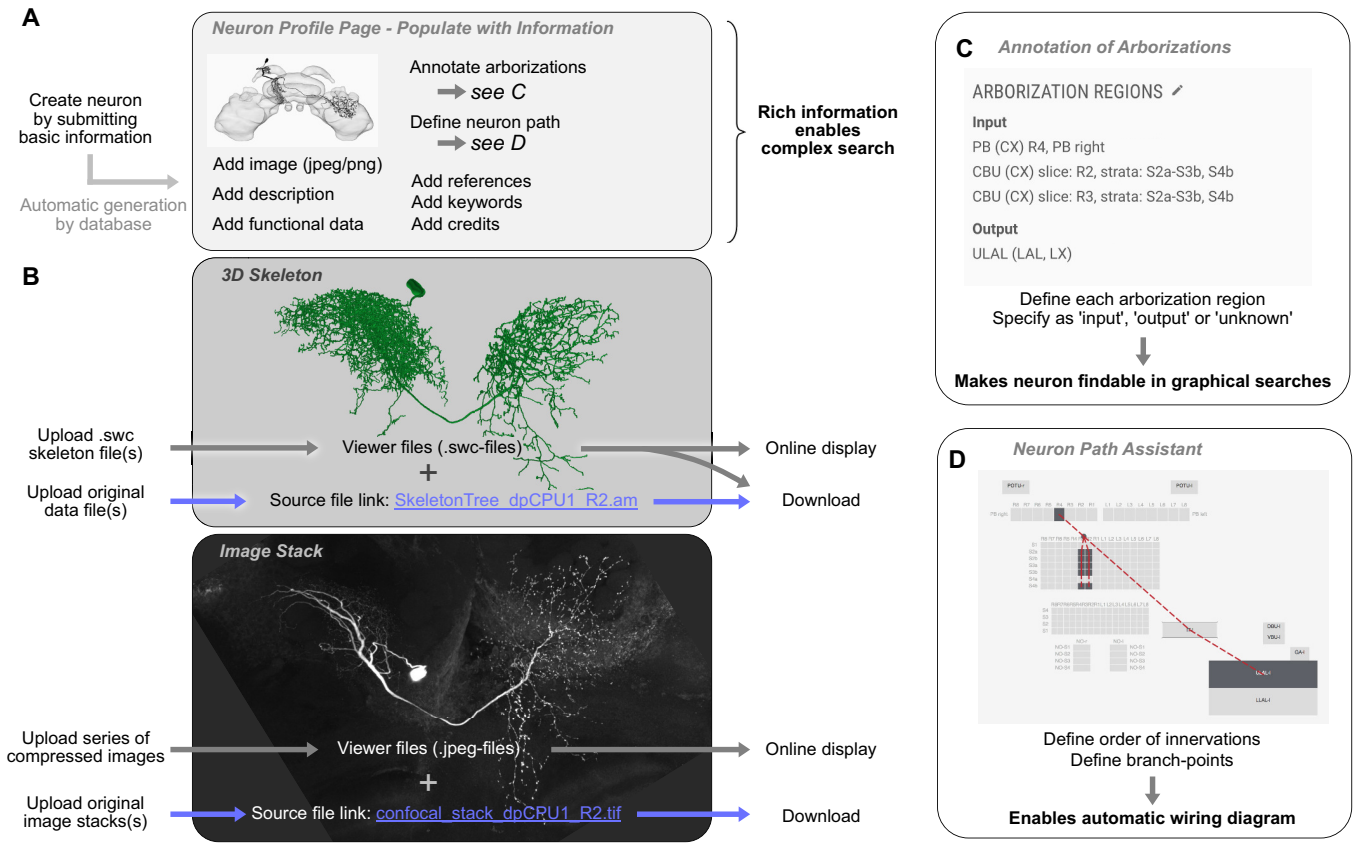

Figure 5. Contributing a neuron type to the *IBdb*. (**A**) A new neuron type can be created by submitting a neuron form containing basic information. This generates a neuron profile page that then has to be populated with information by the owner. Each entry is findable by the expanded search function. (**B**) 3D-skeletons are added as swc-files (online display) and source files (download). Confocal image stacks are uploaded as jpeg series for online display and as original data files for download. (**C**) All arborization regions of the neuron must be defined (at the level specified in the species' schematic brain) and labeled as either input, output, or unknown polarity. (**D**) To enable automatic drawing of wiring diagrams in schematic search results, the order of innervation of neuropils and the branch-points of the neuron must be defined using the path assistant. All visualizations generated with Insectbraindb.org.

structures available in the schematic brain of the respective species. One arborization entry has to be created for each branching domain of the neuron, leaving no part of the neuron un-annotated. To enable the automatic generation of a wiring diagram view of the new neuron for displaying schematic search results, an outline of its branching structure has to be generated in an embedded tool called the neuron-path assistant (***Figure 5D***). This branch tree defines which neuropils are innervated in which order and where main branch points are located.

The remaining procedure for neuron contribution is largely identical to species contribution and follows the dual approach towards source data and display data for 3D reconstruction and image stacks (***Figure 5B***). All other information, that is images, bibliography, keywords, representative functional data, transmitter content, and textual descriptions, can be added to the profile page at any time prior to publication. To ensure common minimal standards and to avoid rudimentary datasets, several data fields have to contain valid information before a request for publication can be made. These include an image of the neuron that allows to clearly identify the cell type, a complete morphology section (including soma location, a description of the neuron's morphology, and arborization regions), as well as a link to a publication (or preprint) that contains data on the cell type depicted in the new entry. If no publication is available, a note in that section will state that the neuron is not part of any publication.

Importantly, the *IBdb* can be used to house data that have been obtained by classical methods, for example camera lucida drawings of Golgi impregnated neurons. While no 3D information is available in those cases, drawings can be uploaded as images after which annotation of the neuron's morphology (arborization regions) is performed as described. These neurons will therefore become findable in the schematic search interface and will be added to the publicly available pool of neuronal data. To allow these datasets to exist in the database, 3D reconstructions and image stacks are not mandatory content. Similarly, 3D data that is not registered to a common reference frame can be deposited in the database, with or without individual brain region reconstructions, but a shared display in the context of a reference brain will not be available for these datasets.

Experiments

Experiment entries are created by adding them directly to the profile page to which they are linked (species, brain structure, or neuron). The automatically generated experiment profile page must then be filled with basic meta-information about the experiment (date, what was done, who did it), after which a series of files can be uploaded. These files can be in any format and are made available for download. This allows users to provide not only the raw data of any experiment, but also, for example, analysis scripts, custom made equipment-control software, and analysis results. Image files can be selected for direct online display on the experiment profile page to allow online examination of the data. Importantly, experiment entries are independently published from neuron entries.

Curation and administration

The database is managed via a group of voluntary curators, a scientific administrator, and a technical administrator. Importantly, no single person curates all data in the *IBdb*, but each species is managed by a specialized curator, who is an expert for that species. This distributed curation system ensures that no single person is responsible for too many datasets, and that no curator has to evaluate data outside their area of expertise. To additionally reduce the workload for species with many entries, more than one curator can be assigned to any given species. The scientific administrator (the lead author of this publication) oversees the curators, while technical administration is carried out by the technical administrator (last author of this publication). The technical administrator is the only person who has potential access to all data in the database.

The responsibility of the scientific administrator is to approve new species and to train and support the curators for individual species. This training is carried out during a training period during which actions of the curator have to be approved by the scientific administrator before they take effect. Once a new curator is sufficiently trained to carry out all tasks independently, the scientific administrator grants full curator privileges. The responsibility of each curator is to approve new neuron-type datasets and to re-evaluate major updates of these (data re-approval). This process entails checking for formal errors in the submitted data, ensuring that new data do not accidentally duplicate already existing data, and that the quality of the data meets acceptable standards. To ensure

swift correction of any issues, we have implemented a private communication channel between curator and data owner. This was realized through a commenting function that enables the curator to post comments on a neuron page, which are only visible to the data owner. The owner can then directly respond to the comments and any issues raised can be resolved.

While our distributed approach to curation has many advantages, it creates challenges towards ensuring that curation of data across all species and levels is accurate, consistent and complete. We have therefore designed multiple tools and features to facilitate effective and consistent data curation. Besides formalized training and approval for each new curator, we have provided checklists for both data contributors and curators (found in the online help menu) that must be followed to ensure that database entries fulfill predefined standards. Yearly meetings among all curators will ensure that these standards are known and can evolve over time. If mandatory data is not provided by a data contributor, request for approval of the dataset is automatically blocked, preventing rudimentary datasets to enter the public section of the database. Finally, if an entry becomes obsolete, for example when new research data provides conclusive evidence that cell types listed as separate entries belong to the same type, existing entries can be archived. This process preserves the persistent handle of the entry, but removes it from public lists and search results in the *IBdb*. This way, references to these datasets remain resolvable, while, at the same time, obsolete data cannot clutter the database. In the long run, this function provides the means to keep the database clean without violating the principle of data persistence.

The definition of what constitutes minimal standards for a neuron or species entry reflects a scientific consensus among curators. Rather than imposing these standards onto the field, the *IBdb* generates the means to develop a common set of rules by providing the platform for continued discussions among curators as well as to reinforce an evolving consensus.

To enable all users to provide feedback and to discuss topics relevant to other database users, we have added a discussion forum directly to the *IBdb* website. This forum is intended as a means for reporting potential bugs, suggesting new *IBdb* features, or for discussing scientific content (methods for data processing or acquisition, requests for literature, staining protocols etc.).

The *IBdb* as tool for data management and data deposition

Each database entry has to be explicitly published by the contributor. In the process, it is approved by either the database administrator (species), or the species' curator (neurons). While this procedure was initially intended only as a quality control measure to prevent incomplete or inaccurate data from compromising the database, we have developed it into a unique feature: the *IBdb* private mode. Before a dataset is made public, it is invisible to all other users, curators and the scientific database administrator. The dataset can thus be updated and even deleted. This creates the potential of using the *IBdb* to deposit data while they are being collected or prepared for publication in a research paper, that is, for data management (***Figure 6A***). The API can be used to programmatically integrate the *IBdb* into any individual data management workflow; a community driven MATLAB implementation for automatic deposition of cell types and experiments is available on GitHub (https://github.com/zifredder/IBdb-matlab).

To facilitate the use of the *IBdb* as a data management tool, we have enabled three operational modes of the database site: private, public, and mixed. Any user logged in can thus choose to either access only (own) private data, only public data, or both. The first mode turns the *IBdb* into a data management site for ongoing research, the second mode is the default mode for viewing publicly available data, and the third mode allows the user to compare their own unpublished data with public data.

As efficient data management requires researchers from the same laboratory, as well as collaborators, to have access to relevant unpublished data, each user can grant access to their own private datasets (***Figure 7***). To this end, a user can create a user group and invite other database users to join. Datasets can then be added and made visible or editable to all members of the group. These data can either comprise individual entries at all levels of the database, or collections of entries defined by common features.

Finally, users are often reluctant to make datasets available to the public before they are included in a research paper, yet, these data should be available to editors and anonymous reviewers. We have therefore created the possibility for 'pre-publishing' database entries (***Figure 6A***). This function allows a user to assign a persistent handle to a dataset (e.g. a neuron profile page) without approval

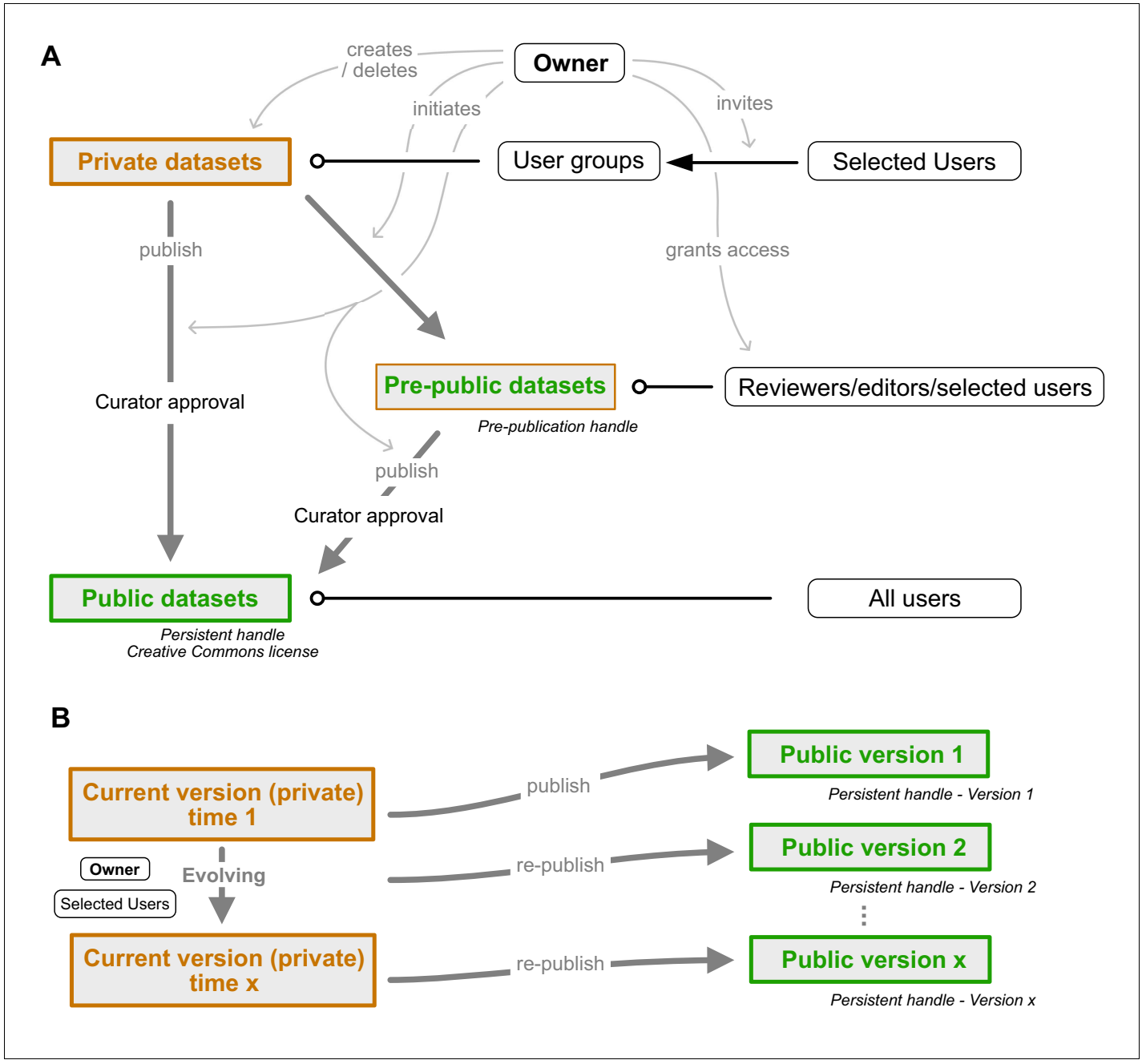

Figure 6. Dataset publication concept. (**A**) Interconnection of private, public, and pre-public datasets. Private datasets can be viewed and edited by members of user groups with access granted to a particular dataset. Pre-public datasets can be viewed by anyone in possession of the pre-publication handle (distributed by the data owner, e.g. within a manuscript). Public datasets can be accessed by all users. Publication of data cannot be undone as persistent handles are generated. Gray arrows indicate control actions employed by the dataset owner. (**B**) Re-publication strategy of evolving datasets. A current version of each public dataset remains present in the owner's private database mode and can be edited at wish. Once sufficient updates have accumulated, the dataset can be re-published. A new version of the persistent handle is assigned and the now public dataset (version 2) becomes locked. Datasets can be edited by the owner and anyone who has been granted permission to edit by the owner.

by the curator and without making the dataset findable through search or lists in the *IBdb*. Editors and reviewers of the research paper (anyone in possession of the handle) then have direct access to the linked pages. Once the manuscript is accepted for publication, the user can submit the respective datasets for publication, obtain curator approval, and thus make them findable in the *IBdb* public mode.

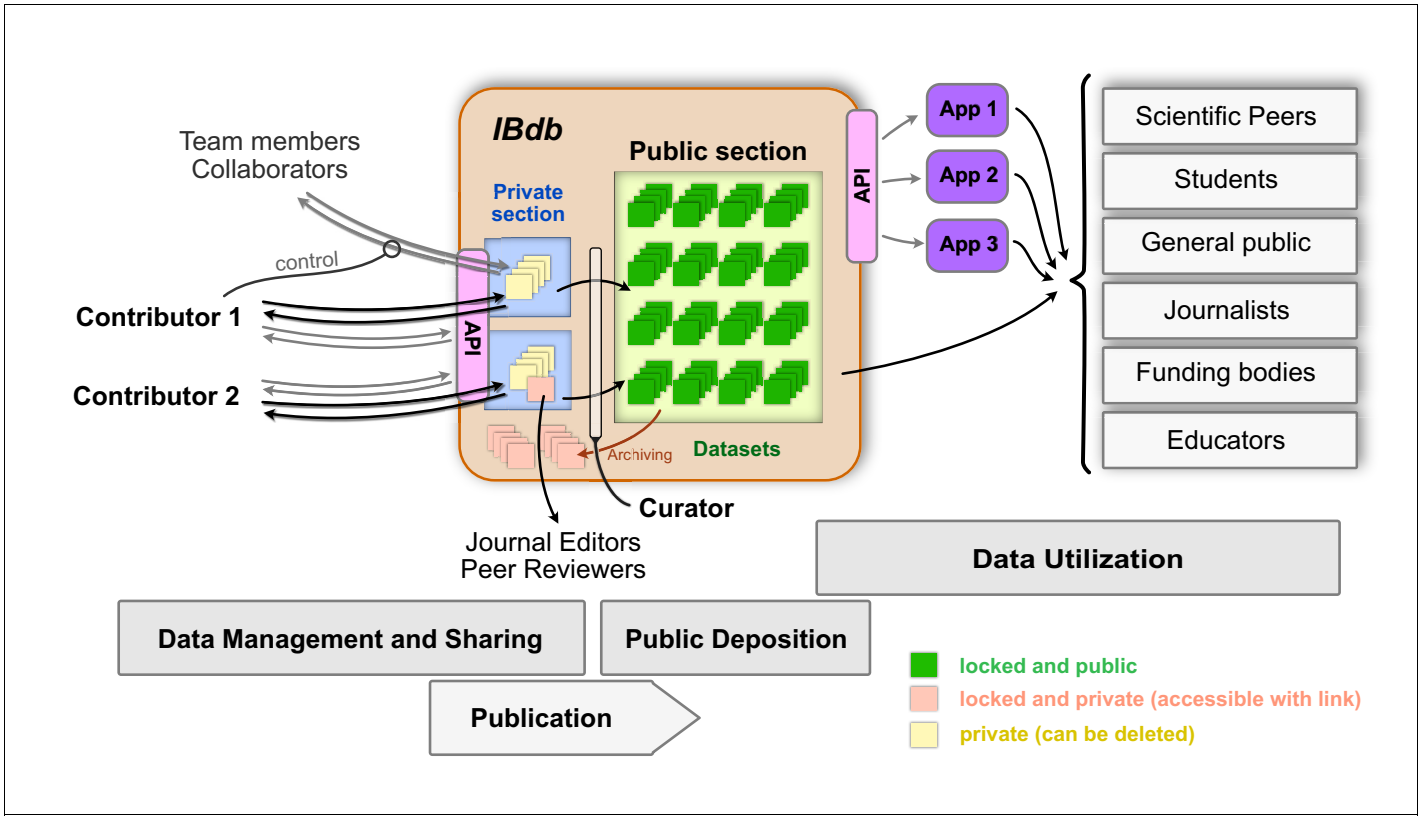

Figure 7. The Insect Brain Database and the possible interactions between users and deposited data. The private sections of the database are accessible to only the owner of the data, and datasets within this section can be shared with team members and collaborators. Up- and download of these data are possible either directly or via an application programming interface (API). As these datasets are unlocked, they can continuously be updated and also be deleted. Upon publication and curator approval, datasets become locked (persistent) and are deposited in the public section of the database. As an intermediate step, datasets can be pre-published (locked but private) and made available to journal editors and peer reviewers when including datasets in manuscripts of journal articles. Data in the public section of the database are accessible directly for all interested users (relevant user groups are shown on the right). Additionally, an API also allows automated access of public data, which can therefore be used by third party applications (illustrated as 'App 1–3') for generating specific user experiences with additional capabilities, for instance in the context of teaching. To remove obsolete datasets from the public domain, they can be archived, a process that preserves persistence but prevents datasets from being findable without the explicit handle.

The online version of this article includes the following figure supplement(s) for figure 7:

Figure supplement 1. Database usage statistics.

To avoid having to separately provide numerous independent handles when sharing data, individual entries can be grouped into datasets. These receive a unique link that grants access to the entire collection. Only public or pre-public data can be included in datasets.

Public entries of the *IBdb* are maintained in a dual way; the persistent version is locked and cannot be changed, whereas a second, current version remains visible to the owner and to all members of user groups with appropriate access rights (***Figure 6B***). This current version is fully private and can be freely edited or expanded. Importantly, no data that is already part of a public version can be deleted. Rather, when for instance a confocal image stack should be replaced by a better one, the old stack can be archived, so that it will not be visible in new versions of the dataset, but will remain present in the database for display of earlier versions. Once all required updates of a dataset have been made, the edited version can be re-published and will be assigned a new version of the persistent identifier after re-approval by the assigned curator. This new version is now also locked and any further edits will again have to be done in the current version of the dataset. This ensures that all data that have been assigned a persistent identifier will remain valid and accessible, while at the same time allowing each entry to evolve. The described strategy of publishing and re-publishing

and the associated duality of persistent and current versions are implemented at the levels of species, neurons and experiments.

Drosophila and interoperability with Virtual Fly Brain

The *IBdb* does intentionally not include *Drosophila melanogaster* as a species. This is because huge efforts have been spent developing highly efficient resources for this widely used model system and, as a result, the Virtual Fly Brain (VFB) resource has been created (**Osumi-Sutherland et al., 2014**). It bundles data from several older *Drosophila* databases (e.g. FlyCircuit) to the most recent connectomics datasets (**Scheffer et al., 2020**). Serving as the main repository for anatomical data from the *Drosophila* brain it has become the main site to locate GAL4 driver lines, single-cell morphologies, and synaptic connectivity data. It contains tens of thousands of datasets and is designed to specifically meet the needs of the *Drosophila* research community. By being less specialized, the *IBdb* has a wider scope. We are hosting many species and include both functional and anatomical data. We also do not require neuronal anatomies to be registered to a reference brain, if this is not possible for some reason. This opens the *IBdb* up to more diverse data, but as a result cannot provide most of the specialized services that VFB can deliver (e.g. automatic bridging registrations of 3D data between different reference brains). Cross-linking the two databases to effectively enable comparing neurons from the insect species deposited in the *IBdb* with *Drosophila*, nevertheless, was highly desirable. Importantly, both databases have converged on highly similar hierarchical frameworks. As the brain nomenclature used by the *IBdb* and VFB is identical, neuropil identities were mapped across both databases. In cases were homology between corresponding neuropils is unclear, regions map to the next higher order brain region (e.g. Monarch butterfly dorsal bulb maps to the entire *Drosophila* bulb). For some neuropils, there are no known counterparts in the fly (e.g. the posterior optic tubercle).

We use the APIs of both databases to allow direct communication between the *IBdb* and VFB. In principle, when searching the *IBdb* for neurons, an API mediated query can be automatically sent to VFB and search results are displayed as a list of single neuron entries. Each item on the list contains information obtained from VFB and is directly linked to the corresponding entry at VFB. This feature is available for the graphic, brain region based search. This includes complex multi-neuropil searches, aimed at identifying neurons connecting several brain regions. Effectively, this enables a user to launch a query in the *IBdb* and directly view corresponding neuron data in VFB, including data from recent connectomics efforts (**Scheffer et al., 2020**). This seamless interoperability makes maximal use of both complementary resources, without duplicating functionality.

Discussion

Specific problems solved by the *IBdb*

Previous and current online databases hosting insect neuroscience data have suffered from several shortcomings: Most severely for old databases, a lack of maintenance often quickly led to outdated file formats, rendering the deposited information no longer compatible for viewing with current web browsers (anticipated by **Ito, 2010**). Second, while some databases originally allowed interactive viewing of the data, no possibility for contribution of one's own data existed and data download was limited to very few files, for example **Brandt et al., 2005**, **Kurylas et al., 2008**. Usability of larger databases was generally impaired by a layout that often required expert knowledge to be able to launch meaningful database queries or to understand search results (e.g. FlyCircuit, Invertebrate Brain Platform [now: Comparative Neuroscience Platform]). This not only applies to old databases, but the restriction to individual species and often highly complex interfaces limit the potential user base to specialists even in cutting edge databases such as VFB or visualization tools such as FruitFlyBrainObservatory. Finally, the limitation to purely anatomical data, including in the major current cross-species database NeuroMorpho.org, does not account for one of the key advantages of insect neuroscience: the high level of tractable structure-function relations.

The *IBdb* addresses each of these issues. Firstly, we have developed the database software to be independent of the operating system and type of web browser used, as well as to not rely on any third party plugins. Additionally, we implemented the database as a classic, relational database without experimental data structures (e.g. intelligent, adaptive search), aiming at maximal robustness.

Having created a conceptionally simple software that uses standard web-technology with standard file-formats makes continued compatibility and technical maintenance comparably simple.

Second, we have invested substantial effort in making the *IBdb* intuitive to use and visually attractive to provide a positive user experience. The latter factor should not be underestimated in its importance. One of the problems encountered in previous databases were user interfaces that were difficult to use, creating an immediate negative experience when attempting to use a site for the first time and therefore reducing the motivation to interact with it. As for commercial software, we aspired to generate a user interface that is largely self-explanatory, provides immediate visual feedback when a user action was successful, and which clearly shows what actions can be performed. Several years of beta-testing by a multitude of users have streamlined the site to a point at which interacting with the *IBdb* is both straight forward and fun.

As the success of the database depends on many users sharing their data, we aimed at making contributing data as intuitive and as easy as searching and visualizing data. We have thus simplified the data contribution process to a point where only very limited anatomical knowledge is needed, aiming at enabling physiologists without deep anatomical training to submit data as well.

Finally, to our knowledge the *IBdb* is the first database in the field of invertebrate neuroscience that combines functional data with anatomical data, and at multiple levels ranging from entire brains to single neurons. This ability, together with the possibility to deposit not only representative data but concrete sets of experiments, provides an opportunity for anatomists to directly interpret their findings in a functional context, as well as allowing physiologists to tether their findings to a coherent anatomical framework that automatically generates context for any functional data. The ease of use of the *IBdb*, combined with housing functional and anatomical data, has the potential to facilitate interactions between expert anatomists and physiologists and thereby strengthen structure-function analysis across the diversity of insect brains.

Motivation to contribute

The landscape in the insect neuroscience research community has changed dramatically, and most relevant funding bodies are in the process of implementing open data mandates or have already done so (e.g. European Research Council, National Institutes of Health, Wellcome Trust, etc). Thus, the initial driving force for data deposition is much larger compared to that surrounding earlier database attempts. Yet, why should researchers use the *IBdb* for meeting these new mandates rather than other available databases? Different from open databases, for example Figshare.org, the *IBdb* is dedicated to insect neuroscience and thus provides all tools required to manage, annotate, and cross-link the specific data formats generated in this field. However, it is not rooted within a single laboratory, nor a single species, thus providing a framework for data from a broad research community. The unique possibility for cross-species comparison and the combination of anatomical and functional data additionally broadens the relevance of the *IBdb*.

Visualization of anatomical research data is often difficult and particularly complex when involving data from other research groups. We have implemented a range of tools enabling the visualization of data in fast, flexible, and effortless ways. This saves considerable time compared to other available software tools, in particular for complex 3D neuron data (e.g. Amira). The data contributed are also immediately incorporated into the framework of existing data. Outside the *IBdb* these data are distributed across many publications. Comparison of one's own data to any published data would entail contacting authors, obtaining files in unpredictable formats and finding ways to compare them to one's own work within the software a research group is currently using. The *IBdb* solves these issues and delivers such comparisons within seconds. Crucially, these advantages are already present immediately after data upload, prior to publication. Via the private mode of the *IBdb*, individual neurons can already be compared to their counterparts in other species while datasets are being obtained, enabling the user to generate visualizations suitable for conference contributions and publication figures. This possibility is to our knowledge unique to the *IBdb* and provides a major motivation for data contribution.

Importantly, the dual function of the *IBdb* as data repository and data management tool eliminates the need to reformat and prepare datasets for publication, a process that is required when submitting datasets to websites dedicated to only data deposition. The *IBdb* therefore provides a streamlined and integrated experience from data acquisition to publication, aimed a minimizing researcher workload. This is additionally relevant as formulating a data management plan has also

become mandatory for projects funded by most funding organizations. By using the *IBdb*, users in insect neuroscience not only have access to a dedicated data repository, but at the same time have a tool at hand for efficient handling of ongoing research data, making data management plans easy to design and effective. This is particularly the case when using the API for accessing the data, as up- and download can be automated and custom designed interfaces can be programmed according to the needs of any particular research group.

Independent from these aspects, the API of the *IBdb* offers users the opportunity to expose their published data directly to approved third party applications. The bundled availability of data from many research groups generates a possibility of data reuse with a much broader scope than any individual solutions, providing an increased motivation for developers to design workflows that incorporate deposited data. High-quality data deposited in the *IBdb* therefore additionally increases the visibility of the data owners.

Biological insights

While the data currently deposited in the *IBdb* represents only a starting point to illustrate the functions and possibilities of our database concept and user interface, the neurons and species present in the *IBdb* already highlight new biological insights as well as concrete paths towards such insights.

Most obvious insights can be gained from data deposited in the *IBdb* that is not published or publishable elsewhere. For example, isolated neural morphologies from the Monarch butterfly have been published solely in the *IBdb* and demonstrated a previously unknown connection between the gall of the lateral complex and the mushroom body lobes (dp-GA-MB(L) neuron, NIN-0000383), thus directly linking the output of the central complex with the mushroom body for the first time in insects.

The possibility for direct comparison of neuropil and neuron data from many insect species has the potential to identify discrepancies in neuropil definitions across species and pinpoint solutions for revised homologies. For example, the main output neurons of the central complex (PFL or CPU1 neurons) are most likely homologous across insects and target the dorsal LAL in all species in which this region has been described (e.g. butterflies, moths, flies, beetles), except in locusts, in which they terminate in the ventral LAL. This discrepancy suggests that the definition of subregions of the LAL and their borders to surrounding brain regions (e.g. crepine) might have to be re-evaluated.

Along similar lines, the *IBdb* has generally the potential to expose discrepancies in functional data. Work carried out in a research group interested in sensory processing might define the function of a particular cell type very differently than a group focused on motor control, or one focused on neuromodulatory functions, simply because different experimental paradigms are aimed at different aspects of neural function and interpretations of results might be biased toward the underlying hypotheses. Such diverging views of neuron function can silently coexist in the literature for long times, but if bundled in side-by-side function entries on the same neuron profile page in the *IBdb* they become highly obvious. Such exposure will facilitate scientific discussion and the emergence of unified ideas of neural function.

Finally, in any field it is important to consistently define technical terms, agree on key concepts, and have consistent standards regarding what is acceptable data to validate conclusions. During the development phase of the *IBdb* it became clear that the isolated work in many insect model species has led to a wide range of cases in which similar terms have different meanings in different species and where views on what is acceptable proof for, for example, neural function varies. The definition of cell type is one such example, where researchers working in different species and brain regions attached substantially different meaning to the term. With the unifying approach of the *IBdb* we had to therefore identify common ground and define cell type in a way that was acceptable to each contributing party. Similar issues for other aspects of insect neuroscience research will likely be exposed by the increased levels of communication enabled by the *IBdb*. While resolving these issues will often take time and effort (and will involve researchers from across the field), the main function of the *IBdb* in this context is not to impose a strict set of rules, but to provide the framework in which inconsistencies can be exposed and resolved, eventually facilitating biological insight.

Scalability and long-term sustainability

The *IBdb* is designed for long-term accumulation of data by many contributing research groups across the field of insect neuroscience. To successfully provide this service, the *IBdb* has to address several challenges of sustainability. These challenges are threefold: First, ensuring technical and financial maintenance of the database infrastructure; second, guaranteed, continued scientific oversight and expert curation, and third, lasting scientific relevance. We have therefore taken steps to address each of these points.

In the light of fast changing web technology, maintenance of high technical standards requires continuous effort and active updating of the database code, which in turn requires financial resources. The first issue is covered by an ongoing agreement with the web-developers that built and maintained the database software over the period of the last six years. Financially, voluntary contributions from research groups that initiated the database have paid for its creation. As the maintenance costs are a small fraction of the development costs, it will be easily possible to run the database within the framework of the existing service agreement for at least the next 5 years without any changes required. However, when the data volume increases substantially, the static costs of housing the data will increase accordingly. While keeping all public, persistent data available free of charge is mandatory (given that the *IBdb* functions as a public data repository), maintaining the *IBdb* as a free data management tool, that is allowing unlimited private data for each user, will likely become unsustainable over time. If this becomes a problem, free space in the private section of the database will have to be restricted. All space required beyond a certain limit will have to be rented to directly offset the costs for maintaining and administering these data. At the same time, research groups involved in creating the *IBdb* use this platform as their primary tool for management of research data and public data repository. The obligation to formulate data management plans and strategies for public deposition of research data, combined with the lack of equally suitable alternative platforms, will ensure that third party funding dedicated to maintaining the database will continuously be available via research funding of the founders of the *IBdb*.

To anticipate the slowly growing costs of housing the database due to increasing data volume, we aim at eventually relocating the data from the currently used commercial Amazon cloud platform to an academic server that is provided at minimal costs or free of charge. To this end we have ensured that the *IBdb* does not depend on any core functions of the Amazon cloud storage service, enabling to move the database to a new location with comparably moderate effort.

The second issue of continued quality control and expert curation is addressed at several levels. Firstly, at the level of species, the scientific administrator has the main responsibility to oversee the curation of the species entries by each species' dedicated group of curators. Given the limited number of species that can realistically be included in the *IBdb* over the coming years (our estimate is a maximum of several hundred), the associated workload for general oversight is limited and manageable by a single person. As species curators actively perform research on the species they are responsible for, there is a substantial self interest to maintain high standards to advertise their work and thus facilitate their research.

At the level of neuron entries, the workload is higher due to larger data volumes. Accordingly, the main responsibility for oversight is more distributed and lies with the species' curators. Once datasets exist in the database, updating is generally optional and will only in rare cases be necessary. In those cases, the strongest incentive for keeping data up to date lies with the data owners and research group leaders, who also possess the highest expertise for these data. Overall, expertise is mostly required to approve new datasets, a process requiring substantial overview over the data available for the relevant species. With an increasing number of species, the number of curators will also have to increase. This makes curator recruitment and training key requirements both for quality assurance and for enforcing consistent curation strategies. For this purpose, regular meetings of all curators will be held and approval of new curators will be carried out only after an extended training period. To attract new curators in the future, the *IBdb* administrators will actively approach researchers in the field of insect neuroanatomy. Finally, to identify existing quality issues with deposited data, establish routine workflows, to support curators and contributors at all levels, and to recruit new users, a dedicated, full time database curator position is being created, initially funded by members of the *IBdb* consortium for a minimum of one year.

Third, continued scientific relevance of the database will have to be ensured to attract users and contributors long term. Most crucially, after introducing the database to the field, the available deposited information has to grow beyond a critical point, at which the *IBdb* becomes the natural choice for depositing insect neuroscience data. We believe that this point has already been reached, as the number of deposited data sets is growing extensively (***Figure 7—figure supplement 1***) and users without affiliation to the founding consortium have begun to deposit data. Nevertheless, attracting more data will remain a key mechanism to increase the attractiveness and acceptance, and, consequently, the relevance of the database in the field. As one of the key advantages of our concept is the possibility to deposit all anatomical and functional data from insect neuroscience, irrespective of data format, we have begun to approach authors of published work to enable them to make old data available to the growing *IBdb* user base.

IBdb usage for outreach and teaching

While highly useful for classroom teaching of structure-function relations in neural systems, the *IBdb* has proven to be invaluable to introduce new members of a research team to the basic layout of brains, neurons, and neural circuits in a particular species. Using the database serves as an easy (and fun) access point to available information on a research species, including key publications, and therefore saves significant effort when writing review papers, PhD thesis introductions, background sections for travel grants, etc. While this is true for established researchers as well, it is especially true for younger scientists and students who are new to the field or are at the beginning of their careers.

Finally, the *IBdb* provides the possibility for anyone to access original research data in intuitive and attractive ways (***Figure 7***). This provides opportunities to design teaching assignments for neuroscience students to carry out meta-analyses. With access to the data in the *IBdb* via the application programming interface (API), we have provided the possibility for third parties to develop dedicated teaching tools that provide streamlined methods to use the data for specific classroom exercises. Beyond researchers and students, journalists, interested members of the public, or members of funding bodies can also view and explore neuroscience data. Ideally, this will contribute to a more transparent understanding of what the output of science is and could spark increased interest in insect neuroscience.

Widening the scope toward other animal groups

The framework we have generated with the *IBdb* is not limited to housing insect brain data. Without major modifications it would be equally suited for hosting data from other animal taxa. While the intuitive, schematic search engine would not be useful for comparing species that do not share a common basic brain outline (i.e. a relevant 'generic brain'), the text-based expanded search could allow the construction of queries across multiple groups, for example searches according to functional terms. We are currently conceptualizing the expansion of the database toward including spiders and envision that crustaceans and other arthropods would be logical next groups.

The *IBdb* therefore provides not only a tool for the insect neuroscience community to facilitate data management, data visualization, transparency of results and effective teaching, but it can easily be expanded toward related fields. Additionally, it might also serve as a blueprint for how to set up similar databases in unrelated research areas. In principle, the strategies used in the *IBdb* are applicable to any scientific field that can be linked to a hierarchical framework.

Materials and methods

Data location

All web infrastructure is hosted by Amazon web services on servers located in Frankfurt, Germany. Data is stored using a PostgreSQL relational database hosted by the Amazon Relational Database Service and files are stored using the Amazon S3 object storage service. The servers hosting the website and the local HANDLE system are running in Amazon EC2 containers, which runs Linux. Resources communicate using Amazon Virtual Private Cloud.

Database framework

The database structure and interaction is managed by a python based Django application. User authentication, permissions, and data security are also managed within the Django application. A NGINX web server hosts static content and serves as a reverse proxy for dynamic content served by a uWSGI application server hosting the project's Django application. Asynchronous tasks are implemented using the Celery distributed task queue and RabbitMQ message broker.

Data is externally accessible via a web API delivering content in the JSON format to the front-end web application. The web API was implemented with Django and the Django REST framework.

Long-term data persistency is provided to allow users to reference information or profile pages on the site in scientific publications and other external media in a static state, while continuing to allow data to be updated as more information is acquired. When a request is made by a user for a persistent copy of a dataset to be created, a copy of the data related to the current state of the dataset is serialized and parsed into JSON. A persistent unique identifier is then assigned (HANDLE). The JSON data, HANDLE and additional metadata is recorded in a separate table and can no longer be modified. All files associated with the persistent dataset are marked as locked in the database and can no longer be modified by the user. The recorded state of that dataset can be accessed and viewed on the site using the url associated with the assigned HANDLE. The original data copied to create the persistent dataset can be modified without effecting the persistent dataset. Additional files may also be added, but will not be reflected in earlier persistent records.

Graphical user interface

The front-end of the database is primarily implemented using the Angular web framework in Typescript, HTML and SASS (CSS extension language). The Typescript, HTML and SASS are compiled and bundled with the Angular CLI using WebPack to create the distributed application files targeting ECMAScript 2015 capable browsers. Graphical consistency is targeted for browsers using Webkit and Gecko-based layout engines adhering to web standards.

The web based three-dimensional viewer was implemented using Typescript, WebGL and the Three.js three-dimensional graphics framework. The two-dimensional schematic view, brain designer and path designer was implemented using Typescript, the Canvas API and Paper.js vector graphics scripting framework.

Security measures

User to server communication is protected by the Hyper Text Transfer Protocol Secure (HTTPS). User authentication is managed by the Django authentication system. Access to data is restricted by object based permissions limited to authorized users through the web interface or API arbitrated by the Django server.

File downloads of protected content stored on Amazon S3 are accessed using time limited urls, assigned to an authorized user at the time of a download request by the Django server. Files are directly downloaded from the S3 storage to the user using the temporary URL. The process is seamless to the end user who needs only be logged into the website and click the link associate with the intended file. Downloads are logged and accessible to the owner of the data being accessed. Files can be uploaded to the S3 object storage only by authorized users with a time limited URL provided by the server. The upload is logged and associated with the contributing user. Publicly available thumbnail images and other reduced quality images are stored separately in a publicly accessible (read-only) S3 bucket.

Content explicitly designated as public is accessible through the graphical user interface or via the API to any authorized visitor. Private content is only accessible to authorized users given permission to access the data.

The PostgreSQL database is protected by a firewall allowing access only via the Amazon Virtual Private Cloud and is not open to direct access via the web.

Nomenclature and brain hierarchy

All names for brain areas are in line with previous research. The brain regions of the generic insect brain follow the new insect brain nomenclature introduced for *Drosophila* by ***Insect Brain Name Working Group et al., 2014***. Accordingly, we have established three hierarchical levels of brain

regions: super-regions, neuropils, and sub-regions. Super-regions are stereotypical and can be expected to comprise the ground pattern of the brain in all insects (although some might be reduced in certain species). The only exception to the ***Insect Brain Name Working Group et al., 2014*** scheme is the anterior optic tubercle, which we have raised to the level of super-region, given its prominence and distinct nature in most insect species. Sub-regions are often specific to individual species and therefore, if such regions were defined, we used the names given to them within the relevant species. We did not unify for example names of the mushroom body calyx divisions across species, as this would firstly imply homology where there might not be any, and second, novel naming schemes will have to be developed by the community and not be imposed by a data repository. Anticipating that changes to brain names can and will happen in the future, all names, as well as the level of a region within a hierarchy, can be modified.

Within some neuropils, regular, repeating elements can be found, usually defined as columns and layers. We have implemented such a system in the central complex, that is without having to define an array of sub-regions, several strata and orthogonal slices (following the new brain nomenclature) can be generated. The default number of slices in the generic brain is 16, assuming that this number is the ancestral state of this region.

Neuron names follow the conventions within each species, as there is no common naming scheme for insect brain neurons yet in place. However, we provide the possibility to define several alternative names for each cell type to allow the parallel use of names. This is possible as the identity of a neuron is linked to the persistent ID, and not to the neuron's name. Given that we house neurons from multiple species, we add a prefix to the full name of each cell type specifying the species, for example 'am' for *Apis mellifera*.

Acknowledgements

We are indebted to the many test users of the *IBdb* who patiently located bugs and inconsistencies and thereby helped to streamline the database outline and make the user interface more intuitive. We also thank all members of the Heinze lab for many helpful discussions that improved the *IBdb* and this manuscript.

Additional information

Competing interests

Kevin Tedore: Kevin Tedore is a commercial web developer (founder and owner of Kevin Tedore Interactive) who designed and developed all software and interfaces underlying the insect brain database. The other authors declare that no competing interests exist.

Funding

Funder	Grant reference number	Author
H2020 European Research Council	714599	Stanley Heinze
H2020 European Research Council	817535	Marie Dacke
Air Force Office of Scientific Research	FA9550-14-1-0242	Eric Warrant
Deutsche Forschungsgemeinschaft	EL784/1-1	Basil el Jundi
Deutsche Forschungsgemeinschaft	HO 950/24-1	Uwe Homberg
Deutsche Forschungsgemeinschaft	Me365/34	Randolf Menzel
Julius-Maximilians-Universität Würzburg		Keram Pfeiffer
Norwegian Research Council	287052	Bente G Berg

Freie Universität Berlin		Randolf Menzel
Swedish Research Council	2014 - 04623	Marie Dacke
Deutsche Forschungsgemeinschaft	HO 950/25-1	Uwe Homberg
Deutsche Forschungsgemeinschaft	HO 950/26-1	Uwe Homberg
Zukunftskolleg University of Konstanz		Randolf Menzel

The funders had no role in study design, data collection and interpretation, or the decision to submit the work for publication.

Author contributions

Stanley Heinze, Conceptualization, Resources, Data curation, Funding acquisition, Validation, Visualization, Writing - original draft, Project administration, Writing - review and editing; Basil el Jundi, Conceptualization, Funding acquisition, Validation, Writing - review and editing; Bente G Berg, Data curation, Supervision, Funding acquisition, Writing - review and editing; Uwe Homberg, Randolf Menzel, Keram Pfeiffer, Data curation, Supervision, Funding acquisition, Validation, Writing - review and editing; Ronja Hensgen, Data curation, Validation, Visualization, Writing - review and editing; Frederick Zittrell, Data curation, Software, Validation, Visualization, Writing - review and editing; Marie Dacke, Data curation, Funding acquisition, Validation, Writing - review and editing; Eric Warrant, Funding acquisition, Writing - review and editing; Gerit Pfuhl, Jürgen Rybak, Data curation, Validation, Writing - review and editing; Kevin Tedore, Conceptualization, Resources, Data curation, Software, Validation, Visualization, Methodology, Writing - original draft, Project administration, Writing - review and editing

Author ORCIDs

Stanley Heinze https://orcid.org/0000-0002-8145-3348
Basil el Jundi https://orcid.org/0000-0002-4539-6681
Bente G Berg https://orcid.org/0000-0003-4035-9125
Uwe Homberg https://orcid.org/0000-0002-8229-7236
Randolf Menzel https://orcid.org/0000-0002-9576-039X
Keram Pfeiffer https://orcid.org/0000-0001-5348-2304
Ronja Hensgen https://orcid.org/0000-0002-4876-9084
Frederick Zittrell http://orcid.org/0000-0001-7878-4325
Marie Dacke https://orcid.org/0000-0001-6444-7483
Eric Warrant https://orcid.org/0000-0001-7480-7016
Gerit Pfuhl https://orcid.org/0000-0002-3271-6447
Jürgen Rybak https://orcid.org/0000-0003-0571-9957
Kevin Tedore http://orcid.org/0000-0002-2722-8393

Decision letter and Author response

Decision letter https://doi.org/10.7554/eLife.65376.sa1
Author response https://doi.org/10.7554/eLife.65376.sa2

Additional files

Supplementary files

- Transparent reporting form

Data availability

All data underlying the figures of the paper are freely available in the insect brain database: https://insectbraindb.org/. Access to the database is free and can be achieved either by browsing https://

insectbraindb.org/ or by API access. Documentation see https://insectbraindb.org/static/IBdb_User-guide.pdf.

The following datasets were generated:

References

Armstrong JD, Kaiser K, Müller A, Fischbach KF, Merchant N, Strausfeld NJ. 1995. Flybrain, an on-line atlas and database of the *Drosophila* nervous system. *Neuron* **15**:17–20. DOI: https://doi.org/10.1016/0896-6273(95)90059-4, PMID: 7619521

Ascoli GA, Donohue DE, Halavi M. 2007. NeuroMorpho.Org: a central resource for neuronal morphologies. *Journal of Neuroscience* **27**:9247–9251. DOI: https://doi.org/10.1523/JNEUROSCI.2055-07.2007, PMID: 17728438

Bates AS, Manton JD, Jagannathan SR, Costa M, Schlegel P, Rohlfing T, Jefferis GS. 2020. The Natverse, a versatile toolbox for combining and analysing neuroanatomical data. *eLife* **9**:e53350. DOI: https://doi.org/10.7554/eLife.53350, PMID: 32286229

Brandt R, Rohlfing T, Rybak J, Krofczik S, Maye A, Westerhoff M, Hege HC, Menzel R. 2005. Three-dimensional average-shape atlas of the honeybee brain and its applications. *The Journal of Comparative Neurology* **492**:1–19. DOI: https://doi.org/10.1002/cne.20644, PMID: 16175557

Chiang AS, Lin CY, Chuang CC, Chang HM, Hsieh CH, Yeh CW, Shih CT, Wu JJ, Wang GT, Chen YC, Wu CC, Chen GY, Ching YT, Lee PC, Lin CY, Lin HH, Wu CC, Hsu HW, Huang YA, Chen JY, et al. 2011. Three-dimensional reconstruction of brain-wide wiring networks in *Drosophila* at single-cell resolution. *Current Biology* **21**:1–11. DOI: https://doi.org/10.1016/j.cub.2010.11.056, PMID: 21129968

de Vries L, Pfeiffer K, Trebels B, Adden AK, Green K, Warrant E, Heinze S. 2017. Comparison of Navigation-Related brain regions in migratory versus Non-Migratory noctuid moths. *Frontiers in Behavioral Neuroscience* **11**:158. DOI: https://doi.org/10.3389/fnbeh.2017.00158, PMID: 28928641

Dreyer D, Vitt H, Dippel S, Goetz B, El Jundi B, Kollmann M, Huetteroth W, Schachtner J. 2010. 3d standard brain of the red flour beetle tribolium castaneum: a tool to study metamorphic development and adult plasticity. *Frontiers in Systems Neuroscience* **4**:3. DOI: https://doi.org/10.3389/neuro.06.003.2010, PMID: 20339482

El Jundi B, Huetteroth W, Kurylas AE, Schachtner J. 2009a. Anisometric brain dimorphism revisited: implementation of a volumetric 3D standard brain in *Manduca sexta*. *The Journal of Comparative Neurology* **517**:210–225. DOI: https://doi.org/10.1002/cne.22150, PMID: 19731336

El Jundi B, Heinze S, Lenschow C, Kurylas A, Rohlfing T, Homberg U. 2009b. The locust standard brain: a 3D standard of the central complex as a platform for neural network analysis. *Frontiers in Systems Neuroscience* **3**:21. DOI: https://doi.org/10.3389/neuro.06.021.2009, PMID: 20161763

el Jundi B, Warrant EJ, Byrne MJ, Khaldy L, Baird E, Smolka J, Dacke M. 2015. Neural coding underlying the cue preference for celestial orientation. *PNAS* **112**:11395–11400. DOI: https://doi.org/10.1073/pnas.1501272112, PMID: 26305929

El Jundi B, Warrant EJ, Pfeiffer K, Dacke M. 2018. Neuroarchitecture of the dung beetle central complex. *Journal of Comparative Neurology* **526**:2612–2630. DOI: https://doi.org/10.1002/cne.24520, PMID: 30136721

Heinze S, Florman J, Asokaraj S, El Jundi B, Reppert SM. 2013. Anatomical basis of sun compass navigation II: the neuronal composition of the central complex of the monarch butterfly. *Journal of Comparative Neurology* **521**:267–298. DOI: https://doi.org/10.1002/cne.23214, PMID: 22886450

Heinze S, Reppert SM. 2012. Anatomical basis of sun compass navigation I: the general layout of the monarch butterfly brain. *The Journal of Comparative Neurology* **520**:1599–1628. DOI: https://doi.org/10.1002/cne.23054, PMID: 22473804

Immonen EV, Dacke M, Heinze S, El Jundi B. 2017. Anatomical organization of the brain of a diurnal and a nocturnal dung beetle. *Journal of Comparative Neurology* **525**:1879–1908. DOI: https://doi.org/10.1002/cne.24169, PMID: 28074466

Insect Brain Name Working Group, Ito K, Shinomiya K, Ito M, Armstrong JD, Boyan G, Hartenstein V, Harzsch S, Heisenberg M, Homberg U, Jenett A, Keshishian H, Restifo LL, Rössler W, Simpson JH, Strausfeld NJ, Strauss R, Vosshall LB. 2014. A systematic nomenclature for the insect brain. *Neuron* **81**:755–765. DOI: https://doi.org/10.1016/j.neuron.2013.12.017, PMID: 24559671

Ito K. 2010. Technical and organizational considerations for the long-term maintenance and development of the digital brain atlases and web-based databases. *Frontiers in System Neuroscience* **4**:26. DOI: https://doi.org/10.3389/fnsys.2010.00026

Kurylas AE, Rohlfing T, Krofczik S, Jenett A, Homberg U. 2008. Standardized atlas of the brain of the desert Locust, Schistocerca gregaria. *Cell and Tissue Research* **333**:125–145. DOI: https://doi.org/10.1007/s00441-008-0620-x, PMID: 18504618

Mayernik MS. 2017. Open data: accountability and transparency. *Big Data & Society* **4**:205395171771885. DOI: https://doi.org/10.1177/2053951717718853

Osumi-Sutherland D, Costa M, Court R, O'Kane CJ. 2014. Virtual fly brain - Using OWL to support the mapping and genetic dissection of the *Drosophila* brain. *CEUR Workshop Proceedings* **1265**:85–96. PMID: 29724079

Rybak J. 2012. The Digital Honey Bee Brain Atlas. In: Galizia C, Eisenhardt D, Giurfa M (Eds). *Honeybee Neurobiology and Behavior*. Dordrecht: Springer. p. 125–140. DOI: https://doi.org/10.1007/978-94-007-2099-2_11

Scheffer LK, Xu CS, Januszewski M, Lu Z, Takemura SY, Hayworth KJ, Huang GB, Shinomiya K, Maitlin-Shepard J, Berg S, Clements J, Hubbard PM, Katz WT, Umayam L, Zhao T, Ackerman D, Blakely T, Bogovic J, Dolafi T, Kainmueller D, et al. 2020. A connectome and analysis of the adult *Drosophila* central brain. *eLife* **9**:e57443. DOI: https://doi.org/10.7554/eLife.57443, PMID: 32880371

Stone T, Webb B, Adden A, Weddig NB, Honkanen A, Templin R, Wcislo W, Scimeca L, Warrant E, Heinze S. 2017. An anatomically constrained model for path integration in the bee brain. *Current Biology* **27**:3069–3085. DOI: https://doi.org/10.1016/j.cub.2017.08.052, PMID: 28988858

Wilkinson MD, Dumontier M, Aalbersberg IJ, Appleton G, Axton M, Baak A, Blomberg N, Boiten JW, da Silva Santos LB, Bourne PE, Bouwman J, Brookes AJ, Clark T, Crosas M, Dillo I, Dumon O, Edmunds S, Evelo CT, Finkers R, Gonzalez-Beltran A, et al. 2016. The FAIR guiding principles for scientific data management and stewardship. *Scientific Data* **3**:160018–160019. DOI: https://doi.org/10.1038/sdata.2016.18, PMID: 26978244